

DDC

AFWL-TR-77-34

AD-E-200 000
AFWL-TR-
77-34



AD A 046947

HIGH POWER LASER COUPLING

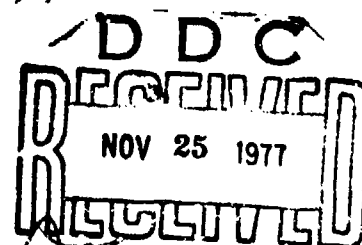
Boeing Aerospace Company
Seattle, WA 98124

June 1977

Final Report



Approved for public release; distribution unlimited.



AD NO. _____
DDC FILE COPY

Prepared for
ADVANCED RESEARCH PROJECTS AGENCY
1400 Wilson Boulevard
Arlington, VA 22209

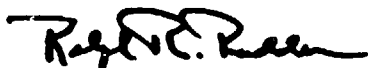
AIR FORCE WEAPONS LABORATORY
Air Force Systems Command
Kirtland Air Force Base, NM 87117

This final report was prepared by The Boeing Aerospace Company, Seattle, Washington, under Contract F29601-76-C-0030, Job Order 19051007 with the Air Force Weapons Laboratory, Kirtland Air Force Base, New Mexico. Dr. Ralph R. Rudder (PGV) was the Laboratory Project Officer-in-Charge.

When US Government drawings, specifications, or other data are used for any purpose other than a definitely related Government procurement operation, the Government thereby incurs no responsibility nor any obligation whatsoever, and the fact that the Government may have formulated, furnished, or in any way supplied the said drawings, specifications, or other data is not to be regarded by implication or otherwise as in any manner licensing the holder or any other person or corporation or conveying any rights or permission to manufacture, use, or sell any patented invention that may in any way be related thereto.

This report has been reviewed by the Office of Information (OI) and is releasable to the National Technical Information Service (NTIS). At NTIS, it will be available to the general public, including foreign nations.

This technical report has been reviewed and is approved for publication.

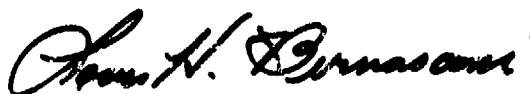


RALPH R. RUDDER
Project Officer

FOR THE COMMANDER



HECTOR REDE
Major, USAF
Chief, Effects & Vulnerability Branch



LOUIS H. BERNASCONI
Colonel, USAF
Chief, LEAPS Division

(18) AFWL, SBIE

UNCLASSIFIED

SECURITY CLASSIFICATION OF THIS PAGE (When Data Entered)

(19) REPORT DOCUMENTATION PAGE		READ INSTRUCTIONS BEFORE COMPLETING FORM
1. REPORT NUMBER AFWL-TR-77-34, AD-E2004000	2. GOVT ACCESSION NO.	3. RECIPIENT'S CATALOG NUMBER
4. TITLE (and Subtitle) HIGH POWER LASER COUPLING	5. TYPE OF REPORT & PERIOD COVERED Final Report	
7. AUTHOR(s) R. B. Hall, W. E. Maher, D. J. Nelson D. B. Nichols	8. CONTRACT OR GRANT NUMBER(s) F29601-76-C-0030	
9. PERFORMING ORGANIZATION NAME AND ADDRESS The Boeing Aerospace Company Seattle, Washington 98124	10. PROGRAM ELEMENT, PROJECT, TASK AREA & WORK UNIT NUMBERS 62301E/1905 (16) (17) 10	
11. CONTROLLING OFFICE NAME AND ADDRESS Advanced Research Projects Agency Arlington, Virginia 22209	12. REPORT DATE June 77	
14. MONITORING AGENCY NAME & ADDRESS (if different from Controlling Office) Air Force Weapons Laboratory (PGV) Kirtland Air Force Base, NM 87117	13. NUMBER OF PAGES 180-12 182p.	
15. SECURITY CLASS. (of this report) UNCLASSIFIED		15a. DECLASSIFICATION/DOWNGRADING SCHEDULE
16. DISTRIBUTION STATEMENT (of this Report) Approved for public release; distribution unlimited.		
17. DISTRIBUTION STATEMENT (of the abstract entered in Block 20, if different from Report)		
18. SUPPLEMENTARY NOTES		
19. KEY WORDS (Continue on reverse side if necessary and identify by block number) Laser Interactions DF-Laser Melt Removal Pulsed Lasers CO2 Laser Thermal Deposition Multi-Pulse Effects Chemical Laser Impulse Generation HF-Laser Laser Effects		
20. ABSTRACT (Continue on reverse side if necessary and identify by block number) A photoinitiated pulsed chemical laser has been developed for laser effects studies. This laser has produced 292 joules at 2.8 microns (HF) and 144 joules at 3.8 microns (DF). The threshold conditions for forming absorbing plasmas at atmospheric pressure have been extensively studied for both wavelengths and for seven materials. These thresholds have been measured in terms of both irradiance and fluence requirements. After forming a laser-supported absorption wave, the resulting plasma couples energy back.		

DD FORM 1473
1 JAN 73

EDITION OF 1 NOV 65 IS OBSOLETE

UNCLASSIFIED

SECURITY CLASSIFICATION OF THIS PAGE (When Data Entered)

059610

June

UNCLASSIFIED

SECURITY CLASSIFICATION OF THIS PAGE(When Data Entered)

20. ABSTRACT

to the target itself. For the conditions studied, all metal targets absorb a nearly constant energy above the plasma threshold. The plasma does spread radially, however, and the resulting spatial heating profile has been measured by inverting the time-dependent temperature at $r=0$. These measurements largely agree with measurements of thermal coupling to several targets of varying diameter and with both HF/DF radiation. Measurements of mass loss and impulse show a threshold dependence. In addition, the specific impulse and mass loss always have a maximum value at a particular laser irradiance. At 10.6 microns (CO_2), the plasma spreading magnitude has been measured as a function of laser delivered energy. A theoretical study of target melting and vaporization indicates that efficient melt removal can occur at high intensities. This occurs because high surface temperatures lead to vaporization. The resulting pressure gradients then force the molten layer out in the radial directions. Curves of this effect are given for aluminum, titanium, and molybdenum as a function of absorbed irradiance.

UNCLASSIFIED

SECURITY CLASSIFICATION OF THIS PAGE(When Data Entered)

PREFACE

This report on high power laser coupling was funded by ARPA/AFWL on Contract F29601-76-C-0030. The technical work was monitored by R. R. Rudder of the AFWL. The authors thank L. Alexander and D. Botz of The Boeing Company for their excellent assistance.

ACCESSION FOR	
NTIS	White Section <input checked="" type="checkbox"/>
DDC	Buff Section <input type="checkbox"/>
UNANNOUNCED	<input type="checkbox"/>
JUSTIFICATION	
BY	
DISTRIBUTION/AVAILABILITY CODES	
Dist.	AVAIL. and/or SPECIAL
A	

CONTENTS

<u>Section</u>	<u>Page</u>
I INTRODUCTION	11
II PULSED CHEMICAL LASER CHARACTERISTICS	13
1. Background	13
2. Reactor Modification	13
3. Effect of diluent	18
4. DF and HF Energies	23
5. Beam Characteristics	23
III THRESHOLD CONDITIONS FOR FORMATION OF PLASMAS BY HF AND DF RADIATION	30
1. Introduction	30
2. Theoretical Threshold Conditions for Ignition of Laser-Supported Absorption Waves	31
a. Simultaneous Fluence and Irradiance Requirements (e+q Model)	31
b. Simultaneous Bulk Temperature and Irradiance Requirements (T+q Model)	37
3. Experimental Method	40
4. Threshold Definition and Aluminum Results	44
5. Threshold Dependence on Target Material	49
IV THERMAL COUPLING OF HF LASER RADIATION TO METAL TARGETS	64
1. Thermal Coupling Coefficient	64
a. Method	64
b. Thermal Coupling at Large Fluences	65
c. Effect of Ambient Pressure	70
d. Effect of Pulse Length	74
2. Spatial Distribution of Thermal Coupling	74
a. Target Size Effects	77
b. Target Temperature as a Function of Time and Radius	78
c. Central Temperature as a Function of Time	81

CONTENTS (Continued)

<u>Section</u>	<u>Page</u>
V MASS LOSS AND TARGET IMPULSE DUE TO HF AND DF RADIATION	84
1. Mass Loss	84
2. Impulse	87
3. Impulse from Confined Plasma	89
VI LASER INTERACTION AT 10.6 MICRON WAVELENGTH	91
1. Experimental Apparatus	91
2. Thermal Coupling in the Absence of Transverse Air Flow	98
3. Thermal Coupling in the Presence of Air Flow	107
4. Image Converter Photography and Thresholds in the Presence of Air Flow	117
5. Experiments Using Melted Targets	117
VII MELT REMOVAL DYNAMICS DUE TO VAPORIZATION	121
1. Introduction	121
2. One-Dimensional Steady State Melting	129
3. Two-Dimensional Melt Removal	147
4. Time to Reach Steady State	154
5. Melt Removal by Pulsed Laser Beams	158
6. Effect of Gravity	164
VIII CONCLUSIONS	166
APPENDIX A: VAPOR PRESSURES AND EVAPORATION RATES	169
APPENDIX B: FUNCTIONS RELATED TO THE TWO-DIMENSIONAL HEAT FLOW SOLUTION	177
REFERENCES	179

ILLUSTRATIONS

<u>Figure</u>		<u>Page</u>
1	Diagram of Photoinitiated HF-DF Pulsed Chemical Laser	14
2	Variation of Laser Output as a Function of Flash Lamp Energy In. Circles Correspond to 1 atm Initial Pressure Containing 10% Fluorine. Squares are for 0.6 atm With 7.4% Fluorine. Hydrogen Fraction is 1.2% in Either Case.	15
3	Pulse Length versus Flash Lamp Energy. Conditions are Those of Figure 2.	16
4	Pulse Length as a Function of Output Energy. Conditions are Those of Figure 2.	17
5	Pulse Length Variation with Initial Gas Pressure	20
6	FWHM Pulse Length Plotted Against Inverse Pressure	21
7	FWHM Pulse Widths Available Using Nitrogen or Argon as Diluent	22
8	(a) Heavy Outline is Trace of Far-Field Beam Profile, Light Profile is an Analytic Approximation (b) Far-Field Scan Points	24
9	Far-Field Beam Profile Scans	26
10	Time Profile for HF Lasing	28
11	Time Profile for DF Lasing	29
12	Ratio of Fluence at Ignition Time to Incident Fluence as a Function of E_i/Se_t	32
13	Ratio of Fluence at Ignition Time to Incident Fluence as a Function of E_i/Se_t According to the e+q Model	35
14	Ratio of Fluence at Ignition Time to Incident Fluence as a Function of Q According to the T+q Model	41
15	Diagram of Target Room Optics and Experimental Arrangement	42
16	Incident (Lower) and Transmitted (Upper) DF Laser Intensity Profiles for $E_i = 44$ J	45
17	Incident (Lower) and Transmitted (Upper) DF Laser Intensity Profiles for $E_i = 83$ J	46

ILLUSTRATIONS (Continued)

<u>Figure</u>		<u>Page</u>
18	Transmitted Fraction of the Incident Beam Fluence Measured for Aluminum. Circles are HF, Triangles DF Data	47
19	Model Fits for e+q Model (Solid Lines) and T+q Model (Dotted Lines) to the Aluminum Data of Figure 18	50
20	Fluence Reaching an Aluminum Target Versus Incident Beam Fluence	51
21	Fluence Fraction Transmitted for Titanium. Circles are HF, Triangles DF Data.	52
22	Fluence Fraction Transmitted for Stainless Steel. Circles are HF, Triangles DF Data.	53
23	Fluence Fraction Transmitted for Nickel. Circles are HF, Triangles DF Data.	54
24	Fluence Fraction Transmitted for Copper. Circles are HF, Triangles DF Data.	55
25	Fluence Fraction Transmitted for Grafoil. Circles are HF, Triangles DF Data.	56
26	Fluence Fraction Transmitted for Lucite. Circles are HF, Triangles DF Data.	57
27	Comparison of Threshold Fluences for $f_i = 1$ for HF and DF Laser Radiation	60
28	Comparison of Threshold Fluences for $f_i = 0.5$ for HF and DF Laser Radiation	61
29	Comparison of Maximum Irradiances for $f_i = 1$ for HF and DF Laser Radiation	62
30	Comparison of Maximum Irradiances for $f_i = 0.5$ for HF and DF Laser Radiation	63
31	Thermal Coupling of HF Laser Radiation on Aluminum	66
32	Thermal Coupling of HF Laser Radiation on Titanium	67
33	Thermal Coupling of HF Laser Radiation on Stainless Steel	68
34	Thermal Coupling of HF Laser Radiation on Nickel	69
35	Thermal Coupling of HF Laser Radiation on Aluminum for Beam Spots with 0.46 cm Diameter (Circles) and 0.92 cm Diameter (Squares)	72

ILLUSTRATIONS (Continued)

<u>Figure</u>		<u>Page</u>
36	Dependence of Aluminum Thermal Coupling on Ambient Pressure at the Target	73
37	Effect of Pulse Length on Aluminum Thermal Coupling. Circles are for 4 μ sec FWHM Pulses. Triangles are for 7 μ sec FWHM Pulses.	75
38	Effect of Pulse Length on Titanium Thermal Coupling. Circles are for 4 μ sec FWHM Pulses. Triangles are for 7 μ sec FWHM Pulses.	76
39	Normalised Temperature as a Function of Radius and Time, Applicable for a Gaussian Initial Temperature Profile in a Thin Infinite Sheet of Aluminum	80
40	Measured Temperature as a Function of Radius and Time in a Thin Sheet of Aluminum	82
41	Lucite and Teflon Mass Removal by Pulsed HF Laser Radiation	85
42	Dependence of Lucite Mass Loss on Ambient Pressure at the Target $E_i = 85$ J	86
43	Specific Impulse Imparted to Aluminum by HF and DF Pulsed Laser Radiation	88
44	Comparison of Specific Impulse for Aluminum (Small Circles), Titanium (T), Stainless Steel (S), and Lucite (L)	90
45	Subsonic Transverse Flow Apparatus	93
46	Subsonic Transverse Flow System	94
47	Subsonic Transverse Flow Experimental Arrangement	95
48	Laser Beams and the Subsonic Transverse Flow Experimental Arrangement	96
49	Velocity Field of Subsonic Flow	97
50	Thermal Coupling to Nickel with Two Spot Sizes at One Atmosphere	99
51	Thermal Coupling to Titanium for Two Spot Sizes at One Atmosphere	100
52	Edge Effect in Enhanced Thermal Coupling for Two Target Materials	103

ILLUSTRATIONS (Continued)

<u>Figures</u>		<u>Page</u>
53	Heating Profile Gaussian Radius δ from Titanium Target Diameter Variation	105
54	Heating Profile Gaussian Radius δ from Aluminum Target Diameter Variation	106
55	Transverse Air Flow Effect on Thermal Coupling to Titanium Targets of 0.81 cm Diameter	109
56	Transverse Air Flow Effect on Thermal Coupling to Titanium Targets of 1.59 cm Diameter	110
57	Transverse Air Flow Effect on Thermal Coupling to Aluminum Targets of 0.81 cm Diameter	112
58	Transverse Air Flow Effect on Thermal Coupling to Aluminum Targets of 1.59 cm Diameter	113
59	Geometric Model for Flow Effect on Thermal Coupling Based on Data from Two Target Sizes	114
60	Flow-Caused Reduction in Energy Delivered to Target of Radius R_T by a Top Hat Thermal Coupling Profile of Radius R_H , Which Lasts a Time $(R_H = 0.5 R_T)/V$, Where $R_H \geq 0.5 R_T$	115
61	Vertical Arrangement for Melted Target Studies	118
62	Indium Targets Preheated to Just Above Melting Temperature and Extruded Through 0.16, 0.32, and 0.48 cm Diameter Holes by Laser Beam Target Interaction	120
63	Steady State Melt Thickness - Aluminum	123
64	Steady State Melting Velocity - Aluminum	125
65	Specific Melt Volume - Aluminum	126
66	Ratio of Beam Radius to Pressure Radius - Aluminum	127
67	Specific Impulse - Aluminum	128
68	Steady State Melt Thickness - Titanium	130
69	Steady State Melting Velocity - Titanium	131
70	Specific Melt Volume - Titanium	132
71	Specific Impulse - Titanium	133
72	Steady State Melt Thickness - Molybdenum	134

ILLUSTRATIONS (Continued)

<u>Figure</u>		<u>Page</u>
73	Steady State Melting Velocity - Molybdenum	135
74	Specific Melt Volume - Molybdenum	136
75	Specific Impulse - Molybdenum	137
76	Geometry of Laser-Melted Surface	138
77	The $N[A, w]$ Function	145
78	Surface Temperature of Aluminum	155
79	Reaction Pressure due to Evaporation of Aluminum	157
80	Radial Acceleration of Melt	160
81	Melt Removal by Pressure Pulsing and Coasting	163
92	Specific Heats	171
83	Vapor Pressures	173

TABLES

<u>Table</u>		<u>Page</u>
1	Selected Performance Characteristics of the Photoinitiated Pulsed Chemical Laser with the Teflon-Covered Wall	19
2	Spatial Profile Parameters for Beam Spot at the Focal Plane of Various Mirrors	27
3	Variation of Boundary x_0 ($x_0 = t/t_p$) Between Intensity and Temperature Controlled Thresholds p	40
4	Threshold Conditions in Terms of Incident Energy, Fluence and Irradiance	48
5	Threshold Conditions for Formation of Laser-Supported Absorption Waves	59
6	Thermal Coupling Thresholds Compared to $f_i = 0.5$ Pinhole Thresholds	71
7	Effective Gaussian Heating Radius	78
8	Results of Two-Parameter Fits of the Time-Dependent Temperature Measured at $R = 0$	83
9	Material Properties	140

SECTION I

INTRODUCTION

The main goal of this study of High Power Laser Coupling was to examine the coupling of laser energy to solid targets. To accomplish this goal, a broad spectrum of experiments was carried out at 2.8 and 3.8 micron wavelengths using the Boeing pulsed chemical laser ⁽¹⁾ and at 10.6 microns using the Marx Bank CO₂ laser. ⁽²⁾ During the course of this study, the energy output of the chemical laser was increased from 152 to 292 joules at HF wavelengths. In addition, operation at DF wavelength was developed yielding an energy of 144 joules. By operating the laser at various combinations of gas pressure and flashlamp voltages, laser effects have been studied at pulse lengths from 3 to 14 microseconds.

The laser described in Section II was used in an extensive series of plasma threshold experiments described in Section III. Seven materials were studied and thresholds were determined for HF and DF wavelengths. The materials include Lucite, Grafoil, aluminum, titanium, stainless steel, nickel, and copper. In general, it was found that the longer wavelength DF radiation yielded threshold significantly lower than HF radiation. Theoretical descriptions of plasma production thresholds were developed in terms of simultaneous fluence and irradiance requirements as well as simultaneous bulk temperature and irradiance requirements.

Section IV describes the results of thermal coupling experiments at both HF and DF wavelengths for several materials. In addition, a limited number of experiments were carried out over a range of ambient pressures. In almost all cases, it was found that the gross thermal coupling efficiency

-
1. Hall, R. B., Maher, W. E., McClure, J. D., Nichols, D. B., and Pond, C. R., "Laser Beam Target Interaction," Vol. I, 2.8 Microns Wavelength, AFWL-TR-25-342, July 1976.
 2. Maher, W. E., Hall, R. B., and Johnson, R. R., "Experimental Study of Ignition and Propagation of Laser-Supported Detonation Waves," J. Appl. Phys. 45, 2138, 1974.

followed the well-known trend.^(3,4) The coupling coefficient is nearly constant for low irradiances and then, at the plasma threshold, jumps in value. Above threshold there is a broad range of energies for which the total absorbed energy at the target is constant.

Section V describes impulse production and mass loss for both metal and ablative targets. It was found, as expected, that lucite (like other materials) has a threshold below which zero mass is lost. The maximum specific mass was found to be 0.18 gm/kJ and then decreases slowly as the incident fluence increases. An interesting aspect of impulse production was found in this series of experiments when an I/E value of 75 dyne-sec/joule was produced with a transparent target backed by an absorbing layer. Since most I/E ratios are less than 10, one notes that large impulse production occurs any time a nearly confined plasma is produced.

Section VI discusses new work on thermal coupling coefficients at CO₂ wavelengths. By using both different sizes of targets and an external air flow, the plasma coupling, due to plasma spreading, was determined. The width of this spreading was determined as a function of the incident laser energy.

Section VII is a theoretical study of melting and vaporization of targets of aluminum, titanium, and molybdenum. Curves of melt thickness, melting rate, and impulse production were obtained as a function of absorbed laser irradiance. It is found that high melting efficiencies can be obtained if a small amount of vaporization is allowed. Under this condition, the vapor pressure produces a radial outward force which removes the molten material. It is found, however, that melt removal by pulsed laser beams appears to be only marginally useful.

3. Rudder, R. R. and Augustoni, A. L., "Thermal Deposition Experiments with Microsecond Duration CO₂ Laser Radiation," Laser Digest, AFWL-TR-75-229, 1975.
4. Hall, R. B., Wei, P. S. P., and Maher, W. E., "Laser Beam Target Interaction," Vol. II, Laser Effects at 10.6 Microns, AFWL-TR-75-342, July 1976.

SECTION II

PULSED CHEMICAL LASER CHARACTERISTICS

1. BACKGROUND

In order to carry out laser effects studies over a wide range of parameters, the performance of the Boeing pulsed chemical laser was improved. This laser (PHOCL-10) was previously described;⁽¹⁾ a schematic of the device is shown in figure 1. It includes a mixing assembly for hydrogen and fluorine, and is initiated by U-shaped flashlamps which are internal to the reactor volume. Buffer cells isolate the cavity optics from the reacting gases. Both the flashlamp current pulse and the laser output pulse are typically 3 to 4 μ sec full width at half maximum (FWHM). The laser energy had reached 152 J, corresponding to 3.5% electrical efficiency before starting the present study.

2. REACTOR MODIFICATION

A uv-reflective teflon wall lining was installed in the laser reactor to increase the efficiency of fluorine dissociation by flashlamp radiation in the wavelength band 235 to 335 nm. Figures 2 to 4 show the variation of several performance characteristics as a function of input flashlamp energy, using the teflon covered wall with only two flashlamps. Figure 2 shows a maximum output energy from two lamps equal to that previously obtained with eight lamps with no uv reflector. The gas mixture is not identical, but a large part of this improvement from 3.5% to 14% electrical efficiency is due to the improved uv utilization.

Two gas conditions are shown in the figures. The circles correspond to a 1 atm mixture containing 10% fluorine; the squares are for a 0.6 atm mixture with 7.4% fluorine. The hydrogen fraction was 1.2% in either case. The lower-pressure mixture was motivated by an interest in controlling pulse length. Pulse lengths are displayed in figure 3. It is clear the conditions giving longer laser output pulses also give reduced output energy. This result is plotted explicitly in figure 4 where one obtains, for example, a pulse width of 5 μ sec with 80 J (joules) of laser energy.

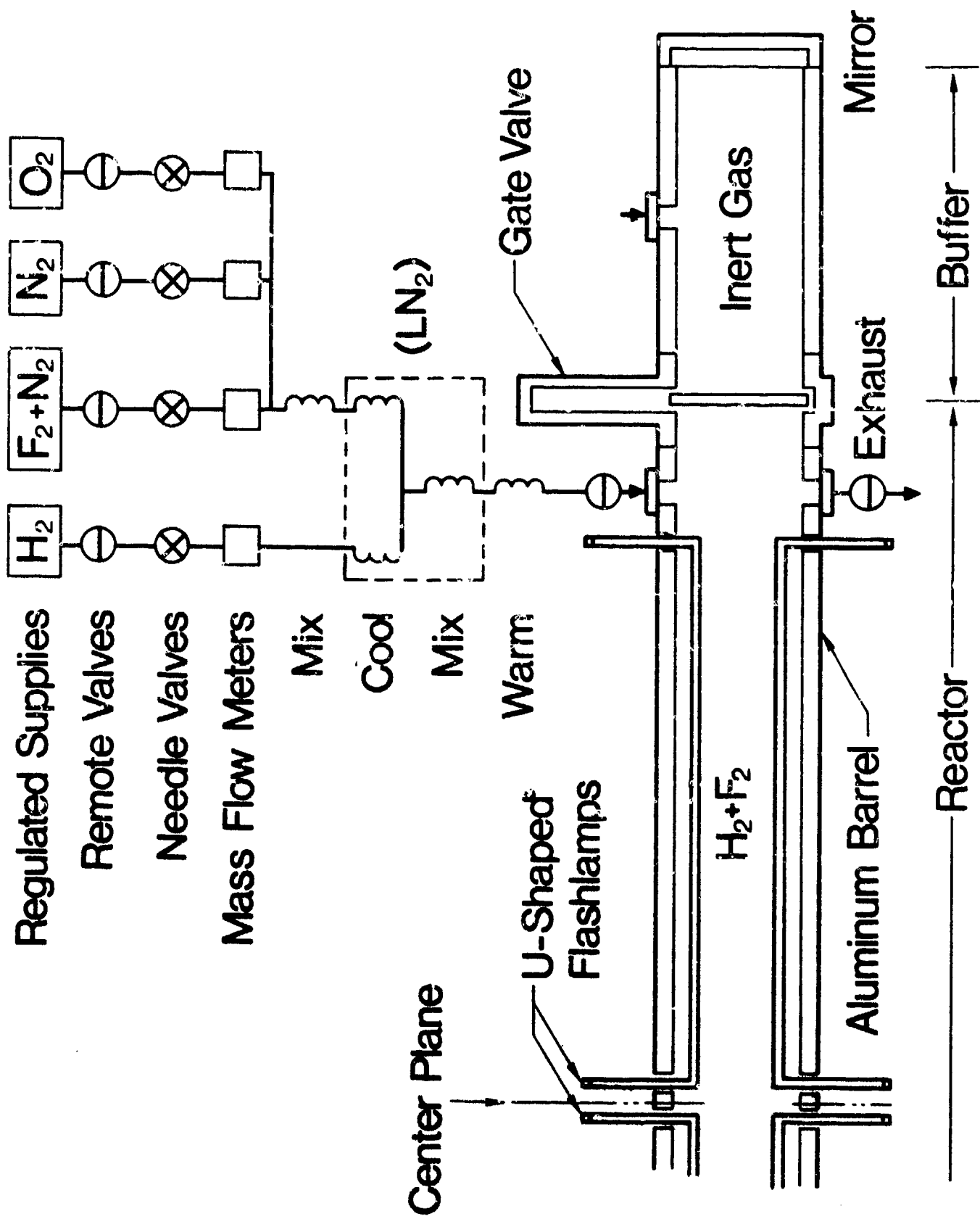


Figure 1. Diagram of Photoinitiated HF-DF Pulsed Chemical Laser

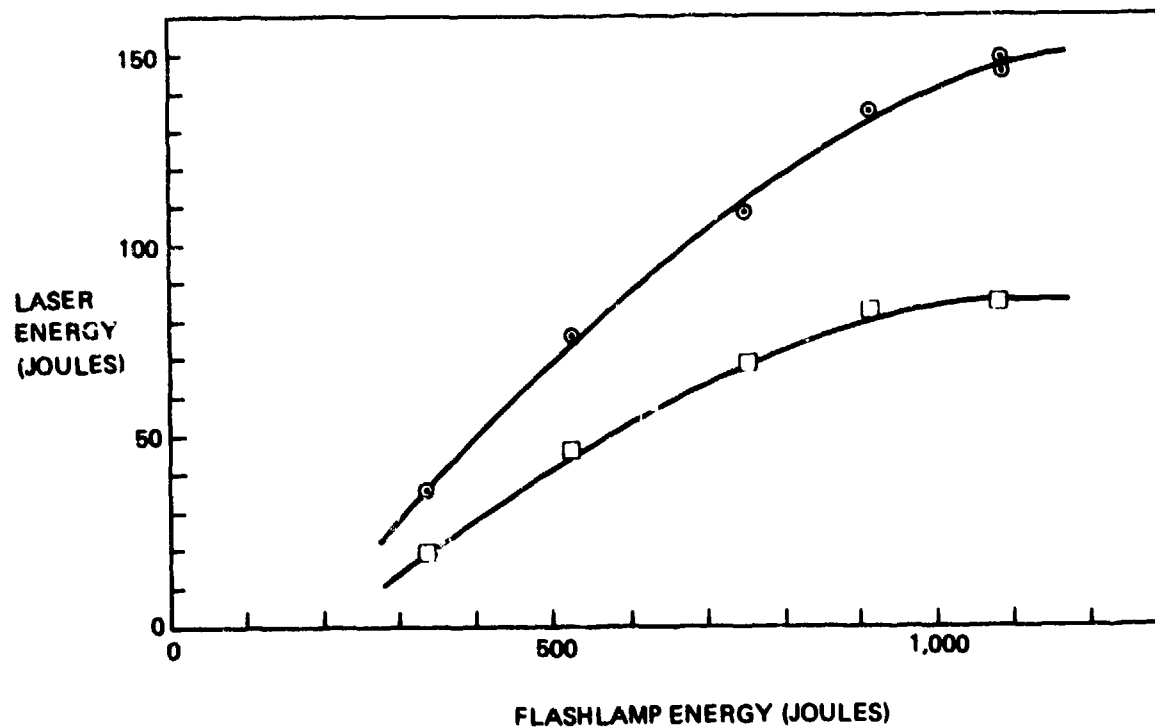


Figure 2. Variation of Laser Output as a Function of Flashlamp Energy In. Circles Correspond to 1 atm Initial Pressure Containing 10% Fluorine. Squares are for 0.6 atm With 7.4% Fluorine. Hydrogen Fraction is 1.2% in Either Case.

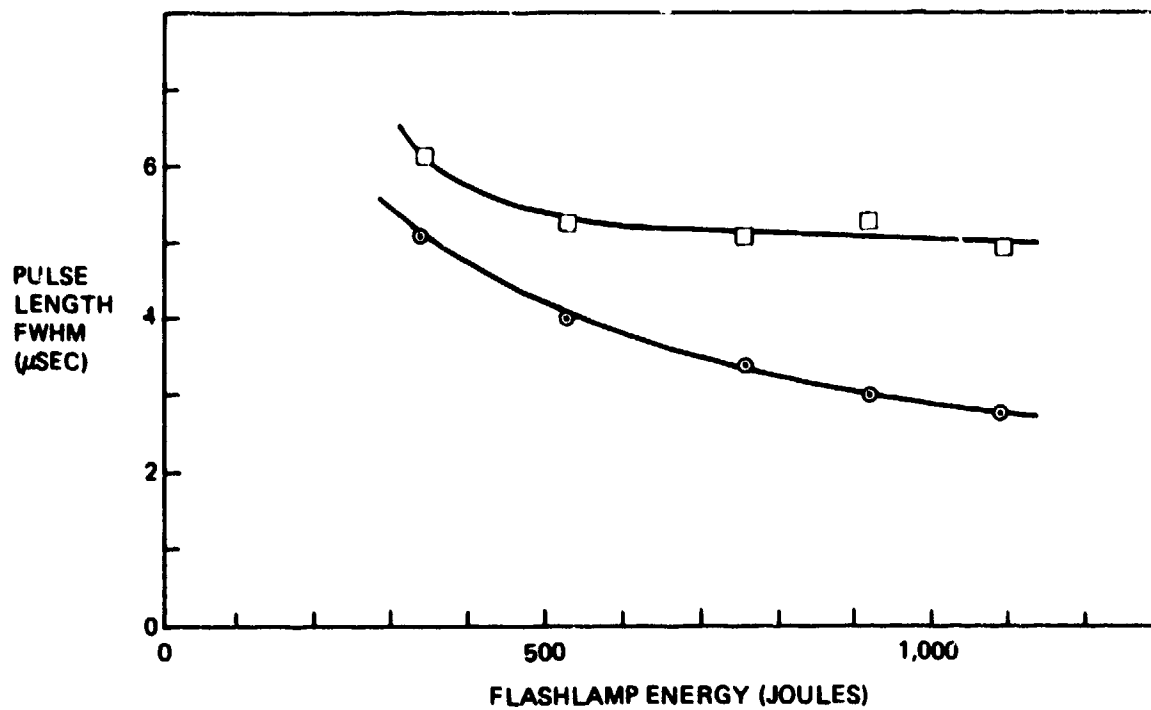


Figure 3. Pulse Length Versus Flashlamp Energy.
Conditions are Those of Figure 2.

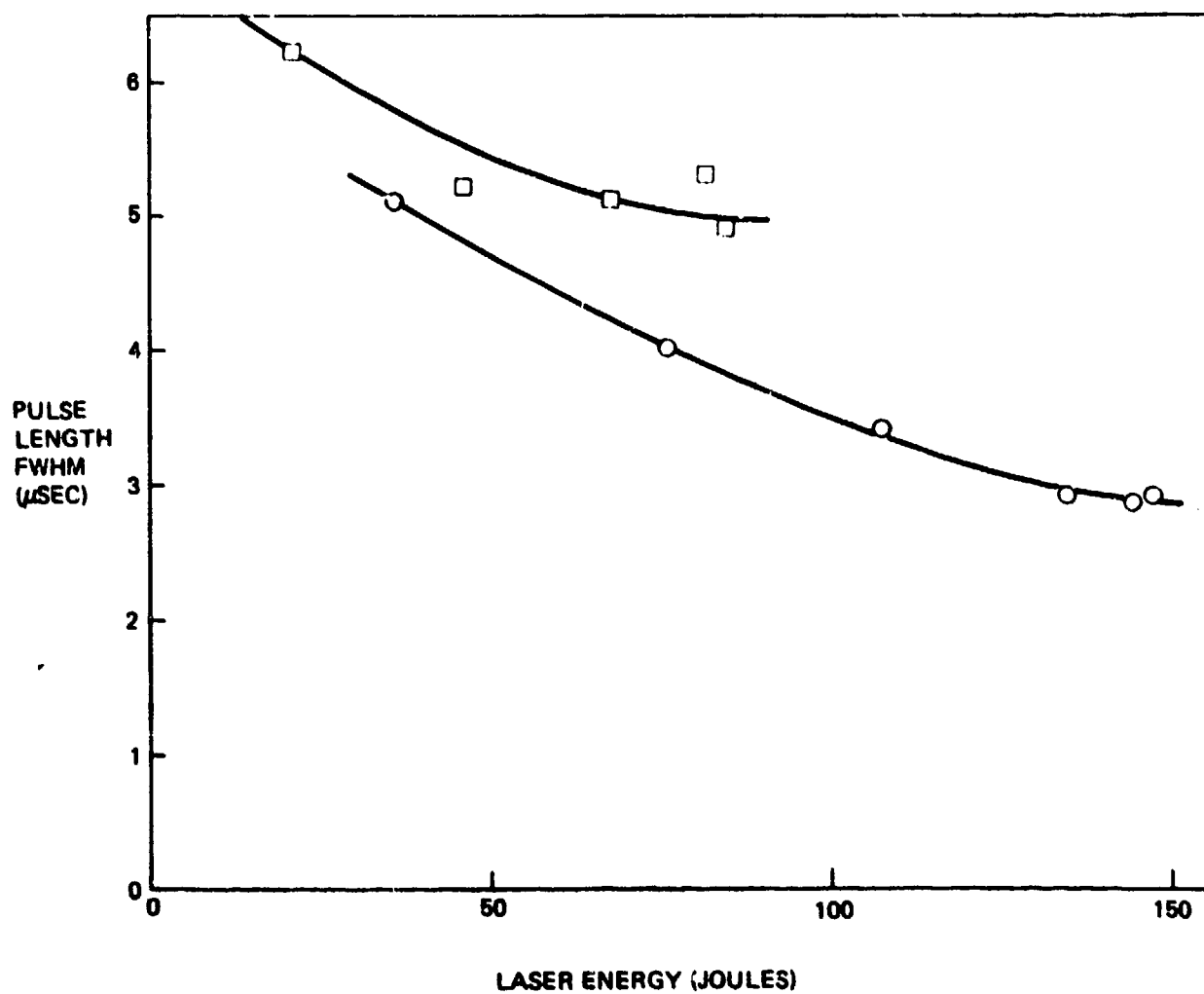


Figure 4. Pulse Length as a Function of Output Energy
Conditions are Those of Figure 2.

Table 1 shows several benchmark performance points obtained during the laser development phase of this work. The highest energy point of figure 2 is entered as the first line of table 1. Chemical and electrical efficiencies are denoted by η_c and η_e respectively.

The dependence of pulse length on the pressure of the gas mixture is shown in figure 5 over the range 0.2 to 1.0 atm for the mixture of line 1, table 1. Figure 6 shows that over most of this range, 0.3 to 1.0 atm, the pulse width varies approximately as the inverse pressure.

3. EFFECT OF DILUENT

The introduction of argon as diluent resulted in a considerable extension of several laser performance characteristics. Line 2 of table 1 shows a factor-of-two-improvement in electrical efficiency for argon compared with line 1 for nitrogen diluent. The associated differences in electrical properties of the two gases imposed some restrictions on the laser operating conditions available, but argon generally allowed the wider range of performance. The improved efficiency can be attributed in part to the lower heat capacity of argon and resulting differences in temperature-dependent rates in the H_2-F_2 reaction chain. An optimized electrical efficiency of 33% is shown in line 3 of table 1, with an output energy over 100 J.

The effort to control the laser pulse length with nitrogen diluent was continued with argon diluent. A condensed version of the results of this study is shown in figure 7, which includes both nitrogen and argon diluent results. Comparison of the general trend of argon data (triangles) with nitrogen data (circles) shows that for a given pulse length larger energy per pulse can be obtained with argon. Within each category, the solid symbols of figure 7 show the result of variation in flashlamp voltage and, therefore, flashlamp energy and level of initial photodissociation of fluorine. The open symbols show results of varying the initial gas mixture pressure. The nitrogen data (open circles) with increasing pulse width represent total pressures decreasing from 1.0 to 0.2 atm. The argon data (open triangles) with increasing pulse length represent pressures of 1.0, 0.8, and 0.6 atm. The longest pulse operation at 14 μ sec and 70 J is shown as line 4 of table 1.

TABLE 1

SELECTED PERFORMANCE CHARACTERISTICS OF THE PHOTOINITIATED PULSED CHEMICAL LASER WITH THE TEFLON-COVERED WALL. THE MOLAR FRACTION OF H_2 OR D_2 IS 1.2% AND THE MIXING TEMPERATURE IS AMBIENT. THE TWO OUTPUT COUPLERS ARE SAPPHIRE (87%) AND SILICON (54%).

Index No.	Lasant	Diluent	p(total) (atm)	O_2	F_2	No. of Lamps	Mirror Coupling	E(laser) (J)	FWHM (μ sec)	η_e (%)	η_c (%)
1	HF	N_2	1.0	0.25	10	2	87	<u>148</u>	2.9	<u>14</u>	3.3
2	HF	<u>Ar</u>	1.0	0.6	10	2	54	149	3.5	<u>29</u>	3.3
3	HF	Ar	1.0	0.6	10	2	54	109	5.0	<u>33</u>	2.4
4	HF	Ar	0.6	0.5	7.4	2	54	72	13.8	21	2.7
5	<u>DF</u>	Ar	1.0	0.6	10	4	87	144	3.8	14	4.0
6	HF	Ar	1.0	0.7	10	4	87	<u>292</u>	2.7	29	<u>8.1</u>

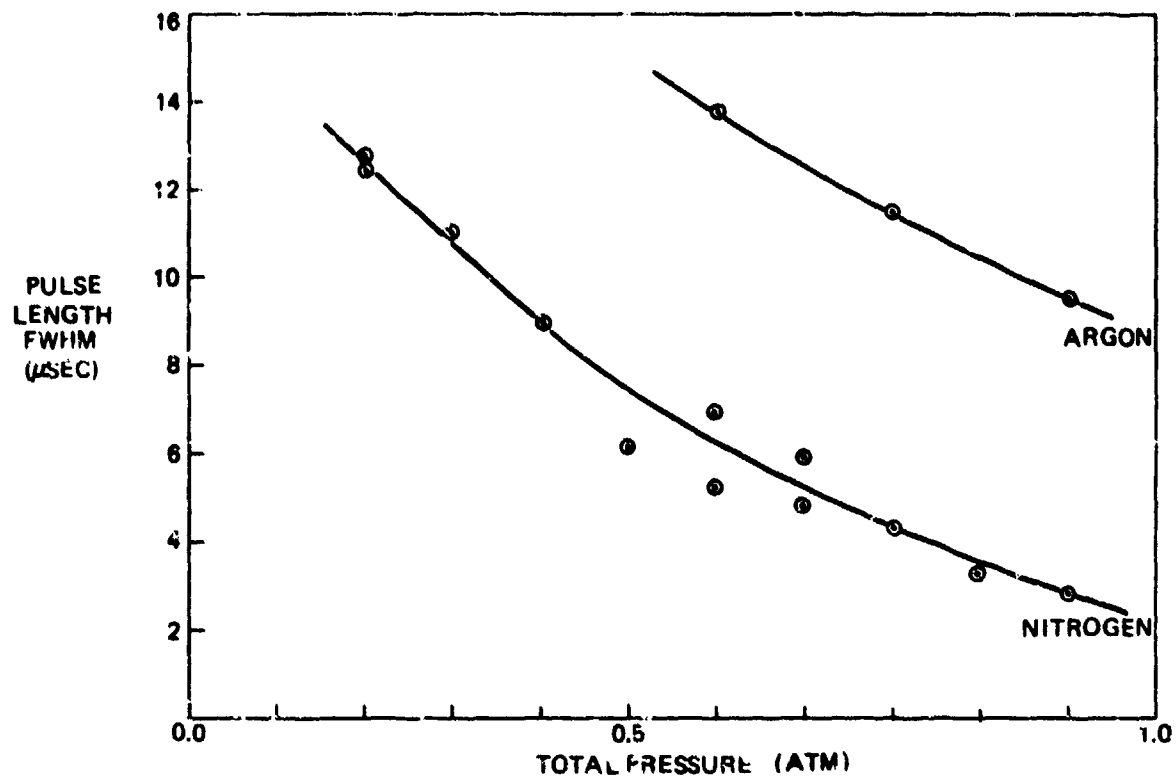


Figure 5. Pulse Length Variation with Initial Gas Pressure

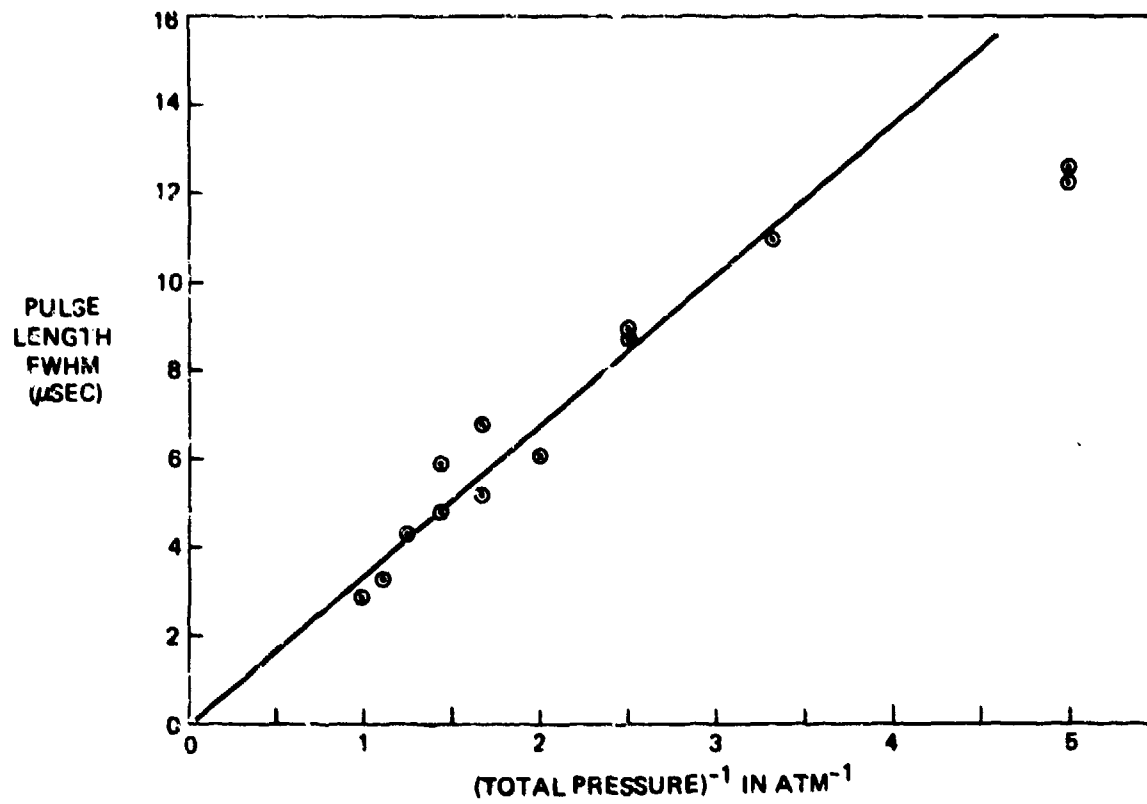


Figure 6. FWHM Pulse Length Plotted Against Inverse Pressure

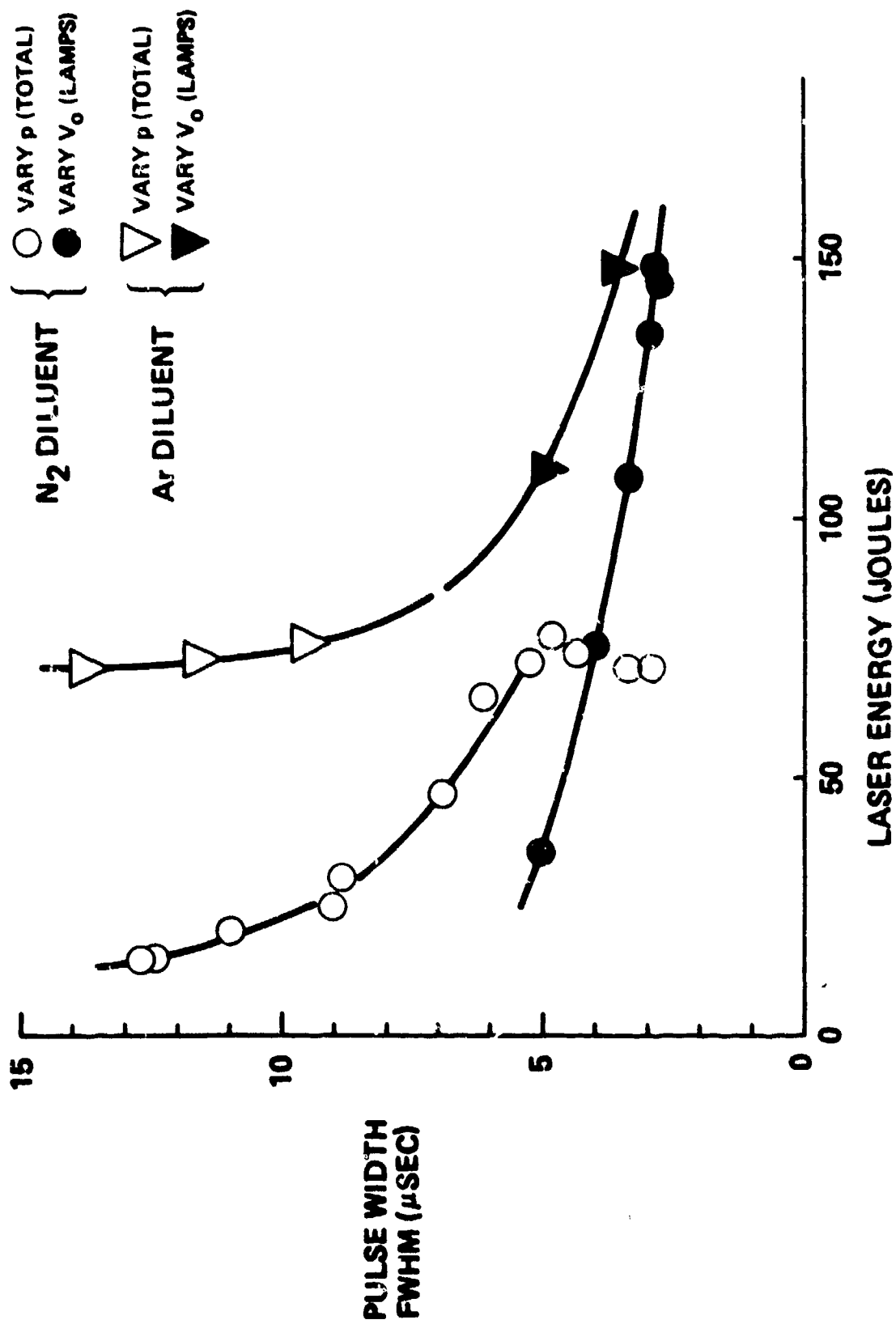


Figure 7. FWHM Pulse Widths Available Using Nitrogen or Argon as Diluent

4. DF AND HF ENERGIES

Efforts to introduce a DF output capability in this device began with nitrogen diluent with disappointing results. The substitution of argon as diluent, however, gave an order of magnitude improvement. Further measurements led to the conditions listed in line 5 of table 1, with 144 J energy, using four flashlamps and the teflon wall reflector.

For HF wavelengths, the use of the teflon wall reflector, argon diluent, and four flashlamps led to the optimum energy conditions listed in line 6 of table 1. The electrical efficiency is 29%, and the chemical efficiency is 8%. For both HF and DF wavelengths, this laser produces the largest energy per pulse, the highest electrical efficiency, and the highest chemical efficiency of any photoinitiated chemical laser reported. The device and its development are reviewed in reference 5; the spectral content of the HF beam is discussed in reference 6.

5. BEAM CHARACTERISTICS

The far-field HF beam profile was measured for the four-lamp laser configuration using the teflon wall lining and argon diluent. The measurements were made in the focal plane of the $f = 2$ m mirror.

The general shape of the focused beam spot, traced from the burn spot recorded on exposed Polaroid film, is shown as the dark curve in figure 8a. This pattern is a contour of equal fluence of about 3 j/cm^2 , or about 10% of the maximum. The four indentations in the pattern correspond to the four flashlamps in the reactor and their insulating feed-throughs. An analytic approximation to the burn pattern is shown as the light curve in figure 8a. In polar coordinates, this shape is given by

-
5. Nichols, D. B., Hall, R. B., and McClure, J. D., "Photoinitiation $\text{F}_2 + \text{H}_2/\text{D}_2$ Chain-Reaction Laser with High Electrical Efficiency," J. Appl. Phys. 47, 4026, 1976.
 6. Pond, C. R., Hall, R. B., and Nichols, D. B., "HF Laser Spectral Analysis Using Near-Field Holography," Appl. Opt. 16, 67, 1977.

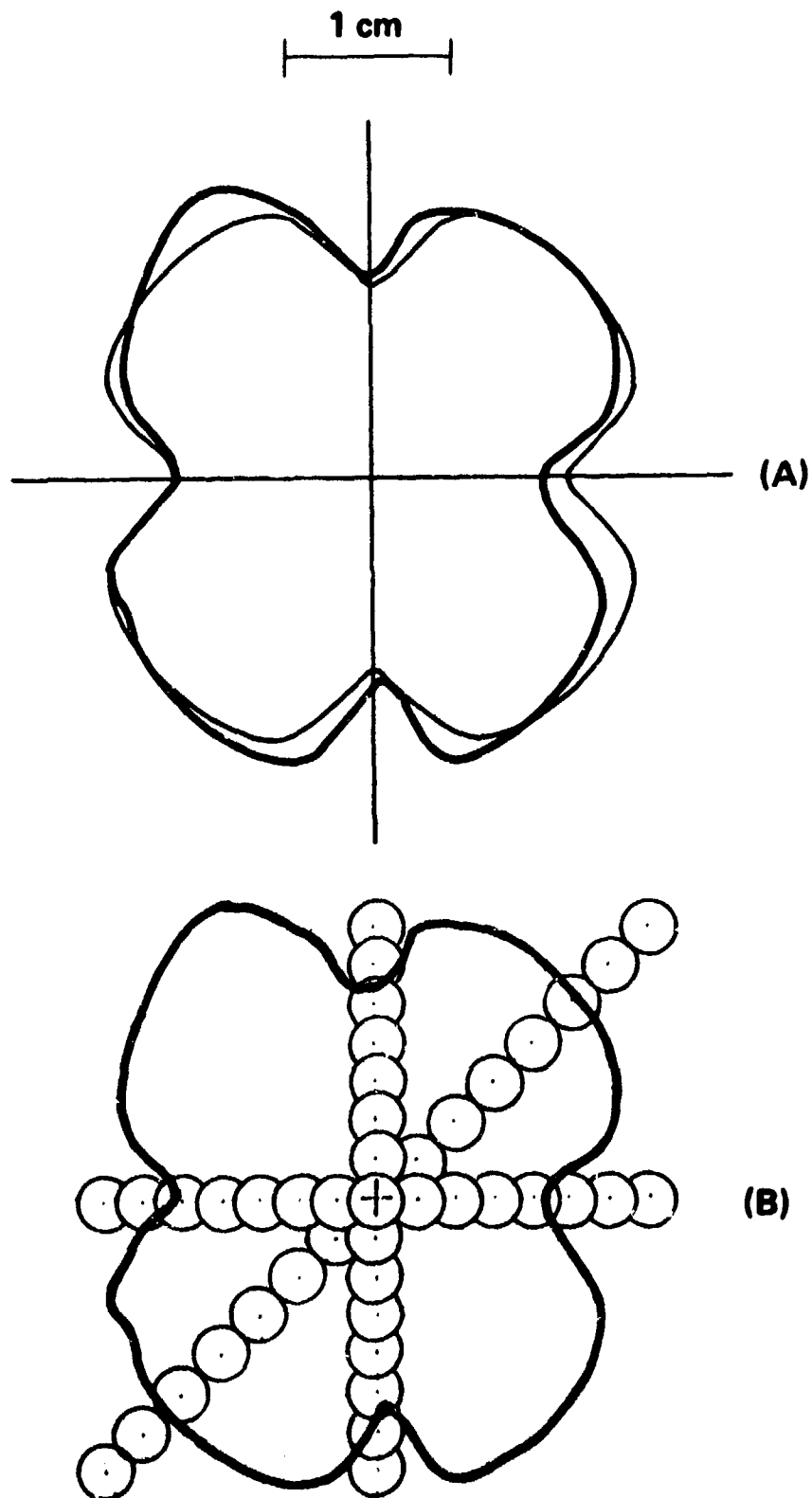


Figure 8. (a) Heavy Outline is Trace of Far-Field Beam Profile. Light Profile is an Analytic Approximation.

(b) Far-Field Scan Points

$$r(\theta) = a_0 - b \cos^8 (2\theta) \quad (1)$$

where $a_0 = 1.73$ cm and $b = 0.57$ cm.

Detailed beam scans were carried out in this same focal plane using a calorimeter apertured to 0.25 cm. Figure 8b shows schematically the three directions of scanning, illustrating the approximate size of the aperture and spacing of the data points on the beam spot. The results of these measurements are shown in figure 9. The high-intensity part of the beam profile is flat-topped as found previously for an eight-lamp configuration. The two scans which intersect the lamp notches show a reduced beam width as expected from the burn pattern. The largest FWHM (for the 45° scan) is 2.8 cm, giving a far-field beam divergence of 14 milliradians.

A "top-hat" approximation to the beam spot may be obtained either from the actual burn shape of figure 1 or from equation 1. The radius r_0 of this equivalent circle is related to the 45° scan radius a_0 by the factor

$$f_\theta = r_0/a_0 \quad (2)$$

where $f_\theta < 1$ due to the areas removed by the lamp images. Direct graphical analysis of the burn area gives $f_\theta = 0.89$. From equation 1, we obtain

$$S_0 = 2 \int_0^{\pi/2} \left\{ a_0 - b \cos^8 \phi \right\}^2 d\phi \quad (3)$$

which gives a similar value, $f_\theta = 0.92$.

As noted above, and from figure 8, the radius of the focal spot is mainly characterized by its 45° parameters. Thus, as noted from equation 2, the "0-averaged" radius r_0 is approximately 0.89 times the 45° radius. We now define the equivalent "top-hat" radius r_θ by

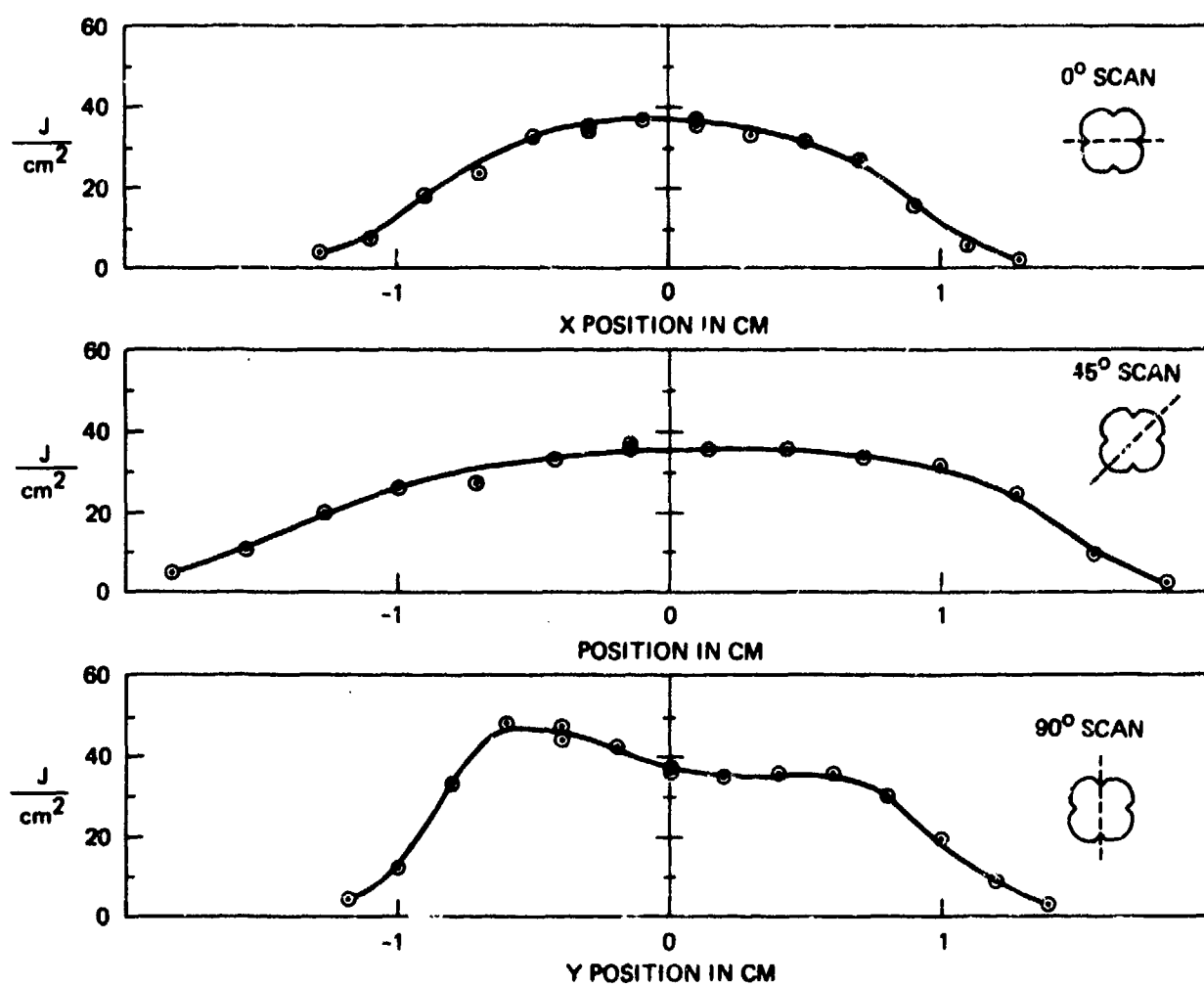


Figure 9. Far-Field Beam Profile Scans

$$\pi r_{\theta}^2 e_{\max} = 2\pi \int_0^{\infty} r e(r) dr \quad (4)$$

where $e(r)$ is the energy density profile at 45° shown in figure 9 and e_{\max} is $e(0)$. The integral in equation 4 was evaluated and $r_{\theta} = 1.38$ cm obtained. The overall effective radius of the laser beam r_1 is then defined by $r_1 = f_{\theta} r_{\theta}$ such that the incident laser energy $E_i = \pi r_1^2 e_{\max}$.

Table 2 summarizes the above defined beam spot characteristics for three mirror focal lengths used in this report.

TABLE 2

SPATIAL PROFILE PARAMETERS OF THE FOCUSED HF LASER BEAM FOR MIRRORS OF VARIOUS FOCAL LENGTHS F. THE VARIABLE θ REFERS TO EQUATION 1. ALL VALUES ARE IN CM.

Beam Spot Radius	f = 200	f = 76.2	f = 37.5
Radius a_0 (0.1 max, $\theta = 45^\circ$)	1.8	0.69	0.34
Radius r_{θ} (r-integrated, $\theta = 45^\circ$)	1.38	0.53	0.26
Radius r_1 (r-integrated, θ -integrated)	1.23	0.47	0.23

HF and DF laser pulse time profiles are shown in figure 10 and 11, respectively. Spikes are not a prominent feature of either profile. The HF pulse is quite symmetric with typical FWHM of 3.7 μ sec. The DF profile has a similar rise time but slightly longer duration, with FWHM typically 4.7 μ sec. These conditions generally apply to the chemical laser results in this report except for studies which explicitly incorporate laser pulse length as a variable.

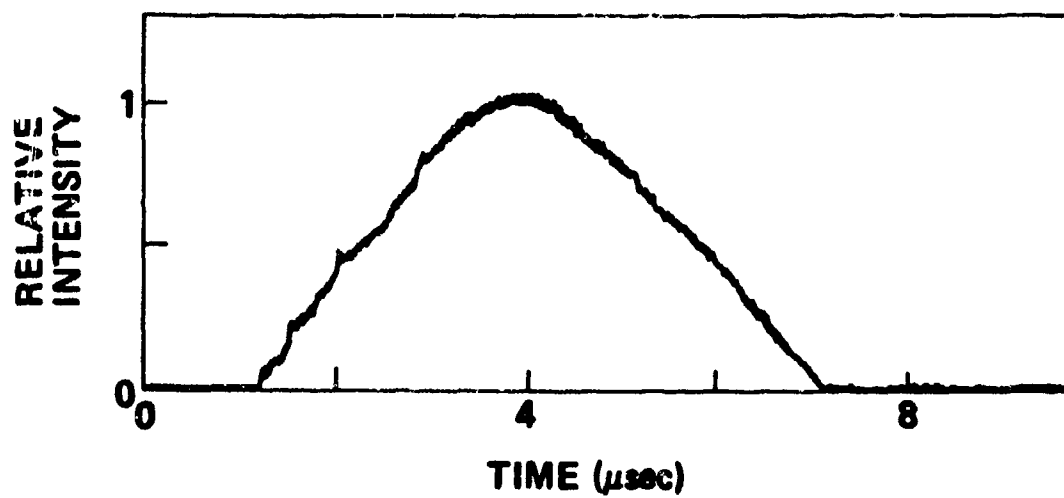


Figure 10. Time Profile for HF Lasing

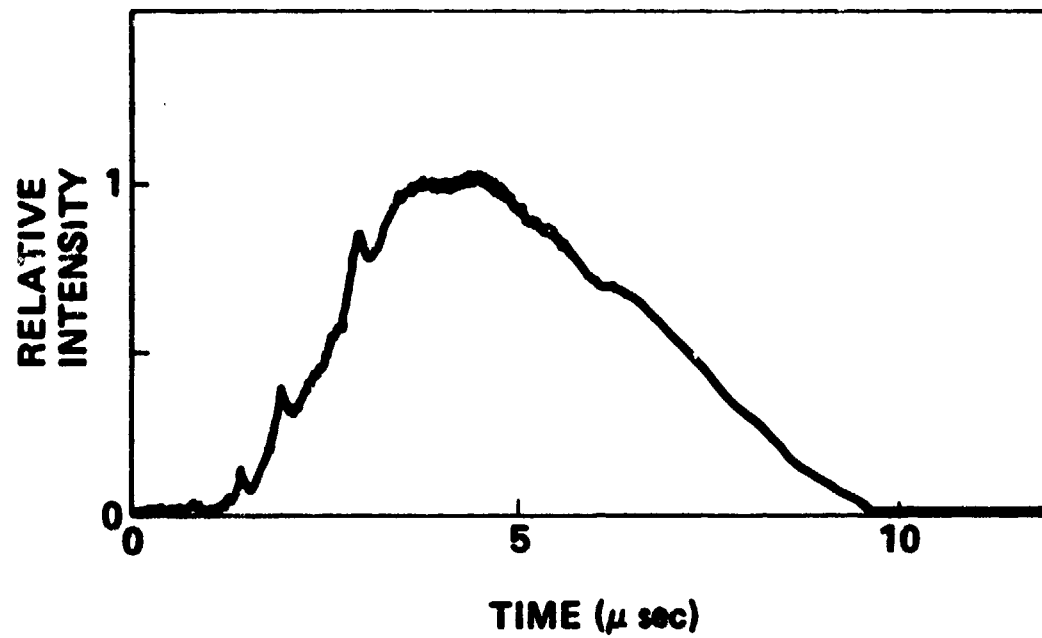


Figure 11. Time Profile for DF Lasing

SECTION III
THRESHOLD CONDITIONS FOR FORMATION OF
TARGET PLASMAS BY HF AND DF LASER RADIATION

1. INTRODUCTION

With increasing exposure of a target material to laser radiation, a point is reached, in terms of both accumulated energy deposition or instantaneous intensity, at which a plasma is formed at the target surface. Under these conditions, the plasma can become opaque to the incident radiation, shifting the principle site of energy deposition from the target surface to the plasma itself. Because this, in turn, sustains the plasma, one forms "laser-supported absorption (LSA) waves." ⁽⁷⁾ When the absorption length of the plasma is short, and the plasma front propagates up the incident laser beam at supersonic speeds, these waves are called "laser-supported detonation (LSD) waves."

Specification of the conditions for the formation of surface plasmas is of considerable interest, due to the wide variety of effects associated with these events. These effects include the enhancement of thermal coupling of the incident beam into the target material, ^(1,3) increased impulse imparted to the target, ^(8,9) and the ionization of both target and atmospheric species. ⁽²⁾

Although the formation of surface plasma is accompanied by several observables in both the target and surrounding media, definitions of the threshold condition have been largely confined to two categories. In the first, visible light from the plasma is observed, often by fast image

-
7. Raizer, Y. P., "Heating of a Gas by a Powerful Light Pulse," Soviet Physics JETP 21, 1009, 1965.
 8. Lowder, S. E. and Pettingill, L. C., "Double-Pulse Pressure and Impulse Measurements," Lincoln Laboratory Optics Research, No. 2., 1973, p. 29, April 24, 1974.
 9. Pirri, A. N., "Theory for Momentum Transfer to a Surface with a High-Power Laser," Phys. Fluids 16, 1435, 1973.

conversion.⁽²⁾ In the second, the developing opacity of the plasma to the incident radiation itself is detected. A third approach has been to detect plasma formation by its electrical conductivity.⁽¹⁰⁾

2. THEORETICAL THRESHOLD CONDITIONS FOR IGNITION OF LASER-SUPPORTED ABSORPTION WAVES

In this section we discuss the conditions necessary for the production and maintenance of dense plasmas near target surfaces. It is assumed that two simultaneous conditions must be satisfied in order to ignite an LSA wave.⁽¹¹⁾

a. Simultaneous Irradiance and Fluence Requirements (e+q Model)

First, it is assumed that the ignition of LSA waves occurs by heating of defects that are found in the surface of typical targets. In this case, the threshold condition is

$$C h T_v = e_t \text{ joules/cm}^2 \quad (5)$$

where h is the thickness of the thin defect, C is the heat capacity of the target material, and T_v is the vapor temperature corresponding to the ambient pressure.

It is similarly assumed that the laser irradiance at the surface q_0 must be greater than a threshold value q_t in order to maintain an LSA wave.

$$q_0 > q_t \quad (6)$$

Let us first assume the laser pulse is a step function of time of length t_p as shown in figure 12. For a focal spot area S and incident

10. Walters, C. T., Barnes, R. H., and Beverly, R. W., "An Investigation of Mechanisms of Initiation of Laser-Supported Absorption (LSA) Waves," Battelle Columbus Laboratories, Final Report on Contract DAAH01-73-A-0776, 1975.

11. Thomas, P. D. and Musal, H. M., "A Theoretical Study of Laser-Target Interaction," LMSC-D352890 Lockheed Missiles and Space Group Report, August 1973.

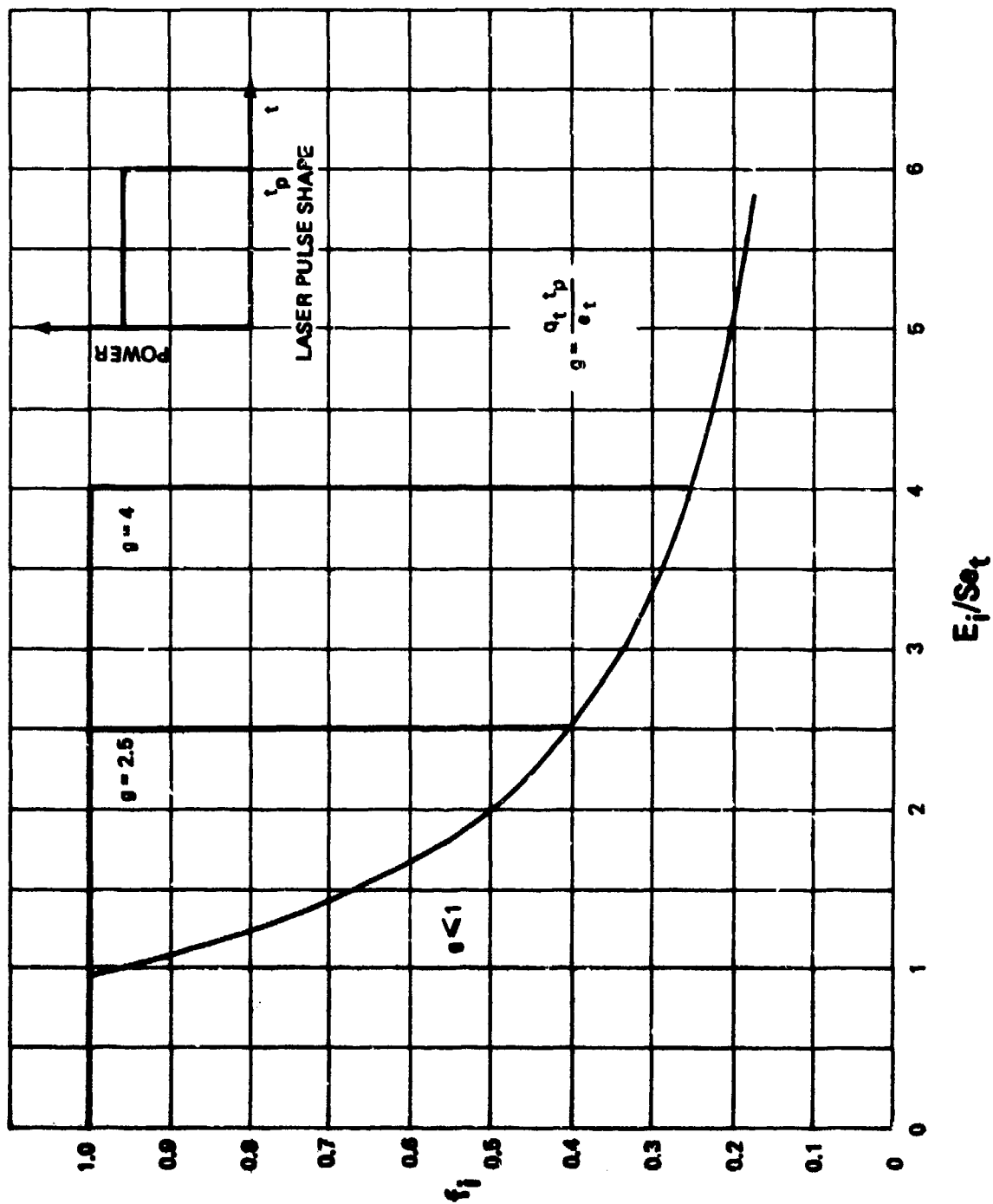


Figure 12. Ratio of Fluence at Ignition Time to Incident Fluence as a Function of E_i/Se_t

laser energy E_i , the laser intensity is

$$q_0 = \frac{E_i}{St_p} \quad (7)$$

We define the ratio of total fluence incident on the target at the time of LSA wave ignition to the total delivered fluence as

$$f_i = \frac{e(t)S}{E_i} \quad (8)$$

The additional requirement that the laser intensity be greater than the threshold irradiance leads to

$$E_i > S q_t t_p \quad (9)$$

If $q_t t_p < e_t$ the curve of f_i as a function of E_i is shown as the $g < 1$ curve of figure 12, where the parameter g is defined as

$$g = \frac{q_t t_p}{e_t} \quad (10)$$

For $g < 1$, the threshold fluence curves versus energy are again shown in figure 12. In general (for $E = E_i/Se_t$)

$$\left. \begin{aligned} f_i &= 1, & 0 < E < 1 \\ &= 1, & 1 < E < g \\ &= 1/E, & E < g \text{ (if } g < 1) \end{aligned} \right\} \quad (11)$$

For laser pulse shapes other than square, the situation is more complex. As an example, we next consider a laser pulse shape given by (see figure 13)

$$q = q_0 \left[1 - \left(\frac{t-t_p}{t_p} \right)^2 \right] \quad (12)$$

for $0 < t < 2t_p$. The peak laser irradiance q_0 occurs at $t = t_p$.

$$q_0 = \frac{3E_i}{4St_p} \quad (13)$$

The irradiance and fluence threshold requirements can be written

$$(3/4) E (2x-x^2) \geq g \quad (14)$$

$$(3/4) E (x^2-x^3/4) \geq 1 \quad (15)$$

where $x = t/t_p$.

When both of the conditions specified by equations 14 and 15 are met, the ratio of absorbed fluence to incident fluence (Se/E_i) is given by

$$\frac{Se}{E_i} = f_i = 3/4 (x^2-x^3/3) \quad (16)$$

For all cases, the threshold requirement for small x is determined by equation 15. For larger x , equation 14 controls the threshold requirements. The boundary x_0 between these two regions is

$$x_0 = \frac{3}{2} \left[1 + \frac{1}{9} - \sqrt{1 - \frac{2}{3g} + \frac{1}{9g^2}} \right] \quad (17)$$

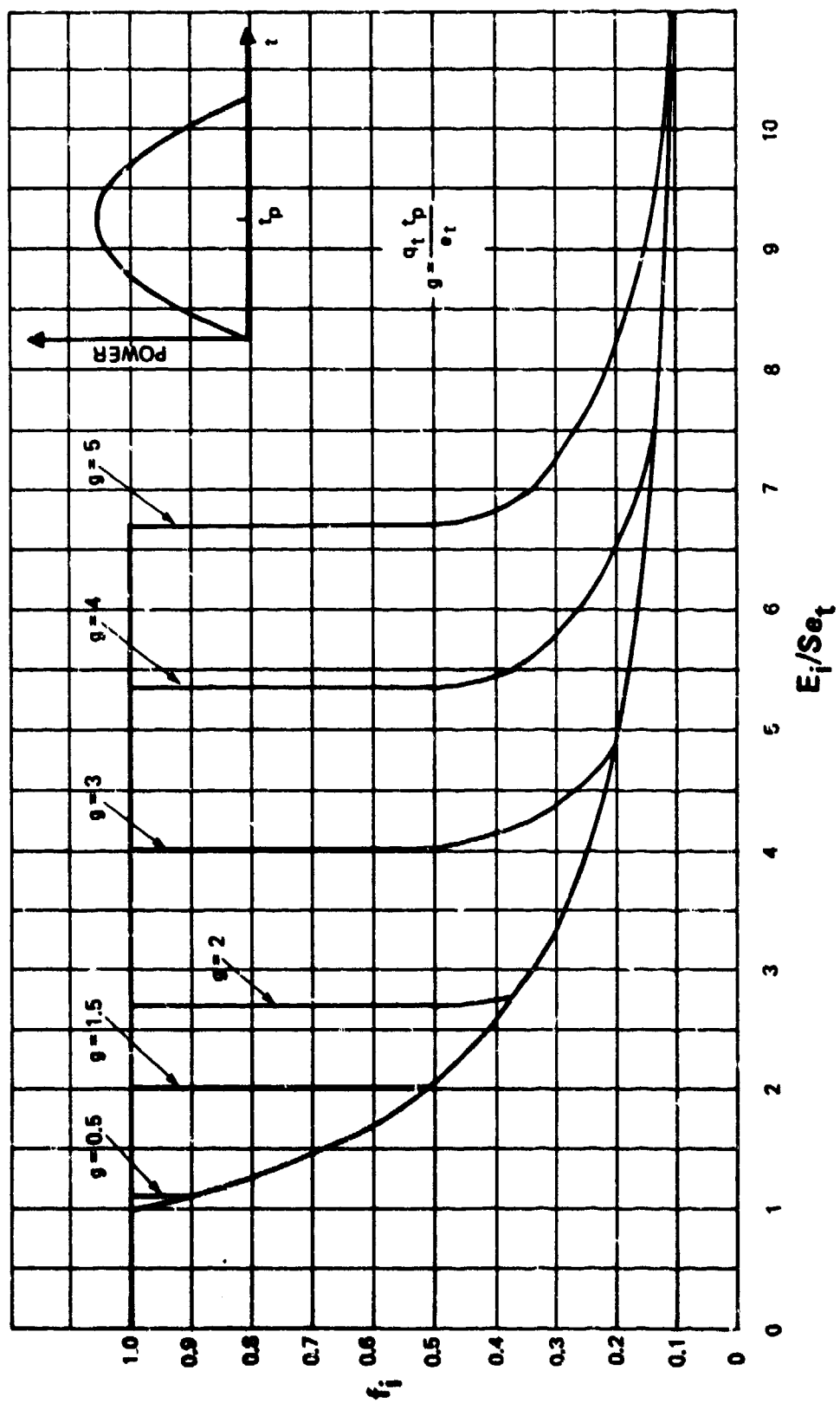


Figure 13. Ratio of Fluence at Ignition Time to Incident Fluence as a Function of E_i/Se_t

Thus, we find the conditions

$$E = \frac{4}{3(x^2 - x^3/3)}, \quad 0 < x < x_0 \quad (\text{for } x_0 > 1) \quad (18)$$

and no LSA waves are possible for $x > x_0$ (when $x_0 > 1$). When $x_0 < 1$, one finds

$$E = \frac{4}{3(x^2 - x^3/3)}, \quad 0 < x < x_0 \quad (19)$$

$$E = \frac{4g}{3(2x - x^2)}, \quad x_0 < x < 1$$

and no plasma waves are ignited for $x > 1$ (when $x_0 < 1$).

The procedure for determining curves of f_i vs. E_i/Se_t is based on first choosing a value of g and then computing x_0 from equation 17.

$$\begin{aligned} (1) \quad \text{For } x_0 > 1 \quad \left. \begin{aligned} f_i &= \frac{Se_t}{E_i} = \frac{1}{E}, \quad 0 < f_i < f_0 \\ \text{and where} \quad f_0 &= \frac{3}{4} (x_0^2 - \frac{1}{3} x_0^3) \end{aligned} \right\} \quad (20) \end{aligned}$$

and $f_i = 1$ otherwise.

$$(2) \quad \text{For } x_0 < 1 \quad f_i = 1/E, \quad 0 < f_i < f_0$$

For $x_0 < x < 1$, one obtains from equation 14

$$x = 1 - \sqrt{1 - \frac{4g}{3E}} \quad (21)$$

For a given value of E_i/Se_t , a value of x is computed and from this value f_i is obtained from equation 16.

It is easily seen from equation 17 that for $g < 1.5$ that $x_0 > 1$. In this case

$$\left. \begin{aligned} f_i &= 1, & 0 < E < \frac{4/3}{x_0^2 - \frac{1}{3}x_0^3} \\ f_i &= 1/E, & E > \frac{4}{3(x_0^2 - \frac{1}{3}x_0^3)} \end{aligned} \right\} \quad (22)$$

For $g > 1.5$, $x_0 < 1$ and one finds

$$\left. \begin{aligned} f_i &= 1/E, & E > \frac{4}{3(x_0^2 - \frac{1}{3}x_0^3)} \\ f_i &= \frac{1}{2} - \left(\frac{1}{2} + \frac{g}{3E} \right) \sqrt{1 - \frac{4g}{3E}}, & \frac{4g}{3} < E < \frac{4}{3(x_0^2 - \frac{1}{3}x_0^3)} \end{aligned} \right\} \quad (23)$$

Finally, for $g > 1.5$

$$f_i = 1, \quad E < \frac{4}{3}g \quad (24)$$

The above results are plotted in figure 13.

b. Simultaneous Bulk Temperature and Irradiance Requirements (T+q Model)

If the target surface is smooth (free of defects) or if the wavelength is short, one may have a threshold condition which depends on the surface temperature itself. Under the assumptions of: (1) a laser pulse shape given by equation 12, (2) a surface heating rate proportional to incident

irradiance q , and (3) one-dimensional heat diffusion into an infinitely thick target, the surface temperature as determined from Carslaw and Jaeger⁽¹²⁾ is

$$T(t)|_{x < 2} = \frac{8\alpha q_0}{3} \sqrt{\frac{t_p}{KC\pi}} x^{3/2} (1-2x/5) \text{ degrees K} \quad (25)$$

where $x = t/t_p$, α is the material absorptivity at the laser wavelength, K is the target thermal conductivity, and C is the target heat capacity. For $t > 2t_p$ ($x > 2$), the temperature declines continuously. The maximum surface temperature as found from equation 25 always occurs at $x = 3/2$.

It is now assumed that simultaneous temperature T_t and irradiance thresholds q_t must be surpassed in order to ignite an absorbing LSA wave. These conditions may be stated

$$Q > \frac{1}{x^{3/2} (1-2x/5)} \quad (26)$$

$$Q > \frac{h}{2x - x^2} \quad (27)$$

In equations 26 and 27, Q is the ratio of the laser peak irradiance q_0 divided by a target-dependent irradiance q_v .

12. Carslaw, H. S. and Jaeger, J. C., Conduction of Heat in Solids, Clarendon, Oxford, 1959.

$$\left. \begin{aligned} Q &= q_0/q_v \\ h &= q_t/q_v \\ q_v &= \frac{3T_t}{8\alpha} \sqrt{\frac{KC\pi}{t_p}} \end{aligned} \right\} \quad (28)$$

It is possible to consider q_v as an equivalent laser irradiance threshold required to raise the target to the threshold temperature T_t in time t_p . For an aluminum target with $\alpha = .06$ and $t_p = 3.5$ microseconds, one obtains $q_v = 3.4 \times 10^7$ watts/cm².

The threshold conditions given by equations 26 and 27 are analagous to the relationships indicated previously by equations 14 and 15. It is evident from the laser and temperature time variation that threshold requirements are not met for $x > 3/2$. It should also be noted that

$$Q = \frac{E_i}{S \left[\frac{T_t}{2\alpha} \sqrt{KC\pi t_p} \right]} \quad (29)$$

which is then of the form given previously. The dependence of Q on x follows equation 26 for small x and then for $x > x_0$ follows curve 27. The boundary x_0 is determined by equating the two expressions.

$$h \sqrt{x_0} \left(1 - \frac{2}{5} x_0 \right) = 2 - x_0 \quad (30)$$

Table 3 shows the dependence of x_0 on h obtained from equation 30.

TABLE 3
VARIATION OF BOUNDARY x_0 ($x_0 = t/t_p$) BETWEEN
INTENSITY AND TEMPERATURE CONTROLLED THRESHOLD

x_0	h
.2	4.37
.3	3.53
.4	3.01
.6	2.38
.9	1.81
1.1	1.53
1.3	1.28
1.5	1.021

Curves of the laser energy threshold f_i as a function of Q are obtained in different regions of Q as shown in Figure 14.

For $h < 1.02$ and $Q > 1.36$, the curve of f_i vs. Q is obtained by the simultaneous solution of equations 26 and 16. This threshold curve is then dependent only on target vaporization of bulk material. For $Q < 1.36$, $f_i = 1.0$.

For $1.36 < Q < 1.67$, a discontinuity in f_i occurs at $Q = h$ at which the value of f_i drops from 1.0 to the above-determined curve for $h < 1.02$.

For $Q > 1.67$, $f_i = 1$ for $0 < Q < h$. At $Q = h$, a discontinuity occurs reducing f_i to 0.5. For $h < Q < Q_0$ the curve of f_i vs. Q is determined by simultaneous solution of 27 and 16. (The value Q_0 is that value of Q occurring at $x = x_0$.) For $Q > Q_0$, f_i again follows the $h < 1.02$ curve.

3. EXPERIMENTAL METHOD

In the present work, plasma formation threshold was determined by observing the cutoff of incident laser radiation transmitted through a small hole in the target.⁽¹⁾ The main elements of the experimental arrangement are shown schematically in figure 15. Two sample beams of about 3%

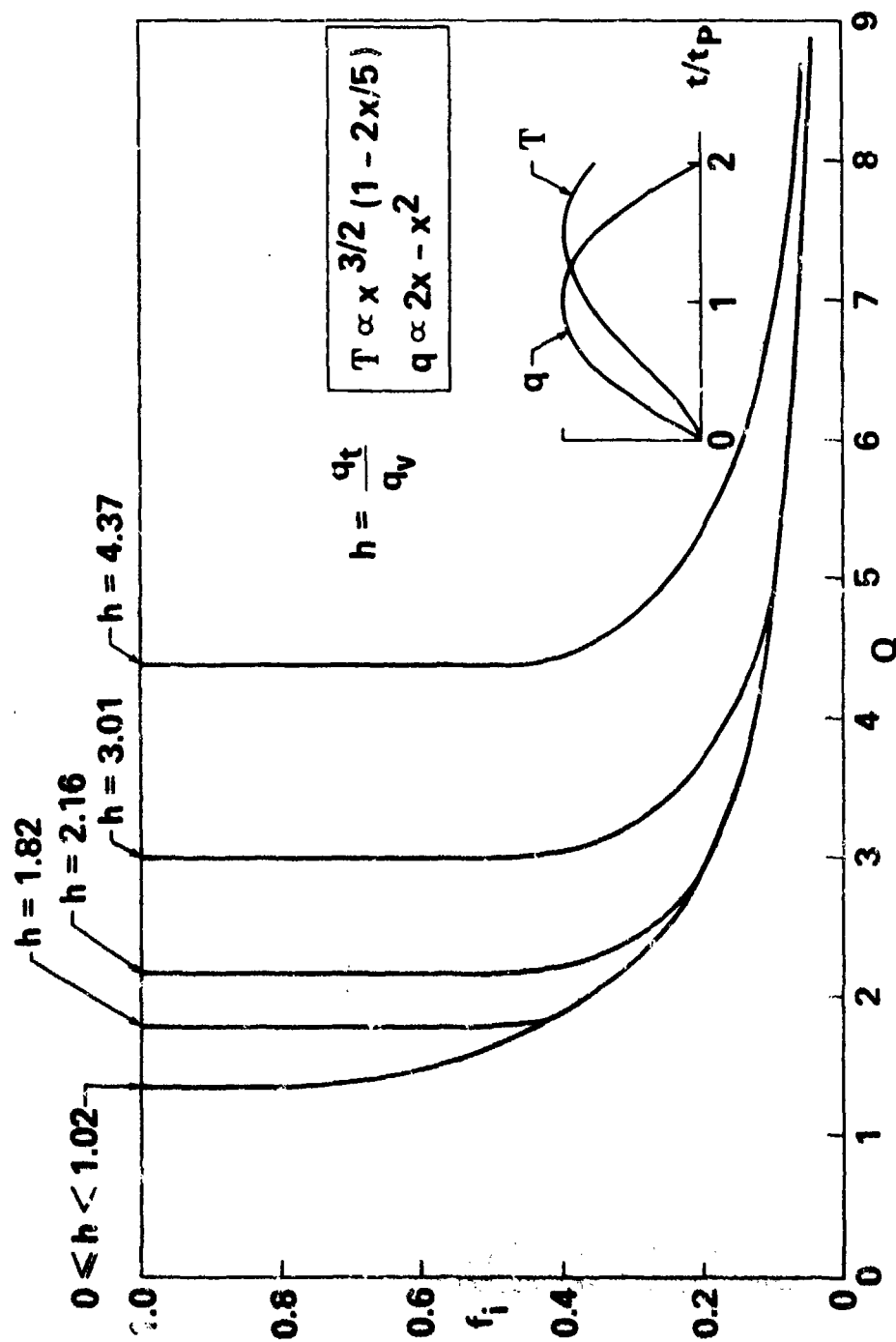


Figure 14. Ratio of Fluence at Ignition Time to Incident Fluence as a Function of Q According to the T+q Model

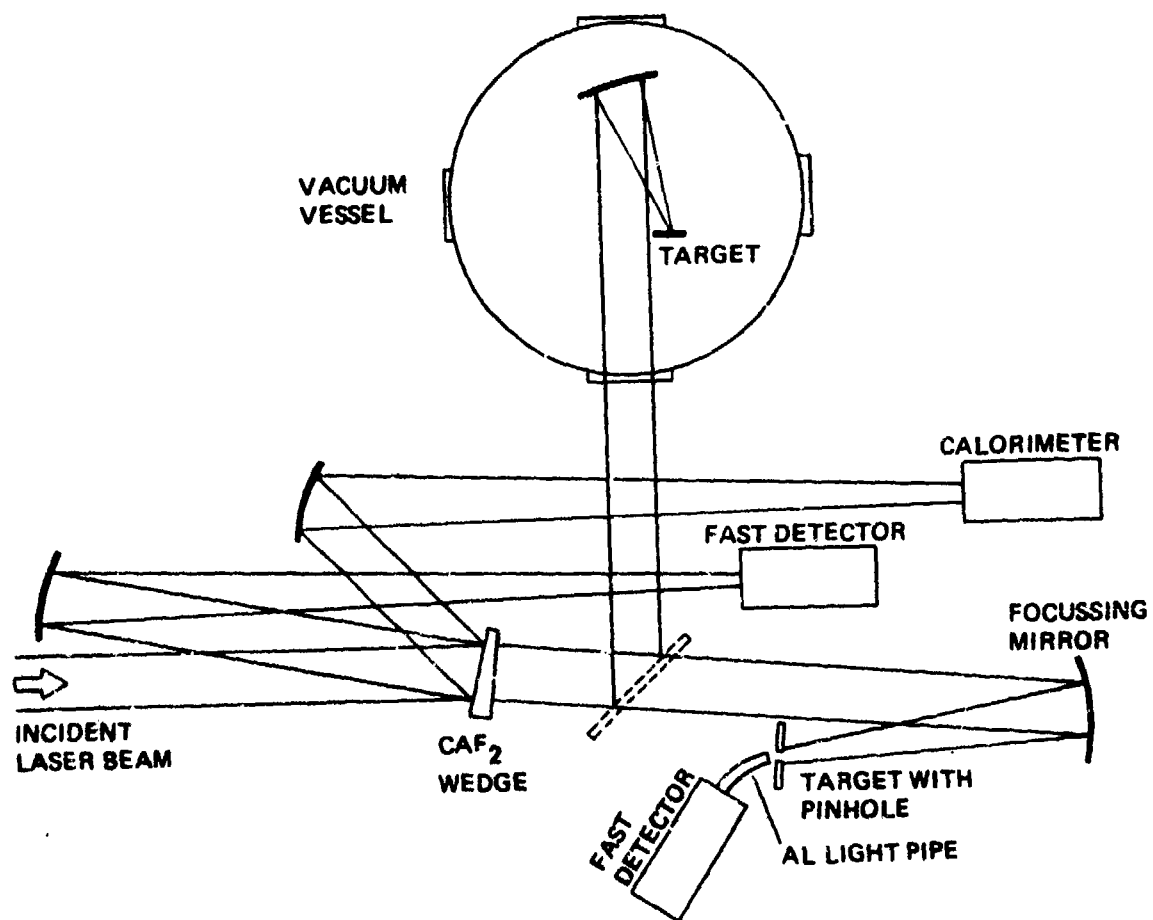


Figure 15. Diagram of Target Room Optics and Experimental Arrangement

each are taken from the primary chemical laser beam which is incident from the left in figure 15. One of these beams is directed to a calorimeter (Sciencetech Model 3604). The other beam is focussed by a 165 cm focal length mirror into a reflective diffuser and a Ge(Au) detector, giving a laser pulse time profile representative of the entire beam cross section. The main beam goes on to the target focussing mirror.

A second calorimeter was placed at the target position and was used to calibrate the energy monitor. Beam paths from the CaF_2 beam splitter to the monitor calorimeter and to the target position are set approximately equal so that small daily variations in the atmospheric water vapor content and hence in the atmospheric absorption coefficient for HF laser radiation are compensated. DF absorption over these distances is negligible. The optional beam path to the vacuum sphere is also shown and was used for the work reported in Section V.

For the present threshold measurements targets were situated at the focus of a 76-cm focal length mirror and were oriented at 8° to the incident beam normal to prevent feedback from specularly reflective targets into the laser and calorimeter. For large f -number mirrors this effect can also distort the far-field spatial profile by redistributing the energy at the mirror focal plane. The beam spatial profile is described in Section II, and has an effective diameter of 0.94 cm for this mirror. The HF and DF far-field profiles are nearly identical. The HF time profile shown in Section II has 3.7 μsec FWHM; the DF pulse is about 25% longer.

The seven materials tested included five metals plus Grafoil and Lucite. The metal samples were discs with 2.22 cm diameter and 0.13 cm. thickness. The Grafoil samples were 0.025 cm thick and 2.54 cm square. The Lucite samples were 2.54 cm squares with 0.33 cm thickness. All materials were tested in the "as received" condition; the only surface preparation was cleaning with methanol before exposure. A new target was used for each laser shot.

The target arrangement for threshold measurements is shown schematically in figure 15. Pinholes 0.7 mm in diameter were centered in each target. A short aluminum light pipe led from this hole to an attenuating diffuser and a second Ge(Au) detector with characteristics matching those of the other fast detector. During the exposure of the target to a laser pulse, intensity time profiles were simultaneously recorded as illustrated in figure 16, for (1) the full beam (lower trace) and (2) the laser radiation transmitted through the pinhole (upper trace), which is truncated by the formation of an LSA wave.

4. THRESHOLD DEFINITION AND ALUMINUM RESULTS

A threshold time t_i is defined as the time at which the transmitted intensity falls to 50% of the uninterrupted value, and the fraction of the total pulse energy (or fluence) delivered before t_i is designated f_i ; f_i is referred to as the "transmitted fraction" of the incident beam fluence

Thresholds will be discussed in terms of three quantities: (1) total pulse incident energy E_i is the total energy directed toward the target. (2) Target fluence e_t is the time-integrated fluence reaching the target before cutoff, or $E_i f_i / S$ where S is the beam spot area. (3) Maximum target irradiance q_m is the largest irradiance which reaches the target. This maximum occurs at ignition time t_i if t_i is before the pulse peak time t_0 ; if $t_i > t_0$, q_m is simply the peak irradiance of the incident pulse.

We have shown previously ⁽¹⁾ that threshold values of each of these three quantities depend strongly on whether LSA ignition occurs early or late in the pulse. Thus each of these thresholds is a function of t_i , or more conveniently f_i . Thresholds previously reported with no reference to an associated f_i are ambiguous.

Figure 16 shows the two detector time profiles for a 44-J DF laser pulse on Al 6061; the transmitted fraction $f_i = 0.71$. In figure 17 the laser pulse energy is increased to 83 J, advancing the plasma ignition to an earlier time, giving $f_i = 0.15$. Figure 18 is a plot of f_i versus

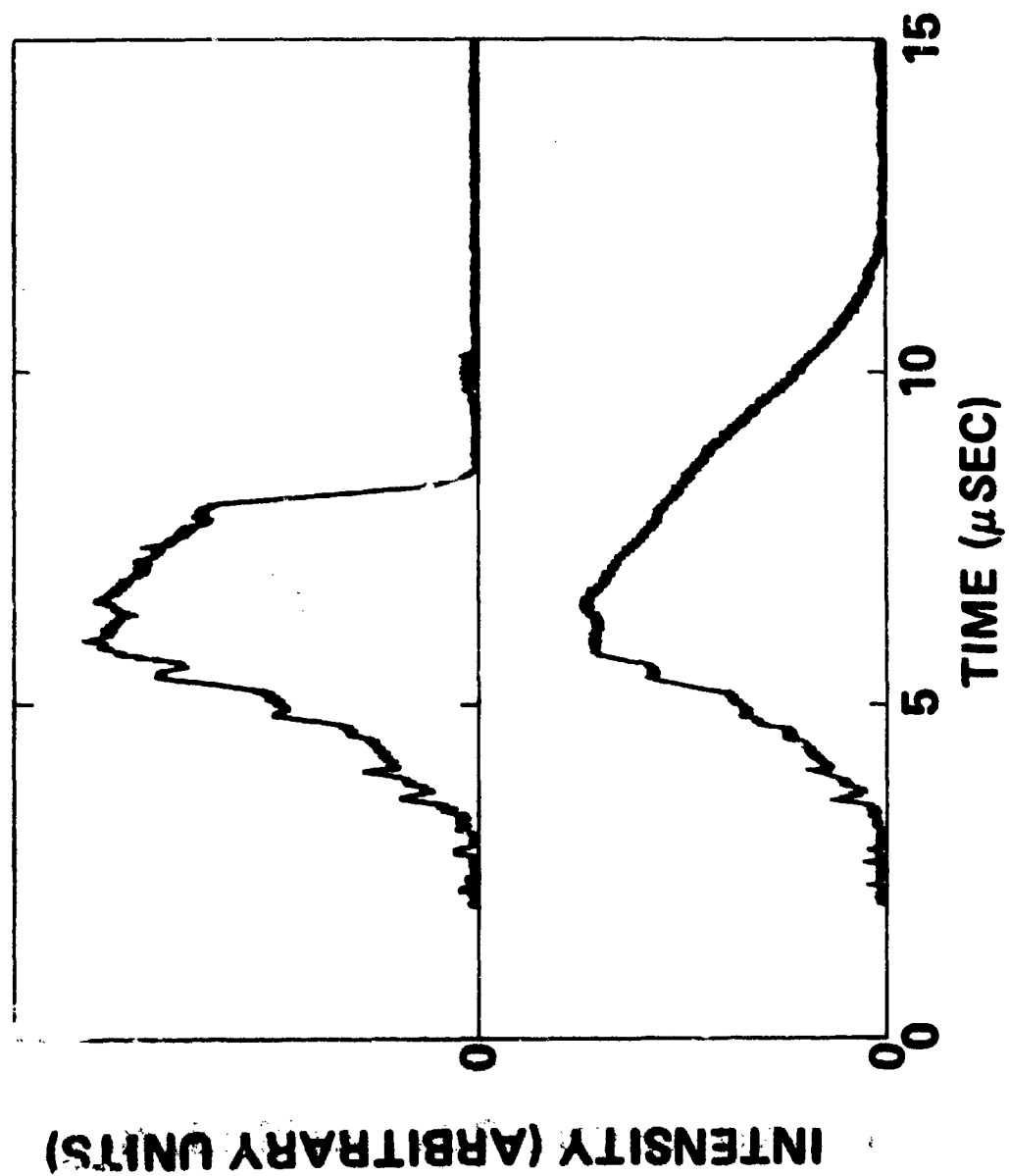


Figure 16. Incident (Lower) and Transmitted (Upper) DF Laser Intensity Profiles for $E_i = 44$ J

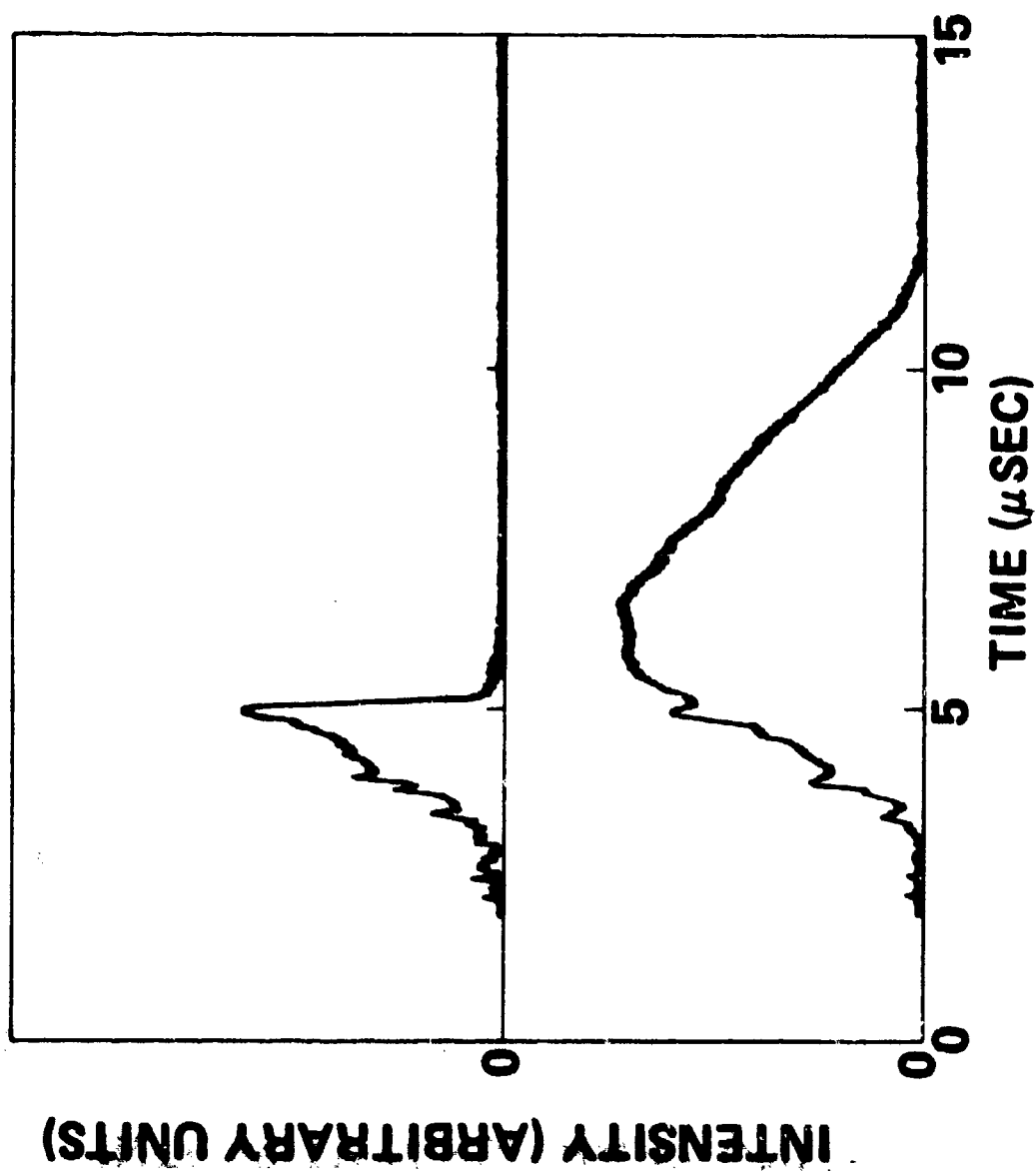


Figure 17. Incident (Lower) and Transmitted (Upper) DF Laser Intensity Profiles for $E_i = 83$ J

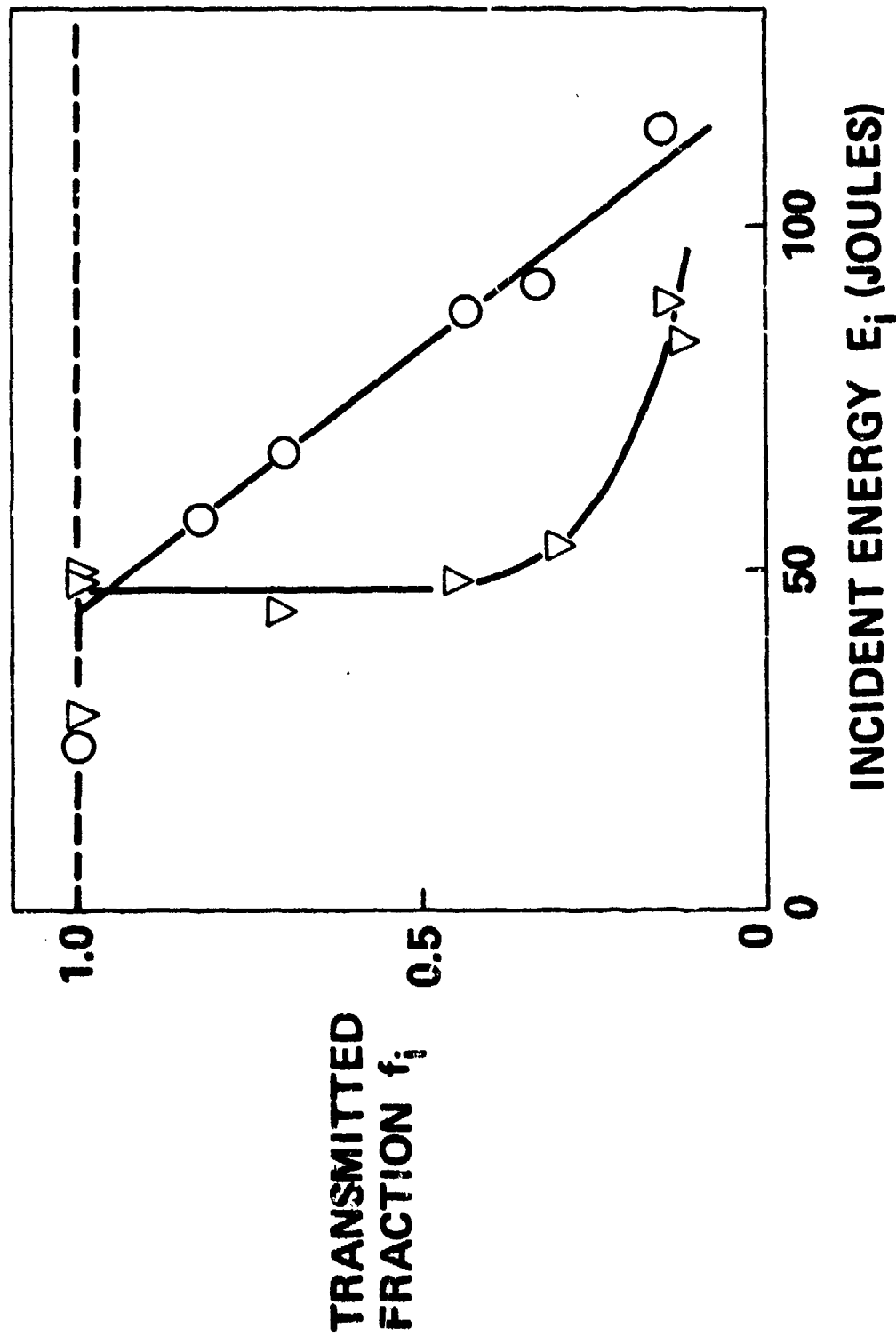


Figure 18. Transmitted Fraction of the Incident Beam Fluence Measured for Aluminum. Circles are HF, Triangles DF Data.

incident energy for both HF and DF radiation on aluminum. Smooth curves are added to indicate the general trends of the data without regard to particular threshold models.

Two definitions of threshold energy can be readily derived from this graph. The first is the value associated with $f_i = 1.0$, which is the largest energy deliverable to the target without any plasma ignition (as observed by cutoff of the pinhole transmission). With a finite number of points available, nearby data may be extrapolated to $f_i = 1$. A second threshold energy is that for which $f_i = 0.5$, when ignition occurs halfway through the incident laser pulse.

Table 4 compares HF and DF thresholds for $f_i = 1$, $f_i = 0.5$, and $f_i = 0.2$ for Al 6061. Also listed is the fluence reaching the target e_t , again as a function of f_i . The maximum intensity reaching the target q_m is tabulated for the same conditions. It appears from table 4 that neither e_t or q_m is an f_i -independent threshold parameter adequately describing all the observed thresholds for a given material, wavelength band, and beam spot size. The maximum DF irradiance reaching the target q_m is found to be approximately a constant for aluminum but not for other materials.

TABLE 4

THRESHOLD CONDITIONS IN TERMS OF INCIDENT ENERGY E_i , FLUENCE REACHING TARGET e_t , AND MAXIMUM TARGET IRRADIANCE q_m , FOR THREE VALUES OF THE FRACTION f_i OF INCIDENT HF OR DF LASER RADIATION TRANSMITTED THROUGH A PINHOLE IN AN ALUMINUM 6061 TARGET, FOR A 0.94 CM DIAMETER BEAM SPOT.

	<u>Lasant</u>	<u>$f_i = 1.0$</u>	<u>$f_i = 0.5$</u>	<u>$f_i = 0.2$</u>
E_i in J	HF	45	83	107
	DF	49	49	65
e_t in J/cm^2	HF	65	60	31
	DF	71	35	19
q_m in MW/cm^2	HF	18	32	33
	DF	15	15	18

The data of figure 18 are replotted in figure 19 as fluence reaching the target e_t versus incident fluence e_i . The HF curve shows that the maximum e_t deliverable to an aluminum target (69 J/cm^2) occurs for $f_i = 0.75$ and does not appear explicitly in table 4. The lines through the origin indicate loci of values for which $f_i = 1.0$ and $f_i = 0.5$.

Figure 20 shows the aluminum data of figure 18 compared to fits using the simultaneous threshold models described in Section III.2. The $e + q$ Model curves are shown as solid lines while the $T + q$ Model calculations are dotted lines. Equation 12 was fit to the time profiles of figures 10 and 11 to give t_p (HF) = $2.6 \text{ } \mu\text{sec}$ and t_p (DF) = $3.3 \text{ } \mu\text{sec}$.

For DF, the curves are identical above $f_i = 0.29$ and either model can provide an acceptable fit to the data. Neither model, however, adequately fits all the HF data. The HF curves shown were fit to the higher f_i points. The divergence between model and measurements increases with increasing E_i and is more pronounced for the $e + q$ Model curve.

Similarly, $e + q$ Model fits have been generated for the other target materials discussed below. Most of these fits are less significant than those for aluminum since fewer data points are available; these fits are not displayed.

5. THRESHOLD DEPENDENCE ON TARGET MATERIAL

Figures 21 through 26 show the transmitted fraction f_i as a function of incident energy, measured for both HF and DF wavelengths for six other materials. These data distributions (and the associated smooth curves) were intended particularly to give good approximations to the $f_i = 1$ and $f_i = 1/2$ threshold conditions. Carbon is included as Grafoil, an exfoliated laminar form of graphite. Lucite was included to allow comparison of the metal results with an ablative material.

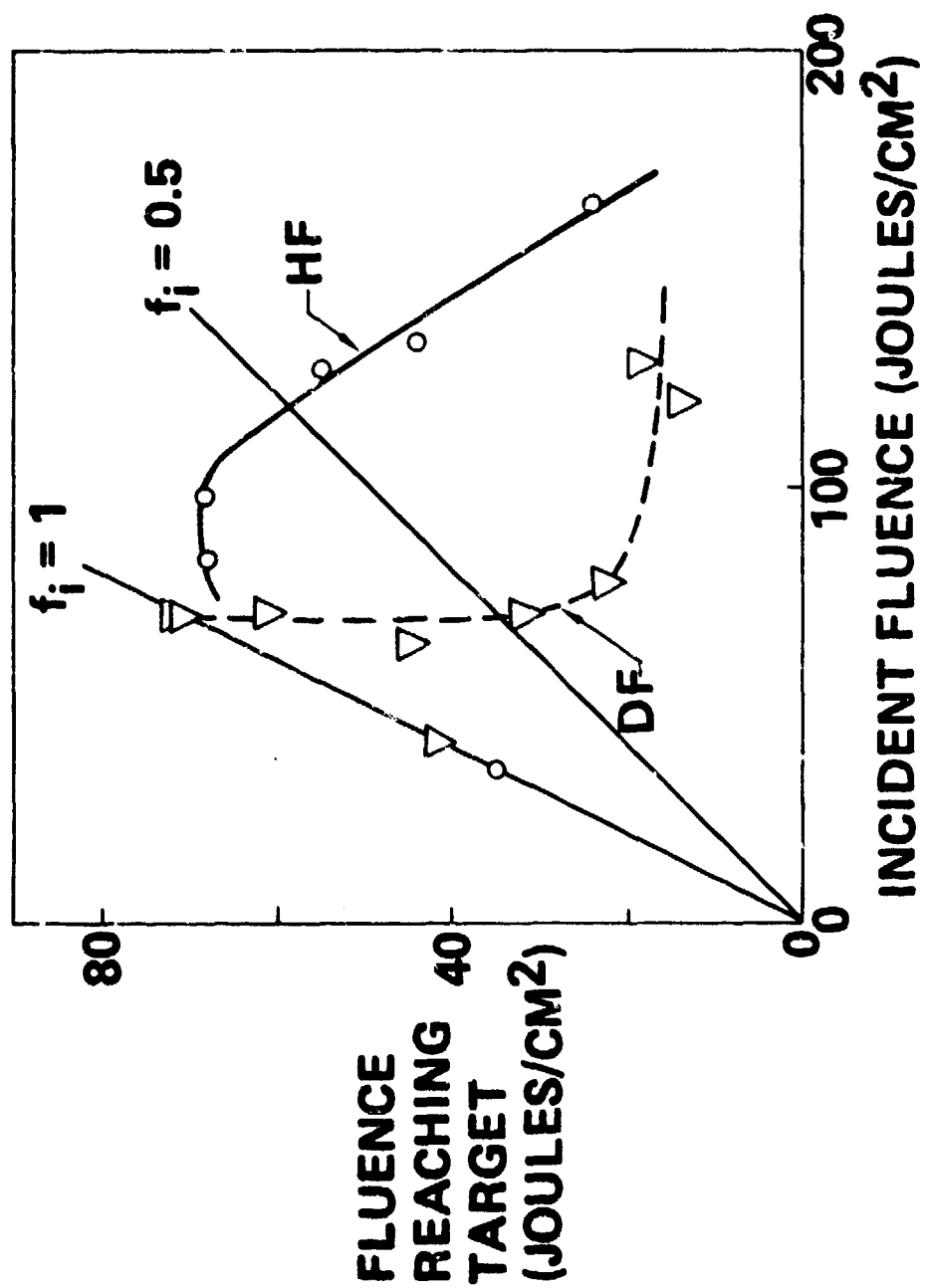


Figure 19. Fluence Reaching an Aluminum Target Versus Incident Beam Fluence

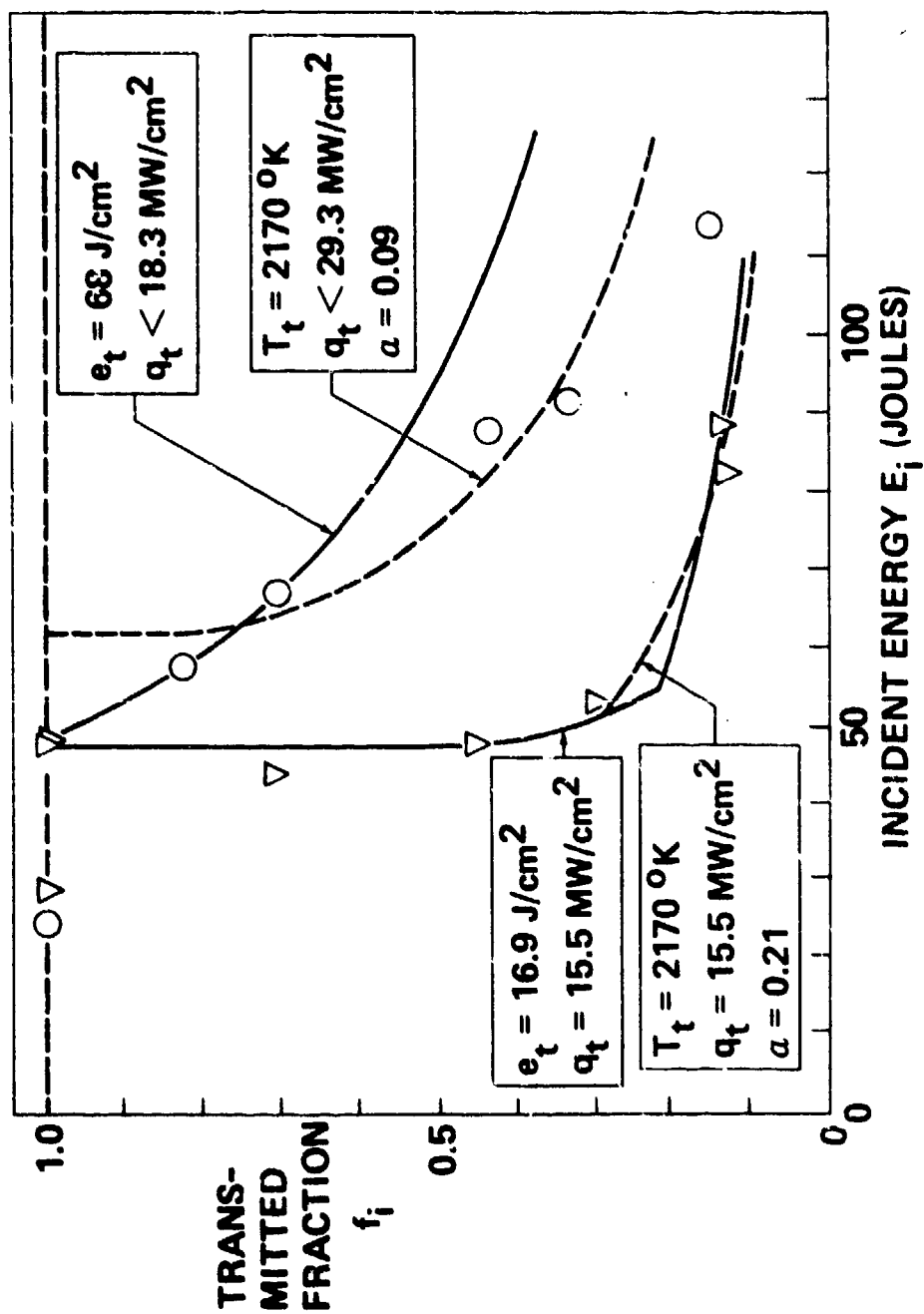


Figure 20. Predictions of the e+q Model (Solid Lines) and T+q Model (Dotted Lines) Compared to the Aluminum Threshold Data of Figure 18. Circles are HF, Triangles DF Data.

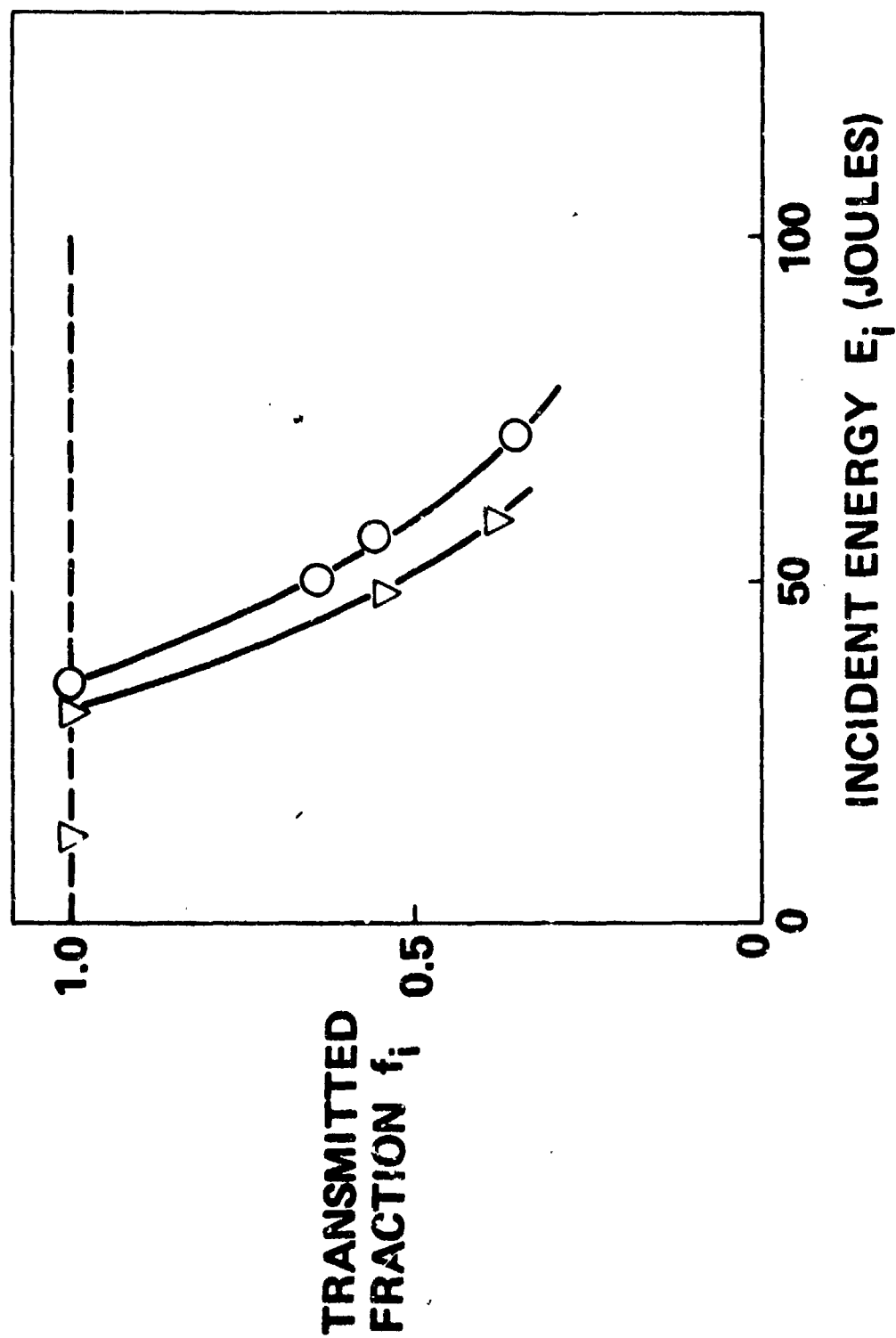
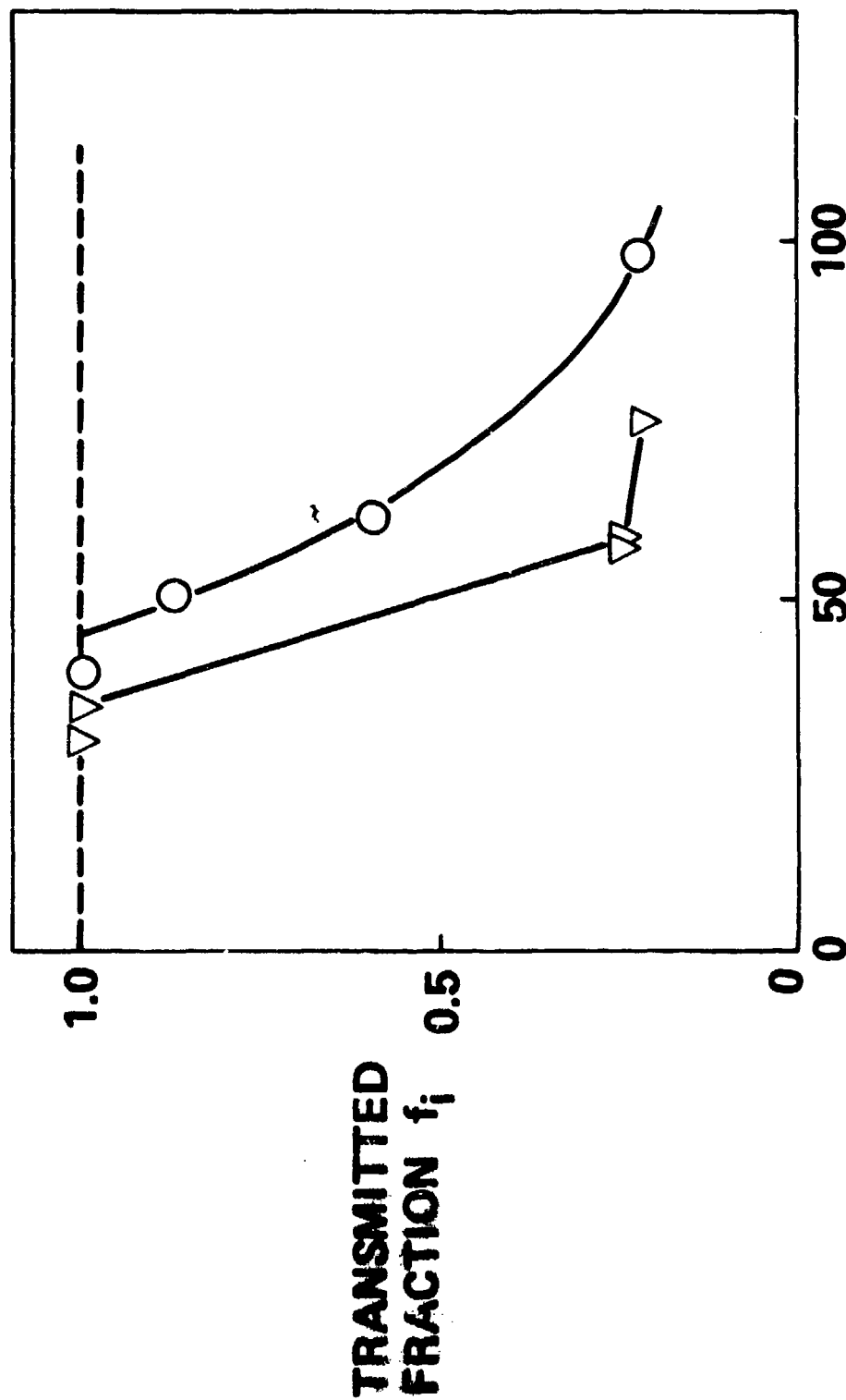


Figure 21. Fluence Fraction Transmitted for Titanium. Circles are HF, Triangles DF Data.



INCIDENT ENERGY E_i (JOULES)

Figure 22. Fluence Fraction Transmitted for Stainless Steel. Circles Are HF, Triangles DF Data.

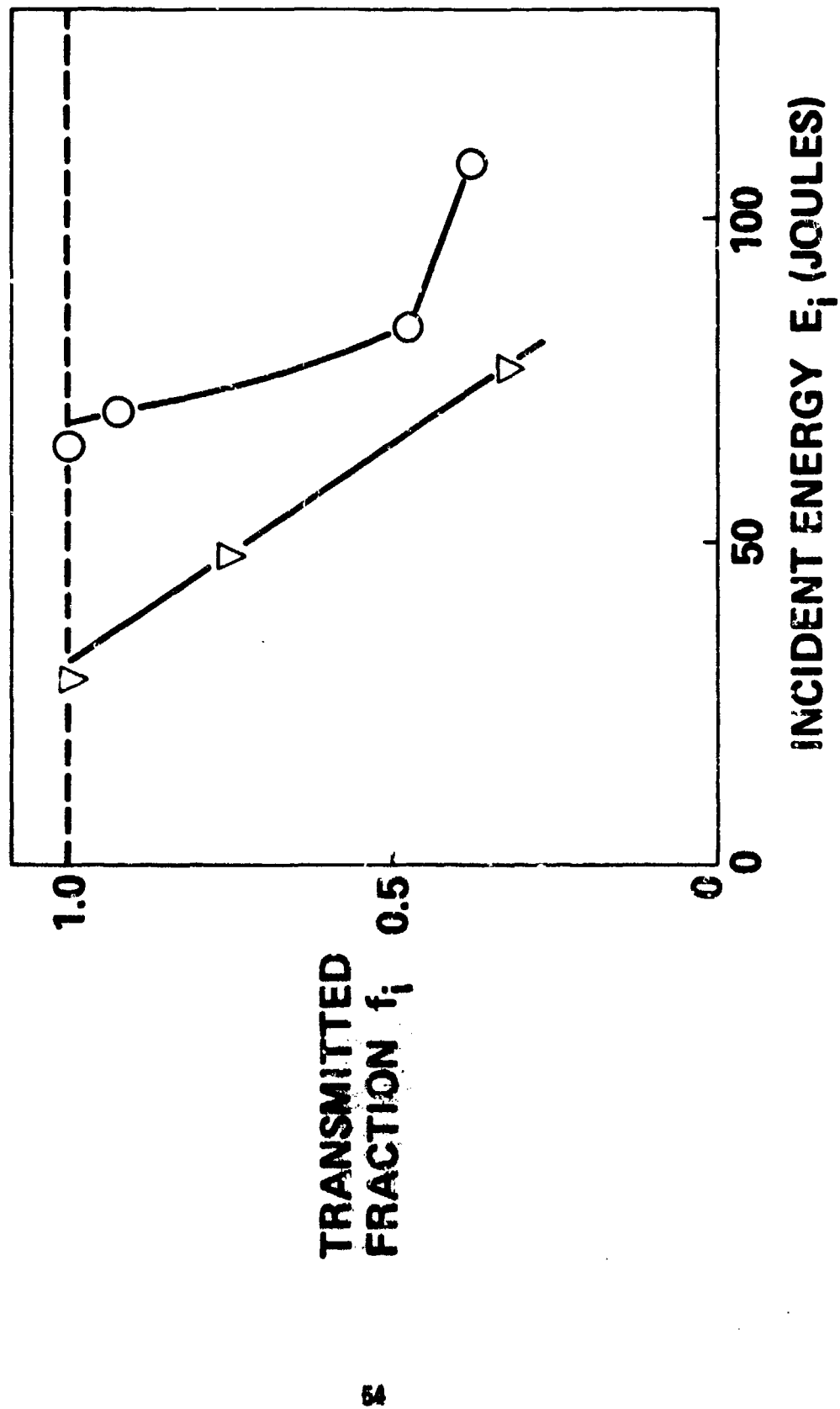


Figure 23. Fluence Fraction Transmitted for Nickel. Circles are HF, Triangles DF Data.

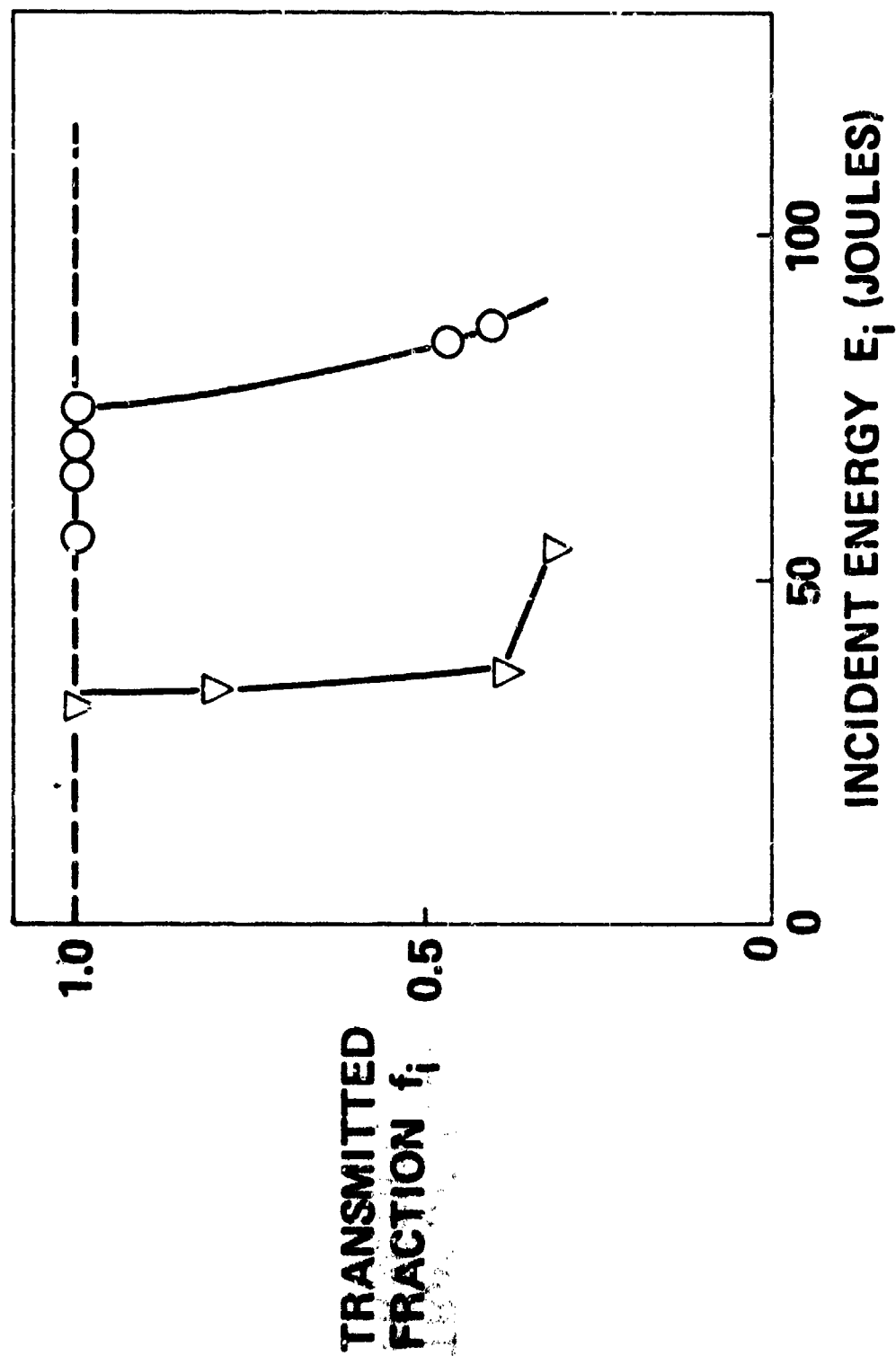


Figure 24. Fluence Fraction Transmitted for Copper. Circles are HF, Triangles DF Data.

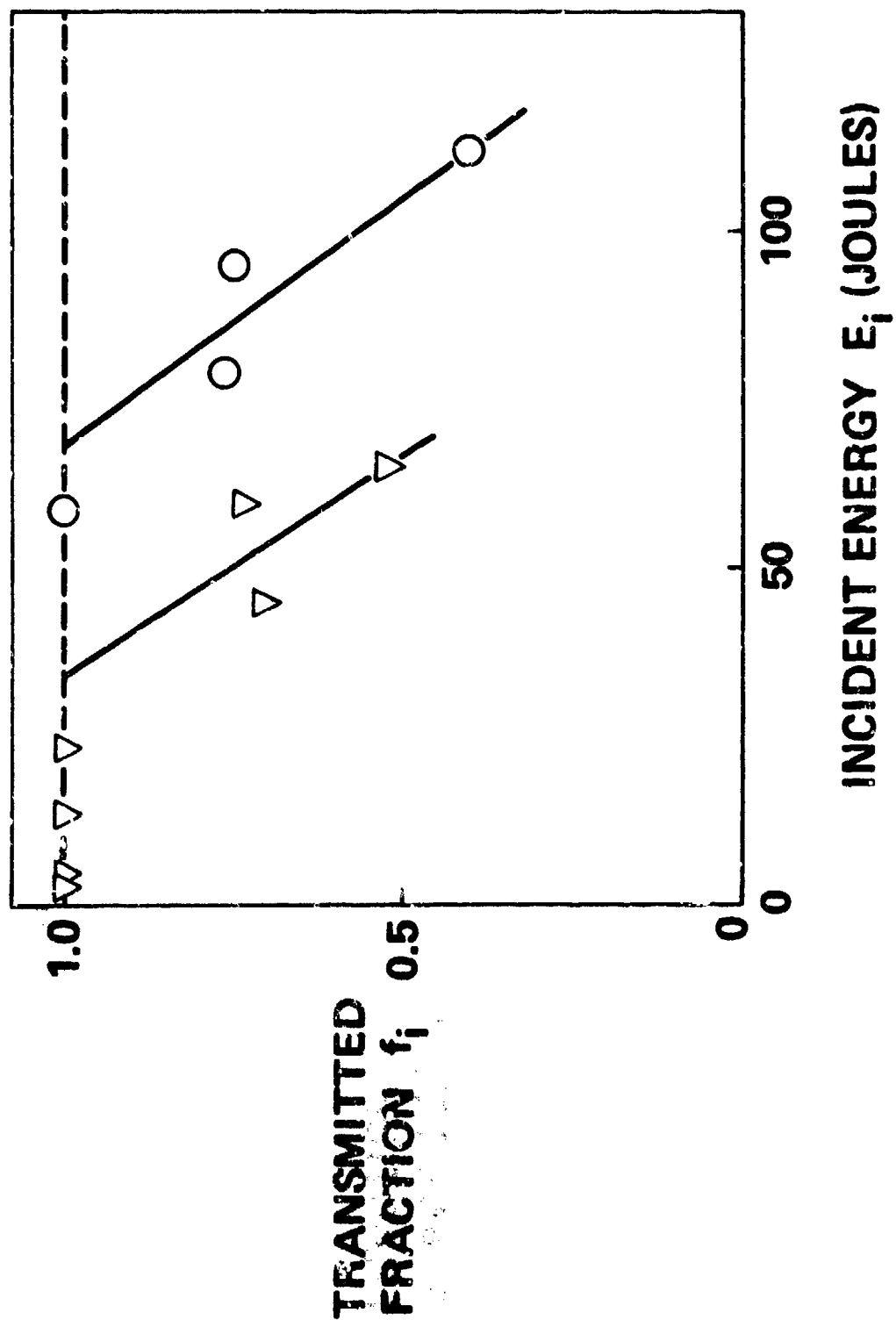


Figure 25. Fluence Fraction Transmitted for Grafo11. Circles are HF, Triangles DF Data.

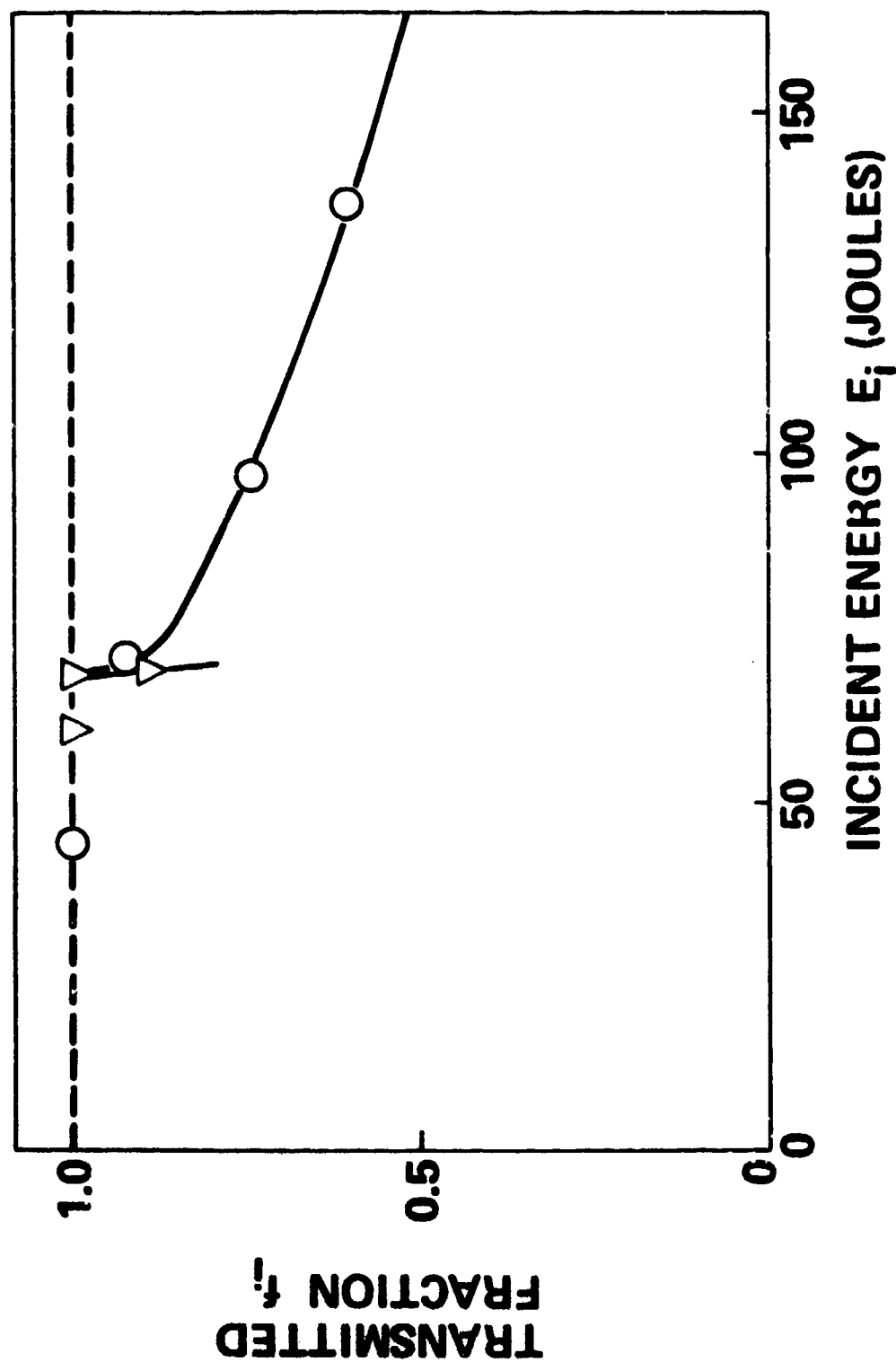


Figure 26. Fluence Fraction Transmitted for Lucite. Circles are HF, Triangles DF Data.

The resulting threshold values of incident energy E_i , fluence reaching the target e_t , and maximum intensity q_m are tabulated in table 5. The aluminum results of table 4 are included for completeness.

Estimated uncertainties (standard error) in the threshold values are also indicated in table 5. Errors due to systematic uncertainties are estimated as 15%. This value governs the total assigned uncertainty except in those cases for which the distribution of data contributes an additional error; the values $E_i(f_i)$ for $f_i = 1$ and $i/2$ for Grafoil, for example (figure 26), are uncertain by $\pm 20\%$; this is combined with the systematic error to give the $\pm 25\%$ indicated in table 5.

The threshold fluence results of table 5 are shown in graphical form in figures 27 and 28. The results for maximum irradiance are shown in figures 29 and 30.

TABLE 5
THRESHOLD CONDITIONS FOR FORMATION OF LASER-SUPPORTED ABSORPTION WAVES AS
DETERMINED BY TARGET PINHOLE TRANSMISSION CUTOFF, FOR SEVEN MATERIALS.

$f_1 =$	Total Incident Pulse Energy E_i (J)		Total Fluence Reaching Target e_t (J/cm ²)		Maximum Irradiance q_m (MW/cm ²)		Assigned Uncertainty (%)
	1	1/2	1	1/2	1	1/2	
Aluminum HF	45	83	65	60	18	32	25
DF	49	49	71	35	15	15	15
Titanium HF	35	58	51	42	14	23	25
DF	30	51	43	37	9	16	25
Stainless Steel HF	45	67	65	48	18	26	15
DF	35	56	51	41	11	17	25
Nickel HF	65	82	94	59	25	32	15
DF	30	65	43	47	9	20	25
Copper HF	76	83	110	60	30	32	15
DF	32	36	46	26	10	11	15
Grafoil HF	65	105	94	76	25	41	20
DF	30	66	43	48	9	20	25
Lucite HF	69	175	100	127	27	69	20
DF	69	--	100	--	21	--	15

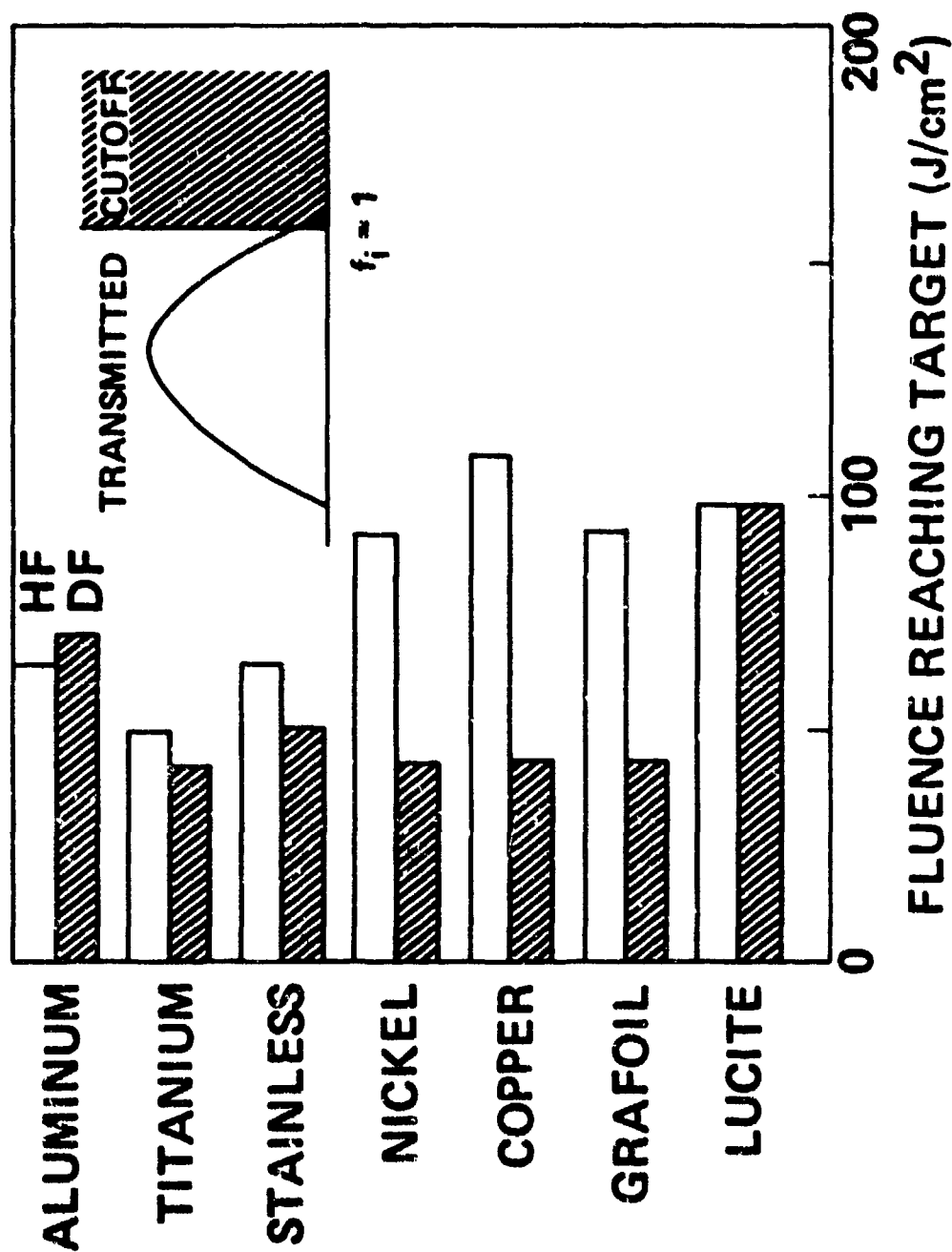


Figure 27. Comparison of Threshold Fluences for $f_i = 1$ For HF and DF Laser Radiation

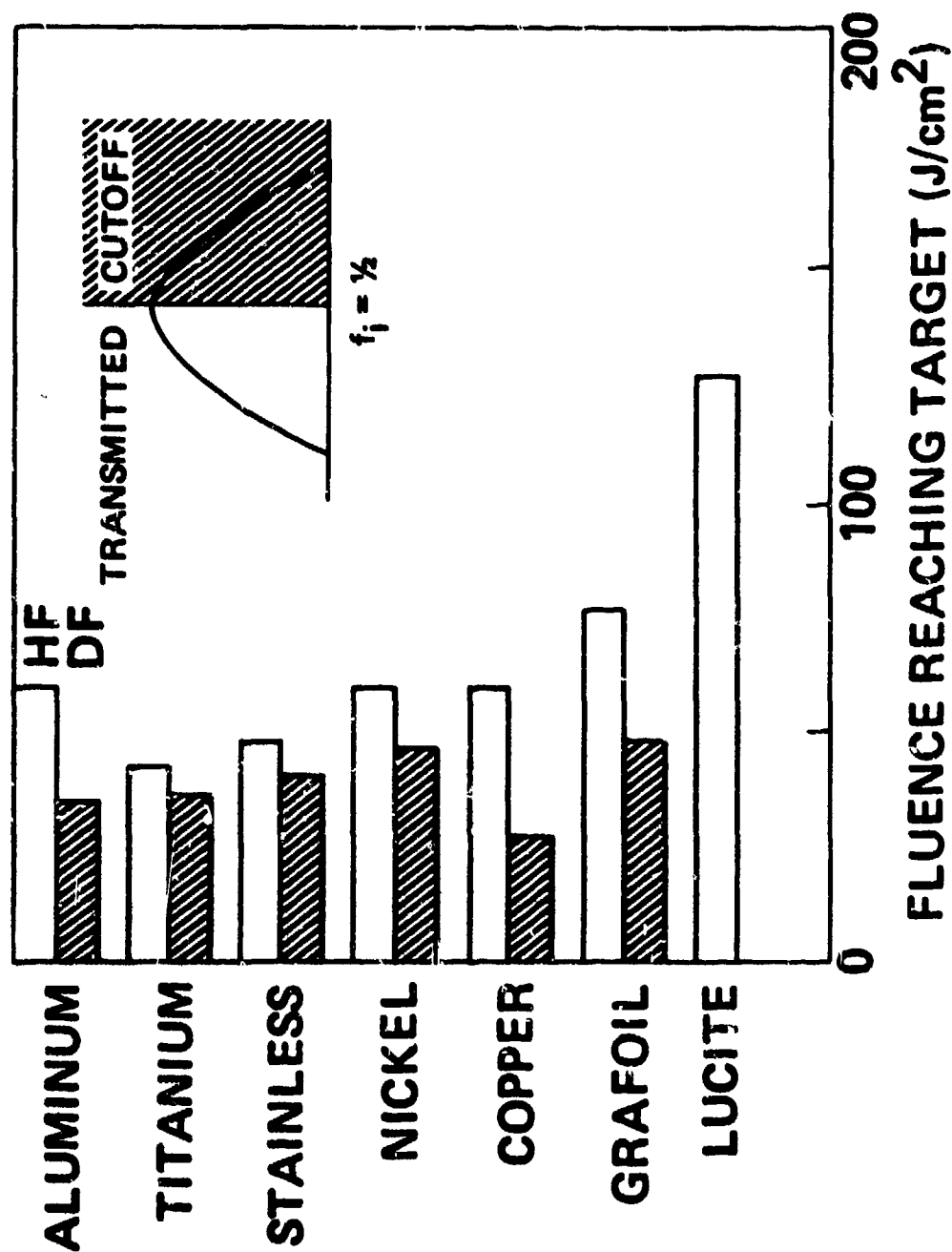


Figure 28. Comparison of Threshold Fluences for $f_i = 0.5$ For HF and DF Laser Radiation

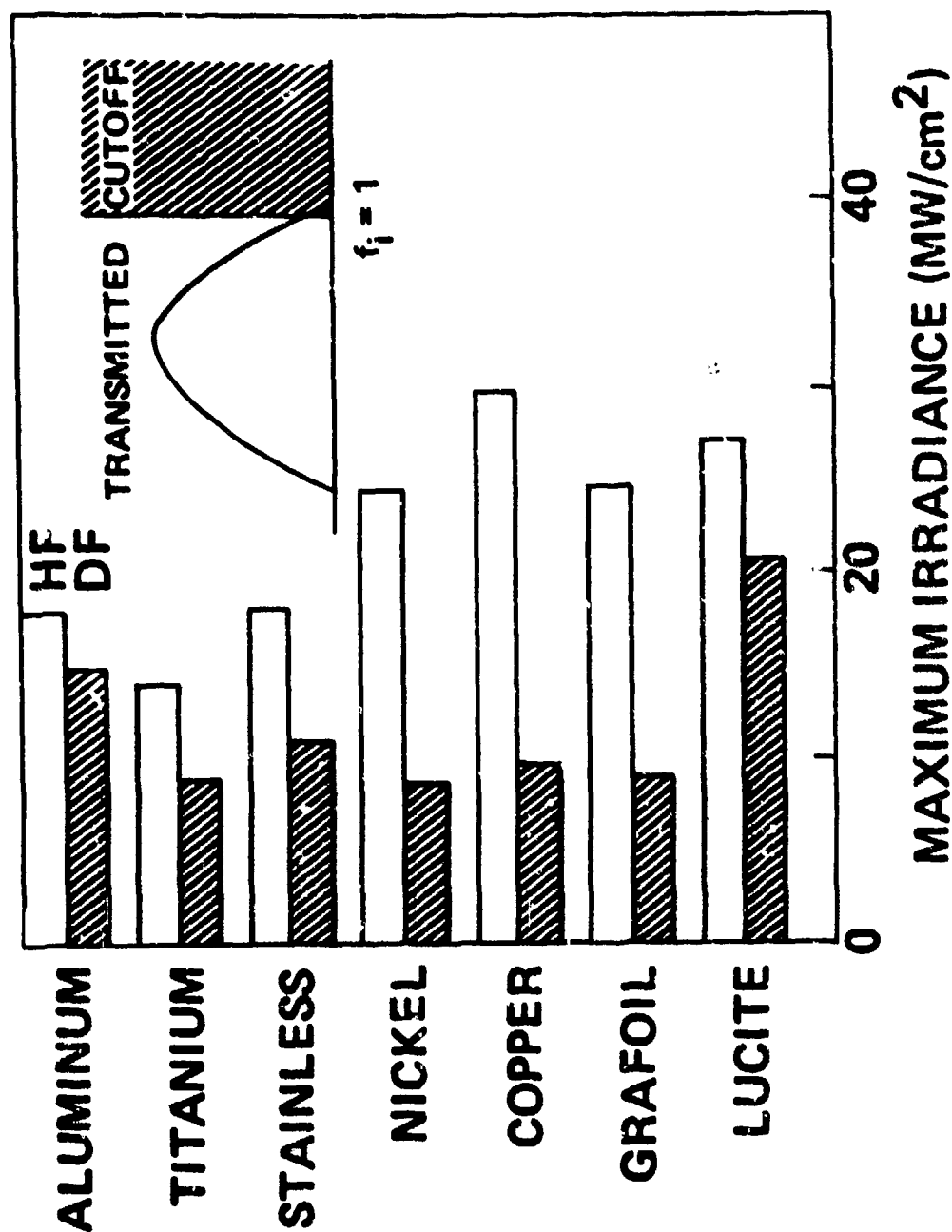


Figure 29. Comparison of Maximum Irradiances for $f_i = 1$ For HF and DF Laser Radiation

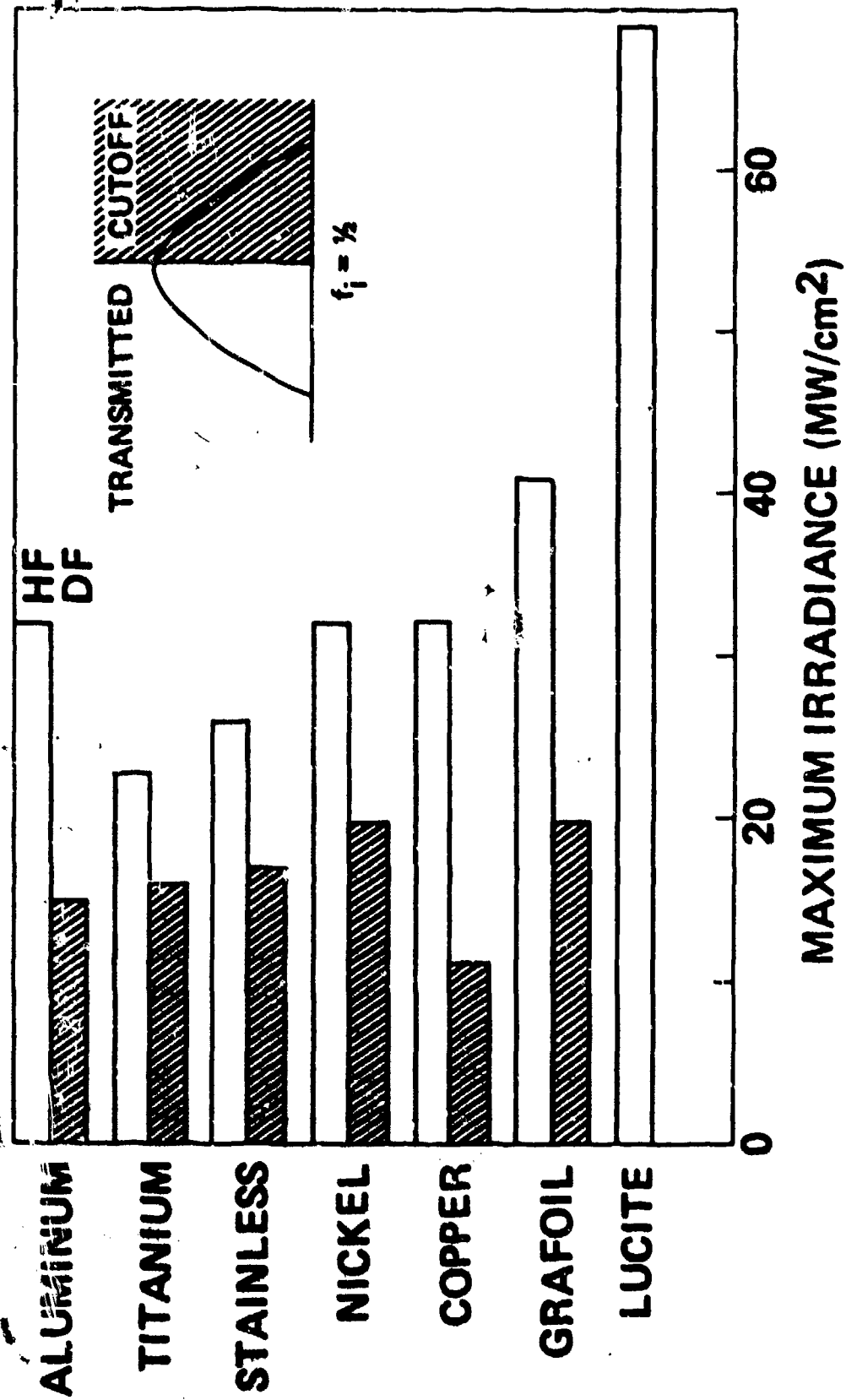


Figure 30. Comparison of Maximum Irradiances for $f_i = 0.5$ for HF and DF Laser Radiation

SECTION IV

THERMAL COUPLING OF HF LASER RADIATION TO METAL TARGETS

In order to examine the efficiency with which laser energy is transferred to target materials, a series of experiments was carried out at high intensity in ambient-pressure air. This topic is of importance because of the well-known enhanced coupling effect in which plasma is formed above a target. The resulting plasma absorbs the laser energy and then radiates optical or uv radiation toward the target.⁽³⁾ For reflective targets such as aluminum, the effective coupling coefficient can be increased by a factor of ten.^(13,14)

1. THERMAL COUPLING COEFFICIENTS

The total thermal coupling coefficient α was measured for four metals as a function of incident HF laser energy. The coupling was measured for two beam spot sizes, and studies were made of the effect of laser pulse length and ambient air pressure at the target.

a. Method

Thermal coupling coefficients of the metal targets were obtained by direct calorimetry. Chromel-alumel thermocouples were formed by spot welding the 0.013 cm diameter wires to the target rear surfaces. Axial diffusion times were only a few milliseconds due to the nominal 0.13 cm target thickness. Radial equilibration times were determined by simultaneous observation of time-dependent temperature readings from thermocouples mounted at the center and at the edge of the target. The time-dependent cooling curves from center-mounted thermocouples were then extrapolated to zero time to obtain an effective whole-target temperature rise ΔT . The associated target heat was divided by the incident beam pulse energy to give the thermal coupling coefficient α .

-
13. Marcus, S., Lowder, J.E., Manlief, S.K., and Mooney, D.L., "Laser Heating of Metallic Surfaces," Project Report LTP-31, Lincoln Laboratory, May 1976.
 14. McKay, J., "High Intensity Coupling Phenomena," Third DOD High Power Laser Conference, Colorado Springs, November 1976.

b. Thermal Coupling at Large Fluences

The variation of thermal coupling with incident laser energy was studied over a wide range of fluence ($0 - 1300 \text{ J/cm}^2$) by using a 37.5 cm collecting mirror to give a beam spot of effective diameter 0.46 cm as discussed in Section II. Target diameters for this work were 1.59 cm. Since target heating due to plasma spreading can occur well outside the beam spot, selected high-energy data points were duplicated with larger targets (2.22 cm) to show that the target heating was not limited by target size for these conditions.

The coupling is plotted in figure 31 for aluminum 6061 as a function of incident HF laser energy. Incident pulse fluence and peak intensity are also shown. The irradiance scale is linear up to about 220 MW/cm^2 due to a constant pulse length of $4.2 \text{ } \mu\text{sec}$ FWHM. Above 140 J energy, modified gas mixtures gave pulse lengths decreasing to $3 \text{ } \mu\text{sec}$ at 220 J.

The low-energy data of figure 31 show about 6% absorbance as expected while the onset of plasma formation gives a factor-of-three enhancement in thermal coupling. The half-height point in this enhancement step occurs at about 120 J/cm^2 fluence. In comparing this threshold with the larger spot pinhole thresholds of Section III, it is not clear what value of f_i should be used. However, this 120 J/cm^2 agrees well with the aluminum results in table 4 which show an incident fluence of $2 \times 60 \text{ J/cm}^2$ for $f_i = 0.5$.

The solid curve of figure 31 is the equation $\alpha = (6.1 \text{ J})/E_i$. This simple curve describes the data very well over the range 200 to 1400 J/cm^2 . The result is a constant absolute energy deposition in the sample, 6.1 J, independent of incident energy.

Figures 32 to 34 give similar data for titanium, stainless steel, and nickel. The general features of the aluminum results are repeated, with a constant energy deposition above 200 J/cm^2 .

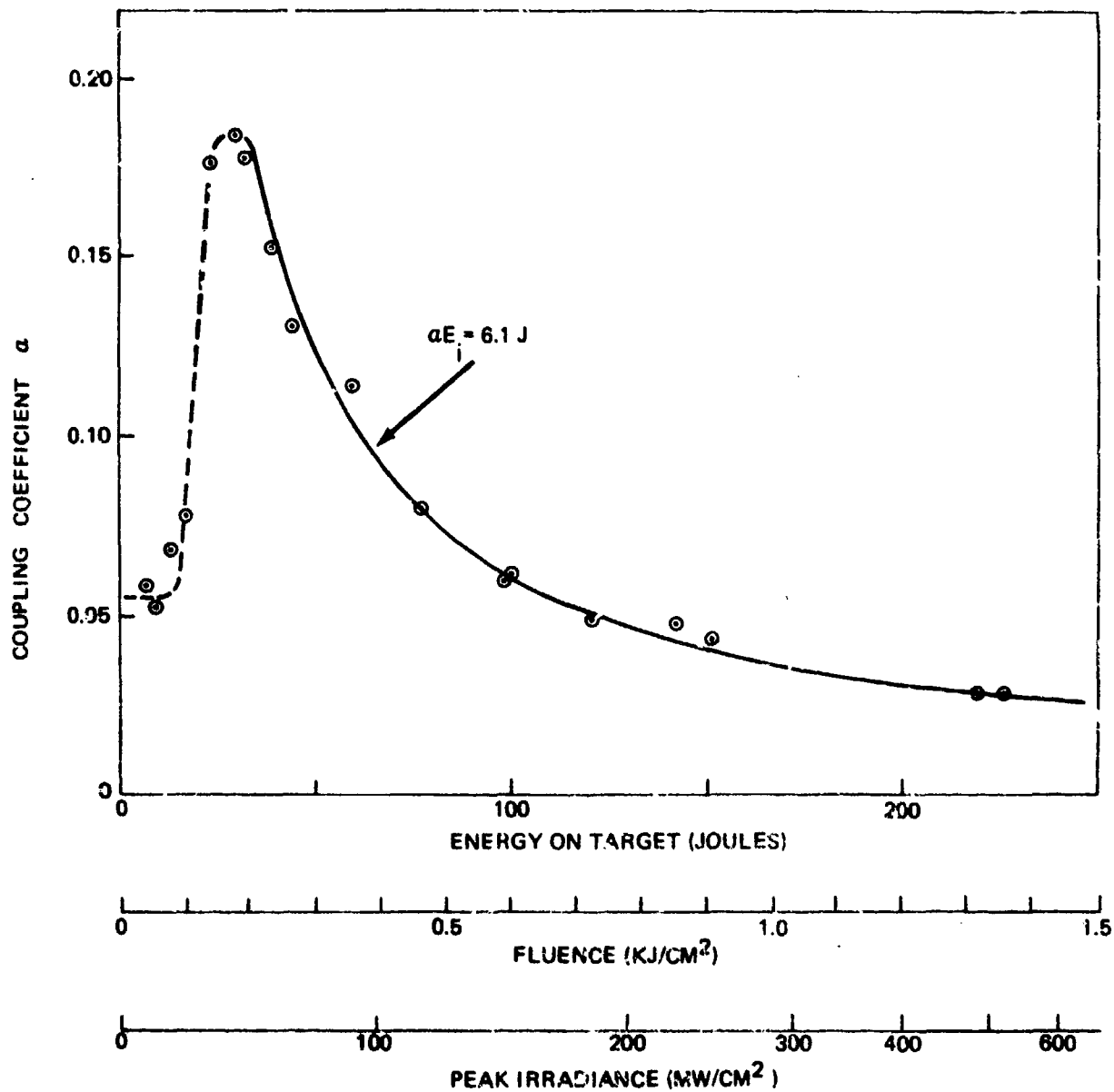


Figure 31. Thermal Coupling of HF Laser Radiation on Aluminum

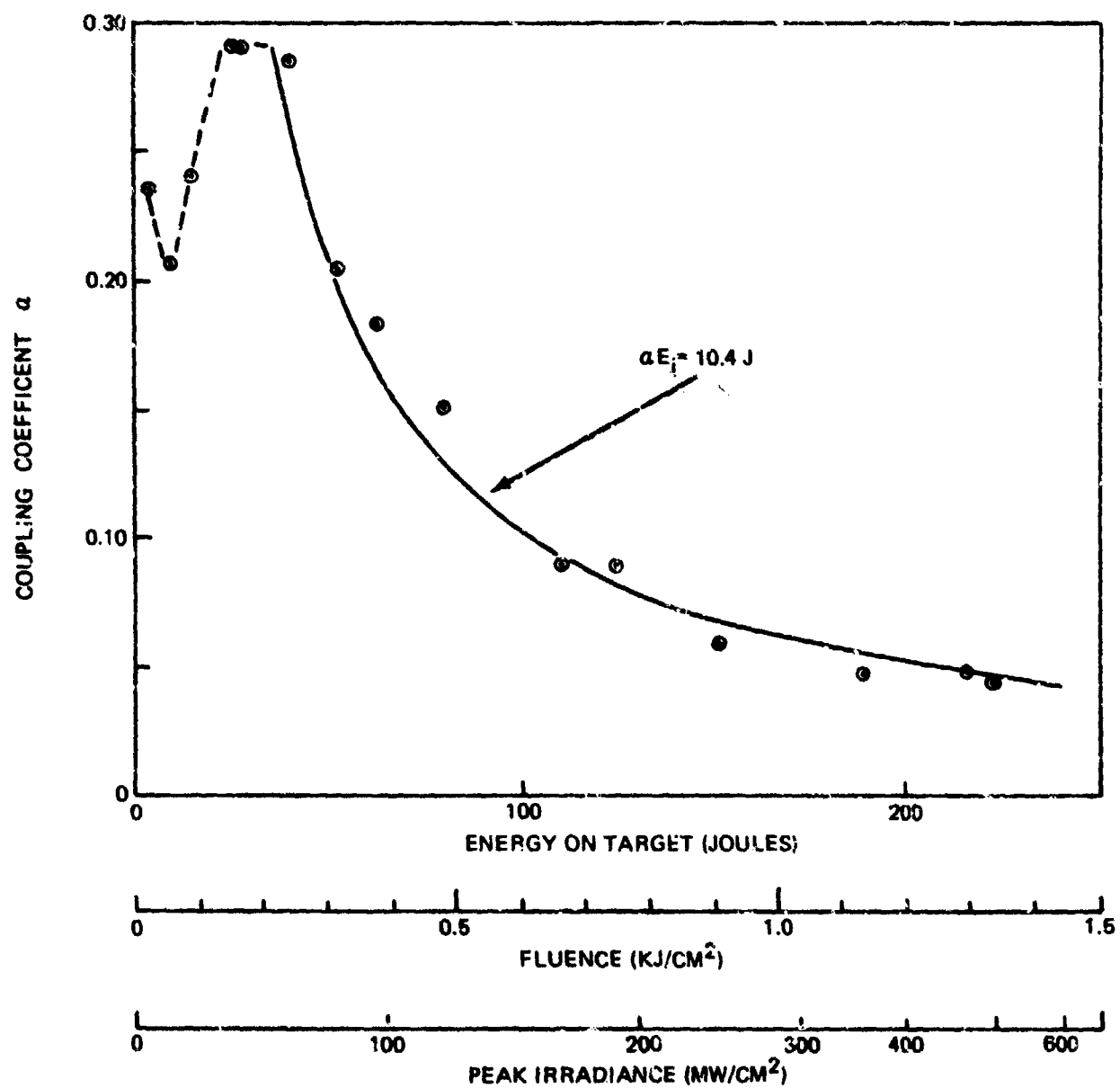


Figure 32. Thermal Coupling of HF Laser Radiation on Titanium

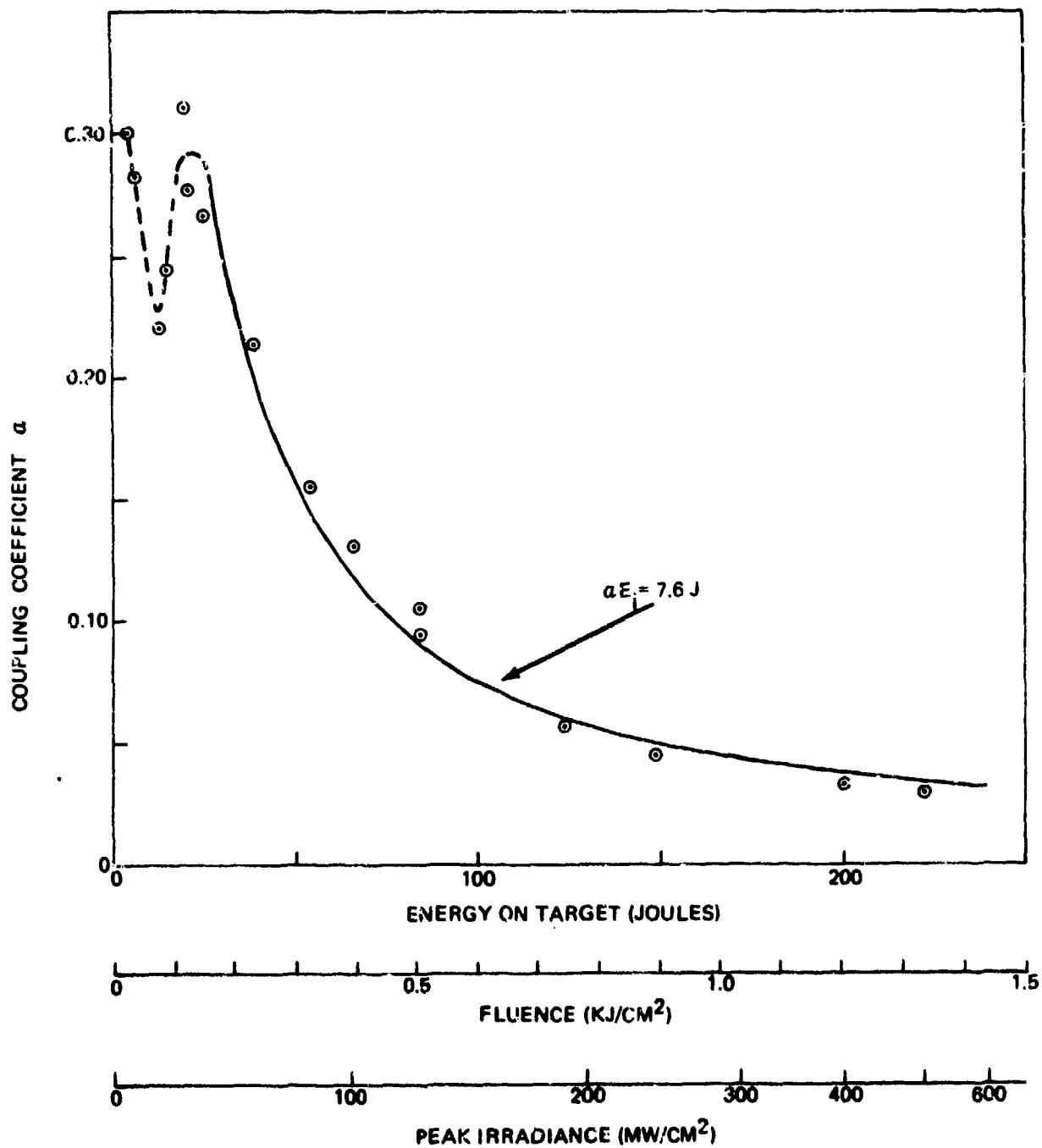


Figure 33. Thermal Coupling of HF Laser Radiation on Stainless Steel

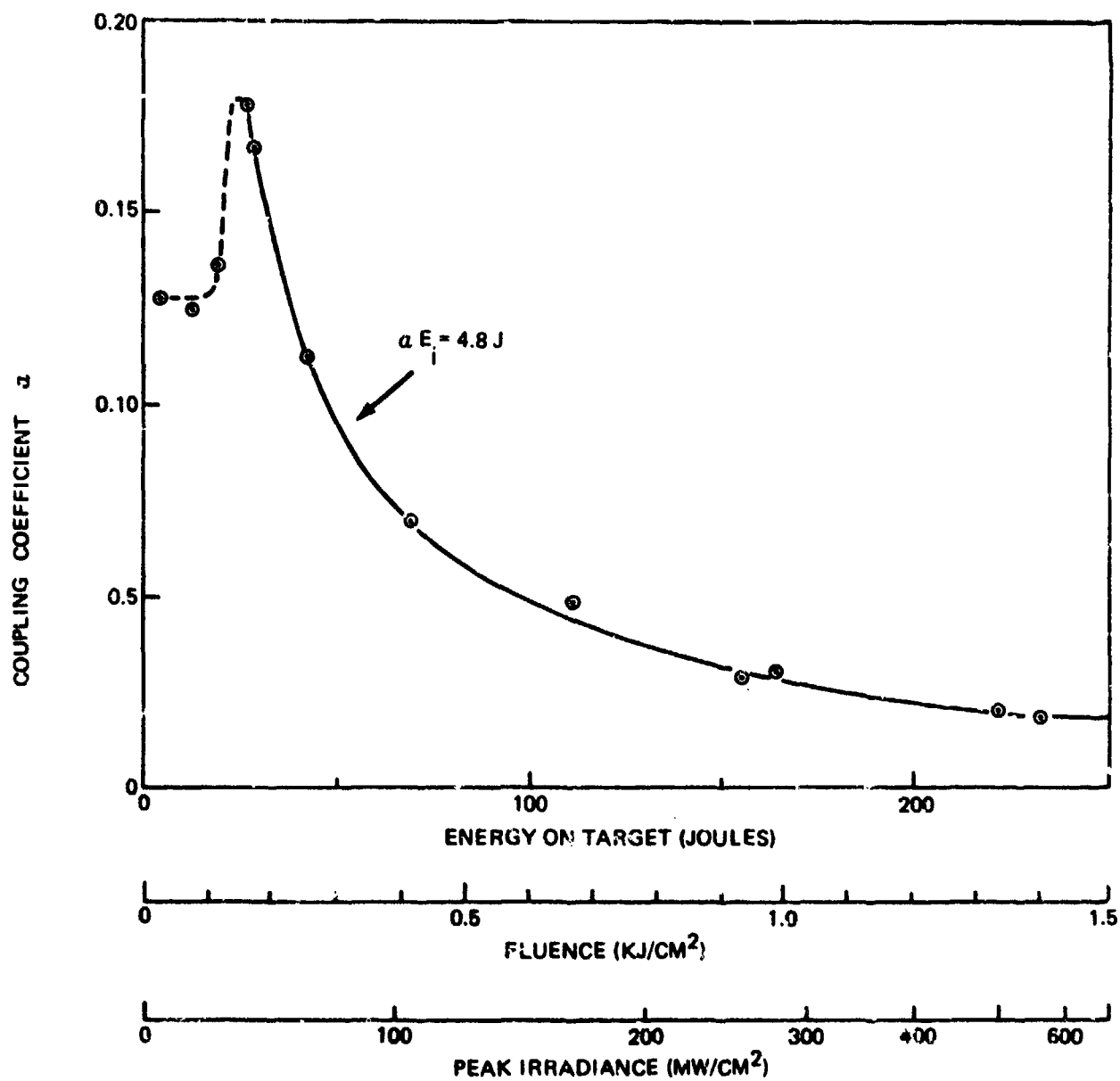


Figure 34. Thermal Coupling of HF Laser Radiation on Nickel

The thresholds observed by enhancement of thermal coupling are compared with pinhole thresholds in table 6. The choice of $f_i = 0.5$ type pinhole thresholds from table 5 gives good agreement with the thermal enhancement thresholds.

Sources of experimental uncertainties in these results include absolute energy calibration ($\pm 8\%$), cooling curve extrapolations ($\pm 8\%$), beam spot area error for conversion to fluence ($\pm 5\%$), and variation in laser pulse time profile for conversion to peak intensity ($\pm 10\%$). Total estimated relative uncertainties are $\pm 9\%$, with absolute uncertainties of $\pm 15\%$.

Figure 35 shows a comparison of the thermal coupling coefficient for beam spots differing in diameter by a factor of two. The circles indicate data obtained with beams of 0.46 cm diameter and are repeated from figure 31. The squares give the results of similar coupling measurements on 2.22 cm diameter targets with beam spots of 0.92 cm diameter. The data indicate a slightly lower value of threshold fluence as well as smaller peak values of thermal coupling for the larger beam spot size, but more measurements are needed to show this in detail.

c. Effect of Ambient Pressure

The dependence of the thermal coupling coefficient α on ambient pressure at the target is shown in figure 36 for aluminum. The measurements with beam spot diameter 0.46 cm extend from 1 to 10^{-3} atm. The data are all for laser pulse energies near 130 J except the 76 Torr point which was for $E_i = 112$ J. The general trend of decreasing α with increasing pressure is associated with the increasing density and shielding effect of the surface plasma formed at these fluences. Similar behavior is seen for Lucite mass removal over this same range of ambient pressure (see Section V).

TABLE 6
THERMAL COUPLING FLUENCE THRESHOLDS COMPARED TO $f_1 = 0.5$ PINHOLE THRESHOLDS
FROM TABLE 4.

	Large-spot $f_1 = 0.5$ pinhole threshold incident fluence from Table 4 (J/cm ²)	Thermal coupling half-step- height incident fluence (J/cm ²)	Constant energy deposited in the α E=const region (J)
Aluminum	120	120	6.1
Titanium	84	95	10.4
Stainless	96	95	7.6
Nickel	118	120	4.8

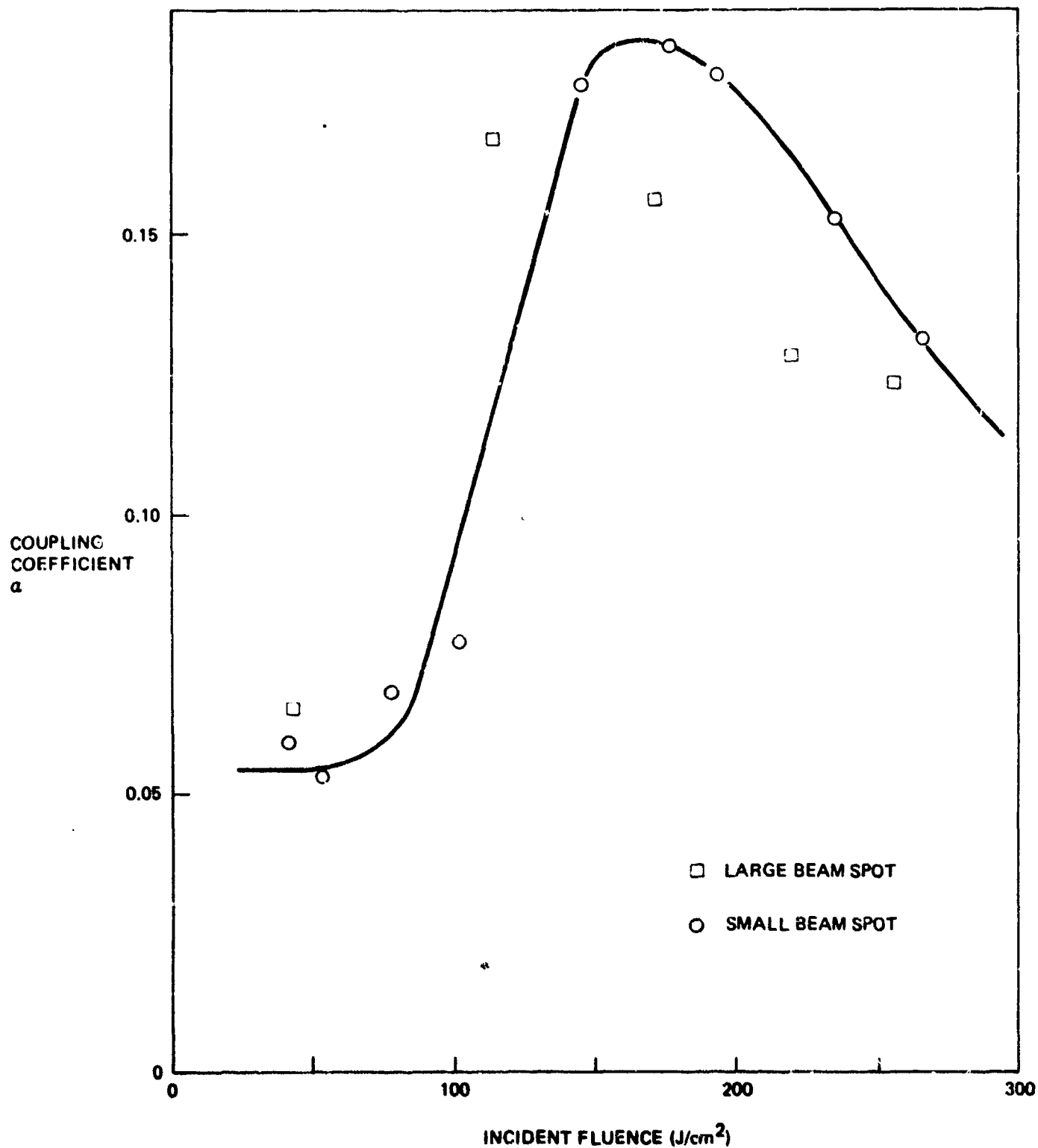


Figure 35. Thermal Coupling of HF Laser Radiation on Aluminum for Beam Spots with 0.46 cm Diameter (Circles); and 0.92 cm Diameter (Squares)

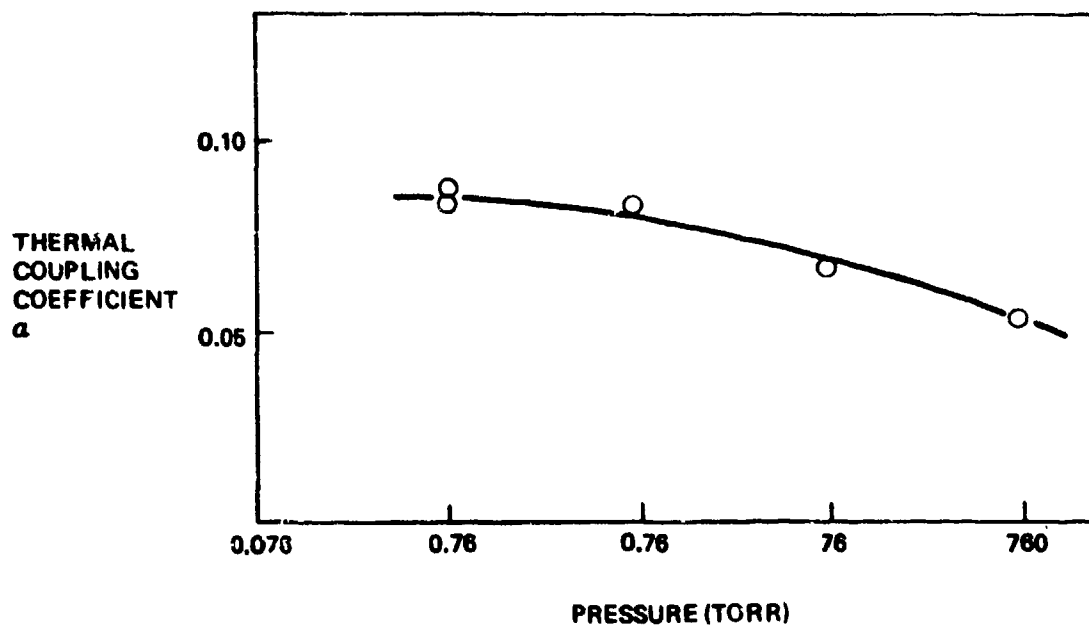


Figure 36. Dependence of Aluminum Thermal Coupling on Ambient Pressure at the Target

d. Effect of Pulse Length

The effect of HF laser pulse length on total thermal coupling coefficients was studied for aluminum and titanium targets in 1 atm pressure air for the 0.46 cm diameter focal spot. The two temporal profiles used are designated "short pulse," referring to the standard HF pulse with 4 μ sec FWHM and about 7 μ sec total length, and "long pulse," with 7 μ sec FWHM and 11 μ sec total length. Aluminum and titanium results are given in figures 37 and 38. The short-pulse results, plotted as circles, are the subset of those plotted in figures 31 and 34 which correspond to a constant pulse length. The long-pulse data are given as triangles.

The data above 35 J, and hence well above plasma threshold, have been least-squares fitted to the power law

$$\alpha = a E_i^{-b} \quad (31)$$

The resulting curves are shown in the plots. The short-pulse thermal coupling gives $b = 0.93$ and 1.04 for aluminum and titanium, corroborating the $b = 1$ fits used in figures 31 and 34. There is no apparent threshold shift due to changing pulse length. For both materials the long-pulse coupling above threshold is larger in magnitude than short-pulse coupling, and also shows less shielding with increasing energy. The exponents of incident energy $b = 0.84$ for aluminum and 0.7 for titanium indicate that, unlike short-pulse behavior, the long-pulse absolute energy deposited in the target continues to increase with incident energy even above the plasma threshold. The total amount of data taken here does not justify the conclusion that longer pulses are preferred, however. This is true especially because we have only measured the total as opposed to the local coupling.

2. SPATIAL DISTRIBUTION OF THERMAL COUPLING

A topic of current interest is the spatial distribution of thermal energy deposited in a metal target by laser beam interaction.⁽¹⁾ Beginning with a deposition profile which corresponds to the incident beam distribution at low intensities, increasing energies lead eventually to plasma ignition and the surface-heating mechanisms associated with a radiating high-temperature gas which is spreading radially as well as propagating axially up the

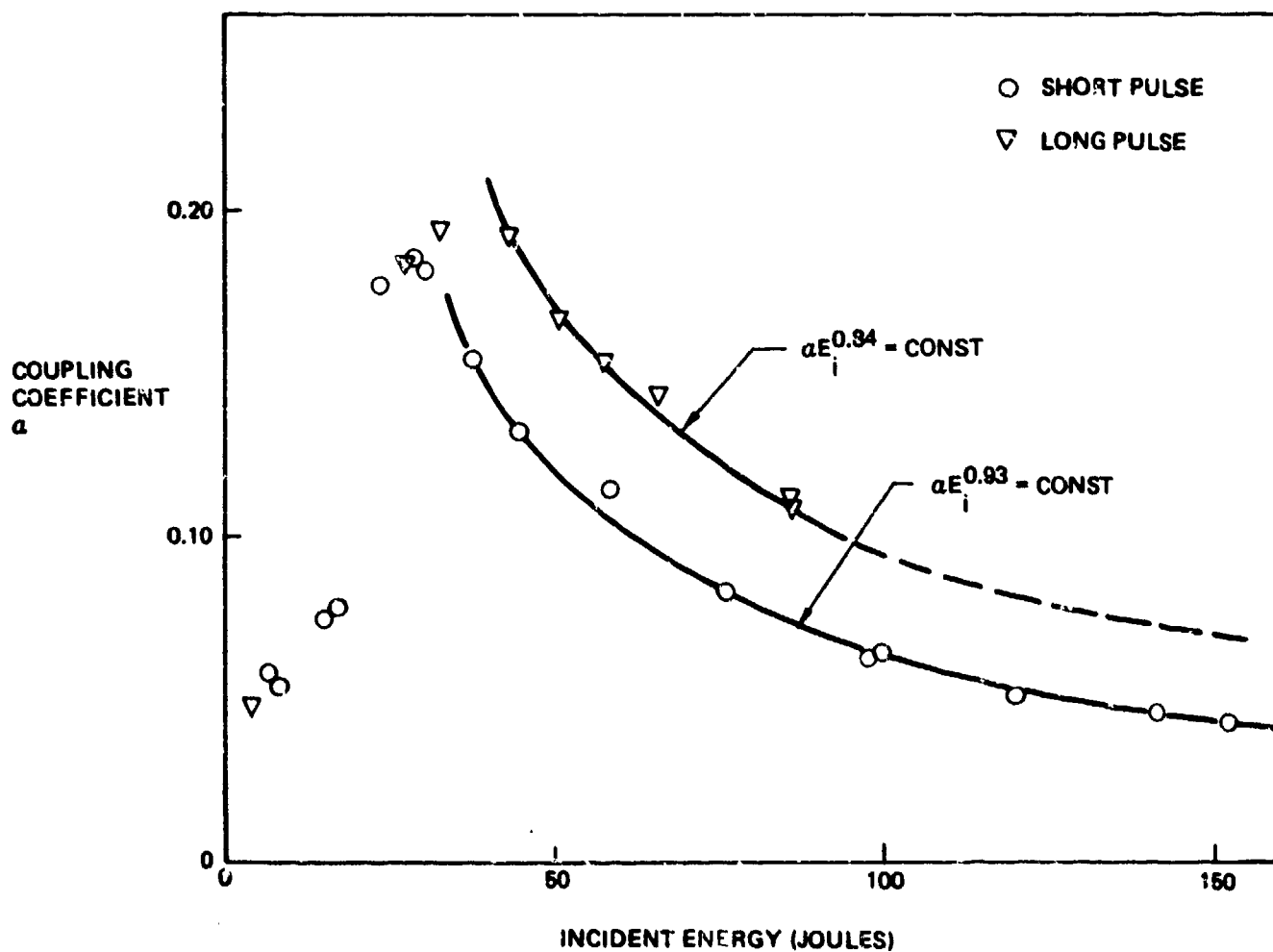


Figure 37. Effect of Pulse Length on Aluminum Thermal Coupling. Circles are for 4 μsec FWHM Pulses. Triangles are for 7 μsec FWHM Pulses.

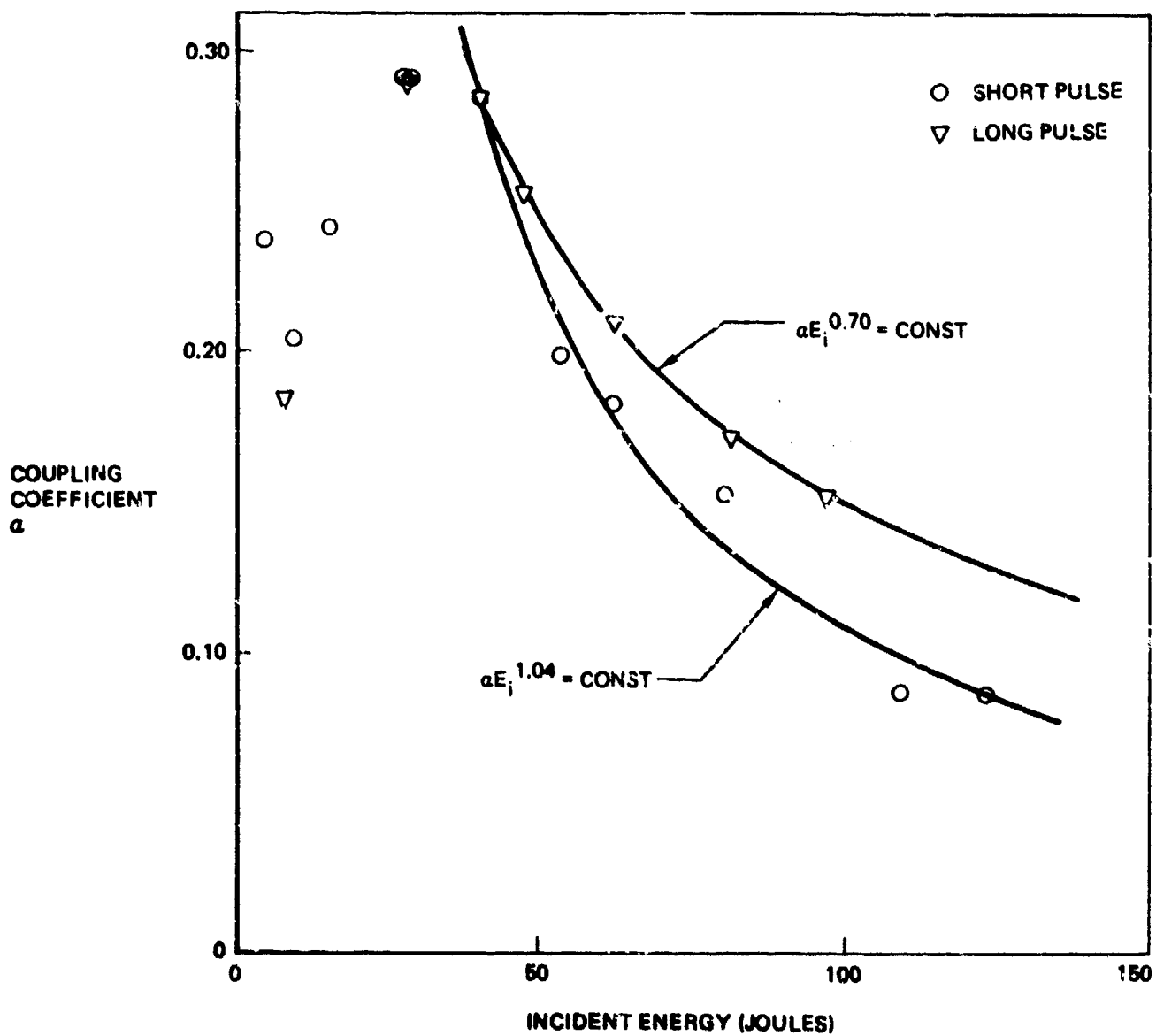


Figure 38. Effect of Pulse Length on Titanium Thermal Coupling. Circles are for 4 μ sec FWHM Pulses. Triangles are for 7 μ sec FWHM Pulses.

incident beam. Thermal deposition measurements at beam energies above LSA wave thresholds have shown heating profiles with widths greater than the incident beam width as discussed below and in Section VI.

a. Target Size Effects

Total thermal coupling coefficients were measured as described in Section IV for targets of three different diameters in order to obtain information on the radial extent of the target heating profile. Aluminum targets with diameters $d_1 = 0.79$ cm, $d_2 = 1.59$ cm, and $d_3 = 2.22$ cm were exposed to HF laser beam pulses near 80 J with a beam focal spot diameter of 0.46 cm. As seen in figure 31, these conditions are well above plasma threshold, lying in the $\alpha E = \text{constant}$ region. For constant incident energy E_i , coupling coefficients α were measured to form the ratios $\alpha_1/\alpha_2 = W_1/W_2$ and $\alpha_2/\alpha_3 = W_2/W_3$ where W_j is the energy deposited in target j , and the subscripts are the target-size indices.

For purposes of defining a time-averaged effective heating width parameter, an axially symmetric gaussian with $1/e$ radius δ was assumed for the thermal deposition profile. (Also see Section VI.) An effective gaussian heating radius δ can be obtained from any two target sizes by solving for δ by the relation

$$\frac{1 - \exp(-r_1^2 / \delta^2)}{1 - \exp(-r_2^2 / \delta^2)} = \frac{W_1}{W_2} \quad (32)$$

where the radii are known and the ratio W_1/W_2 is measured.

The results of table 7 show that the time-averaged heating profile is about twice the diameter of the beam spot. The half-maximum radius $r(\text{heating}) = \ln 2 \delta$. The variation of the effective gaussian radius δ with the size of the target pairs is interpreted as reflecting the inadequacy of the single-gaussian profile assumption.

Targets 2 and 3 (large pair) give a gaussian width $\delta = 0.73$; targets 1 and 2 (small pair), $\delta = 0.44$ cm. This indicates an actual deposition profile which has a high-level central component and a lower-level, broader component. This particular departure from the single gaussian shape is also indicated by time-dependent temperature measurements discussed below.

b. Target Temperature as a Function of Time and Radius

A second method of obtaining the spatial distribution of thermal energy deposited in a metal target is by temperature measurement.⁽⁴⁾ The aluminum targets used are thin so that axial thermal diffusion times are small (typically > 1 msec), and large enough in the radial direction to be effectively infinite as far as thermal behavior near the center is concerned.

TABLE 7

EFFECTIVE GAUSSIAN HEATING RADIUS δ IMPLIED BY TARGETS OF RADII $r_1 = 0.40$ cm, $r_2 = 0.80$, AND $r_3 = 1.11$ cm, FOR INCIDENT HE LATER FLUENCE $e = 480$ J/cm² INTO A BEAM SPOT OF EFFECTIVE RADIUS $r_{\text{eff}} = 0.23$ cm ON ALUMINUM 6061.

Deposited Energy Ratio	Implied Heating Radius δ	$\frac{r(\text{heating})}{r_{\text{eff}}(\text{beam})}$
$\frac{W_2}{W_3} = 0.77$	0.73 cm	2.6
$\frac{W_1}{W_3} = 0.45$	0.52 cm	1.9
$\frac{W_1}{W_2} = 0.58$	0.44 cm	1.6

An established method of obtaining the initial energy deposition profile $T(r, 0)$ is to measure the temperature at the target center as a function of time and infer the initial distribution by a Laplace transform. ⁽⁴⁾ Characteristics of initial amplitude and width are then obtained for an assumed standard profile, which is typically a gaussian.

Here this method has been generalized by including time-dependent measurements of temperature at points away from the target center. Interpretations are again carried out in terms of the gaussian profile model. In principle the time-dependent temperature at any radial distance from the target center may be used to infer the initial temperature distribution:

$$T(r_0, t) \rightarrow T(r, 0)$$

The time-dependent temperature for a gaussian initial profile is:

$$\frac{T}{T_0} = \frac{\tau}{t+\tau} \exp \left[- \frac{r_0^2}{4\kappa(t+\tau)} \right] \quad (33)$$

Where κ is diffusivity, $T_0 = T(0, 0)$, and τ specifies the gaussian $\frac{1}{e}$ width δ at $t = 0$:

$$\delta^2 = 4\kappa\tau \quad (34)$$

Equation 33 is plotted in figure 39 for four values of r_0 .

The maximum temperature for each of these curves (for $r_0 > \delta$) occurs at:

$$t_{\max} = \frac{r_0^2}{4\kappa} - \tau \quad (35)$$

Experimentally the value of t_{\max} is readily obtained and is insensitive to: (1) the thermocouple time constant, which must be taken into account at early times, and (2) baseline zero shifts to which late-time data are most sensitive. Since r_0 is determined by thermocouple location and κ is a

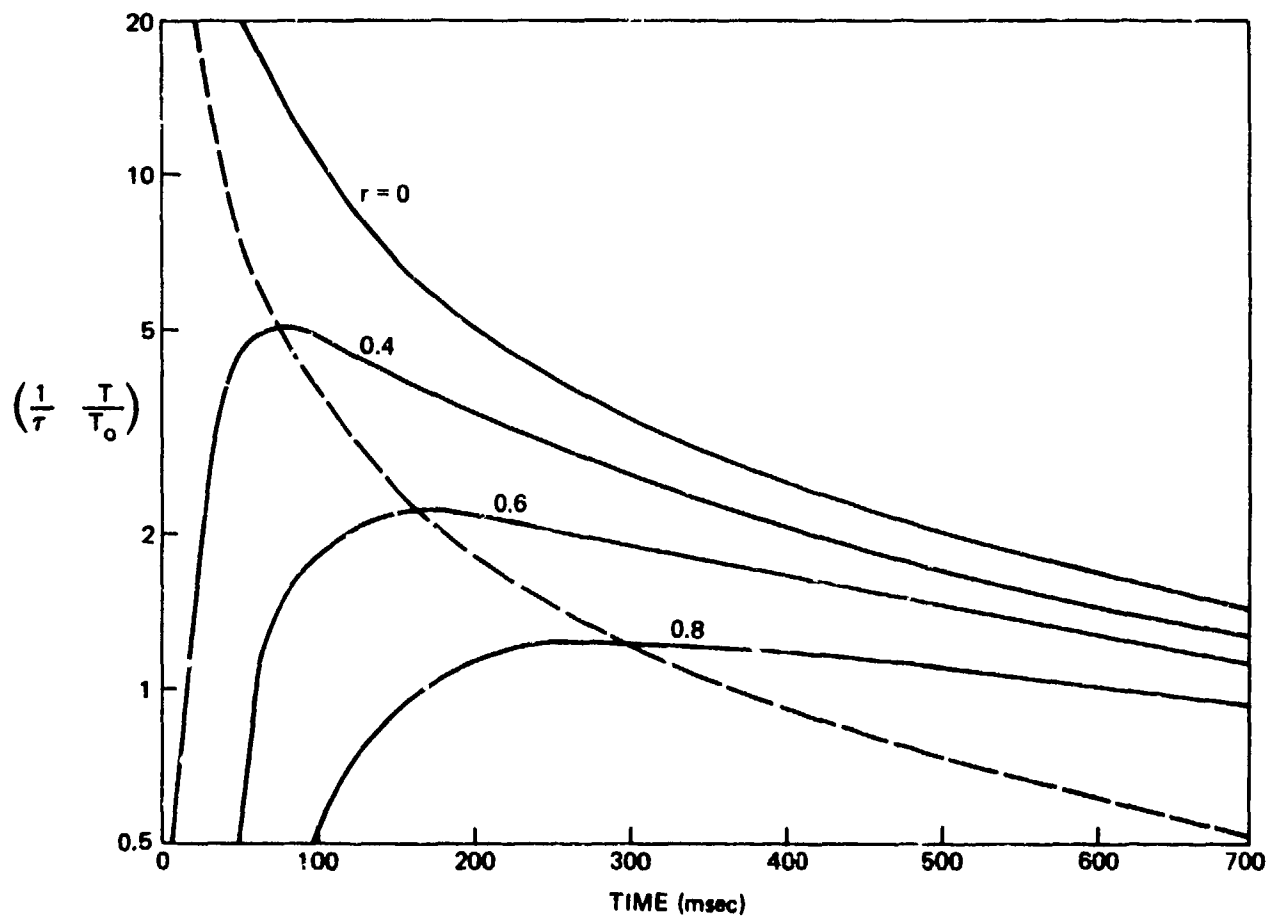


Figure 39. Normalized Temperature as a Function of Radius and Time, Applicable for a Gaussian Initial Temperature Profile in a Thin Infinite Sheet of Aluminum

function of the material, an approximate value of τ can be obtained from each curve of measured $T(r_0 \neq 0, t)$ simply from its t_{\max} . This maximum is expected to occur only if $r_0^2 > 4\kappa\tau$. A better value of τ can be obtained by fitting the entire curve $T(r_0, t)$.

Measured temperature $T(r_0, t)$ for aluminum are shown in figure 40 for laser pulses near 140 J. The general trends expected from figure 39 are observed, with a thermocouple time constant near 10 msec affecting the early time data, particularly for $r_0 = 0$. The value of τ which gives the initial profile width is best obtained from equation 35 using a value of r_0 for which t_{\max} is small. (For large values of t_{\max} , one subtracts two large numbers.) A value of $\delta = 0.29$ cm gives $\tau = 40$ msec, and predicts t_{\max} of 34, 127, and 256 msec for $r_0 = 0.4, 0.6$, and 0.8 cm. This agrees reasonably well with the values of t_{\max} in figure 40. (The focal spot radius is 0.23 cm.) The fact that the $r_0 = 0$ data at late times indicates a larger value of τ and larger δ is due to an actual initial profile which has a high-level central component as well as a lower-level broader component. Therefore, the single gaussian approximation is not always adequate.

c. Central Temperature as a Function of Time

Setting $r_0 = 0$ in equation 33 gives the time dependence of temperature at the center of the thermal deposition profile. This "central" temperature was observed as a function of time for 200 msec for a 0.46 cm diameter beam spot on aluminum samples. Table 8 shows the result of a two-parameter fit to (4)

$$T = \frac{T_0 \tau}{t + \tau} \quad (36)$$

over the time range 20 to 200 msec for three incident energies: 8, 54, and 145 J. The parameters τ and δ are related by equation 34. T_0 is the initial temperature rise, E_d is the total deposited energy, and α_c is the corresponding thermal coupling coefficient. For comparison, total measured thermal coupling coefficients as obtained from figure 31 are tabulated as α_t .

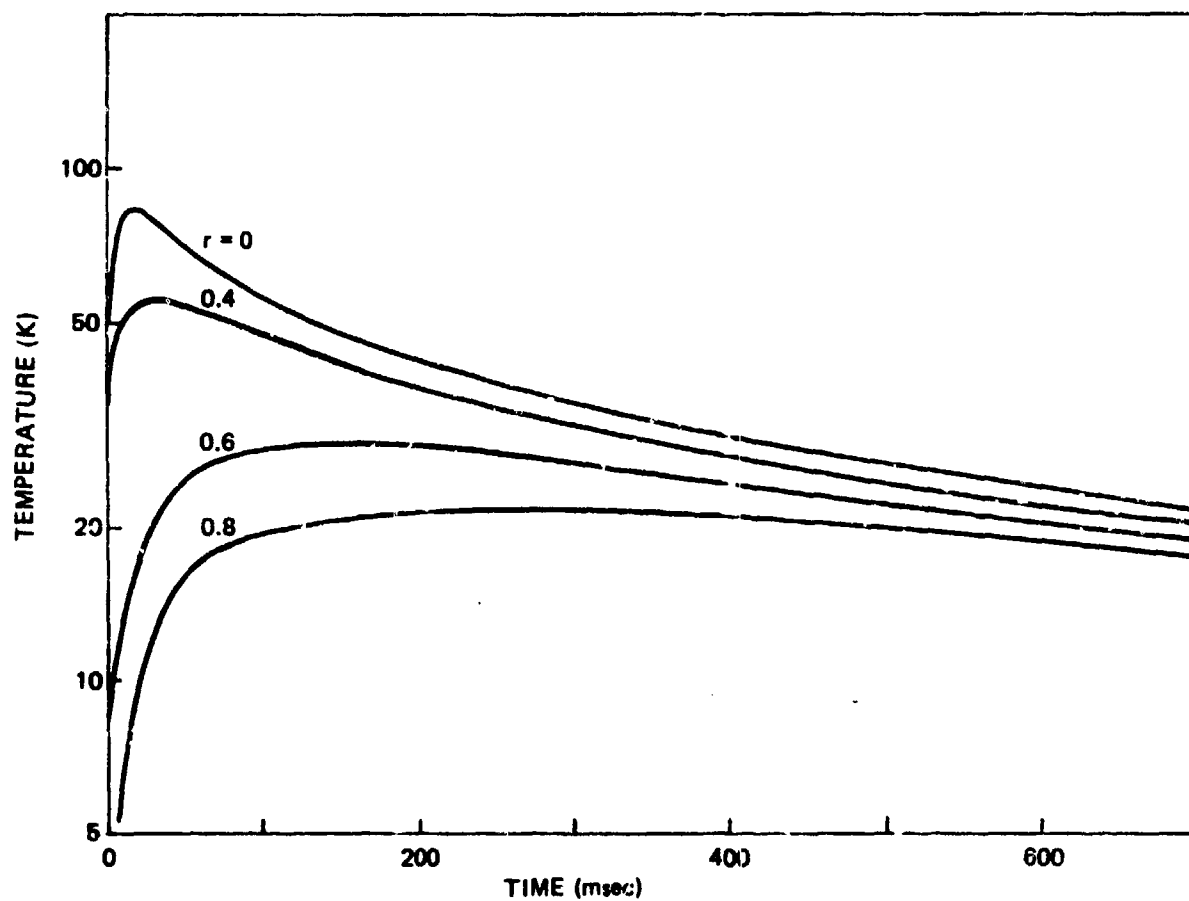


Figure 40. Measured Temperature as a Function of Radius and Time in a Thin Sheet of Aluminum

TABLE 8

RESULTS OF TWO-PARAMETER (T_0 , τ) FITS OF THE TIME-DEPENDENT TEMPERATURE
MEASURED AT $r = 0$.

E_i (J)	τ (msec)	δ (cm)	T_0 (°K)	E_d (J)	α_c	α_t
8.1	180	0.61	4.6	0.32	0.039	0.051
54	170	0.61	118	7.7	0.14	0.113
145	270	0.76	89	9.3	0.064	0.042

SECTION V
MASS LOSS AND TARGET IMPULSE DUE TO HF AND DF RADIATION

1. MASS LOSS

Mass removal of two ablators by pulsed HF radiation was investigated for large spot conditions at 1 atm air pressure. Lucite and Teflon samples were exposed at the focal plane of a 76 cm focal length mirror. The focal spot was described in Section II and had an area inside the half-maximum intensity contour of 0.69 cm^2 .

The energy range available allowed the study of mass removal for total pulse fluences from 0 to 250 J/cm^2 with peak intensities up to 75 MW/cm^2 . In this region, inspection of exposed Lucite and Teflon targets showed distinctly different types of target response. Lucite mass removal was observed as a shallow crater with approximately the shape of figure 8 with effects confined to the region near the surface. Teflon, on the other hand, transmits most of the HF radiation to a significant depth. Damage in this case appeared as a blackening of the white Teflon samples throughout the 0.16 cm thickness. The only apparent mechanism for mass loss is localized small-scale blistering on the target front surface and, to a smaller extent, on the rear surface.

Mass loss curves are shown in figure 41 as a function of incident energy for both materials. The mass loss of Teflon is zero on this scale. The solid circles show the specific energy required to remove Lucite, in kJ/g.

The dependence of Lucite mass loss on the ambient pressure p was investigated in the vacuum vessel of figure 15. The mass loss was measured at four pressures from 1 to 10^{-4} atm corresponding to altitudes of about 0, 16, 31, and 49 km. The open circles of figure 42 are for 85-J incident laser pulses. (The point at 7.6 Torr is an interpolation between 91 J and 59 J points, which are indicated by rectangular symbols. The measured energies for the other points are $85 \pm 1 \text{ J}$.) The decrease in the density and the opacity of laser-formed surface plasma results in increased coupling and mass loss at reduced pressures.

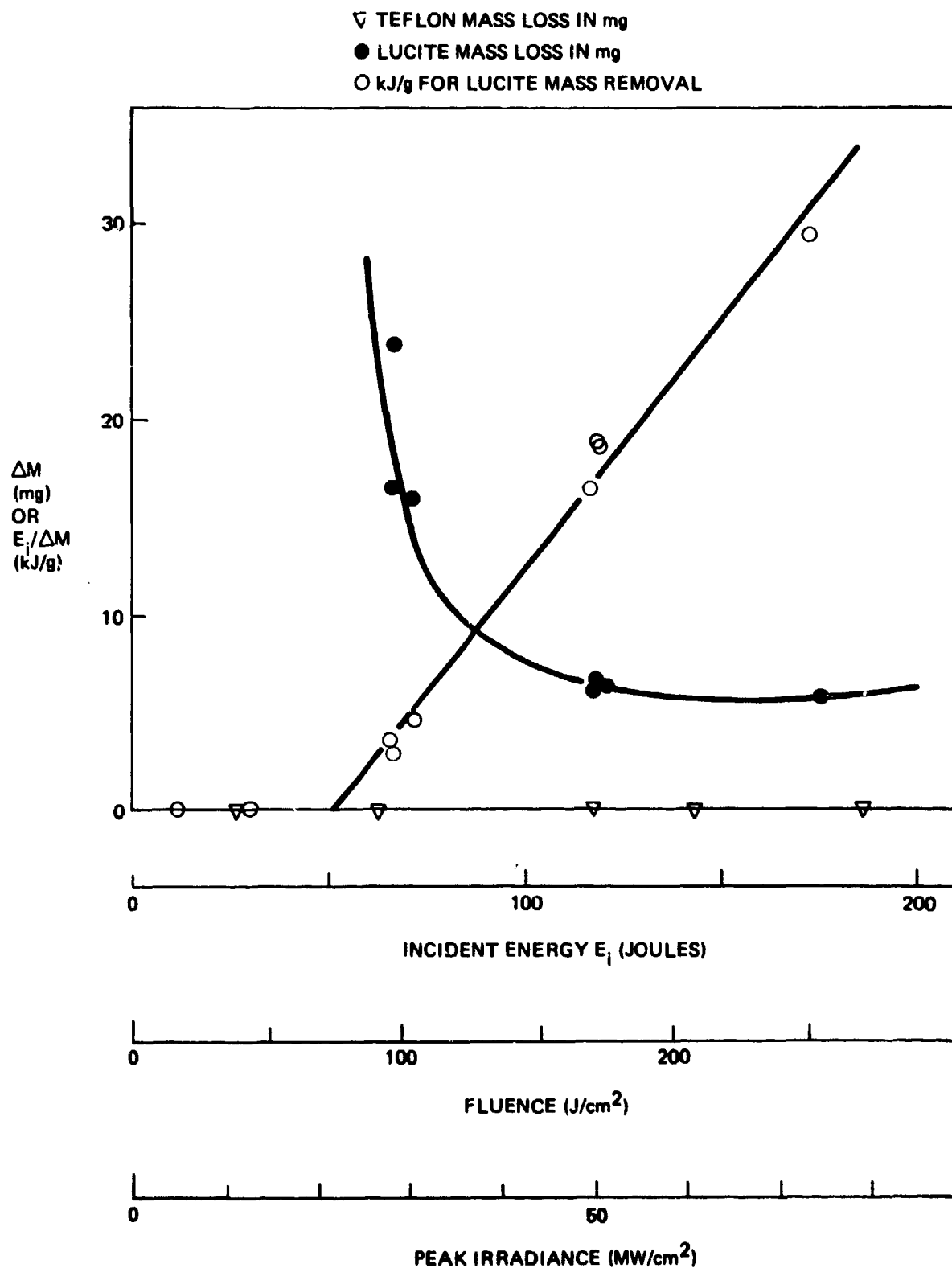


Figure 41. Lucite and Teflon Mass Removal by Pulsed HF Laser Radiation

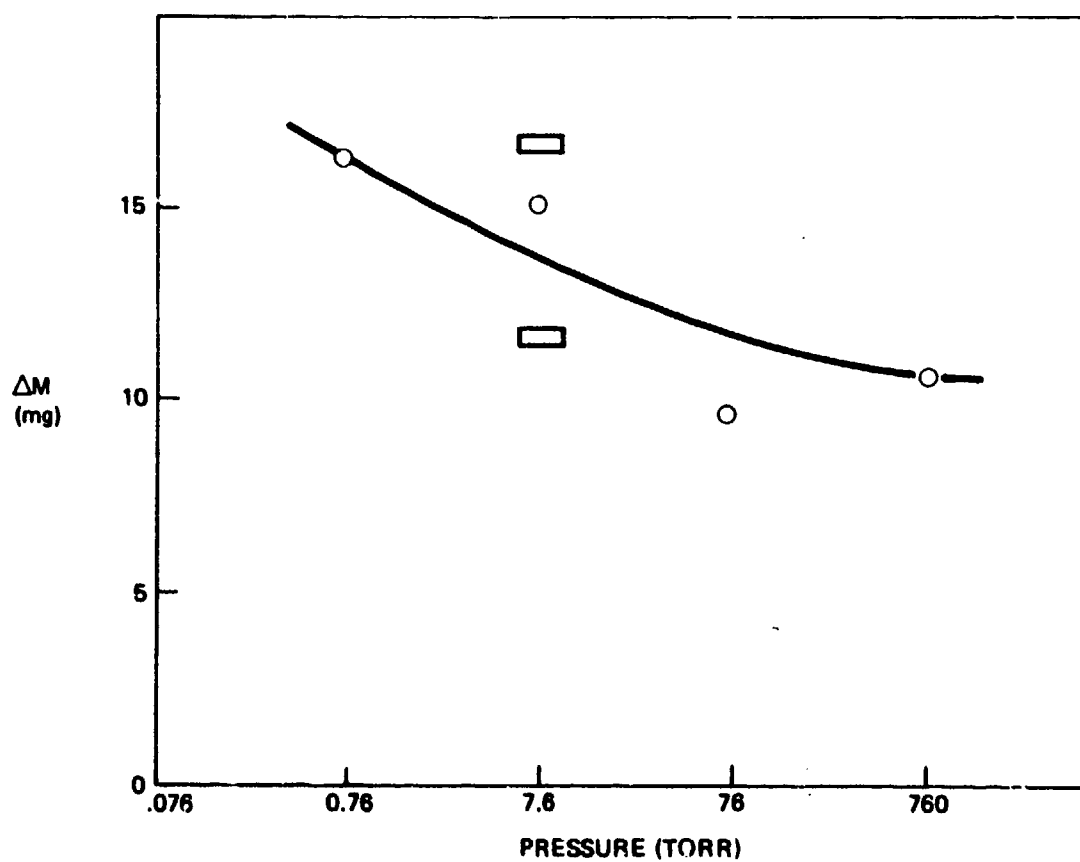


Figure 42. Dependence of Lucite Mass Loss on Ambient Pressure at the Target, $E_i = 85$ J

2. IMPULSE

The 0.94-cm diameter HF laser focal spot was also used for measurements of the momentum imparted to several materials in air. A linear velocity transducer (LVT) provided a continuous record of the instantaneous velocity of the target and supporting plunger through about 0.7 cm of travel occurring over a few milliseconds after the laser shot. The voltage output of the LVT was recorded as an oscillograph. Because the distance of travel was well defined and readily measured, the LVT calibration could be monitored for each shot.

Initial impulse measurements were made to determine the effect of target geometry. All targets were 2.54 cm in diameter. Aluminum targets were exposed to pulses between 150 and 180 J for two target geometries: (1) The target was mounted on the LVT moving core by a cylindrical post to the center of the target rear surface so that the target edge was exposed. In this case pressure waves occurring on the front surface flowed around the target edge, and decreased the net impulse delivered to the target (1). (2) The target was mounted as in (1) except for the addition of an edge shield consisting of a large planar surface with a 2.54 cm hole through which the target could move. In this second geometry, the target was initially flush with the shield surface, forming an almost uninterrupted plane. Radial clearance was typically 0.015 cm. The shield plane was 0.1 cm thick. The impulse measured with the shield in place was typically larger by a factor of 1.4 than that observed without the shield. The measurements reported here were all taken with the shield in place.

The specific impulse delivered to aluminum 6061 is shown in figure 43 as a function of incident energy for both HF and DF radiation. The DF and HF thresholds are both near 50 J, but the DF curve shows a step increase while the HF-produced impulse increases gradually up to about 120 J. These impulse curves are similar to the DF and HF threshold behavior shown in figure 18 which showed the beam plasma cut-off for the same target material and the same beam spot size and configuration. For DF, both plasma cut-off and impulse show a steep threshold near 50 J (70 J/cm^2). For HF, both plasma cut-off and impulse show an initial threshold at about the same energy, but a gradual variation with energy over the range 50 to 120 J.

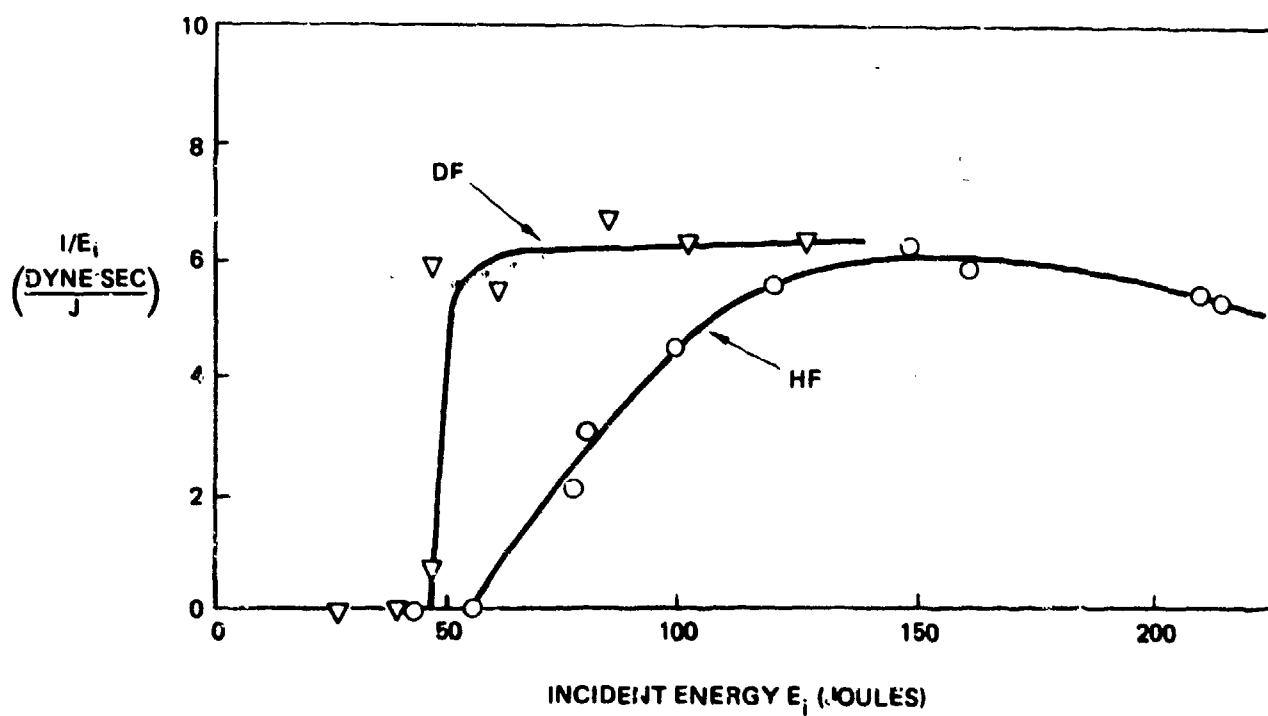


Figure 43. Specific Impulse Imparted to Aluminum by HF and DF Pulsed Laser Radiation

Less detailed momentum measurements were made for HF radiation incident on stainless steel, titanium, and Lucite. These data are plotted in figure 44 with the aluminum HF data of figure 43 as a background for comparison. The four materials show similar behavior in the energy range studied except for Lucite where vaporization contributes to the impulse delivery. Except for titanium, the approximate impulse thresholds observed correlate well with the plasma threshold observed in figures 21, 22, and 26.

3. IMPULSE FROM CONFINED PLASMA

Values of I/E about one order of magnitude greater than the largest values shown in figure 44 have been observed for a target geometry which results in confinement of the target-produced plasma. The resulting large values of delivered impulse can be expected wherever an absorbing surface is covered by an IR-transparent material having significant mass.

A 0.16 cm thick teflon wafer was attached to an aluminum disc (both 2.54 cm diam) with an opaque adhesive. An HF laser pulse of 143 J delivered to the teflon side of the assembly imparted a specific impulse I/E of 75 dyne-sec/J to the aluminum backing disc. This event shattered the teflon disc and deformed both the aluminum backing disc and the LVT plunger. The velocity of the backward-moving assembly reached 1.9×10^3 cm/sec. If uniform acceleration for 30 μ sec is assumed an acceleration of 6×10^4 g's is obtained. Distributing the force over the entire 2.54 cm disc diameter gives an average pressure during that 30 μ sec of 70 atm; if the force is applied only over the beam spot area of 0.69 cm² the average pressure is 730 atm.

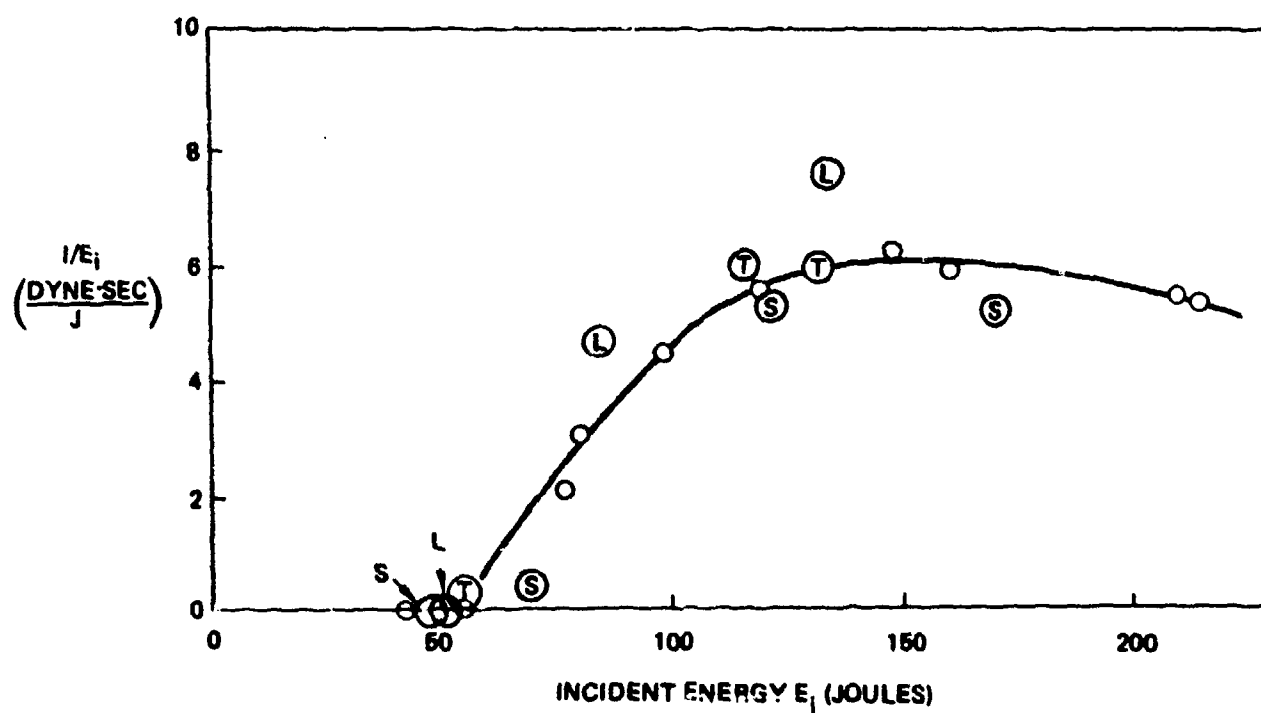


Figure 44. Comparison of Specific Impulse for Aluminum (Small Circles), Titanium (T), Stainless Steel (S), and Lucite (L).

SECTION VI

LASER INTERACTION AT 10.6 MICRONS WAVELENGTH

Although the primary emphasis in the experiments of this report was on interactions at chemical laser wavelengths, a number of new experiments were carried out at the longer CO₂ laser wavelength in order to determine some aspects of wavelength scaling and on mechanisms of enhanced coupling. From experiments reported here, using different size targets, we have determined the dependence of the plasma spreading on delivered laser energy. These results were found to be in approximate agreement with new experiments using a transverse air flow facility. With a high speed wind, the plasma is blown partly away from the desired target area and the net coupling is reduced.

We also attempted experiments using molten targets to determine those conditions under which the pressure from LSD waves would blow out the molten material.

1. EXPERIMENTAL APPARATUS

These measurements were made using the Boeing Double Pulse CO₂ lasers whose focal spot intensity profiles have been measured. The focal spot has a 0.16 cm radius for a 37.5 cm focal length. Both lasers have an approximate 6 nsec full-width half maximum temporal width, with peak power at 1.5 μ sec and a long tail. (15) Laser energy in each beam can reach 15 J with an arbitrary delay between the two pulses. In the work reported here, however, only single pulses or simultaneous double pulses were used with each beam incident at 90° to their common axis which was, in turn, perpendicular to the surface of the target. The operation of the lasers was always unchanged as far as discharge voltage or gas mixture is concerned and energies were varied by the insertion of attenuators. Laser power and energy were monitored by beam sampling diagnostics which viewed the beams after attenuation. In the focal plane there were no hot spots.

-
15. Hall, R.B., Maher W.E., and Wei, P.S.P., "An Investigation of Laser-Supported Detonation Waves," AFWL-TR-73-28, June 1973.
16. Hall, R.B., Maher, W.E., and Nelson, D.J., "Double-Pulse Laser Interaction Experiments," AFWL-TR-73-296, July 1974.

A transverse air flow facility was constructed during this study. Its flow field was examined so that laser target interaction experiments could be performed in a well defined uniform transverse air flow. A diagram of the subsonic transverse flow apparatus is shown in figure 45. The air is stored in a 1000 liter vessel at 6 atmospheres. A 10:1 area ratio is used for the long profile nozzle which leads to the open test volume. Beyond that a catcher and diffuser section recovers the air and sends it through a filter. The high flow regulator valve can be adjusted for plenum pressure and hence average velocity, leading to a limited time available for nearly uniform flow. After the on-off valve is opened, approximately five seconds are required for the flow to stabilize. Over the next ten seconds the average velocity is nearly constant, varying less than 1%. The exit of the nozzle is 2 x 2 cm and the open region length is 4 cm. Figure 46 is a photograph of the entire facility with the storage tank in the lower foreground and with the high flow regulator valve in the last leg in the piping (seen angling to the upper left) before the plenum. The experimental area is between the nozzle and the catcher in the upper right portion of the picture, just to the left of the mirror. This area is shown in an enlarged view in figure 47. In the foreground is the large focusing mirror, which focusses both beams on a position shown by the bright spot in the center of the wall forming one side of the test volume. It is fastened to the nozzle outlet which is in the tapering metal tube near the right side of the photograph. The flow moves from left to right through the test volume as it is shown in this photograph. Figure 48 is a line drawing of the same scene as figure 47 with the laser beam geometry also indicated. These two parallel beams enter the scene from the right with beam #1 on top. After skirting the test volume, nozzle, and catcher, they reach the mirror which then sends them to the common focal point.

The test volume was probed with a 0.1 cm diameter tube pointed upstream and connected to a pressure meter. Each datum point was recorded 10 seconds after flow initiation and determined the local velocity to within one percent. In addition, flow fluctuations contributed 2 to 3% uncertainty. These data were evaluated to find the uniformity conditions in the test volume which are summarized in figure 49. Within the shaded areas in the planes 0, 1, 2, and

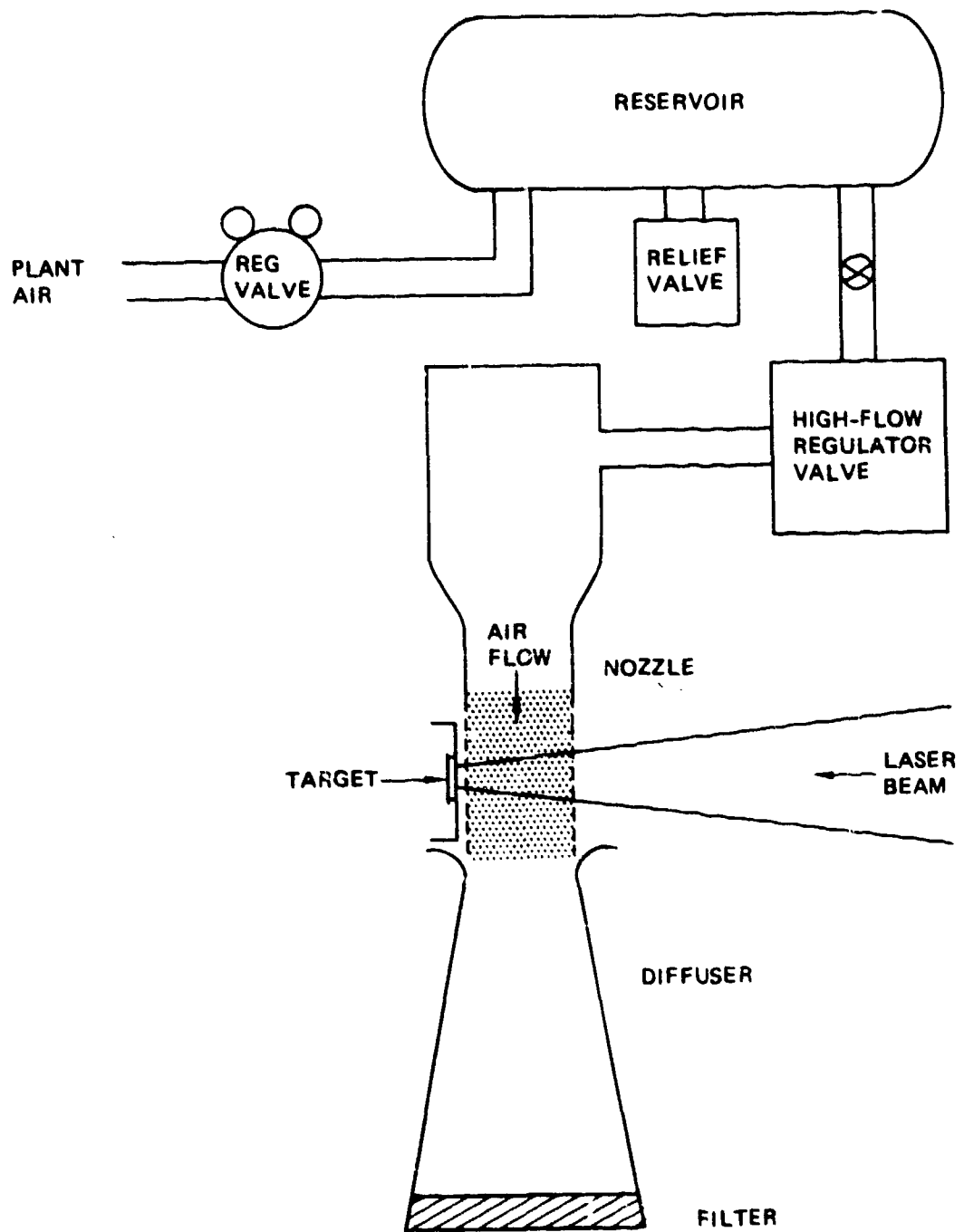


Figure 45. Subsonic Transverse Flow Apparatus

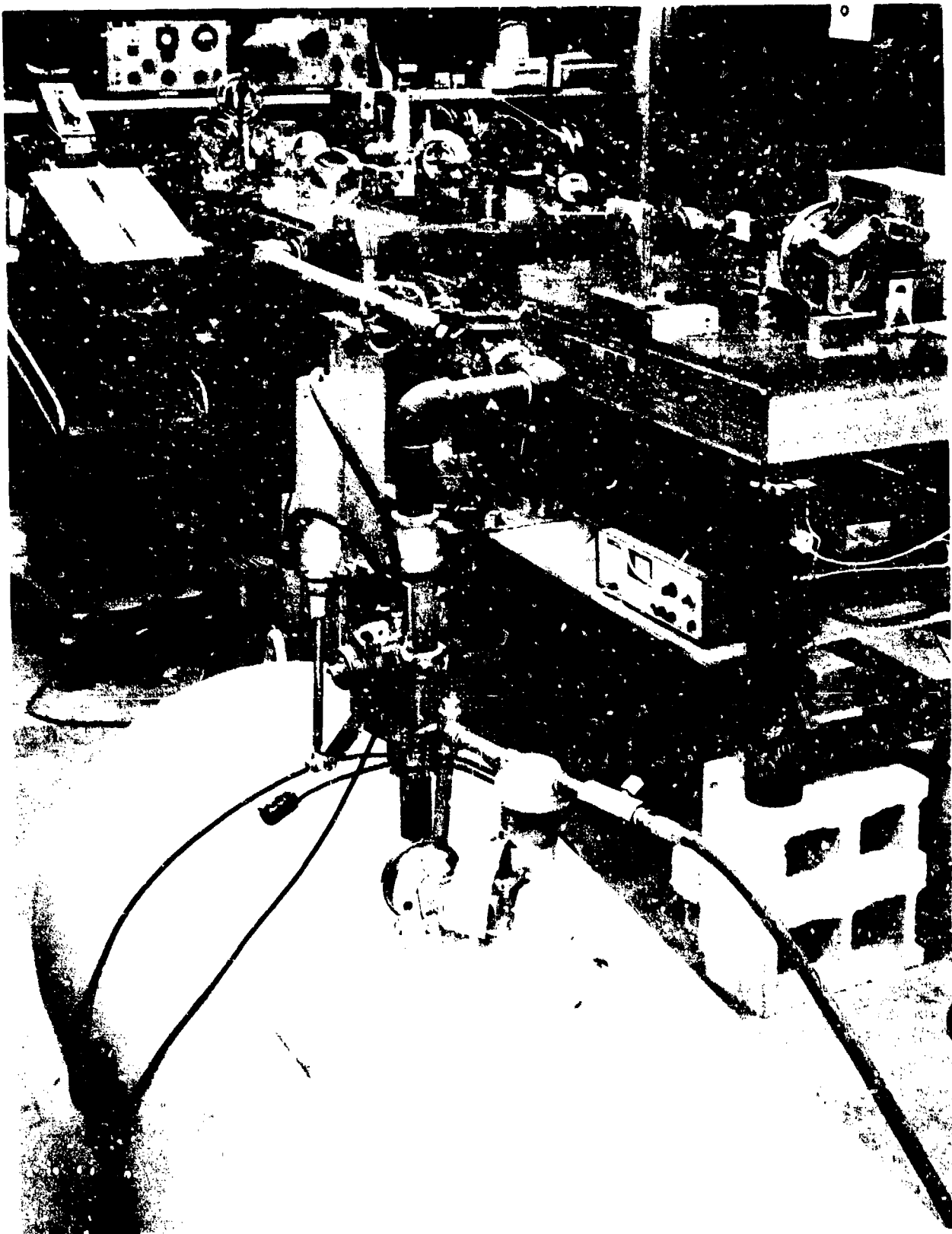


Figure 46. Subsonic Transverse Flow System

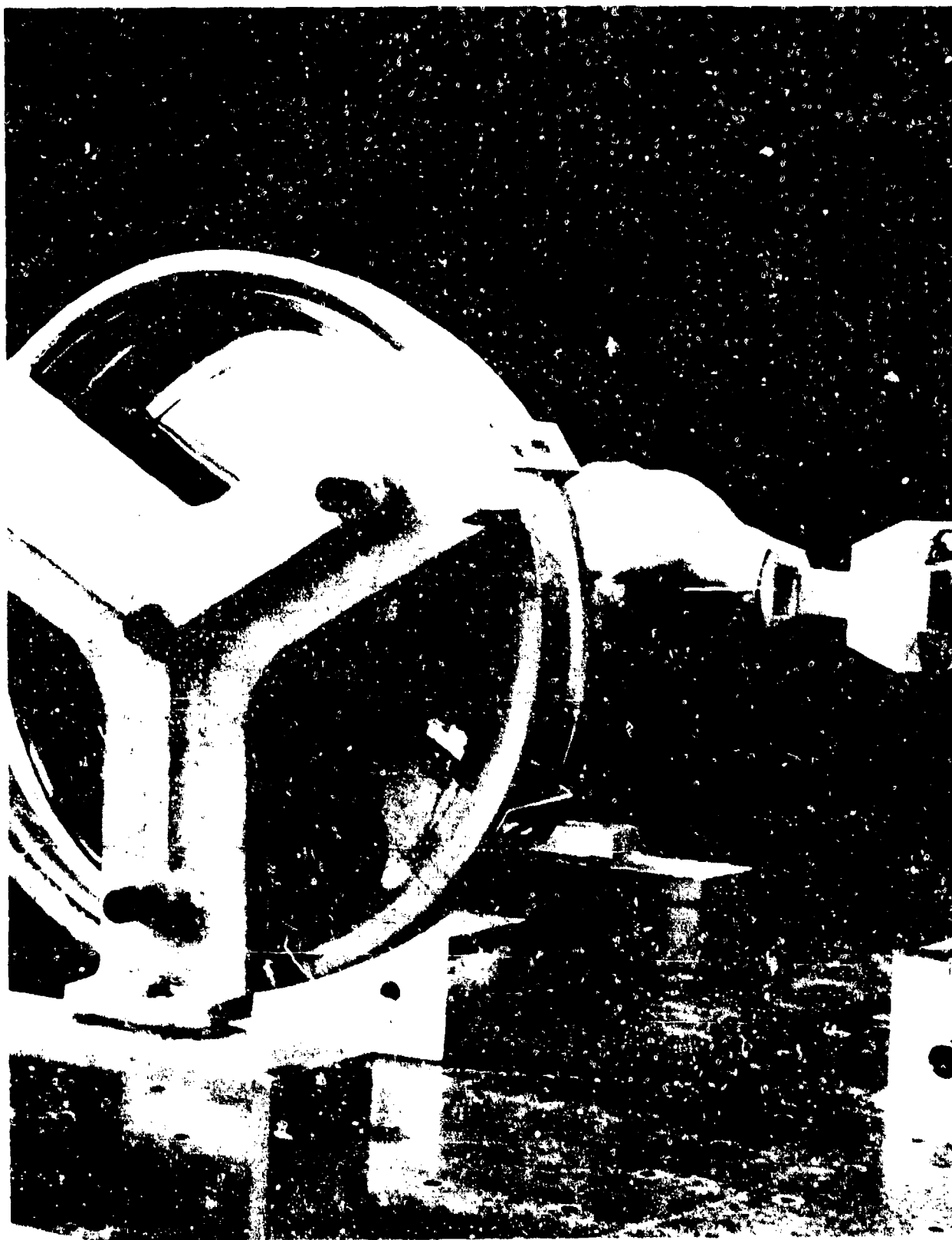


Figure 47. Subsonic Transverse Flow Experimental Arrangement

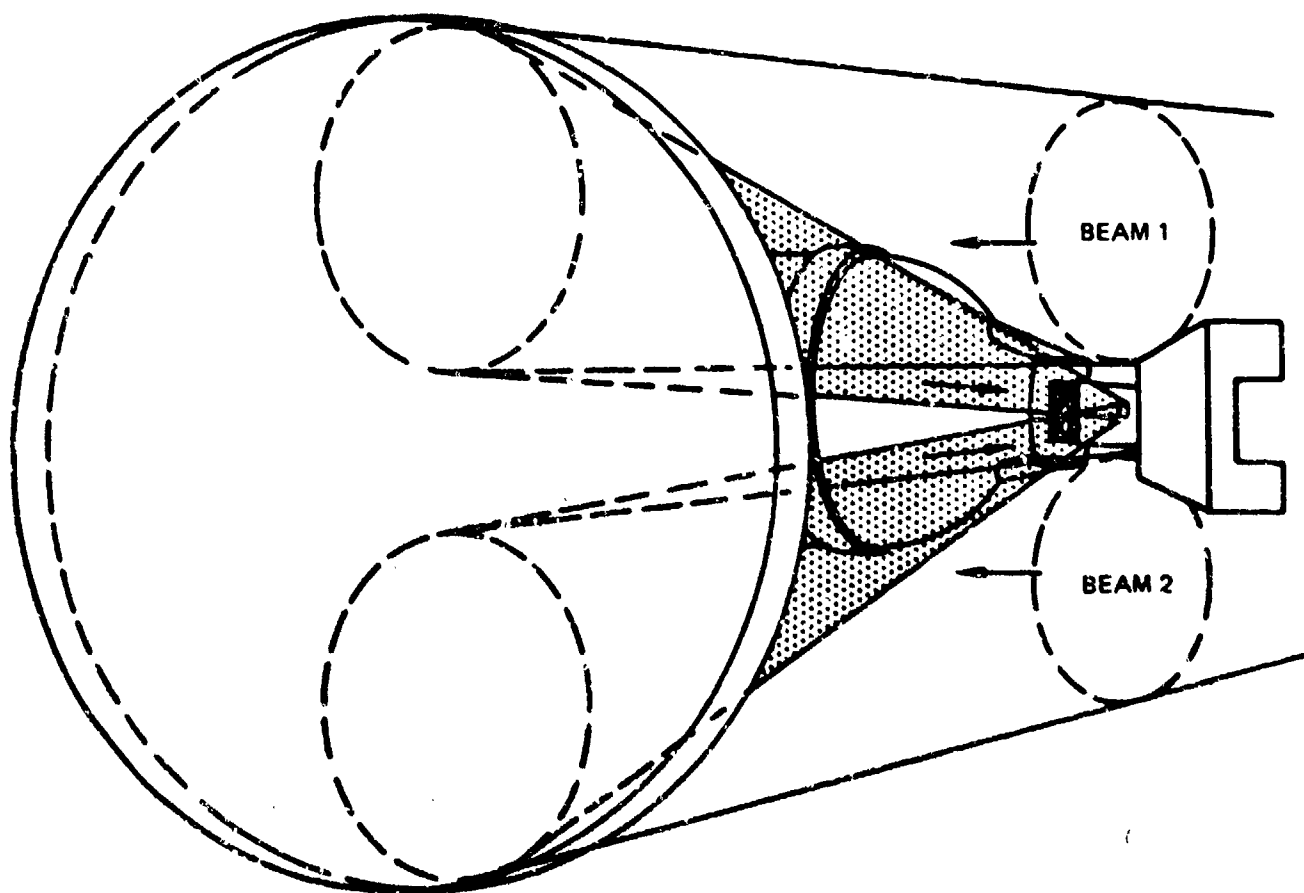
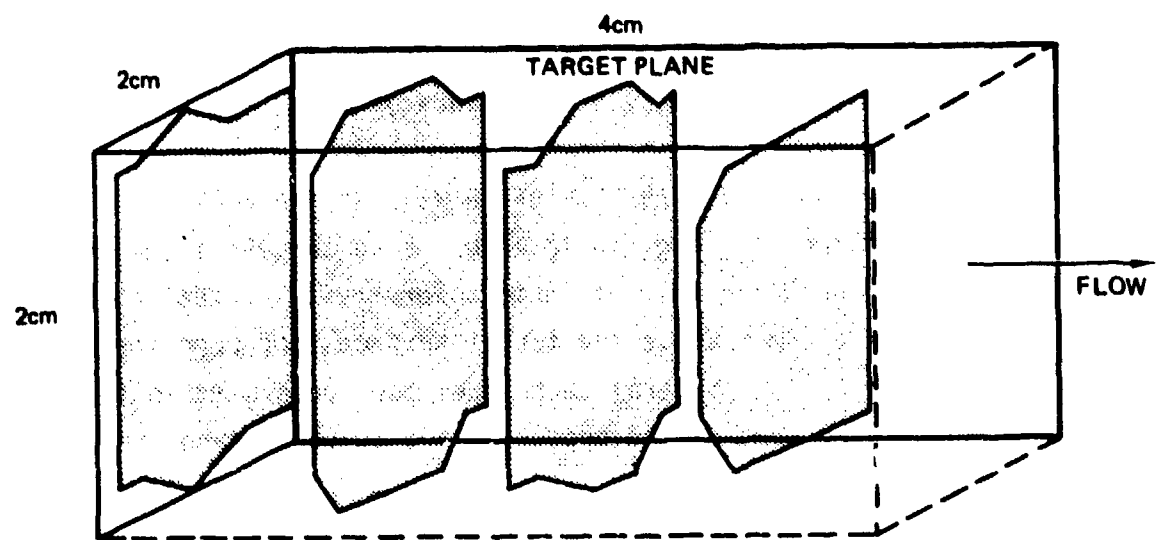


Figure 48. Laser Beams and the Subsonic Transverse Flow Experimental Arrangement



WITHIN SHADED AREA $160 \leq u \leq 172$ m/sec, i.e., $166 \text{ m/sec} \pm 4\%$.

NOTE: $T \sim 270^\circ\text{K}$

Figure 49 Velocity Field of Subsonic Flow

3 cm downstream from the nozzle exit the velocity field u is 166 m/sec $\pm 4\%$ at $T = 270^\circ\text{K}$. These measurements were made to within 0.1 cm of the target plane. The magnitude of the boundary layer δ_b was calculated from

$$\delta_b = \left(\frac{\mu x}{\rho u} \right)^{1/5} \quad (37)$$

where $\mu = 1.82 \times 10^{-4}$ poise and $\rho = 1.22 \times 10^{-3}$ gm/cm³.

In equation 37, u is the measured flow velocity and x is the distance from the point at the nozzle throat where the boundary layer begins. In the experiment reported here, $x = 5$ cm, indicating $\delta_b = 0.034$ cm.

2. THERMAL COUPLING IN THE ABSENCE OF TRANSVERSE AIR FLOW

Thermal coupling of energy in laser beams to targets is dependent upon many parameters including the intrinsic absorptivity at the laser wavelength, the formation of plasmas above the target surface, and upon the subsequent plasma spreading.⁽¹⁷⁾ Several techniques have been used in this study to distinguish between some of the processes and to understand the way plasma spreading takes place.

In these investigations, 0.012 cm diameter chromel-alumel thermocouples were spot welded together on the target samples so that the thermal junction was at the rear surface. In all the tests discussed in Section VI, the gross thermal coupling was determined by measuring the equilibrium temperature of the target.⁽³⁾ The equilibrium time for the 1.59 cm diameter targets used here was found to be approximately 0.5 sec for aluminum. A 10 second or longer cooling record was used, however, to give an accurate value for the equivalent equilibrium temperature rise at the time of the laser beam irradiation.

In figure 50, thermal coupling to nickel is shown for two focal lengths. The spot sizes are the areas corresponding to the full width half-maximum

17. Pirri, A. N., "Enhanced Thermal Coupling", Second DOD High Energy Laser Conference, Colorado Springs, November 1976.

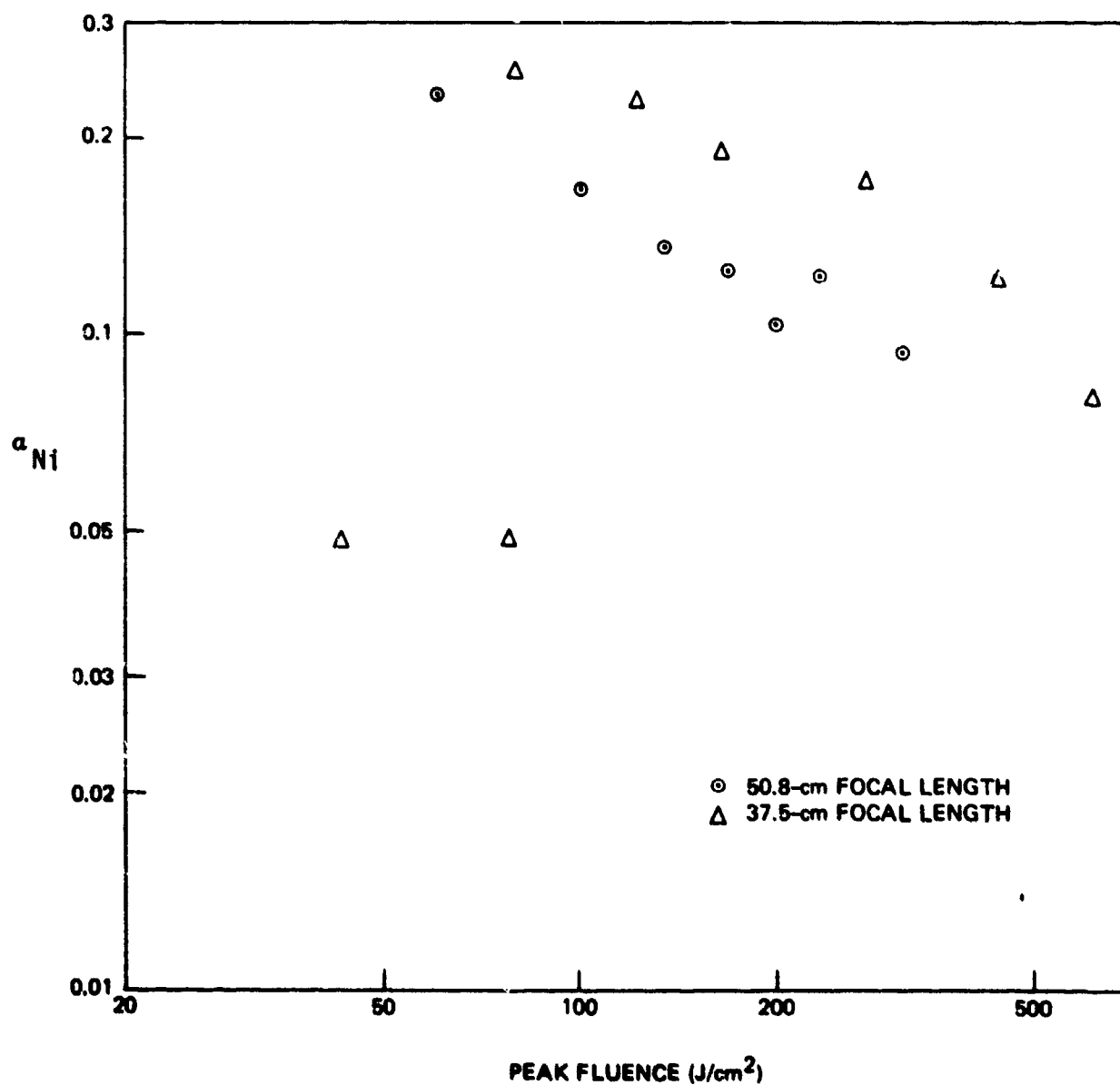


Figure 50. Thermal Coupling to Nickel for Two Spot Sizes at One Atmosphere

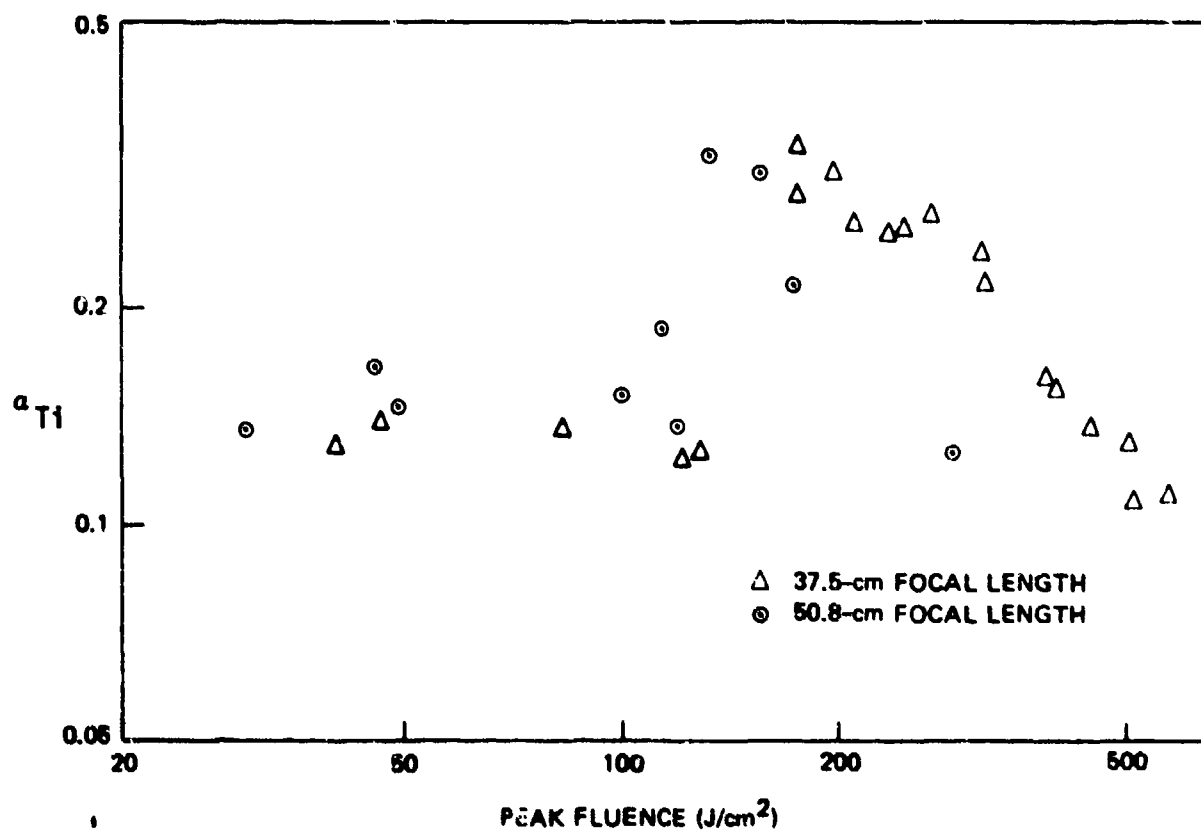


Figure 51. Thermal Coupling to Titanium for Two Spot Sizes at One Atmosphere

intensity. The total coupling, as discussed above, had a maximum value of 0.25 for both spot sizes. This represents an enhancement of about a factor of five over the intrinsic absorptivity of 5% at 10.6 μ . The threshold for this behavior can be seen to occur at 25% lower peak fluence for the larger laser spot area. However, the monotonically decreasing absorptivity keeps the larger spot coupling below that of the smaller spot. The continued high coupling at large intensities arises because the plasma is spreading out across the surface and heating the target outside the laser spot. Since the larger laser beam spots on these 1.59 cm diameter targets lead to somewhat smaller values of α , one speculates that α will tend to be a constant for large beam areas.

Similar data for titanium are shown in figure 51. Again, the data obtained with the larger laser spot have a lower thermal enhancement threshold. In addition, lower values of α throughout the enhancement region are obtained. These features indicate plasma spreading where a part of the heating profile for the larger laser spot extends beyond the 1.59 cm diameter target. Data presented in a previous report⁽⁴⁾ for magnesium showed the same kind of behavior for laser spot radii of 0.16 and 0.35 cm on the same size targets (1.59 cm diameter).

In order to determine the magnitude of the plasma spreading, the thermal coupling was measured for target disks of different diameters. A wide heating profile will couple a larger thermal energy into a larger diameter target assuming all other conditions are constant. The approach used here was to obtain data for such a variation of target diameter and then to determine a single parameter for the heating profile.

For these measurements, targets of aluminum and titanium with diameters of 0.80 and 1.59 cm were used. All of the measurements were otherwise similar. The focal spot of 0.16 cm radius was produced by a 37.5 cm focal length mirror. Each target had a single centered chromel-alumel thermocouple and was used as received except for a methanol wash. The thermal enhancement threshold was about 4 J for aluminum and about 6 J for titanium for this spot size.

Since the laser energy varies somewhat from shot to shot, it was of interest to fit analytic expressions to the gross thermal coupling variation with laser energy. Thus, data taken with different size targets could be easily compared. For 1.59 cm diameter targets:

$$\alpha = .29 \exp (-.078 E_i) \quad (38)$$

(for aluminum)

$$\alpha = 1.83 E_i^{-.93} \quad (39)$$

(for titanium)

In equations 38 and 39, E_i is the total incident laser energy while the peak fluence e_{\max} is

$$e_{\max} = E/.043 \text{ joules/cm}^2 \quad (40)$$

Figure 52 gives plots of the ratio of the thermal coupling coefficient obtained with the two sizes of targets. This ratio $\alpha_{1.59}(E_i)/\alpha_{0.79}(E_i)$, is unity below the threshold for plasma interactions. The titanium data are represented by x symbols, and the aluminum data by circles. Both data sets show that plasma spreading increases with incident energy in an approximately linear manner, after a step appears at their respective thresholds. A value of this ratio greater than unity means that thermal energy is being deposited in the area outside of the smaller target. In any case, since the focal spot area is much smaller than even the smallest target, it is clear that a considerable plasma spreading occurs. In addition, since the ratio increases with increasing energy, the spreading also increases with increasing incident energy.

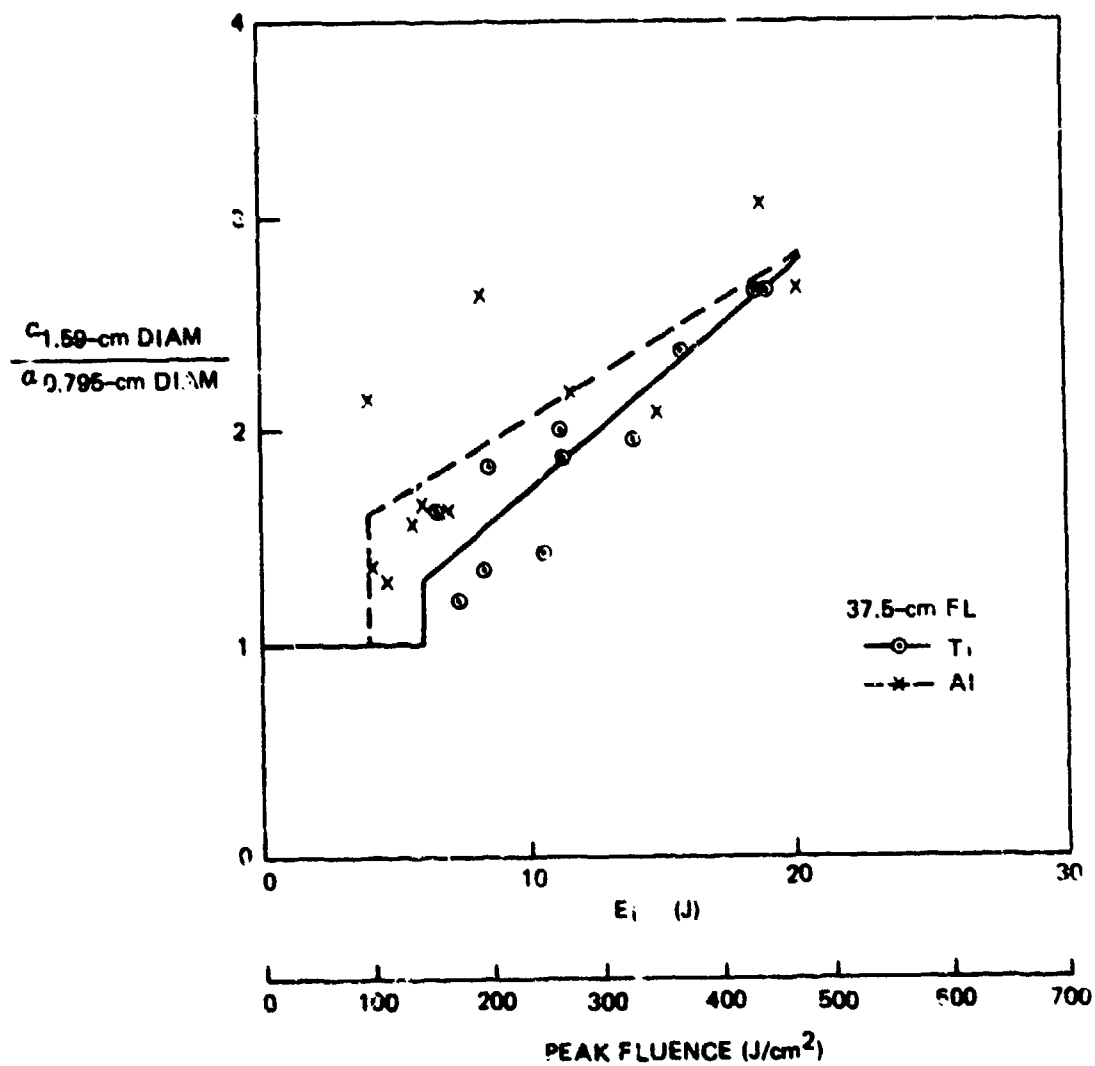


Figure 52. Edge Effect in Enhanced Thermal Coupling for Two Target Materials

It is assumed that the total absorbed energy fluence $e(r)$ has the Gaussian form

$$e(r) = A \exp(-r^2/\delta^2) \text{ joules/cm}^2 \quad (41)$$

where A and δ are constants for a given laser energy. Using the data of figure 52, one can then determine δ as a function of the incident laser energy.

In figure 53, δ is shown as a function of incident energy above the threshold for titanium and indicates a nearly linear dependence of δ on energy. Even at the threshold energy, δ has a value three times the laser beam spot radius which is coincidentally nearly the same as the small target radius. When the incident energy triples, δ doubles and the coupling area increases by a factor of four.

In figure 54, aluminum is the target. The results are almost identical to those found for titanium. The scatter in the data is larger for aluminum than it was for titanium, but the same trend is unmistakable as the coupling area increases by a factor of four over the range of incident energies investigated (4 to 20 J).

In an earlier experiment, a Laplace inversion of the central time dependent temperatures was used to determine an absorbed energy density profile width.⁽⁴⁾ These results showed a best estimate for δ of 0.44 cm when 9.3 J was incident on an aluminum target with a focal spot radius at half maximum intensity of 0.078 cm. Ignoring, for the moment, the difference in focal spot size, this 0.44 cm value for δ is nearly the same as the results shown in figures 51 and 52 where the average δ for the two target diameters is 0.51 cm for 9.3 J.

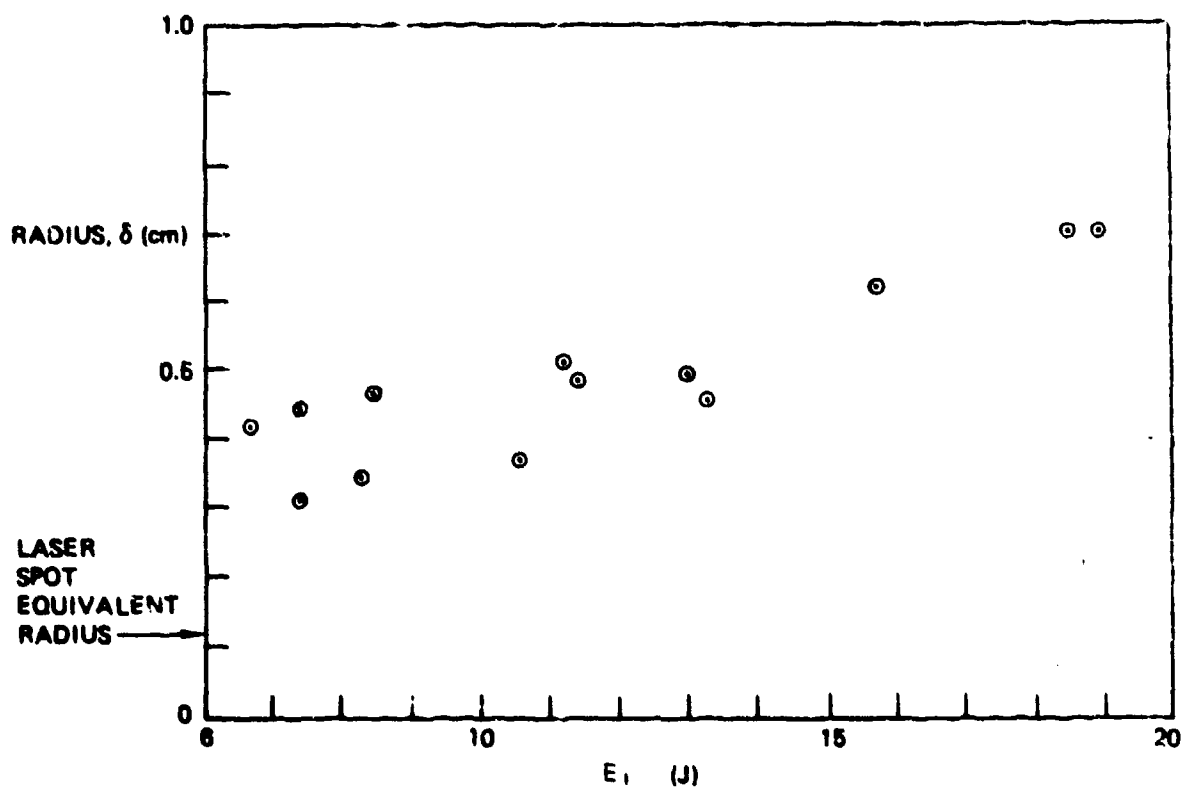


Figure 53. Heating Profile Gaussian Radius δ From Titanium Target Diameter Variation

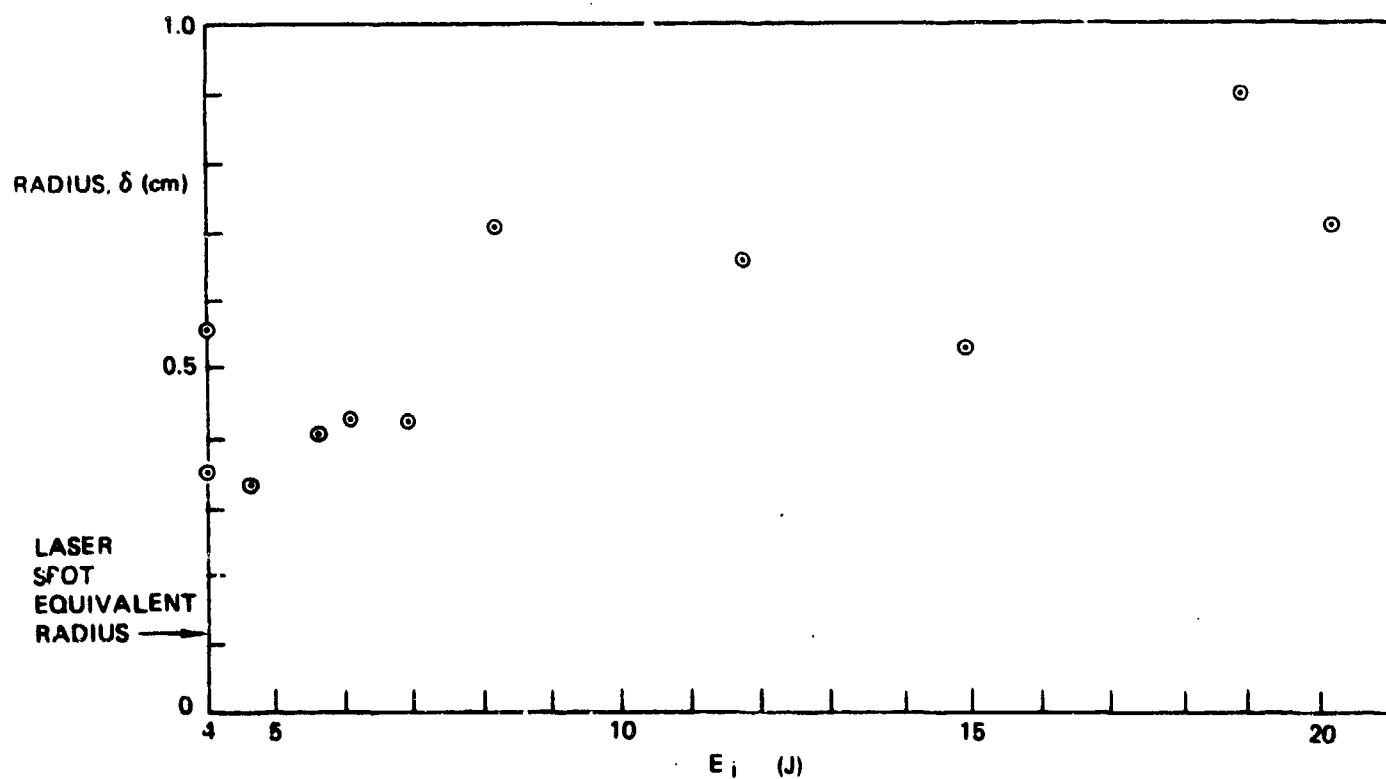


Figure 54. Heating Profile Gaussian Radius δ From Aluminum Target Diameter Variation

3. THERMAL COUPLING IN THE PRESENCE OF AIR FLOW

In the experiments reported in this section, the transverse-flow wind tunnel was used to simulate a fast-moving target. In addition, it was hoped that the experimental results would aid in understanding the mechanisms of enhanced coupling.

In these experiments using the transverse air flow, however, adjustments had to be made in the experimental procedures compared with the no flow case. There is strong convective cooling of the target by the air flow which had a temperature of 270°K . This flow was found to cool the adjacent targets at rates of $-0.6^{\circ}\text{K sec}^{-1}$ by the time 5 seconds has elapsed. Most of the data taken below utilized an electrical compensation circuit to avoid a reduction of temperature measuring sensitivity. With the chart recorder dynamic voltage range available and the sensitivity setting normally used in no flow thermal coupling, only 13 seconds of flow would cover the total available voltage range. Of this, the first 5 seconds during flow stabilization wasn't useable. A ramp voltage derived from an oscilloscope triggered when the flow commenced was placed in series with the input to the chart recorder so that after a predetermined time, usually 5 seconds, the signal to the recorder was not changing rapidly. Then a laser-interaction thermal-coupling temperature excursion could be easily triggered and analyzed.

Again, a single target-centered chromel-alumel thermocouple was used. A Plexiglas holder gripped each target by the edge and positioned it so that it was flush with the holder surface which formed one side of the test volume. Every datum was from a fresh sample in an as-received condition except for a methanol wash. Every test began with the target at room temperature. Maximum equilibrium temperature excursions due to laser thermal coupling were under 10 K. Where two simultaneous laser pulses were used to increase the laser energy, an oscilloscope monitored detectors for both beams and a photographic record of the oscilloscope traces was used to assure that both pulses were simultaneous to within 1 μsec .

Two target sizes were used, and flow could be present or absent. In figure 55, data for a titanium target of diameter 0.81 cm are shown for a flow velocity of 166 msec^{-1} and for the case of no flow. It is apparent that the presence of flow makes no appreciable difference in the thermal coupling measured at any incident energy in the range 6 to 20 J. The thermal coupling decreases as $E_i^{-2.5}$ and leads to values of α near 0.03 at the highest energies. This 0.03 value is far below the intrinsic 10.6μ absorptivity of 0.14 for titanium. Even at the plasma threshold, the maximum coupling is below the 0.34 peak values seen in figure 51.

Using 1.59 cm diameter targets and for the same laser beam focal spot size, a large change in thermal coupling occurred when the transverse flow was on. These data are shown in figure 56. The no-flow data are the same as those shown in figure 49 and fall off nearly as E_i^{-1} . When the transverse flow is added, the thermal coupling values fall by 60%. This is in great contrast to the 0.81 cm diameter target data and occurs because of the relatively large values of δ (the effective plasma coupling radius). When the plasma radius is either very small or large compared to the target size, the external flow moves the plasma with respect to the target during the coupling time t_c and the same amount of coupling occurs. Strictly speaking, this occurs when

$$ut_c \ll \text{greater of } (R, \delta) \quad (42)$$

The plasma coupling time is approximately equal to the laser pulse time.

For $(R/\delta) \sim 1$, the external flow displaces the coupling plasma with respect to the target and a reduction in α is found.

A similar behavior is found in tests with aluminum targets exposed to both laser beam irradiation and transverse flow. The data for the 0.81 cm

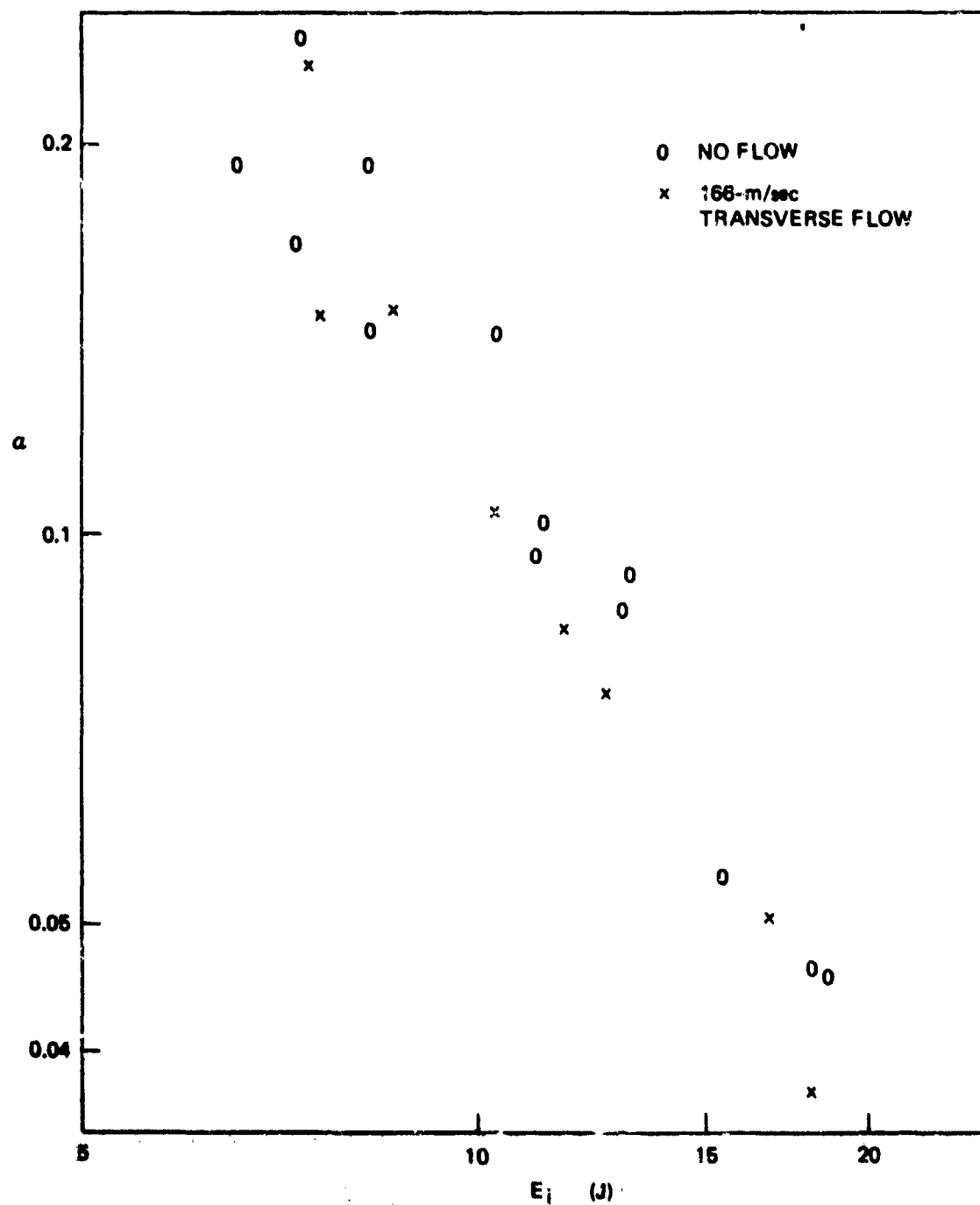


Figure 55. Transverse Air Flow Effect on Thermal Coupling To Titanium Targets of 0.808 cm Diameter

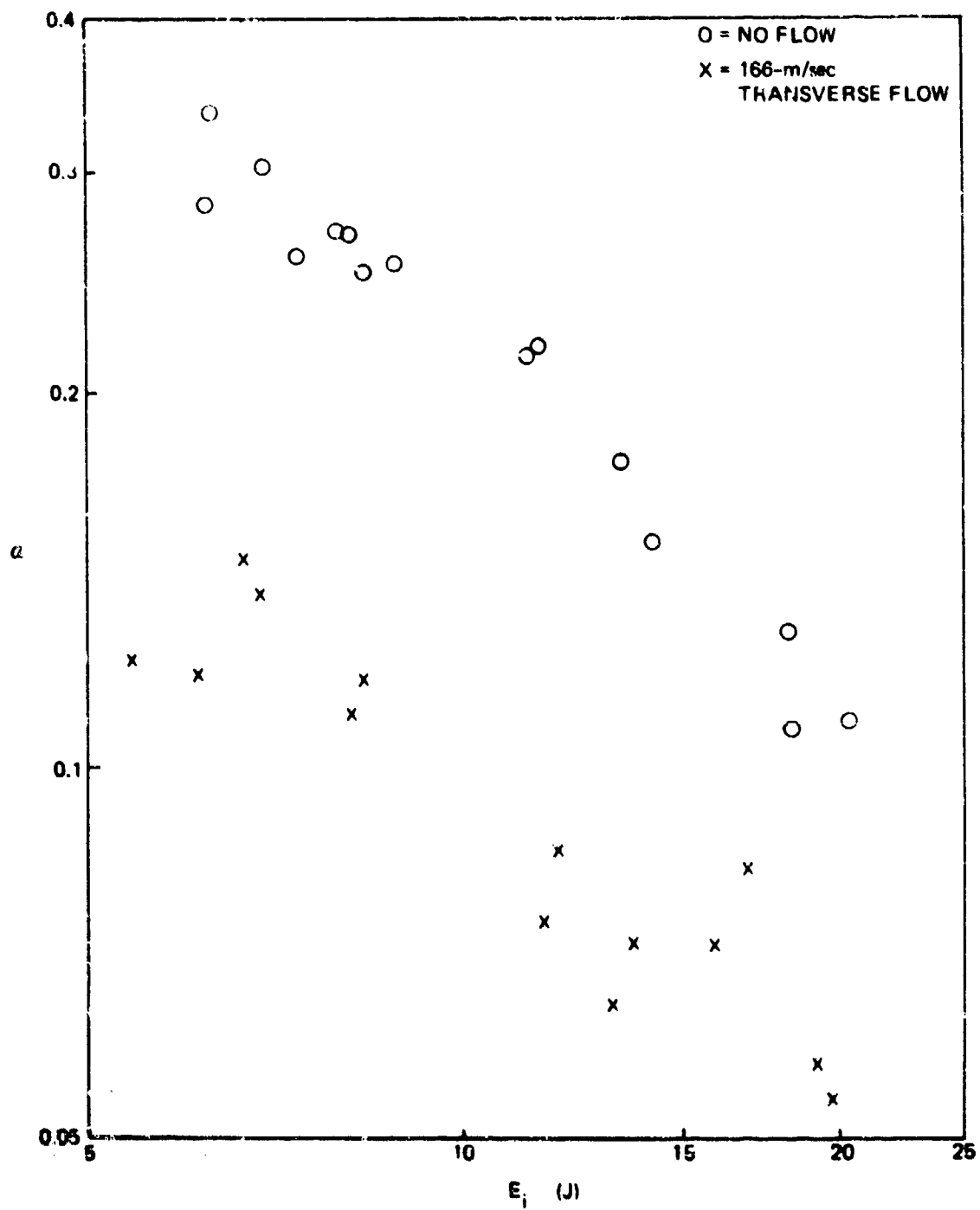


Figure 56. Transverse Air Flow Effect on Thermal Coupling To Titanium Targets of 1.59 cm Diameter

diameter targets are displayed in figure 57. There is an enhancement region above the threshold at 3.5 to 4 J incident energy which yields values of α of about 0.16. Such a thermal coupling maximum value lies below the maximum α value of 0.33 presented in an earlier report.⁽⁴⁾ In this case, α decreases approximately as E^{-1} and air flow causes a negligible change in coupling. For 1.59 cm diameter aluminum targets, the variation in thermal coupling is shown in figure 58. Again, there is a greater reduction in α than found with small targets. This reduction of 28% is only about 1/2 of that seen for titanium. The maximum α values are only slightly above 0.2, and the nearly E^{-1} behavior seen at the higher incident energies does not carry all the way down to threshold.

The reduction in thermal coupling caused by transverse air flows occurs only for the larger targets. This observation can be explained using a simple thermal coupling model. This coupling model assumes: (1) that the thermal coupling radial profile is a constant "top-hat" distribution of radius R_H , (2) that the external transverse air flow moves this profile with respect to the target at the velocity of the air flow, and (3) the thermal coupling to the 0.81 cm diameter targets is unchanged as found by experiment.

Figure 59 indicates the geometry of the situation. The two shaded concentric areas represent the two different target sizes with air flow incident from the left. R_T is the radius of the larger target. Representative plasma heating areas are designated by the displaced circles of areas A_i , A_j , and A_k . These heating areas are all shown displaced such as to be tangent to the smaller target. Under these conditions, obviously, no decrease in power transfer to the smaller target occurs. Thermal heating profiles of radii R_H below $3 R_t/4$ never cause a net decrease in power transfer to the large target. For larger heating radii, the instantaneous transverse-flow caused coupling reduction γ is shown in figure 60. Since the net energy reduction to large targets is an integral of the power transfer, figure 60 represents an upper limit to the actual reduction that can occur.

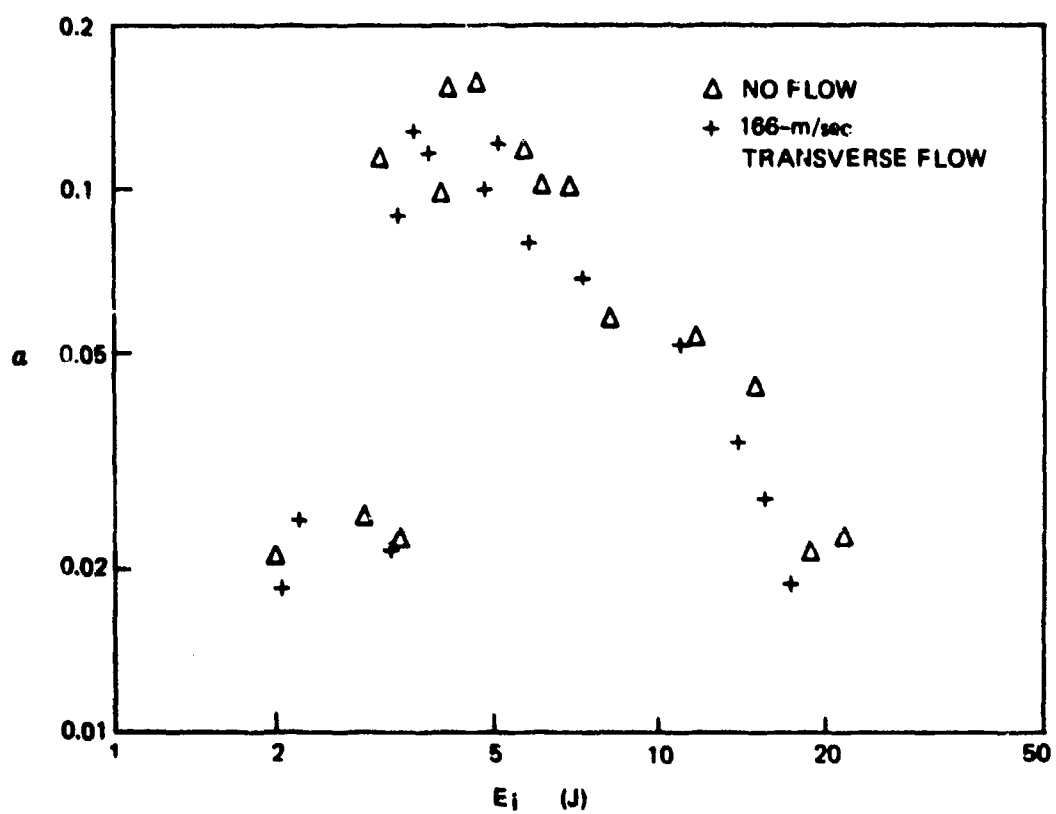


Figure 57. Transverse Air Flow Effect on Thermal Coupling To Aluminum Targets of 0.808 cm Diameter

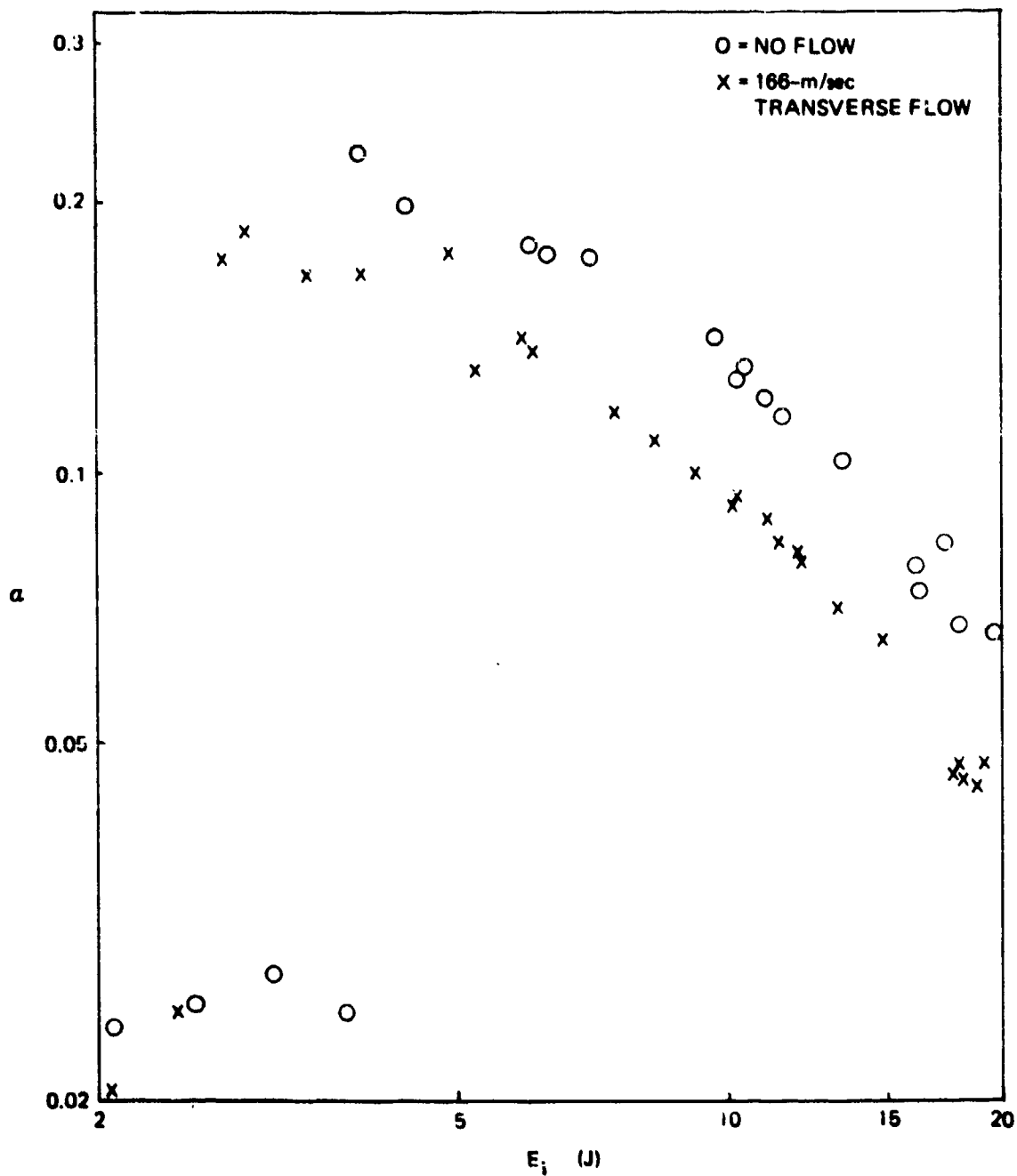


Figure 58. Transverse Air Flow Effect on Thermal Coupling To Aluminum Targets of 1.59 cm Diameter

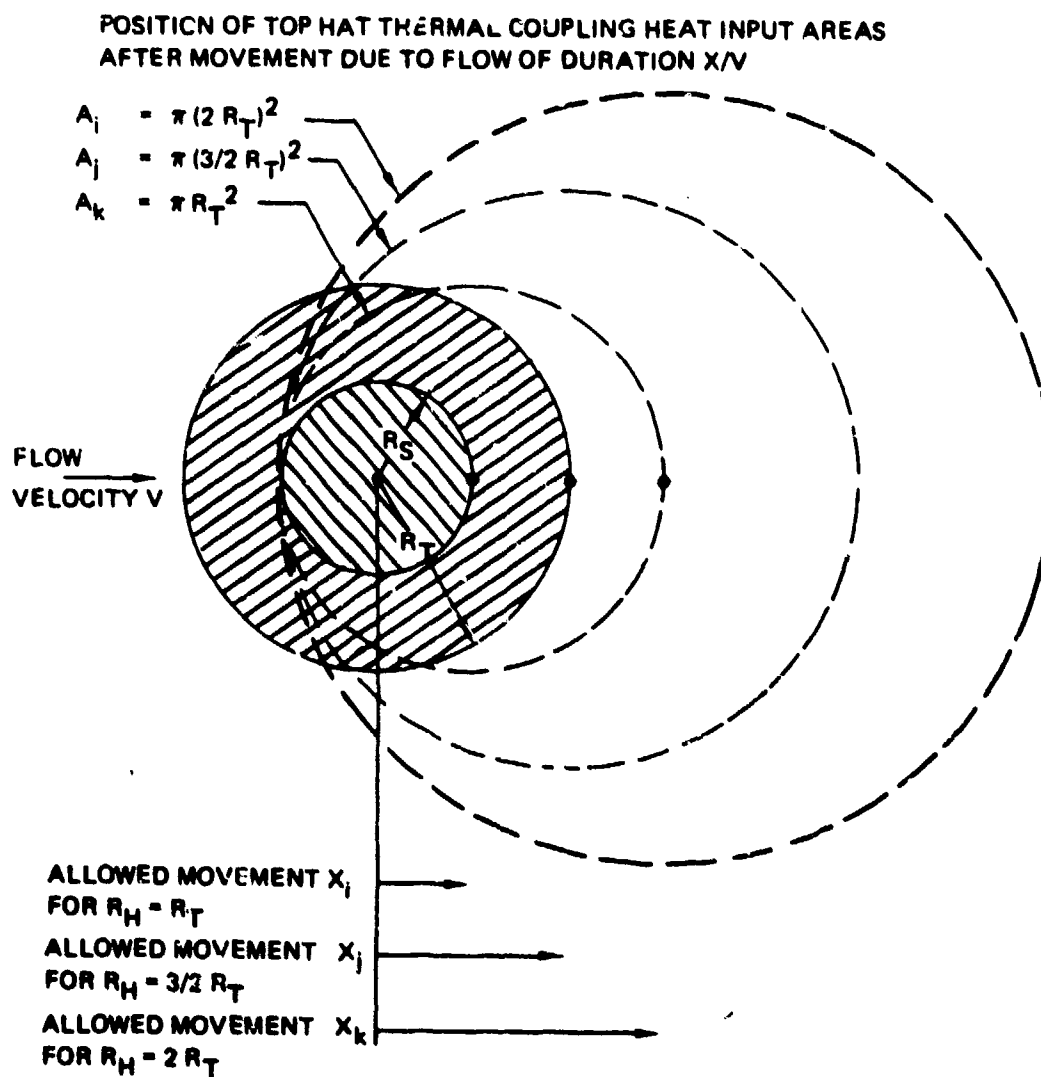


Figure 59. Geometric Model for Flow Effect on Thermal Coupling Based on Data from Two Target Sizes

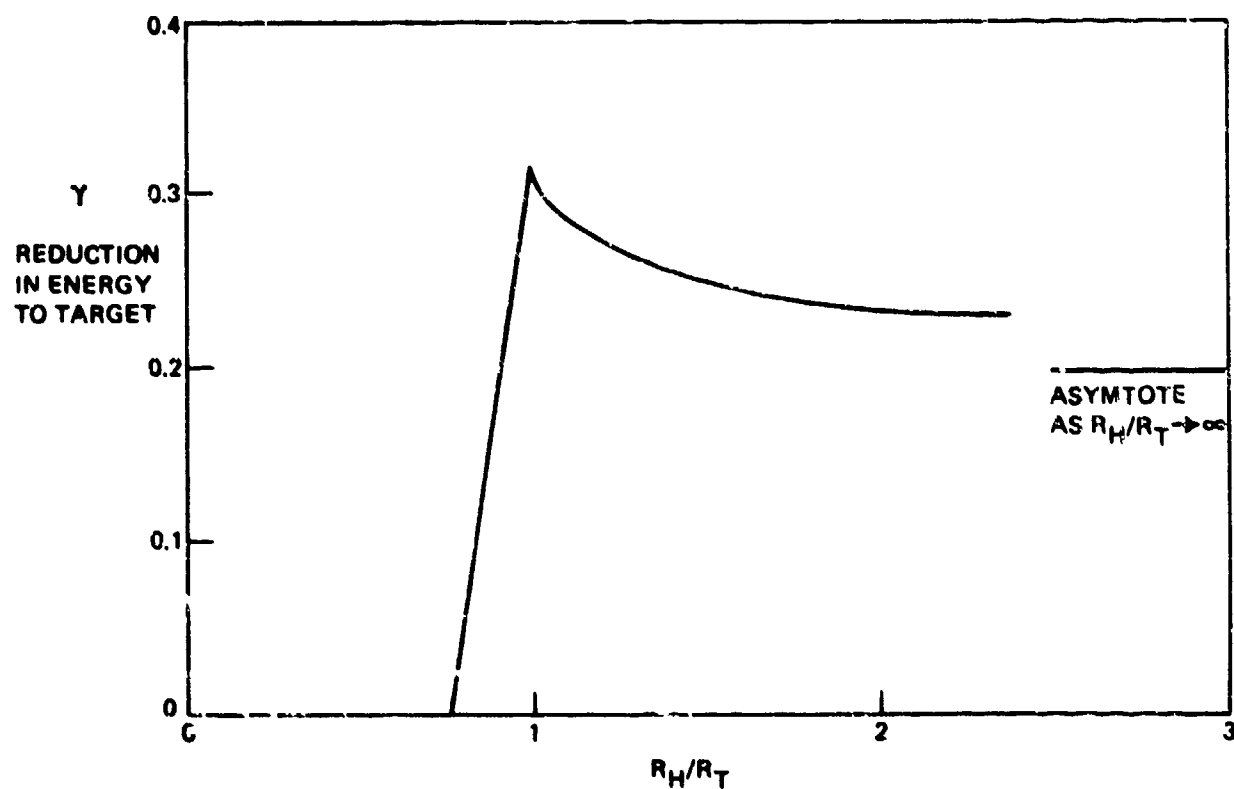


Figure 6C. Flow-Caused Reduction in Energy Delivered to Target of Radius R_T By a Top Hat Thermal Coupling Profile of Radius R_H , Which Lasts a Time $(R_H - 0.5 R_T)/V$, Where $R_H \geq 0.5 R_T$

When R_H/R_T is unity, this reduction reaches a maximum value of 31%. The model results shown are only intended to show graphically the combined effects of transverse flow and plasma spreading on measured thermal coupling. It is evident that not much reduction ever occurs for very small targets. For maximum coupling reduction on the large target, the plasma must be moved a distance of 0.4 cm. This implies that the coupling time t_c is as long as

$$t_c = \frac{0.4}{1.66 \times 10^4} = 24 \text{ microseconds} \quad (43)$$

which is long compared to the time of maximum luminosity of observed laser-supported detonation waves,⁽¹⁾ but is approximately equal to the length of the laser pulse.

4. IMAGE CONVERTER PHOTOGRAPHY AND THRESHOLDS IN THE PRESENCE OF AIR FLOW

Image converter camera photographs with a resolution of 0.05 cm were taken of laser-produced plasma events both with and without flow. These all were obtained using exactly the same setup and delay times, and approximately same incident energies for the cases with and without flow. The luminous phenomena projected more than 1 cm from the surface when the energies were in the laser-supported detonation wave regime. Experimental apparatus allowed both absolute translation to 0.05 cm and angular changes to 3° to be observed. During the approximately 9 μsec when luminosity was sufficient for photography, no changes were ever seen during flow as compared with no flow. During the 9 μsec a velocity of 166 m/sec would move gases in the flow region 0.15 cm.

The incident intensity or incident fluence required for the ignition of LSA waves on aluminum targets was investigated for differences caused by the presence of an $M = 0.5$ transverse air flow. A fresh unexposed target was used each time, in as-received condition except for a methanol wash. Two separate series of tests were completed and the measured thresholds were identical both with and without flow.

5. EXPERIMENTS USING MELTED TARGETS

In order to simulate a sequence of previous pulses of a repetitively-pulsed train, a series of experiments was carried out using molten targets and single pulses of CO₂ radiation. One of the primary goals of these experiments was to determine the conditions under which the pressure from either an LSD wave or the vaporizing target itself would blow away the molten target material. (18)

In order to permit experiments with variations in target temperature; gallium, indium, and tin targets were obtained. This gave us the opportunity to do melting point tests at 303°K, 430°K, and 505°K. Mercury was also available for room temperature tests. The standard target was 0.125 cm thick and 1.59 cm in diameter. Each was placed in a recess in a heating block attached to a thermostatically controlled heater. A thermocouple in the heating block allowed its temperature and temperature stability to be measured. The arrangement for the incident laser beam, target, target block, and heater is shown in figure 61. In this arrangement

18. Fox, J. A., "A Method for Improving Continuous Wave Laser Penetration of Metal Targets," Appl. Phys. Lett 26, 682, 1975.

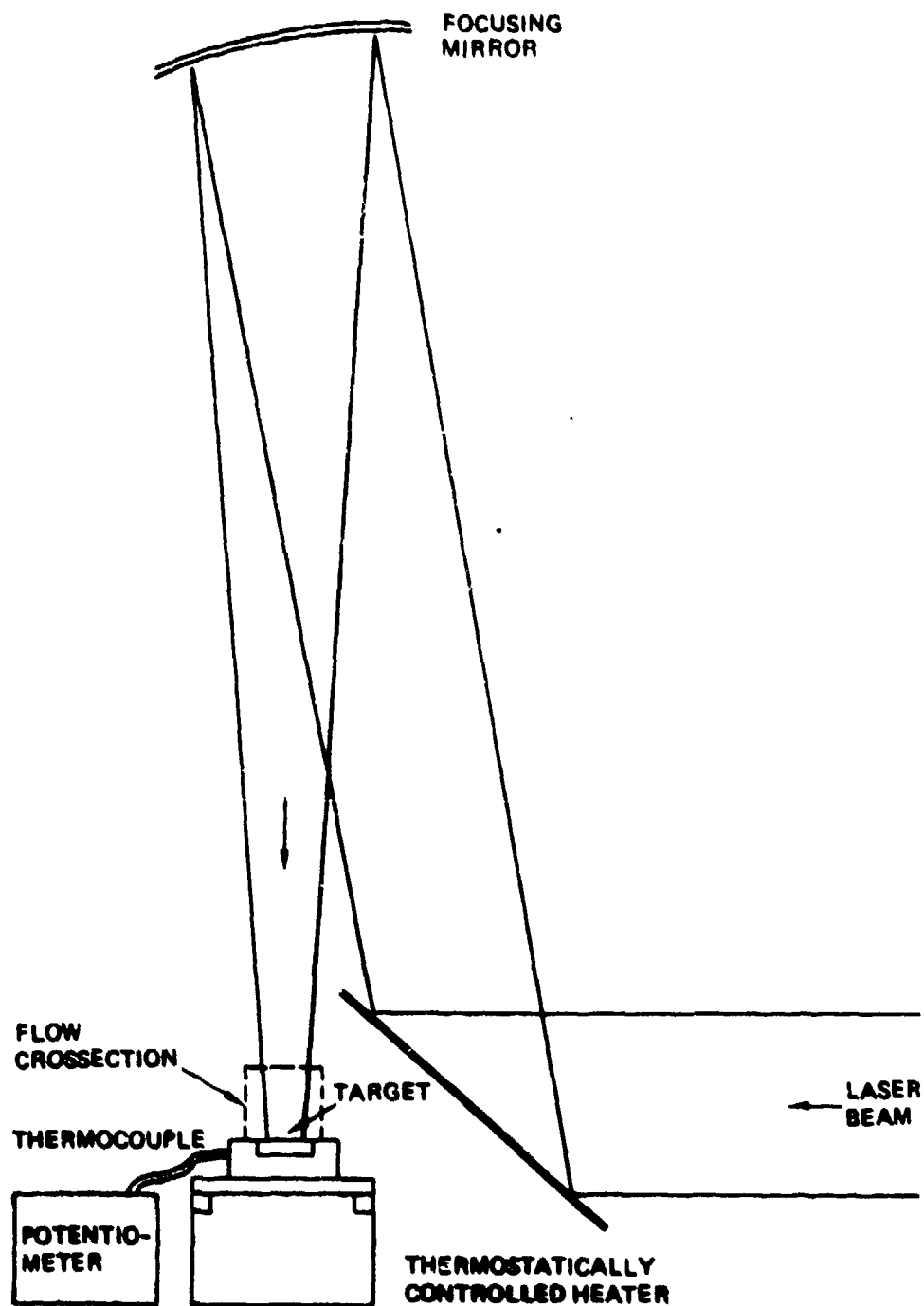


Figure 6). Vertical Arrangement for Melted Target Studies

the position of the flow apparatus is undisturbed with the melted target in the horizontal plane which forms the bottom side of the open flow channel. A vertically incident laser beam is provided by a folding mirror which sends the beam upward to the 50.8 cm focal length focussing mirror. This provides a focal spot 0.22 cm in radius.

Without describing in detail all the laser experiments on melted targets, it should be noted that no gross removal of metal target material was ever observed. The main effect, with these small spot CO₂ laser beams, was to cause an oxidation of the molten surface. In this oxidized surface, a permanent set of "wrinkles" remained as a result of the formation of the LSD wave pressure pulse.

Following ignition of a laser-supported detonation wave a high surface pressure occurs which has a strong radial gradient. When the target is molten, this pressure pulse might be expected to push material away from the focal spot. This was not observed in the preceeding tests possibly due to surface tension and viscosity, so two other series of experiments were devised to look for this effect. In the first series, horizontal 0.81 cm diameter targets were melted in holders which had holes completely through the back. The high pressure pulse was expected to push some of the target material out this hole. Without irradiation the surface tension prevented the melted target from running out the holes or from doing anything other than bulging slightly downward. Hole sizes were 0.16, 0.32, and 0.48 cm in diameter. In figure 62 the results of these tests are shown. In every case, molten metal was extruded and remained hanging down in a drop of tubular shape. The photographs show the results after the target and holder was cooled back to room temperature. Evidently, target temperatures were insufficient to allow anything but highly viscous motion.

Additional tests were done with water and mercury to look at mass loss with molten materials with lower viscosity. In tests with water, almost all the water in the holder cavity was blown out by the pressure pulse from the laser beam-target interaction, however, similar tests with mercury removed 0.06 g of material, approximately 1% of the target.



Figure 62. Indium Targets Preheated to Just Above Melting Temperature And Extruded Through 0.16-, 0.32-, and 0.48-cm-Diameter Holes by Laser Beam Target Interaction

SECTION VII

MELT REMOVAL DYNAMICS DUE TO VAPORIZATION

1. INTRODUCTION

It is apparent that high intensity laser pulses lead to melting and vaporization. At relatively low intensities the molten layer can flow off the surface due to gravity or be removed due to aerodynamic forces. (19, 20)

This report summarizes initial concepts and calculations on the mechanisms by which a molten fluid layer can be pushed rapidly outward by a local pressure distribution. In general, the solutions of the combined continuity of mass, continuity of momentum, and continuity of energy equations are complex for fluid flows. However, we have developed relatively simple approximate solutions for special cases of interest for high power laser coupling. A laser-melted surface usually can be described by a thin molten layer on top of the underlying solid target. In this case (of a thin molten layer), one can describe the local pressure distribution as having only radial gradients and being uniform along the axial direction. As a model of this situation the molten layer is visualized as a slab of incompressible fluid with constant thickness. This slab is bounded by a plane rigid surface on one side and with a parabolic pressure variation applied to the other side. The source of the pressure distribution can be considered to be either a laser-supported detonation wave (LSD wave) or by the existence of the vaporizing surface itself. In the first case, the LSD wave is produced in air and generally spreads out over an area greater than that of the laser focal spot. In the second case, where vaporization is important, the pressure is constrained to be within the focal spot. In addition, this pressure is easily produced in vacuum and may be important for laser space applications.

-
19. O'Keefe, J. D. and Johnson, R. L., "Laser Melt-Through Time Reduction Due to Aerodynamic Melt Removal," AIAA J. 14, 776, 1976.
Robin, J. E., and Nordin, P., "Effects of Gravitationally Induced Melt Removal on CW Laser Melt-Through of Opaque Solids," Appl. Phys. Lett. 27, 593, 1975.

With high intensity CW or pulsed lasers one expects surface vaporization to exert enough reaction pressure on the molten surface to blow away in the radial direction some of the molten surface.⁽²¹⁾ Thus, although the vaporization of a unit mass of solid takes between 10 and 20 times as much energy as is required to just melt the solid, the vaporization process itself can aid in removing the melt.

The analysis given in Sections 7.2 and 7.3 describes the manipulation of the conservation equations of mass, momentum, and energy to obtain approximate relations describing the dependence of the melt recession velocity v_m and the melt thickness s on the laser irradiance and focal spot size. The surface pressure variation is analyzed in self-consistent terms using the Clausius-Clapeyron equation. At the higher intensities (as described in Section 7.3) the mass loss in vapor form becomes important and leads to a significant decrease in the effective overall mass removal efficiency.

The results of the analyses of Sections 7.2 and 7.3 are shown in figures 63 through 75. The specific targets studied include aluminum, titanium, and molybdenum.

Section 7.5 discusses the efficiency of removing a liquid melt layer by a combined CW and pulsed laser. In this preliminary analysis, the potential of this technique appears quite limited. This is due to the large melt removal times (for large beam areas) compared to characteristic times required to melt the target itself.

Figure 63 shows the calculated steady state thicknesses of a molten layer of aluminum as a function of the absorbed intensity in the center of the laser beam with the scale length of the parabolic pressure variation as a parameter. The curves in this and following figures are not continued into the range where the melt thickness is greater than a tenth of the pressure radius. The steady state melt thickness decreases with increasing absorbed intensity. The curves

21. Robin, J. E. and Nordin, P., "Improved CW Laser Penetration of Solids Using a Superimposed Pulsed Laser," Appl. Phys. Lett. 29, 3, 1976.

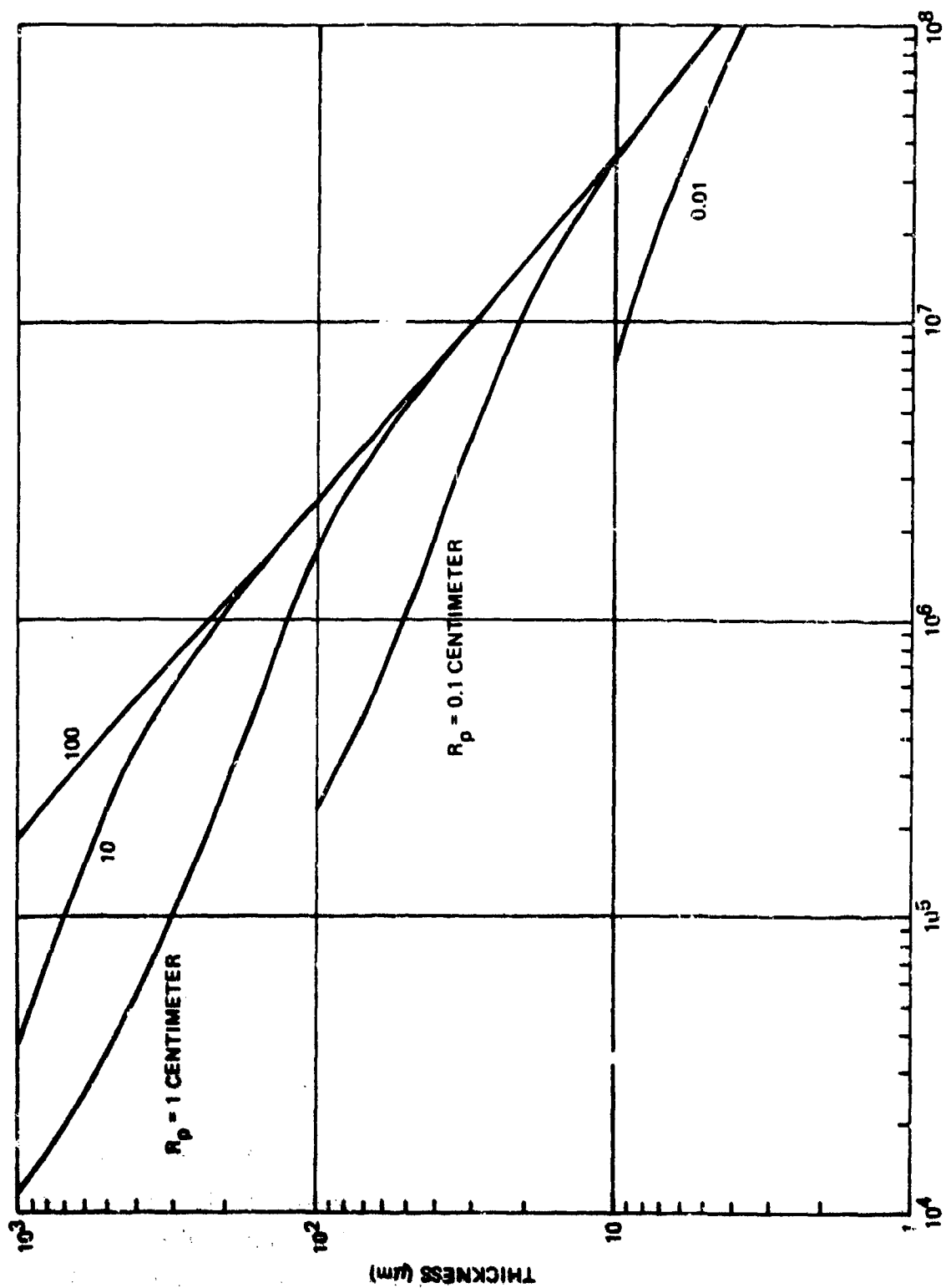


Figure 63. Steady-State Melt Thickness - Aluminum

transfer from a smaller thickness curve dominated by melt removal by radial flow of the liquid to a larger thickness curve dominated by melt removal by vaporization. The range of absorbed intensities over which the transfer occurs depend on the pressure radius with the transfer occurring at lower intensities for larger pressure radii.

Figure 64 shows the calculated steady state melting velocity of aluminum. The steady state melting velocity increases with increasing absorbed intensity. The curves transfer from a larger velocity curve dominated by melt removal by radial flow of the liquid to a smaller velocity curve dominated by melt removal by vaporization. Figure 65 shows the calculated specific melt volume of aluminum, the volume of melt removed from the crater per joule of absorbed energy. The curves again change from a larger specific volume curve dominated by melt removal by radial flow of the liquid to a smaller specific volume curve dominated by melt removal by vaporization. All the values are considerably below the ideal one dimensional value with zero melt thickness. For a certain pressure radius, the specific melt volume curves show maxima with respect to the absorbed intensity. The pressure radius is the radius of the crater. The radius of the molten region is larger but only the molten material out to the pressure radius is removed by the radial pressure gradient.

Figure 66 shows that the calculated pressure radii are approximately equal to the laser beam radii for aluminum for the larger absorbed intensities but the pressure radii are smaller than the laser beam radii for the smaller absorbed intensities. With laser beam radius as a parameter, specific melt volume curves do not show maxima but decrease monotonically with increasing absorbed intensity. Figure 67 shows the calculated specific impulse of aluminum, the force on the surface per watt of absorbed power or the impulse on the surface per joule of absorbed energy. The specific impulse always becomes nearly asymptotic to a certain value for large absorbed intensities. For lower absorbed intensities, when melt removal is dominated by radial flow of the liquid, the melting is relatively efficient. For higher absorbed intensities, when melt removal is dominated by vaporization, the application of force to the surface is relatively efficient.

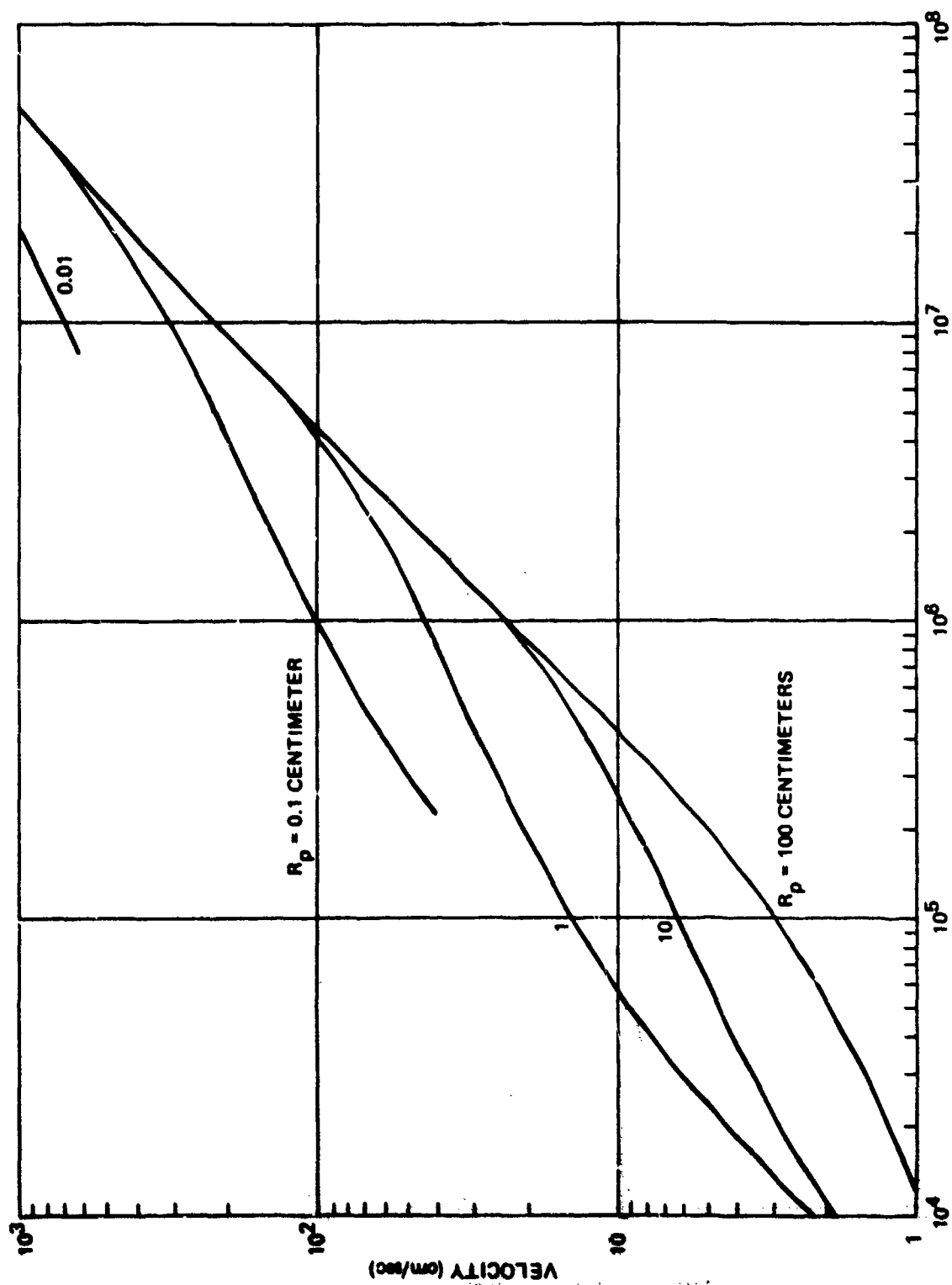


Figure 64. Steady-State Melting Velocity - Aluminum

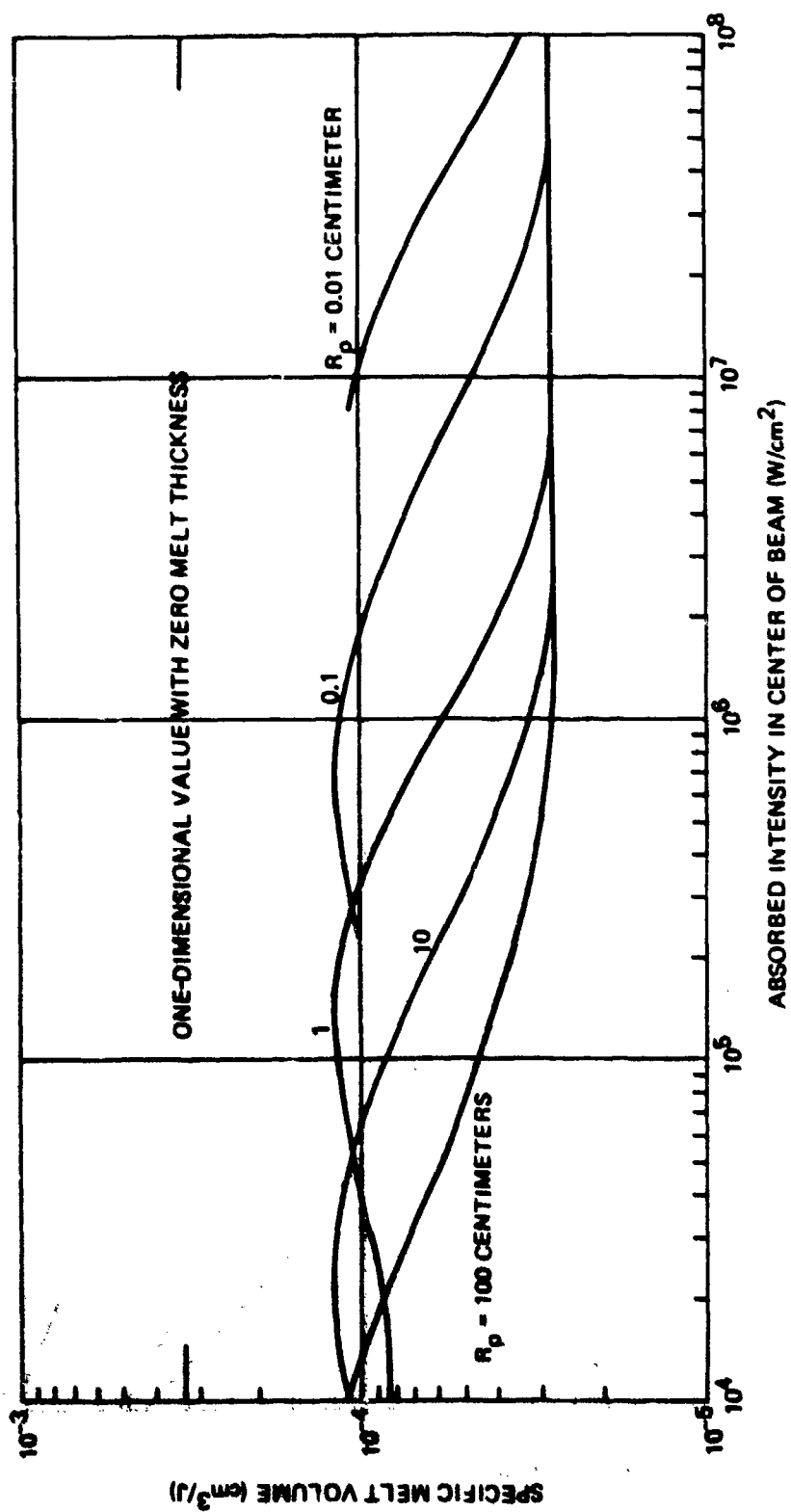


Figure 65. Specific Melt Volume - Aluminum

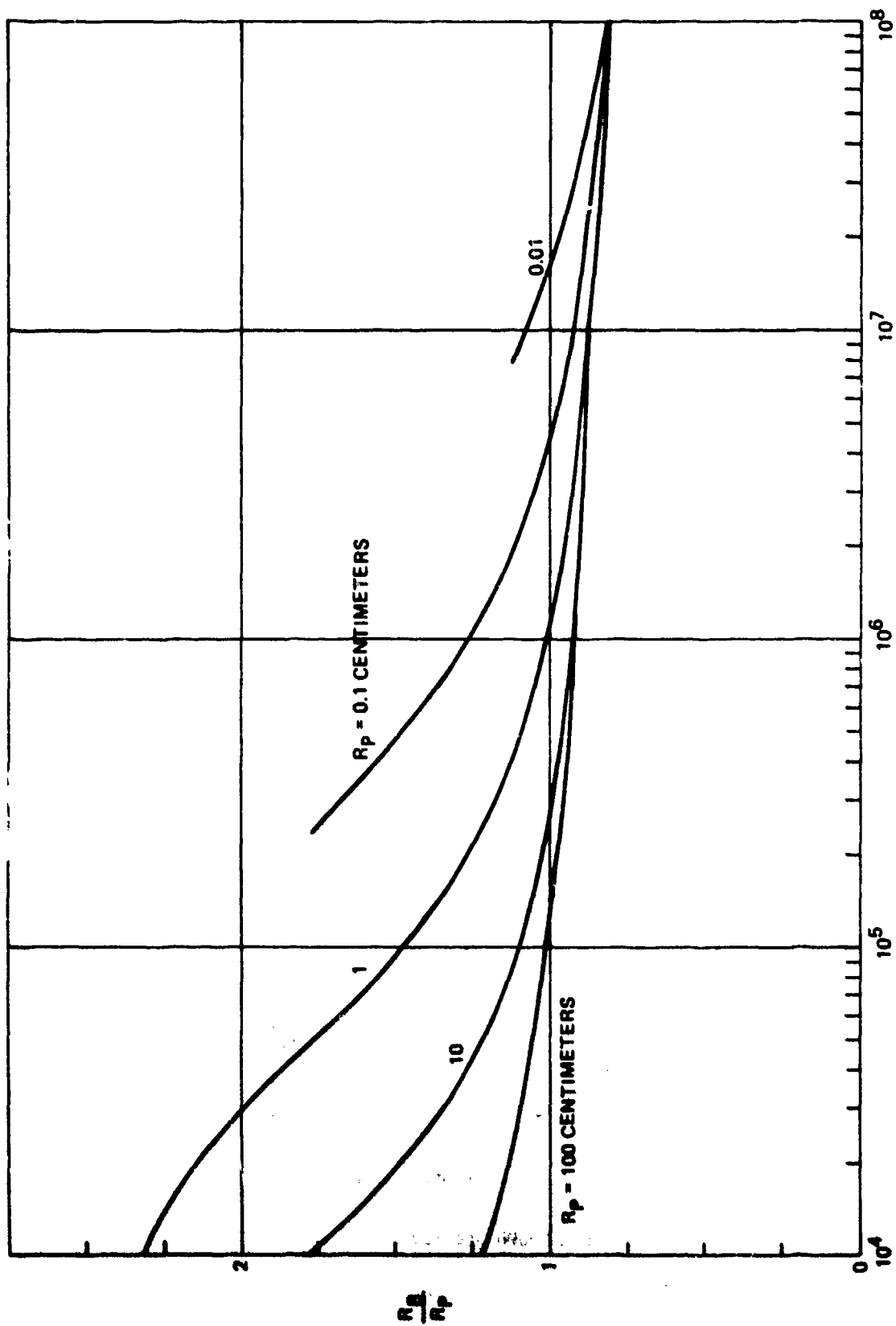
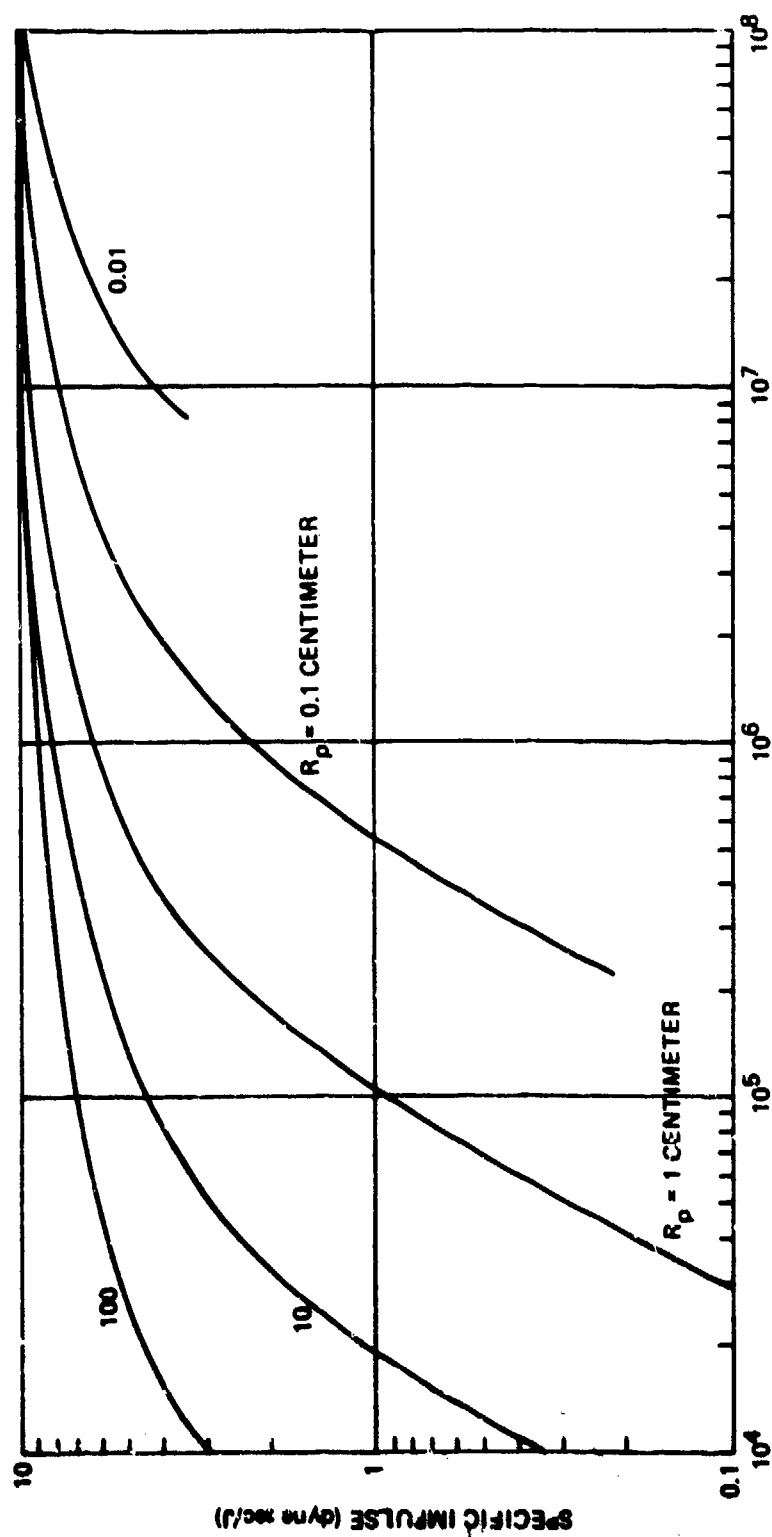


Figure 66. Ratio of Beam Radius to Pressure Radius - Aluminum



ABSORBED INTENSITY IN CENTER OF BEAM (W/cm^2)

Figure 67. Specific Impulse - Aluminum

Figures 68 through 71 show the steady state melt thickness, melting velocity, specific melt volume and specific impulse for titanium. Figures 72 through 75 show the same for molybdenum. These materials, aluminum, titanium and molybdenum, were chosen to represent a low melting temperature metal, a medium melting temperature metal with very low thermal conductivity and a high melting temperature metal, respectively. The steady state melt thickness of molybdenum is less than aluminum but titanium is still less because of its low thermal conductivity. The steady state melting velocity of aluminum is greater than titanium which is greater than molybdenum when melt removal by vaporization is dominant but sometimes molybdenum melts faster than titanium for smaller absorbed intensities. The specific melt volumes are in an inverse order of the melting temperatures, aluminum greater than titanium which is greater than molybdenum. The asymptotic value of the specific impulse of aluminum is larger than molybdenum which is larger than titanium because of its low thermal conductivity. However titanium transfers from melt removal dominated by radial flow of the liquid to melt removal dominated by vaporization at smaller values of absorbed intensity than for aluminum and molybdenum because of the low thermal conductivity of titanium. For the smaller range of absorbed intensities titanium has larger specific impulses than both aluminum and molybdenum.

2. ONE DIMENSIONAL STEADY STATE MELTING

Consider a one dimensional steady state melting situation of a semi-infinite solid in which the axial melting velocity is constant and the liquid layer thickness is kept constant by melt removal in the radial direction by the reaction pressure gradient due to evaporation from the liquid surface. The derivation is an extension of the method used by Masters.⁽²²⁾ For a constant melting velocity, v_m , the geometry is shown in figure 76 where the temperature T is a function only of x where

$$x = z - v_m t \quad (44)$$

22. Masters, J.I., "Problems of Intense Surface Heating of a Slab Accompanied by a Change of Phase" J. Appl. Phys. 27, 477, 1956

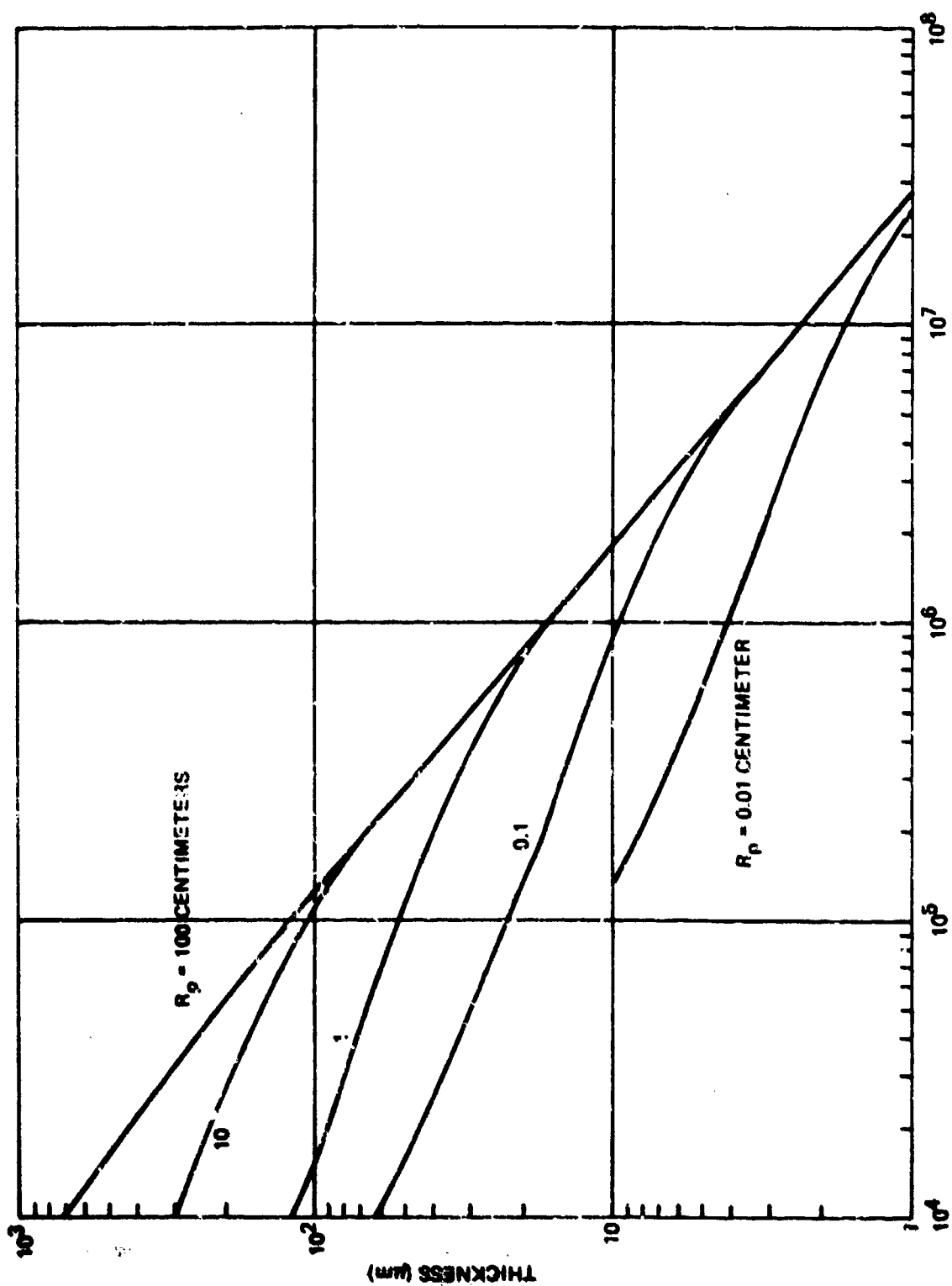


Figure 68. Steady-State Melt Thickness - Titanium

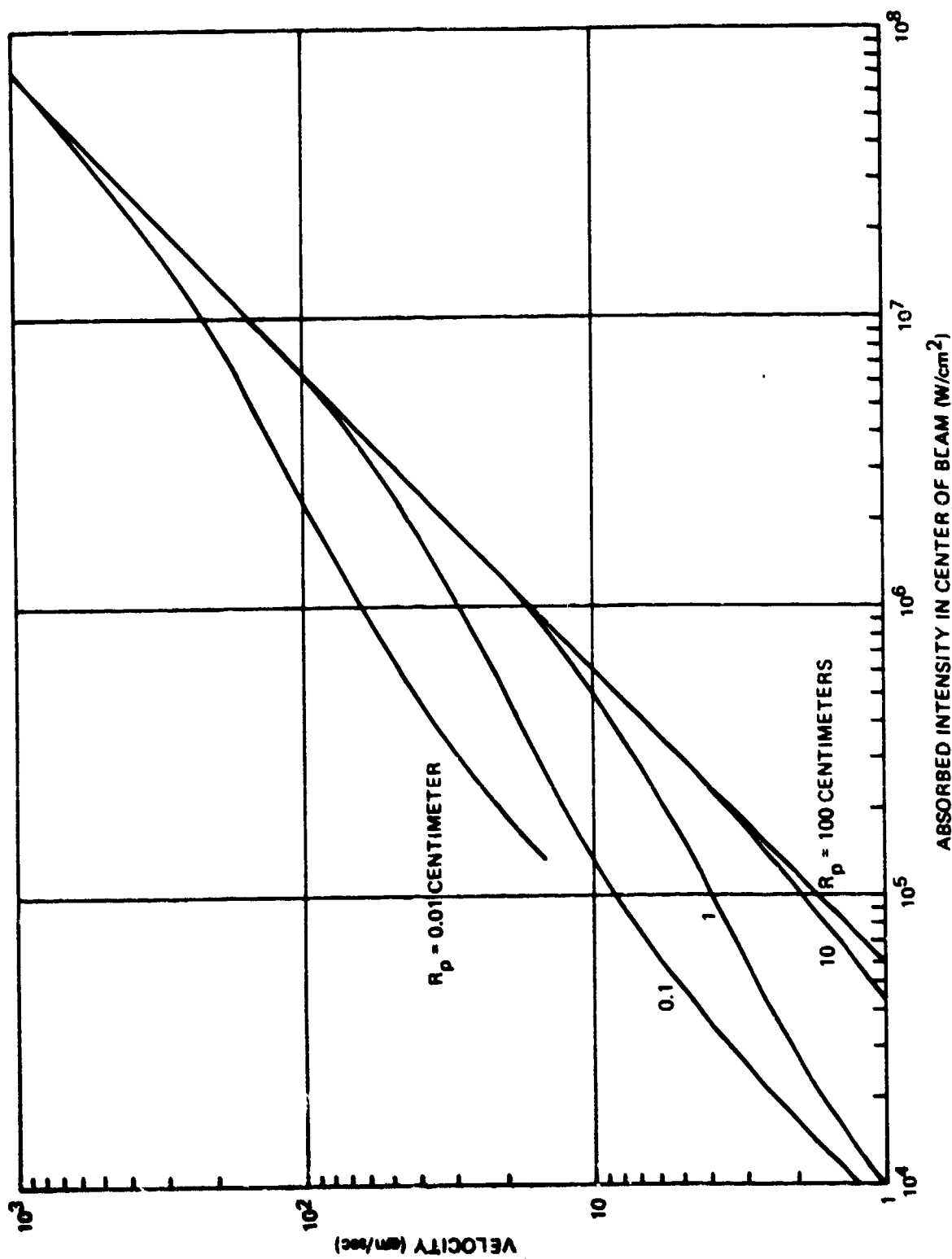


Figure 69. Steady-State Melting Velocity - Titanium

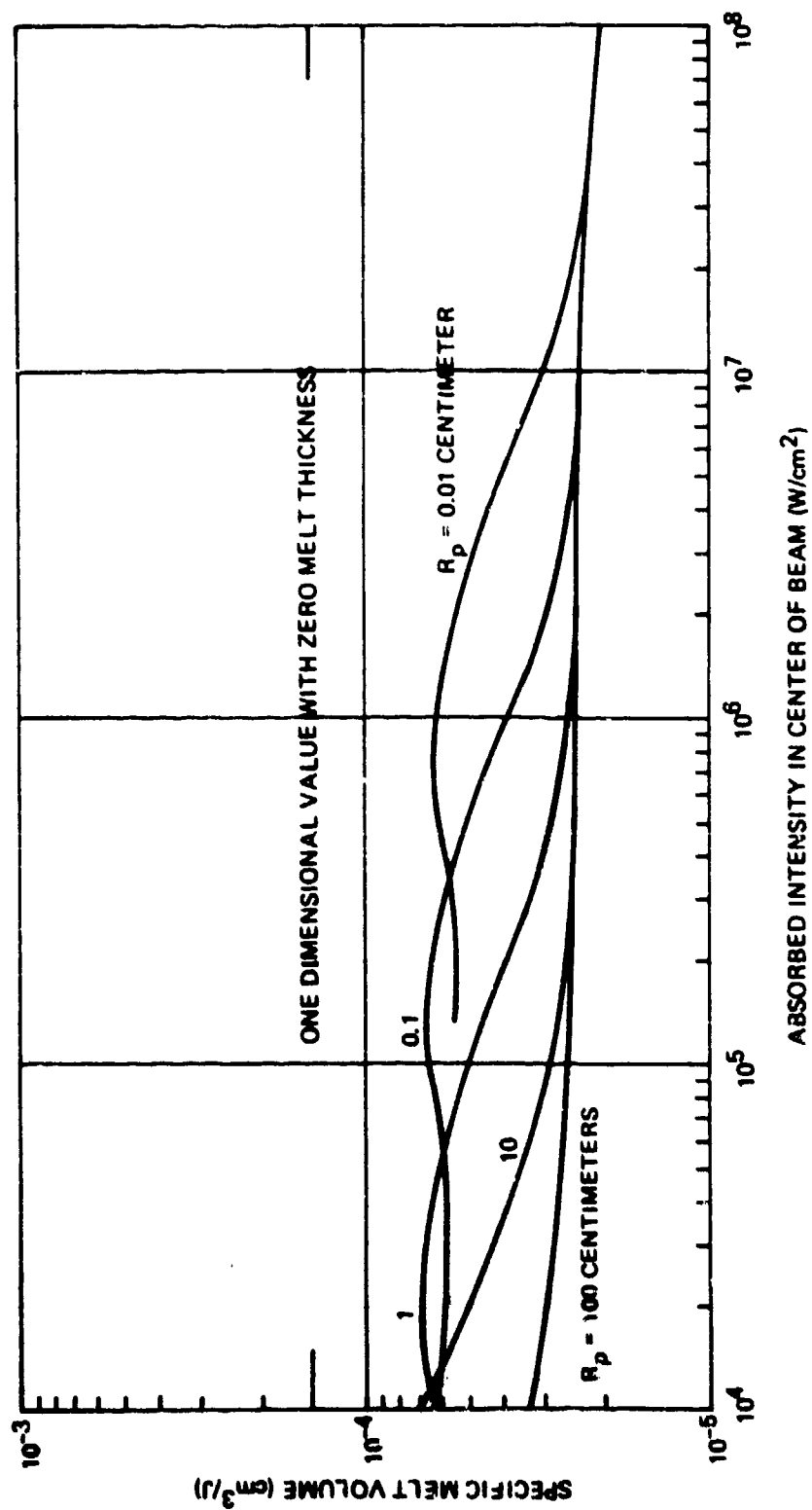
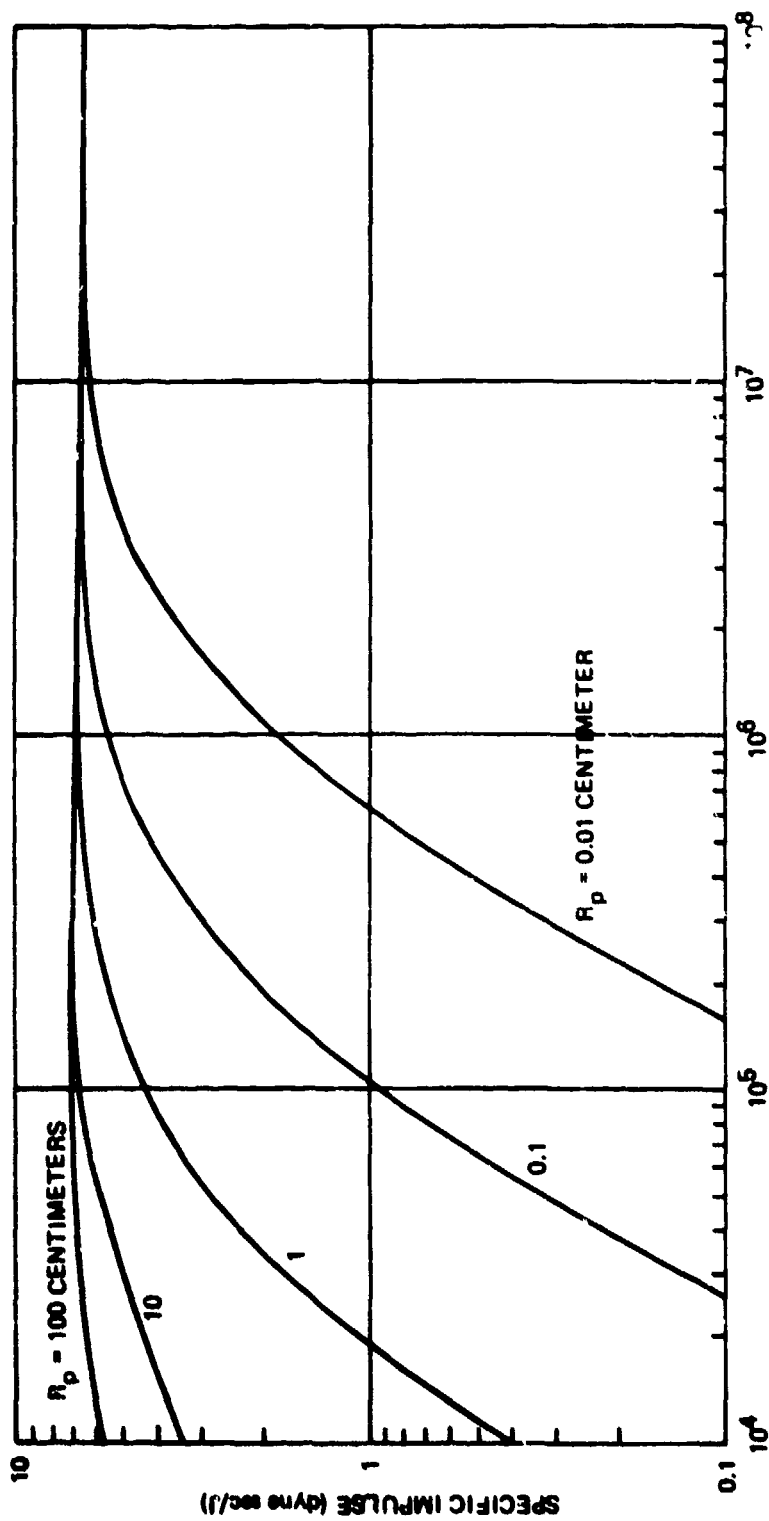


Figure 70. Specific Melt Volume - Titanium



ABSORBED INTENSITY IN CENTER OF BEAM (W/cm²)

Figure 71. Specific Impulse - Titanium

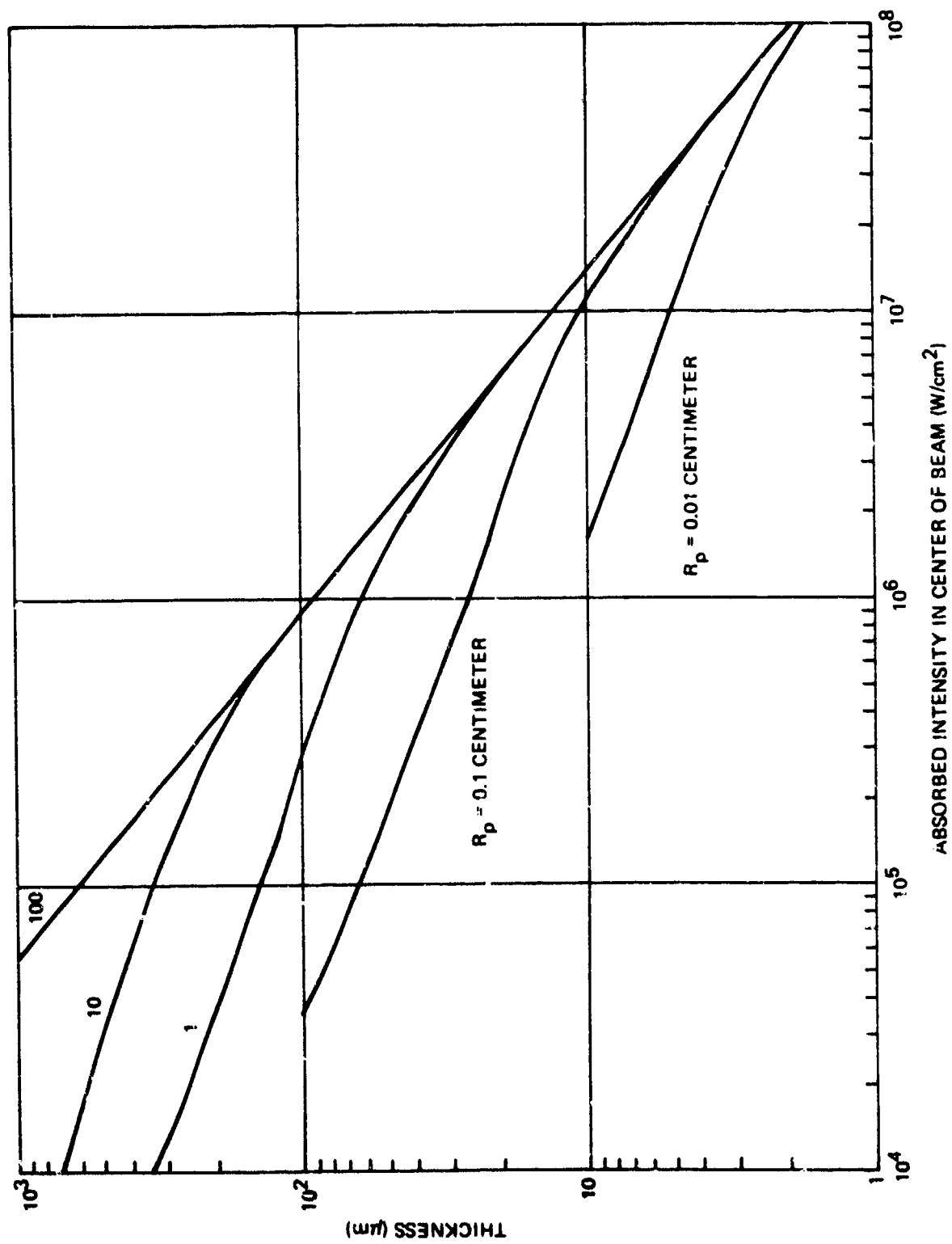


Figure 72. Steady-State Melt Thickness - Molybdenum

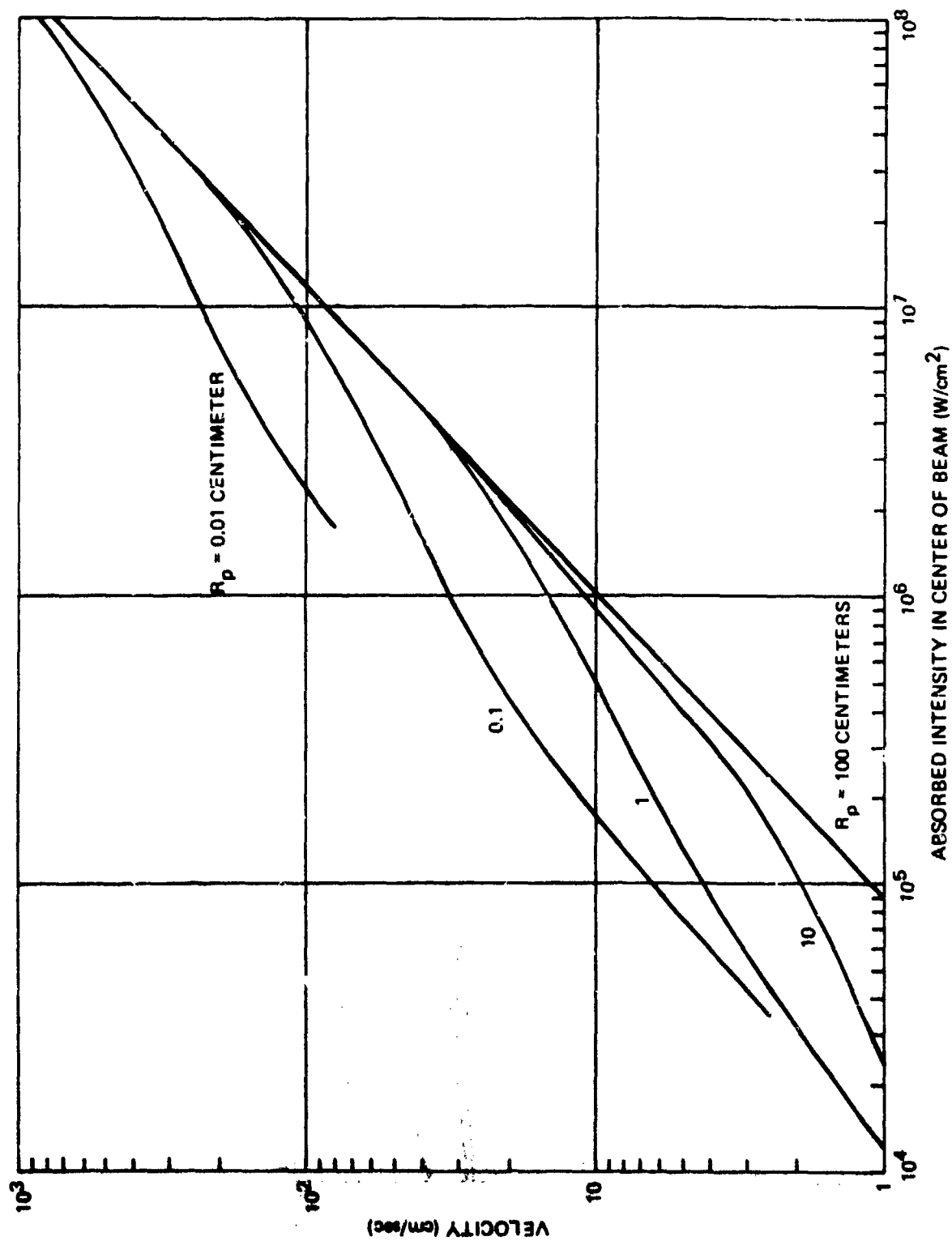


Figure 73. Steady-State Melting Velocity - Molybdenum

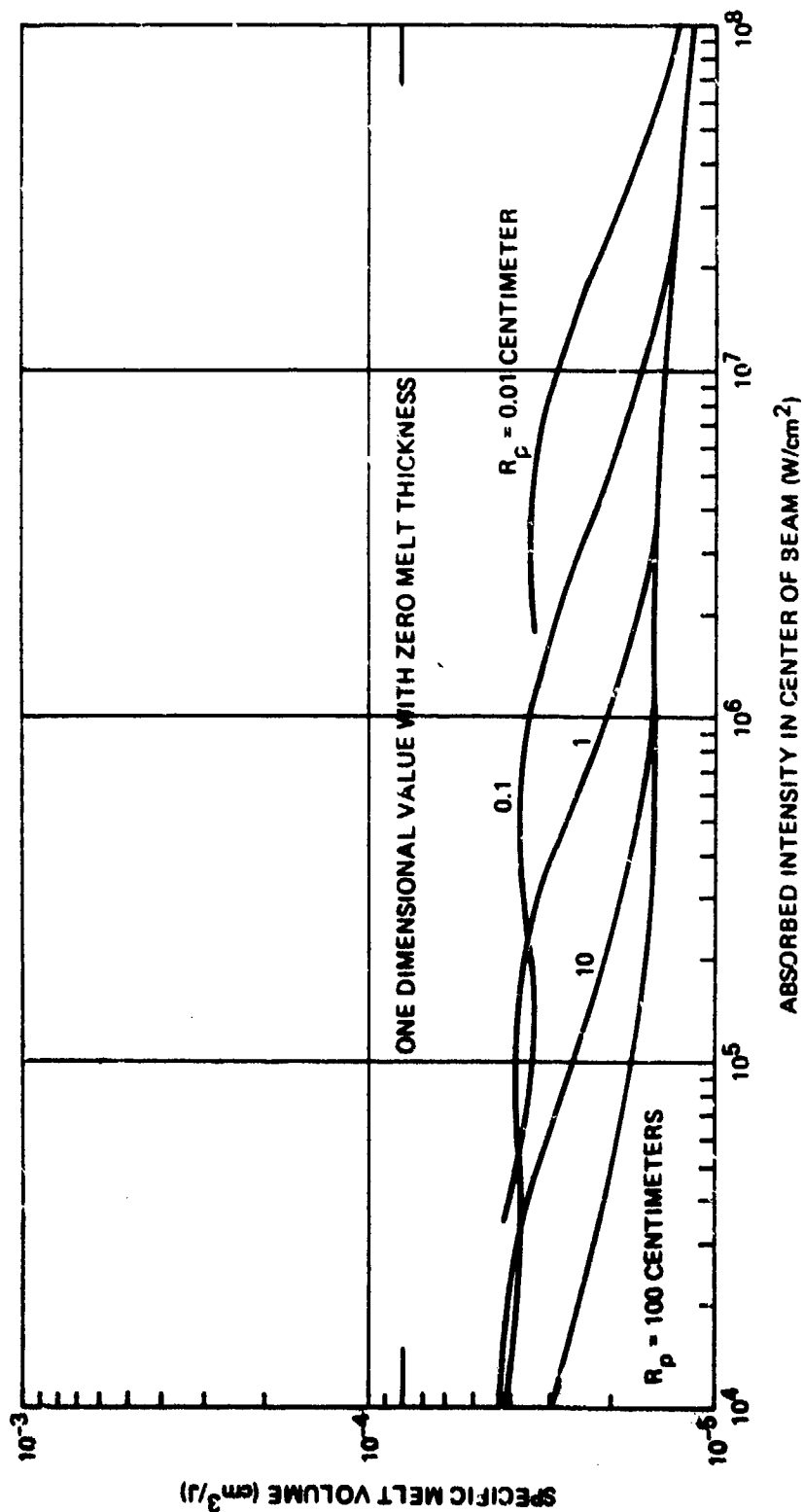
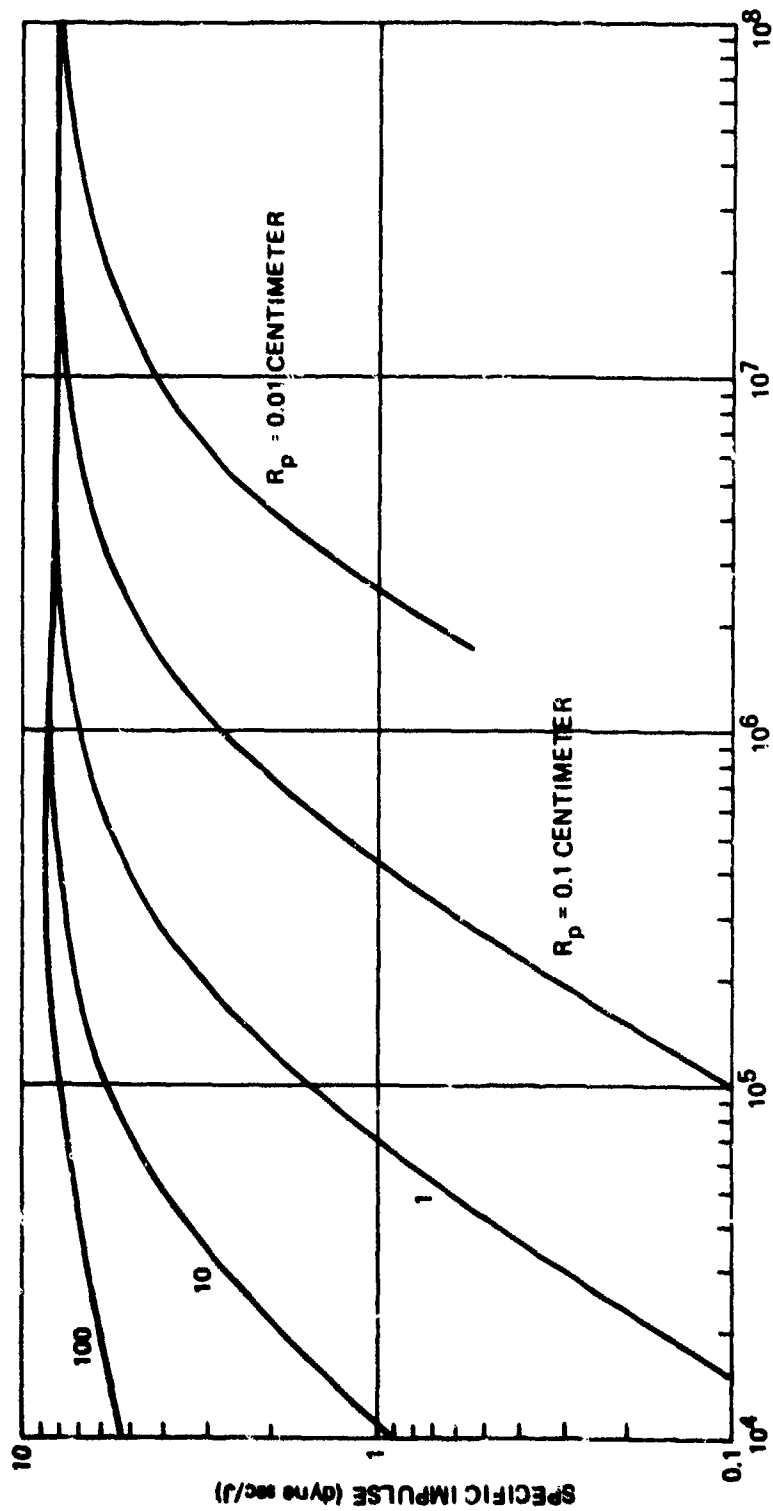


Figure 74. Specific Melt Volume - Molybdenum



ABSORBED INTENSITY IN CENTER OF BEAM (W/cm²)

Figure 75. Specific Impulse - Molybdenum

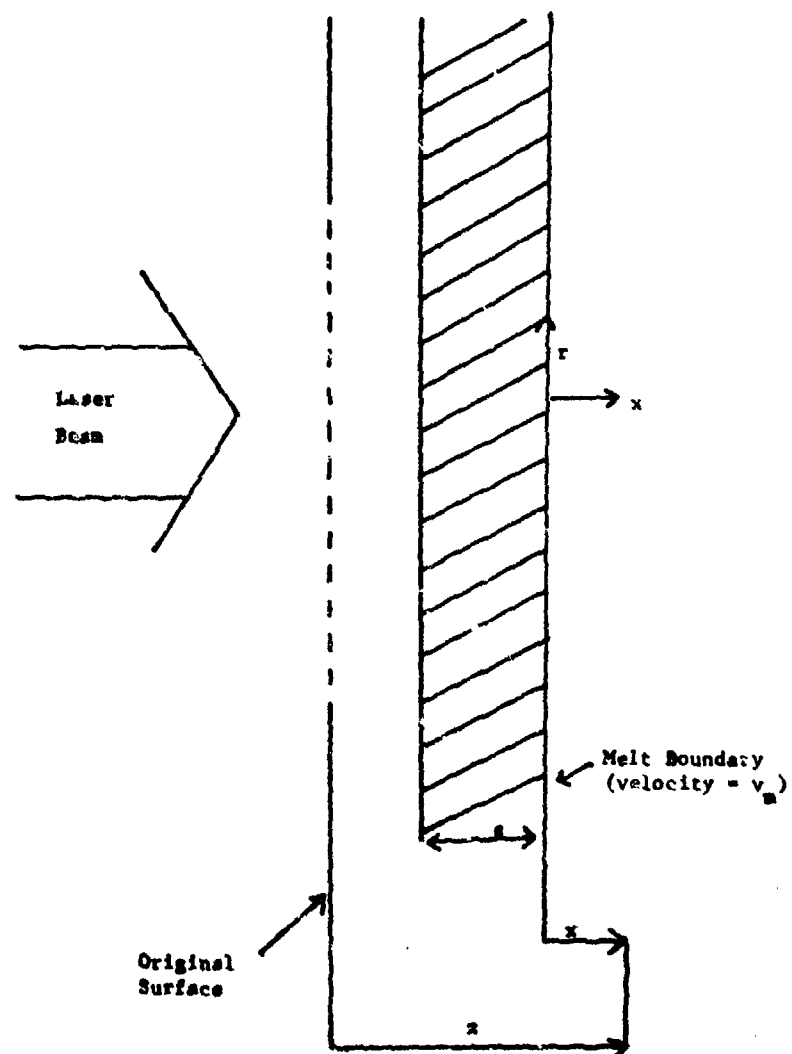


Figure 76. Geometry of Laser Melted Surface

The positive directions for z and x are into the solid. The solid-liquid interface is at $x = 0$ (or $z = v_m t$) and the liquid-gas interface is at $x = -s$, corresponding to a melt layer of thickness s .

In the solid, the heat equation, with constant thermal conductivity K_s , specific heat C_s , and density ρ_s (which implies $C_p = C_v$) is

$$\rho_s C_s \frac{\partial T}{\partial t} = K_s \frac{\partial^2 T}{\partial z^2} \quad (45)$$

In terms of the x variable equation 45 becomes

$$-v_m \rho_s C_s \frac{\partial T}{\partial x} = K_s \frac{\partial^2 T}{\partial x^2} \quad (46)$$

Equation 46 can be integrated using appropriate boundary conditions at $x = 0$ and ∞ . In terms of the solid initial temperature T_0 and the melt temperature T_m , one obtains

$$T = T_0 + (T_m - T_0) \exp \left[- \frac{v_m \rho_s C_s}{K_s} (z - v_m t) \right] \quad (47)$$

The heat flux at $x = 0$ is

$$\left. -K_s \frac{\partial T}{\partial z} \right|_{z = v_m t} = v_m \rho_s C_s (T_m - T_0) \quad (48)$$

For solid aluminum, the averaged thermal properties are

$$\begin{aligned} \rho_s &= 2.64 \text{ gm/cm}^3 \\ C_s &= 1.05 \text{ joules/gm/}^\circ\text{K} \\ K_s &= 2.29 \text{ watts/cm }^\circ\text{K} \end{aligned} \quad (49)$$

for the density, heat capacity, and the thermal conductivity respectively. These thermal properties and those for titanium and molybdenum are shown, for reference, in Table 9, with values taken largely from reference 23.

TABLE 9

MATERIAL PROPERTIES

	Aluminum	Titanium	Molybdenum	
Atomic Weight	26.9815	47.90	95.94	grams/mole
Solid Density	at 0°C 2.706 ave. 2.64	4.502 4.38	10.243 10.0	grams/cm ³
Solid Specific Heat	at 0°C 0.8749 ave. 1.050	0.5085 0.6400	0.2432 0.3532	(joules/gram)/°K
Solid Thermal Conductivity	at 0°C 2.36 ave. 2.29	0.224 0.225	1.39 1.01	(Watts/cm ²)/(°K/cm)
Solid Diffusivity	at 0°C 0.982 ave. 0.834	0.0967 0.0781	0.558 0.314	cm ² /sec
Melting Temperature	933.	1933.	2892.	degree Kelvin
Energy to Melt From 0°C	1.088	1.539	1.227	Kilojoules/gram
Specific Melt Volume	3.395	1.444	0.796	10 ⁻⁴ cm ³ /joule
Liquid Density	at Tm 2.19 ave. 2.01	3.65 3.35	8.31 7.62	grams/cm ³
Liquid Specific Heat	1.177	0.7425	0.4361	(joules/gram)/°K
Liquid Thermal Conductivity	at Tm 0.907 ave. 1.09	0.089 0.107	0.400 0.481	(Watts/cm ²)/(°K/cm)
Liquid Diffusivity	at Tm 0.352 ave. 0.461	0.0328 0.0430	0.120 0.145	cm ² /sec
Boiling Temperature	2766.8	3591.	4919.	degrees Kelvin
Heat of Vaporization	at Tb 10.7768	8.8772	6.1409	Kilojoules/gram

Masters⁽²²⁾ solves the heat conduction equation in the liquid layer using a very similar technique and determines the surface temperature T_s

$$T_s = T_m + \frac{\alpha q}{v_m \rho_L C_L} \quad (50)$$

where αq is the absorbed laser irradiance and v_m is again the melt velocity. Using appropriate boundary conditions, one arrives at

$$v_m = \frac{\alpha q \exp[-v_m s / \kappa_L]}{\rho_s \Omega_m + \rho_s C_s (T_m - T_0)} \quad (51)$$

In equation 51, Ω_m is the latent heat of melting and κ_L is the diffusivity of the liquid layer. It is seen that the melt velocity decreases with increasing melt layer thickness s . For aluminum $\{\Omega_m + C_s (T_m - T_0)\} = 1088$ joules/gm and one obtains the corresponding zero-thickness velocity

$$\left. v_m \right|_{s=0} = 3.4 \times 10^{-4} \alpha q \text{ cm/sec} \quad (52)$$

For the above analysis to be valid the melt layer is assumed to be maintained constant by some external force such as gravity, wind drag forces⁽¹⁹⁾, or evaporation. We will now examine the mechanisms by which the reaction force of a vaporizing surface can maintain a "constant" melt layer thickness. In principle, a similar analysis could be carried out for the case of external surface pressures generated by laser-supported absorption waves⁽⁷⁾.

In order to determine relationships taking into account the surface pressure gradients one must solve, self-consistently, the equations of conservation of energy, mass, and momentum. For analytical simplification, it is assumed that the surface pressure is approximated by

-
23. Touloukian, Y.S., Powell, R.W., Ho, C.Y., Klemens, P.G., Nicolaou, M.C., Kirby, R.K., Taylor, R.E., and Desai, P.D., Thermophysical Properties of Matter, Thermal Conductivity, Volume 1, Thermal Diffusivity, Volume 10, and Thermal Expansion, Volume 12, IFI/Plenum, 1970-1975.

$$\left. \begin{array}{l} p \\ \text{surface} \\ x = -s \end{array} \right\} = P_0 \left(1 - \frac{r^2}{R_p^2} \right) \quad (53)$$

where R_p is the scale length for the pressure variation. The maximum pressure P_0 is to be determined by solving for the vaporization rates. The actual scale length R_p is found to be considerably smaller than the laser spot size due to the strong dependence of the vapor pressure on the exact surface temperature. Thus, it is found that, for $r < R_p$, the maximum variation in surface temperature is only 3 to 10 percent.

Thus, in the conservation of energy equation we neglect $\frac{\partial T}{\partial r}$ and obtain

$$\rho_L C_L \left(\frac{\partial T}{\partial t} + v_z \frac{\partial T}{\partial z} \right) = K_L \frac{\partial^2 T}{\partial z^2} \quad (54)$$

Equation 54 neglects effects of viscosity and the kinetic energy of the fluid in comparison to the heat capacity of the liquid. The conservation of mass equation (with similar assumptions) is

$$\frac{1}{r} \frac{\partial}{\partial r} (r v_r) + \frac{\partial v_z}{\partial z} = 0 \quad (55)$$

Finally the momentum equations in both the radial and axial directions are

$$\frac{\partial v_r}{\partial t} + v_r \frac{\partial v_r}{\partial r} + v_z \frac{\partial v_r}{\partial z} = -\frac{1}{\rho_L} \frac{\partial p}{\partial r} + \frac{\mu}{\rho_L} \left(\frac{\partial^2 v_r}{\partial r^2} + \frac{\partial^2 v_r}{\partial z^2} + \frac{1}{r} \frac{\partial v_r}{\partial r} - \frac{v_r}{r^2} \right) \quad (56)$$

$$\frac{\partial v_z}{\partial t} + v_r \frac{\partial v_z}{\partial r} + v_z \frac{\partial v_z}{\partial z} = -\frac{1}{\rho_L} \frac{\partial p}{\partial z} + \frac{\mu}{\rho_L} \left(\frac{\partial^2 v_z}{\partial r^2} + \frac{\partial^2 v_z}{\partial z^2} + \frac{1}{r} \frac{\partial v_z}{\partial r} \right)$$

In equation 56, μ is the viscosity of the molten target material. Using the fluid boundary conditions

$$v_z \{x=0\} = v_r \{r=0\} = v_r \{x=0\} = 0 \quad (57)$$

$$v_z \{x=-s\} = v_m$$

Using equation 53 one finds from equation 56 that

$$\begin{aligned} v_r &= -v_m \frac{xr}{s^2} & a) \\ v_z &= v_m x^2/s^2 & b) \\ v_m &= \frac{s}{R_p} \sqrt{\frac{2P_0}{\rho_L}} & c) \end{aligned} \quad (58)$$

Finally, the total variation (within the molten layer) of pressure is given by

$$P=P_0 \left(\left(1 - \frac{r^2}{R_p^2} \right) + \frac{4\mu}{R_p^2 \rho_L v_m} (x+s) + \frac{2}{R_p^2} (x^2-s^2) - \frac{(x^4-s^4)}{R_p^2 s^2} \right) \quad (59)$$

It may be noted from equation 59 that all the terms describing the axial pressure variation are small, being of order s^2/R_p^2 . In this case, one may assume that the pressure everywhere is the same as the surface pressure (see equation 53).

Knowing the axial fluid velocity given by equation 58, one can determine the variation of temperature with the molten layer. Setting $Y = \frac{\partial T}{\partial x}$, one finds

$$\frac{dY}{dx} + \frac{v_m}{\kappa_L} \left(1 - \frac{x^2}{s^2} \right) Y = 0 \quad (60)$$

Equation 60 can be integrated twice and with the application of heat flux boundary conditions at $x=0$ (the solid-liquid boundary) and $x=-s$ (the liquid-air boundary) one obtains

$$\begin{aligned}
 T &= T_m + \frac{saq}{\kappa_L} N \left[A, \frac{-x}{s} \right] & \text{a)} \\
 v_m &= \frac{aq \exp \left[-\frac{2}{3} A \right]}{\rho_s \Omega_m + \rho_s C_s (T_m - T_0)} & \text{b)}
 \end{aligned}
 \tag{61}$$

In equation 61

$$A = \frac{v_m s}{\kappa_L} \tag{62}$$

Thus, we find that the melt velocity v_m obtained with fluid motion is identical to equation 51 except for the factor of $2/3$ in the exponent. The function $N(A, w)$ is shown in figure 77 and is defined by

$$N(A, w) = \exp \left\{ -\frac{2}{3} A \right\} \int_0^w \exp \left\{ A \left(W - \frac{1}{3} W^3 \right) \right\} dW \tag{63}$$

and gives the relative temperature distribution through the liquid layer. It is evident that the surface temperature is given by

$$T_s = T_m + \frac{saq}{\kappa_L} N(A, 1) \tag{64}$$

It is a fairly complicated procedure to actually calculate liquid layer thicknesses s and melt velocities v_m as a function of the laser absorbed irradiance aq and scale length R_p . In order to carry out the above computations, however, one must be able to calculate the vapor pressure as a function of temperature. The technique for doing this is given in Appendix A. Assuming this technique is available, one generates curves of s and v_m as a function of aq by:

- 1) Choose the coefficient A and compute $N(A, 1)$. From equation 62, the product $(v_m s)$ is thus set.
- 2) From equation 61b and the above value of A compute the product (saq) .

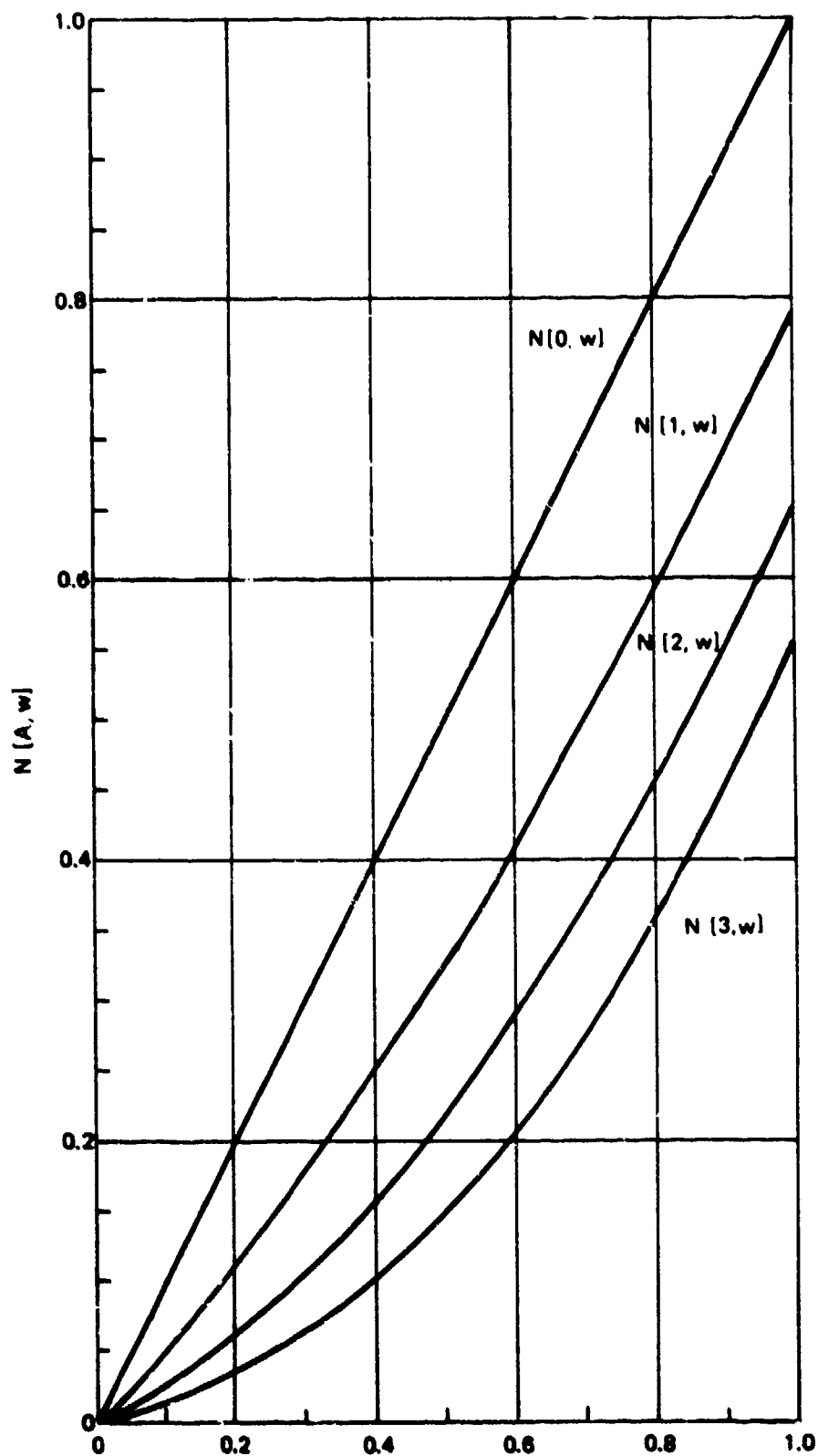


Figure 77. The $N[A, w]$ Function

- 3) Equation 64 then yields the surface temperature T_s .
- 4) From the results of Appendix A compute the reaction pressure P_o .
- 5) From equation 58c compute s .
- 6) Using the results of steps 1, 2 and 5 compute αq and v_m .

The above procedure gives one point on a curve of v_m (or s) vs. αq and the above procedure is repeated until a complete curve is generated.

For high laser intensities, which lead to high surface temperatures, the velocity of recession of the liquid surface due to vaporization v_v is not negligible compared to v_m . As noted previously, the vapor pressure is a very strong function of the surface temperature. For this reason the value of R_p (pressure scale length) is generally less than the laser spot size itself. When large velocities v_v occur, the liquid-gas boundary condition is a function of the radius. This causes all variables to be dependent on r instead of just P and v_r . Section 7.3 considers the case where significant mass is lost in the vapor state.

3. TWO - DIMENSIONAL MELT REMOVAL

We next consider the (azimuthally symmetrical) two-dimensional melt removal process taking into account the radial variation of the melt velocity caused by the radial variation of laser intensity. As a starting point we assume the melt velocity to have a parabolic profile

$$v_m = v_{m0} \left(1 - \frac{r^2}{R_m^2}\right) \quad (65)$$

In general, higher order terms in r could be included in equation 55. However, for simplicity, we use only the first two terms. In addition the vaporization recession rate (discussed in Appendix A) is assumed to have the form

$$v_v = v_{v0} \left(1 - \frac{r^2}{R_v^2}\right) \quad (66)$$

As discussed in section 7.2, we use a coordinate system moving with the local melt boundary (see figure 76). Because of the radial variation of v_m , the melt boundary is not strictly plane.

Because of the coordinate system used ($x = z - v_m t$) the partial derivatives that occur in the conservation equations are replaced by

$$\begin{aligned} \frac{\partial}{\partial t} &\rightarrow \frac{\partial}{\partial t} - v_{m0} \left(1 - \frac{r^2}{R_m^2}\right) \frac{\partial}{\partial x} \\ \frac{\partial}{\partial r} &\rightarrow \frac{\partial}{\partial r} + \frac{2r v_{m0} t}{R_m^2} \frac{\partial}{\partial x} \\ \frac{\partial}{\partial z} &\rightarrow \frac{\partial}{\partial x} \end{aligned} \quad (67)$$

With equation 67, the conservation of mass equation can be written

$$\frac{1}{r} \frac{\partial}{\partial r} (rv_r) + \frac{2v_{m0}t}{R_m^2} \frac{\partial}{\partial x} (rv_r) + \frac{\partial v_z}{\partial z} = 0 \quad (68)$$

Using the boundary conditions $v_r(r=0) = v_z(x=0) = 0$ and

$$v_z[x=-s] = v_{m0} \left(1 - \frac{r^2}{R_m^2}\right) - v_{v0} \left(1 - \frac{r^2}{R_v^2}\right) \quad (69)$$

one obtains

$$v_r = -\left(\frac{xr}{s^2}\right) \left(v_{m0} - v_{v0} - \frac{r^2}{2} \left(\frac{v_{m0}}{R_m^2} - \frac{v_{v0}}{R_v^2} \right) \right) + \frac{v_{m0}tr^3}{2R_m^2s^2} \left(v_{m0} - v_{v0} - \frac{r^2}{3} \left(\frac{v_{m0}}{R_m^2} - \frac{v_{v0}}{R_v^2} \right) \right) \quad (70)$$

and

$$v_z = \frac{x^2}{s^2} \left(v_{m0} - v_{v0} - r^2 \left(\frac{v_{m0}}{R_m^2} - \frac{v_{v0}}{R_v^2} \right) \right) \quad (71)$$

The solutions given by equations 70 and 71 are approximate since the boundary condition $v_r(x=0) = 0$ is not rigorously satisfied. However, as can be seen from the second term of equation 70, the error is small.

Substituting equations 70 and 71 into the momentum equation one determines the pressure.

$$P = P_0 \left(1 - \frac{r^2}{R_p^2} + \frac{r^4}{2R_p^2 R_m^2} \right) \quad (72)$$

Again, as in section 7.2, the fluid pressure is nearly constant through the melt depth. Equation 72 has neglected terms of order $(s/R_p)^2$, $(s/R_m)^2$, and small terms involving viscosity. These neglected terms contribute errors of about one percent if the melt depth to radius ratio is less than 0.1. This assumption was satisfied for the results presented earlier.

The heat conduction equation can be written, in terms of the variable x

$$\frac{\partial^2 T}{\partial x^2} + \frac{\partial T}{\partial x} \left(\frac{v_{mo}}{\kappa_L} \left(1 - \frac{r^2}{R_m^2} \right) + \frac{2xtv_{mo}r^2(v_{mo}-v_{vo})}{s^2 R_m^2} \right) \\ = \frac{\partial T}{\partial x} \left(\frac{x^2}{s^2} \left(v_{mo}-v_{vo}-r^2 \left(\frac{v_{mo}}{R_m^2} - \frac{v_{vo}}{R_v^2} \right) \right) \right) + \frac{v_r}{\kappa_L} \frac{\partial T}{\partial r} - \frac{1}{r} \frac{\partial}{\partial r} \left(r \frac{\partial T}{\partial r} \right)$$

Equation 73 has neglected terms in r^4 and higher order terms.

The solution of equation 73 is written

$$\frac{\partial T}{\partial x} = \exp \left[-A B [r,x] \right] \left(y_L + \int_0^x D [r,x] \exp \left[A B [r,x] \right] dx \right)$$

where the various functions and coefficients are defined in Appendix B. Using those results leads to

$$T [r,x] = D [x] \left(T_s \left(1 - \frac{r^2}{R_T^2} \right) - T_M \right) + T_M$$

where $D(0)=0$ and $D(-s)=1$ satisfy the thermal boundary conditions.

At the melt-solid boundary ($x=0$) the heat flux continuity equation must be satisfied.

$$-K_L y_L = v_m \left(\rho_s \Omega_s + \rho_s C_s (T_m - T_o) \right)$$

Equation 76 therefore shows that the "constant" y_L has the same radial variation as does v_m as shown in equation 65.

At the liquid-gas boundary, at $x=-s$, the heat flux continuity relationship leads to the equality of thermally conducted heat into the liquid and the net power absorbed q_M . The quantity q_M is the amount of absorbed laser irradiance minus the vaporization energy carried away from the surface and given in Appendix A.

$$q_M = \alpha q - q_v \quad (77)$$

In general, the scale length for the variation of q is dependent on the laser spot size R_B while the scale size for q_v , R_v , is usually significantly smaller than the temperature scale length itself.

$$q_v = q_{v0} \left(1 - \frac{r^2}{R_v^2}\right) \quad (78)$$

After a lengthy series of manipulations one finds

$$\begin{aligned} & -K_L \exp\left[A \left(1 - \frac{1}{3} V\right)\right] \left(y_{L0} - \frac{r^2 y_{L0}}{R_m^2} \left(1 + A \left(1 + \frac{v_{mo} t v}{s} - \frac{1}{3} V'\right) - \frac{4sT_s}{R_T^2} \right. \right. \\ & \left. \left(F_0 [A, V, 1] - \frac{r^2 A}{R_m^2} \left(\left(1 + \frac{v_{mo} t v}{s} - \frac{1}{3} V'\right) F_0 [A, V, 1] - \right. \right. \right. \\ & \left. \left. F_1 [A, V, 1] - \frac{v_{mo} t v}{s} F_2 [A, V, 1] + \frac{1}{2} \frac{R_m^2 v}{s^2} F_1 [A, V, 1] + \right. \right. \\ & \left. \left. \left. \frac{1}{3} V' F_3 [A, V, 1] \right) \right) \right) = q_M \end{aligned} \quad (79)$$

The functions F_0 , F_1 , F_2 , F_3 are again defined in Appendix B.

Using algebra similar to that used in section 7.2 (equating terms which are not a function of the radius) one also determines the maximum (at the center of the laser spot) melt recession velocity

$$v_{mo} = \frac{(\alpha q_0 - q_{v0}) \exp\left[-A \left(1 - \frac{1}{3} V\right)\right] - \frac{4K_L s T_s F_0 [A, V, 1]}{R_T^2}}{\rho_s \Omega_m + \rho_s C_s (T_m - T_0)} \quad (80)$$

Equation 80 accounts for the fractional energy going into both melting and vaporization and also accounts for any radial heat flow in the liquid. For very high vaporization rates, the liquid layer thickness will be small ($s \rightarrow 0$) and equation 80 reduces to

$$\alpha q_0 = v_{mo} (\rho_s \Omega_m + \rho_s C_s (T_m - T_0)) \exp [A] + q_{vo} \quad (81)$$

which is equivalent to the standard formulation of laser vaporization (q_{vo} is proportional to $v_{vo} \rho_s \Omega_v$).

After considerable work the liquid temperature as a function of radius and depth is determined by integration of equation 74.

$$\begin{aligned} T[r,x] = T_m - s y_{Lo} & \left(\left(1 - \frac{r^2}{R_m^2}\right) E_0 + \frac{r^2 A E_1}{R_m^2} + \frac{r^2 v_{mo} t A V E_2}{R_m^2 s} \right. \\ & - \frac{r^2 A V / E_3}{3 R_m^2} \left. \right) + \frac{4 s^2 T_s}{R_T^2} \left(G_0 - \frac{r^2 A G_1}{R_m^2} - \frac{r^2 v_{mo} t A V G_2}{R_m^2 s} \right. \\ & + \frac{r^2 A V / G_3}{3 R_m^2} + \frac{r^2}{R_m^2} \left(1 - \frac{R_m^2 V}{2 s^2} \right) A H_1 \\ & \left. + \frac{r^2 v_{mo} t V A H_2}{s R_m^2} - \frac{r^2 A V / H_3}{3 R_m^2} \right) \end{aligned} \quad (82)$$

The functions $E_0, E_1, E_2, E_3, G_0, G_1, G_2, G_3$, and H_1, H_2, H_3 are integrals dependent on the three parameters A, V and W . The definitions are again given in Appendix B. The maximum surface temperature in the center of the melt is determined from equation 82, for $w = 1$, to be

$$T_s = T[0,-s] = \frac{T_m + \frac{S v_{mo}}{K_L} (\rho_s \Omega_m + \rho_s C_s (T_m - T_0)) E_0[A,V,1]}{1 - \frac{4 s^2}{R_T^2} G_0[A,V,1]} \quad (83)$$

From equations 75 and 82, one also obtains

$$D[x] = \frac{\frac{s v_{mo}}{K_L} (\rho_s \Omega_m + \rho_s C_s (T_m - T_o)) E_o [A, v, -\frac{x}{s}] + \frac{4 s^2 T_s G_o}{R_T^2} [A, v, -\frac{x}{s}]}{T_s - T_m} \quad (84)$$

As described in section 7.2, the process of actually computing curves showing the dependence of melt thickness s and melt velocity v_{mo} as a function of absorbed laser irradiance is accomplished by an iterative procedure.

- 1) Select a numerical value for A as defined by equation 62 which also selects the product $s v_{mo}$.
- 2) Select a numerical value of the pressure scale length R_p .
- 3) Select trial values of s , T_s , R_T , and V .
- 4) Compute the integrals G_o and E_o which lead to a new estimate for T_s .
- 5) From the results of Appendix A compute the reaction pressure P_o due to vaporization of the liquid surface at temperature T_s .
- 6) From Appendix A, compute the surface recession rate v_{vo} due to vaporization.
- 7) From the radial momentum equation note that the peak pressure P_o and v_{vo} are related by

$$P_o = \frac{\rho_L R_p^2 v_{mo} (v_{mo} - v_{vo})}{2 s^2} \quad (85)$$

- 8) From equation 85 and step 5 a fourth order polynomial in s is obtained

$$s^4 + \frac{\rho_L R_p^2}{2 P_o} \left((s v_{mo}) (s v_{vo}) - (s v_{mo})^2 \right) = 0 \quad (86)$$

- 9) Equation 86 is solved numerically for a new value of s by Newton's method. This value of s and the product $s v_{mo}$ from step 1 gives a new value of v_{mo} .
- 10) A new value of $V = 1 - \frac{v_{vo}}{v_{mo}}$ is then computed.
- 11) A new value of R_T is computed from an equation obtained by equating the terms proportional to r^2 in equation 82.
- 12) Steps 4 through 11 are iterated until all computed values converge.

Although the above 12 steps seem laborious, they have been carried out for a range of absorbed laser intensities and laser spot sizes. The results are discussed in Section 7.1 where the melt thickness, melt velocity, specific impulse I/E , and the specific mass removal efficiency are computed for aluminum, titanium, and molybdenum, and shown in figures 63 through 75.

4. TIME TO REACH STEADY STATE

The analyses given in sections 7.2 and 7.3 have assumed that a steady state vaporization and melting situation exists. In reality, of course, this steady state takes a certain time to occur. If the applied laser irradiance is a step function of time, the temperature profile with a semi-infinite solid is given by⁽¹²⁾

$$T [z,t] = T_0 + \frac{2 \alpha q}{\sqrt{\pi K \rho C}} \left(\sqrt{t} \exp \left[\frac{-\rho C z^2}{4 K t} \right] - \sqrt{\frac{\pi \rho C z^2}{4 K}} \operatorname{erfc} \left[\left(\frac{\rho C z^2}{4 K t} \right)^{1/2} \right] \right) \quad (87)$$

where the surface temperature (at $z = 0$) is

$$T [0,t] = T_0 + 2 \alpha q \left(\frac{t}{\pi K \rho C} \right)^{1/2} \quad (88)$$

It is easily observed from equation 87 that the heat penetration depth δ is

$$\delta = \left(\frac{4 K t}{\rho C} \right)^{1/2} \quad (89)$$

For aluminum, as an example, the penetration depth is approximately 0.01 cm in a time of 100 microseconds.

Using the results of equation 88 the surface temperature of aluminum is plotted as a function of time in figure 78 assuming the initial temperature was 1000K. The square-root dependence of the temperature on time is, however, valid only up to the point where significant melting and vaporization occurs. For $\alpha q = 10^6$ watts/cm² this occurs in less than 20 microseconds. When $\alpha q = 10^5$ watts/cm² this time increases by a factor of 100.

When the power loss due to vaporization becomes important the surface temperature T_s is a solution of the integral equation⁽¹⁵⁾

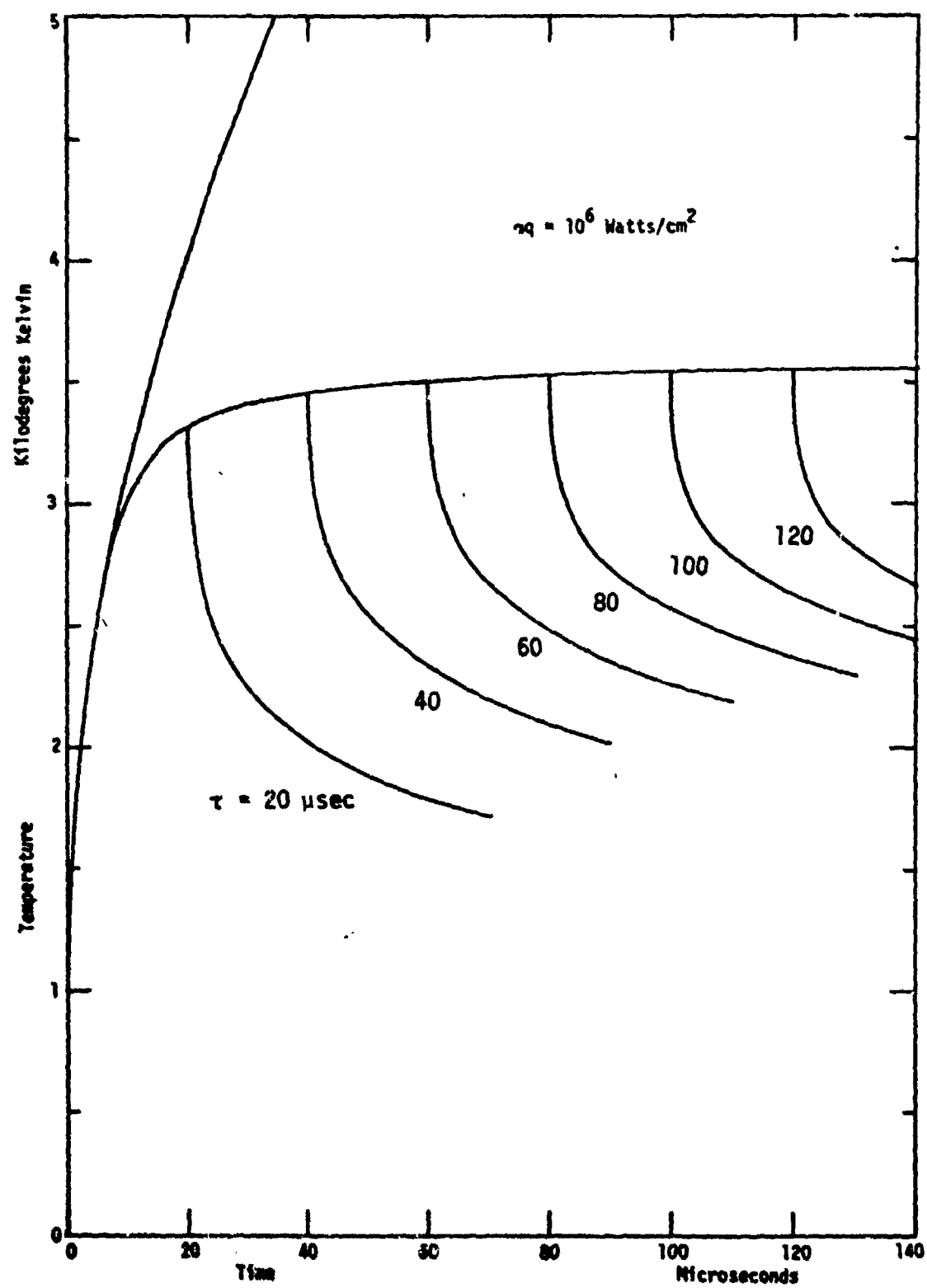


Figure 78. Surface Temperature of Aluminum

$$T_s = T_0 + 2 \alpha q \left(\frac{t}{\pi K \rho C} \right)^{1/2} - \frac{1}{\sqrt{\pi K \rho C}} \int_0^t \frac{q_v(t-\tau) d\tau}{\sqrt{\tau}} \quad (90)$$

In equation 90, the second term is the same as shown in equation 88 while the third term shows the cooling effect caused by vaporization. The vapor heat loss q_v is described in analytical terms in Appendix A (equation A23) and depends explicitly on the vapor pressure and temperature of the surface. The solution of equation 90 has been solved numerically for aluminum and the results are again shown in figure 78. The saturation in the temperature rise is clearly caused by vaporization. The various curves show how the surface temperature falls after the laser pulse is terminated.

Figure 79 shows that the reaction pressure on the surface continues to increase for a considerably longer time than may be apparent from the corresponding slow increase of temperature shown in figure 78. This is indicative of the very sensitive dependence of the vapor pressure on surface temperature.

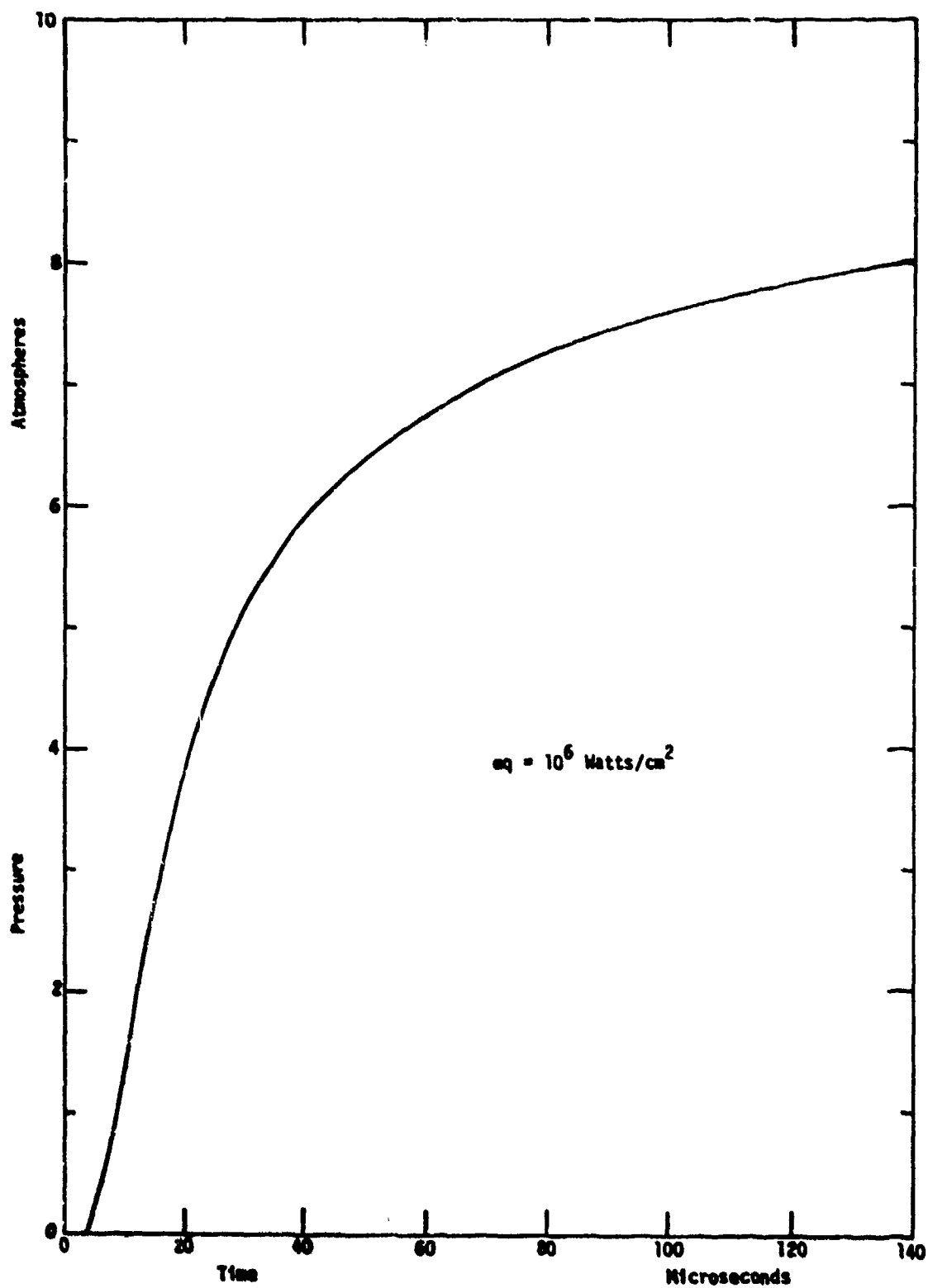


Figure 79. Reaction Pressure Due to Evaporation of Aluminum

5. MELT REMOVAL BY PULSED LASER BEAMS

For repetitively pulsed laser interaction with targets it is important to determine the ability of a partially vaporizing surface to "blow" away a thin liquid layer of molten metal. As demonstrated in Sections 7.2 and 7.3 the melting efficiency of CW laser beams can be relatively high if the irradiance is not too high (or the laser spot size not too large). The reaction pressure due to evaporation produces a radial pressure gradient which keeps the product of the melting velocity and the melt layer thickness at a relatively small value. Otherwise the melting efficiency is small and mass removal by vaporization from the surface dominates over melt removal by radial flow of the liquid. In these large intensity and/or large beam size cases the melting efficiency may be improved by superimposing high intensity pulses on a steady, lower intensity beam. This would keep the liquid layer thickness small so that the melting beam would be more efficient and also at the same time supply pressure pulses.

Consider the case of high intensity laser beam pulses which cause a pressure gradient at the target surface superimposed on a steady moderate intensity laser beam which melts the target surface and determines the pulse width and pulse repetition rate for maximum melt removal. The surface pressure as caused by either LSD waves or vaporization is approximated by

$$P = P_0 \left(1 - \frac{r}{R_p}\right)^2 \quad (91)$$

For the part of the flow which is not in the boundary layer near the solid surface the viscosity terms in the Navier-Stokes equations are negligible and the momentum equation for the radial velocity component becomes

$$\frac{\partial v_r}{\partial t} + v_r \frac{\partial v_r}{\partial r} + v_z \frac{\partial v_r}{\partial z} = - \frac{1}{\rho_L} \frac{\partial p}{\partial r} \quad (92)$$

For the parabolic pressure variation of equation 9.1, the pressure gradient term is

$$- \frac{1}{\rho_L} \frac{\partial p}{\partial r} = \frac{2rP_0}{\rho_L R_p^2} = \frac{r}{\tau^2} \quad (93)$$

in which the characteristic acceleration time is

$$\tau = R_p \left(\frac{\rho_L}{2P_0} \right)^{1/2} \quad (94)$$

An infinite series solution of this equation is

$$v_r = \frac{r}{\tau} \left(\left(\frac{t}{\tau} \right) - \frac{1}{3} \left(\frac{t}{\tau} \right)^3 + \frac{2}{15} \left(\frac{t}{\tau} \right)^5 - \frac{17}{315} \left(\frac{t}{\tau} \right)^7 + \dots \right) \quad (95)$$

This series solution is valid from $\frac{t}{\tau} = 0$ to about $\frac{t}{\tau} = 1$. Figure 80 shows plots of the first five and six terms of the infinite series. For small times the $v \cdot \Delta v$ term is negligible and the radial velocity increases linearly with time. As the velocity increases, the $v \cdot \Delta v$ term becomes important until at long times a constant velocity is approached and the time derivative term becomes negligible.

$$v_r \left(\frac{t}{\tau} \rightarrow \infty \right) = \frac{r}{\tau} \quad (96)$$

A closed form expression which matches well the solution from $\frac{t}{\tau} = 0$ to $\frac{t}{\tau} = 1$ and is asymptotic to the constant long time solution is

$$v_r = \frac{rt}{\tau^2} \left(1 + \left(\frac{t}{\tau} \right)^n \right)^{-\frac{1}{n}} \quad (97)$$

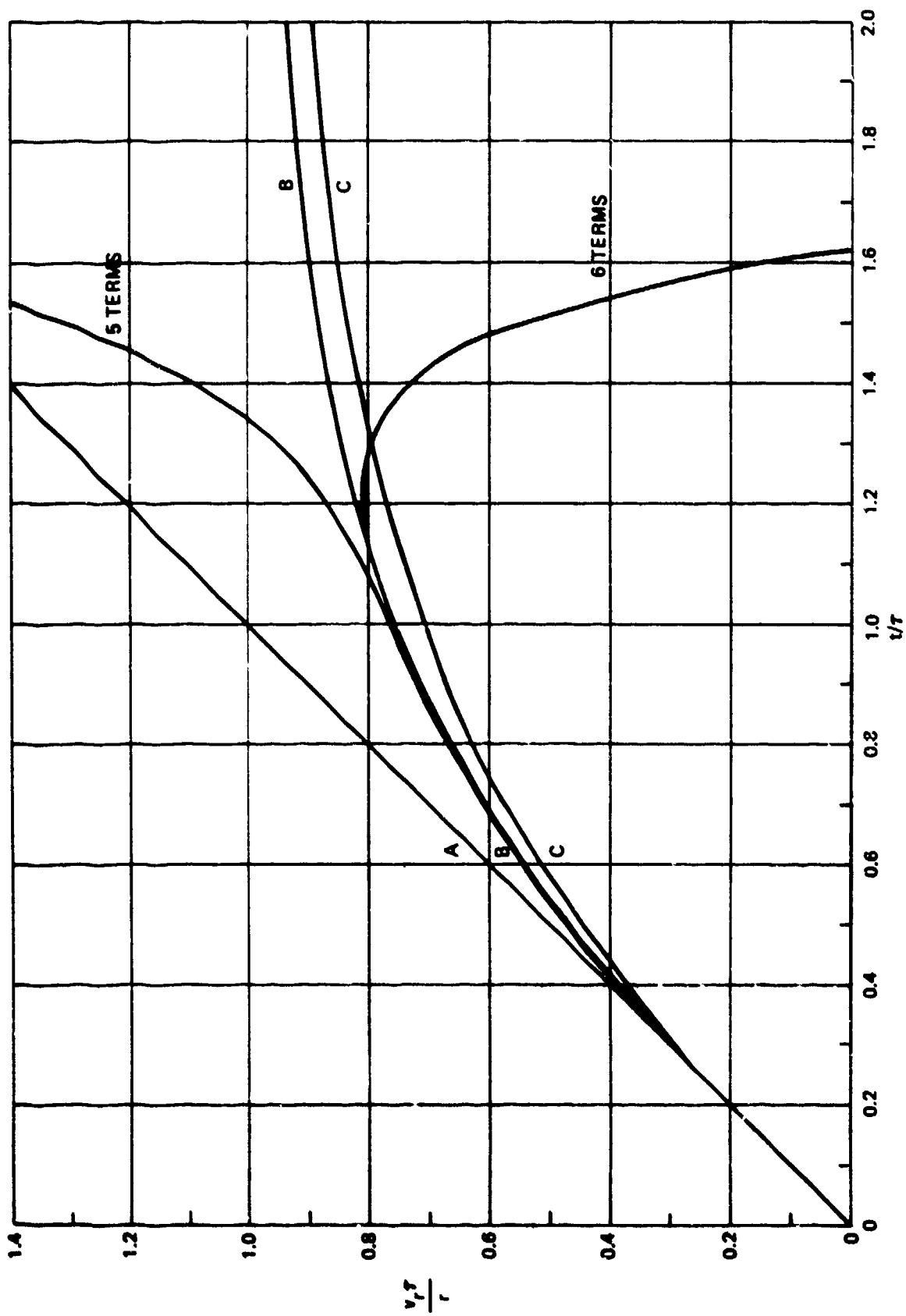


Figure 80. Radial Acceleration of Melt

with $n = 2.5$, and is shown as curve B in Figure 80. A more approximate closed form expression which matches the short time and long time solution but gives slightly low velocity values for intermediate times

$$v_r = \frac{rt}{\tau^2 \left(1 + \left(\frac{t}{\tau}\right)^2\right)^{1/2}} \quad (98)$$

is shown as curve C in Figure 80. Equation 98 has the advantage that it is analytically integrable. It also allows approximately for the small boundary layer which has a smaller average velocity than the rest of the liquid.

Neglecting melting during the short pressure pulse, the time rate of decrease of the liquid volume in the cylindrical melted region equals the rate of flow radially out of the region through the area $2\pi R_m h$

$$\frac{dVol}{dt} = -2\pi R_m h v_r(R_m) = \pi R_m^2 \frac{dh}{dt} \quad (99)$$

The resulting differential equation

$$\frac{dh}{h} = - \frac{2\left(\frac{t}{\tau}\right) \frac{dt}{\tau}}{\left(1 + \left(\frac{t}{\tau}\right)^n\right)^{1/n}} \quad (100)$$

has the solution (when $n = 2$)

$$h = h_0 \exp \left[2 - 2 \left(1 + \frac{t^2}{\tau^2} \right)^{1/2} \right] \quad (101)$$

The melt removal rate reaches a maximum when $t \approx \frac{2}{3} \tau$ and then decreases so that at about $t = 1.4\tau$ the rate approximately equals the rate at $t = 0.2\tau$.

For pulse durations which are short compared with the characteristic acceleration time τ , the acceleration is constant and the solution for the liquid depth is

$$h = h_0 \exp \left[- \left(\frac{t}{\tau} \right)^2 \right] \quad (102)$$

This expression is plotted in Figure 81. When the pressure pulse terminates at $t = t_1$, the fluid continues to flow in a radial direction with the

velocity $v_r = \frac{rt_1}{\tau^2}$ that it had at $t = t_1$. The differential equation for the melt depth is again

$$-2\pi r h v_r = \pi r^2 \frac{dh}{dt} \quad (103)$$

with constant v_r which has a solution

$$h = h_1 \exp \left[-2 \frac{t_1 t}{\tau^2} \right] \quad t_1 < t < \infty \quad (104)$$

These expressions are also plotted in Figure 81 for $t_1 = 0.1\tau$, 0.2τ and 0.3τ .

It is seen that if the pressure pulse duration is short the melt doesn't get accelerated much and the coasting velocity is correspondingly small. Some combinations for effective melt removal are pressure pulsing for 0.1τ and then coasting for 10τ or pressure pulsing for 0.3τ and then coasting for 3τ , etc. For $P_0 = 1$ atmosphere, $R_p = 1$ centimeter and liquid aluminum density of $2.01 \text{ grams / cm}^3$, the characteristic acceleration time is about 1 millisecond. This relatively long time makes it difficult to find a realistic case where pressure pulsing would clearly be effective.

Consider as some examples an aluminum target with $R_p = 1$ centimeter and steady absorbed intensities of 10^4 , 10^5 , and 10^6 watts per square centimeter. A measure of the times required to reach steady state melting after the last pressure pulse pushed away the previously molten material can be obtained by dividing the steady state melt thicknesses $1100\mu\text{m}$, $300\mu\text{m}$, and

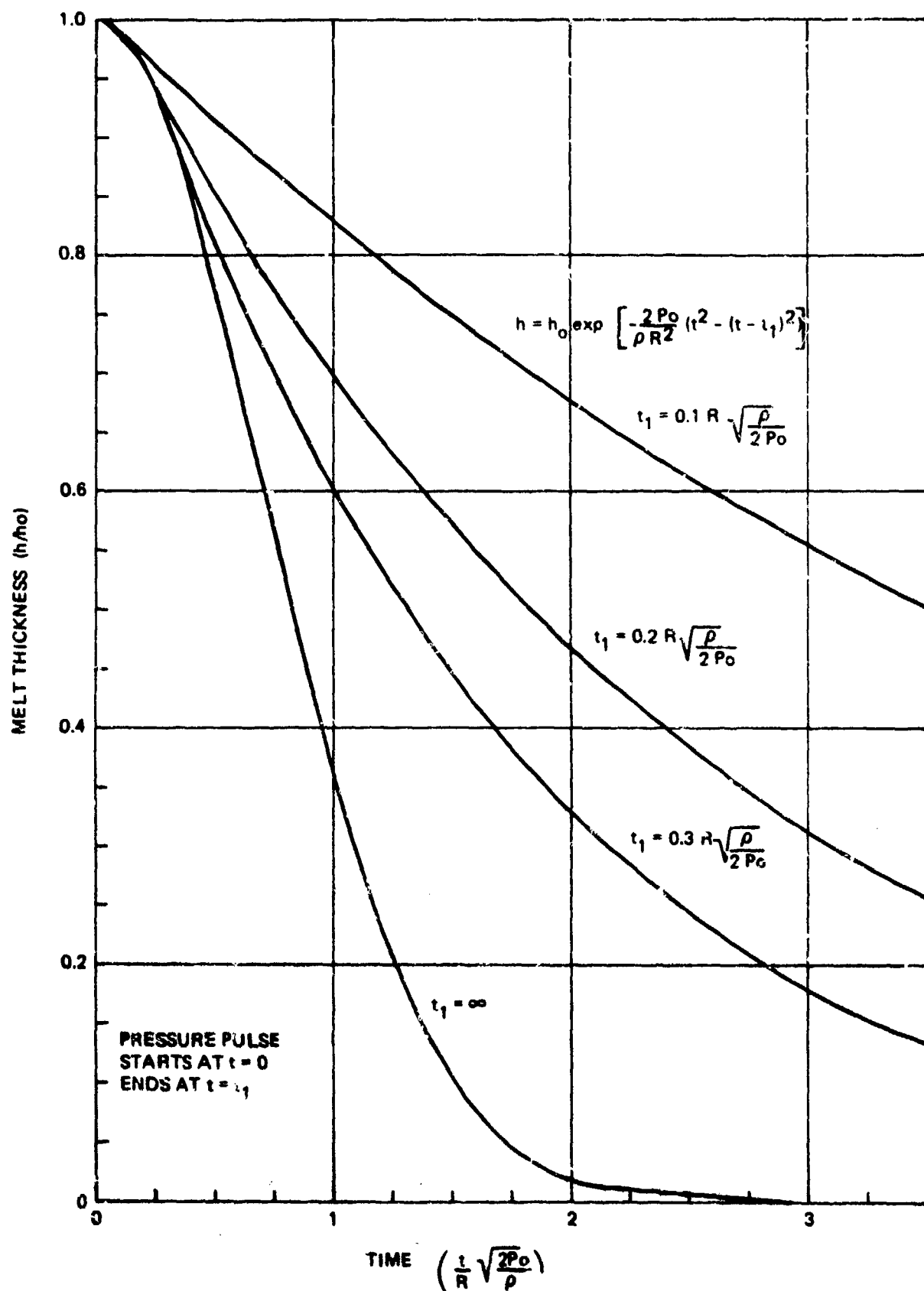


Figure 81. Melt Removal by Pressure Pulsing and Coasting

125 μ m by the steady state melting velocities 2.3 cm/sec, 14 cm/sec and 44 cm/sec to get 48 millisecc, 2.1 millisecc and 0.28 millisecc, respectively. As an example let the pressure-producing laser pulses have ten times the absorbed intensities of the steady intensities and be applied for a duration of 0.1τ and repeated every 10τ .

The pressure pulses would then have one tenth the average intensity of the steady beam. Ten times the characteristic acceleration times would then be 22 millisecc, 3.8 millisecc and 1.1 millisecc respectively. In only the lowest intensity case (10^4 W/cm² CW and, 10^5 W/cm² pulsed) is the coasting time required to remove the melt less than the melting time to make the melt.

At 20 pulses per second and with a pulse length of 200 microseconds the average intensity of the pulsed beam would be 4 percent of the steady intensity. In this case the melting efficiency would only be improved slightly because the steady state melting is already in the efficient melting range. For the middle intensity case (10^5 W/cm² CW, 10^6 W/cm² pulsed), pulsing and coasting could be used with a pulse duration of 0.2τ and a coasting time of 5τ with an average pulsed intensity of 40 percent of the CW intensity. For the highest intensity case (10^6 W/cm² CW, 10^7 W/cm² pulsed) pulsing and coasting could be used with a pulse duration of 0.3τ and a coasting time of 2.5τ with an average pulsed intensity of 120 percent of the CW intensity. In these latter cases, with relatively large proportions of the total average intensity in the pulsed component, it is unclear whether there is a gain or loss in melting efficiency. The pulsed component increases the melting efficiency of the CW component but the melting due to the pulsed component is less efficient than it would be if its average intensity were applied steadily. The situation is similar for other beam radii.

6. EFFECT OF GRAVITY

When the force of gravity ρ_g is superimposed on the radial pressure gradient $\frac{\partial P}{\partial r}$, the melt flows radially outward from a center which is

$$r = \frac{\rho_L g R_p^2}{2P_0} \cos \theta \text{ above the center of vaporization pressure at } r = 0$$

in the center of the melted region. θ is the angle between the direction normal to the surface and the horizontal plane. As long as this center of flow is inside the melted region the previous analysis applies with a greater amount of the melt flowing out of the crater or piling up on the rim

on the bottom than on the top. When P_0 is less than $\frac{9\rho_L R_p}{2} \cos \theta$, the

position where the resultant force is zero is above the melted region and the boundary condition of the flow going outward along $r = R_p$ is not satisfied and the analysis is modified and more complicated. This occurs

for $P_0 \leq 0.973 \times 10^{-3} R_p$ atmosphere/cm for aluminum, $P_0 \leq 1.62 \times 10^{-3} R_p$ atmosphere/cm for titanium and $P_0 \leq 3.69 \times 10^{-3} R_p$ atmosphere/cm for molybdenum for vertical surfaces. This occurs at approximately $\alpha q = 10^4$ watts/cm² for the various materials and beam radii.

SECTION VIII

CONCLUSIONS

The measurement of the conditions for initiation of target plasmas has been carried out for both 2.8 and 3.8 microns wavelength. Both fluence and irradiance (or temperature and irradiance) thresholds are simultaneously required in order to ignite plasmas. This is evident by comparing the theoretical description of these thresholds with the wide range of target materials and the two wavelengths. It is evident that the difference in wavelength (a factor of 1.36) yields significantly different thresholds for our particular pulse shape. Additional measurements and analysis in this area would be of great importance in understanding enhanced coupling phenomenology.

The technique of measuring the heat-addition profile by measuring the time dependence of the temperature of the $r = 0$ position has proven valuable. However, the data, as analyzed, are not completely self-consistent. It appears that a single-Gaussian description of this heating profile is not adequate. Because of this, a true mathematical inversion of the data should be carried out. Since this technique has not been developed, either electronically or mathematically, additional work is needed. This development would greatly aid in understanding the mechanisms of enhanced coupling with either small or large spots.

Only a limited number of measurements were carried out showing the dependence of mass loss of ablaters with laser energy. These data (at both HF and DF wavelength) show interesting limitations at both low and high delivered energies. This is due, for low energies, to the fact that no vaporization occurs. At high energies, on the other hand, plasma production and absorption become important.

One of the goals of this work was to determine mechanisms for melt removal by intense beams. Experimentally, the results were not impressive since molten metals were not directly removed in large amounts from only partially melted surfaces. The surface pressures do, however, push the

molten material through a completely melted surface. This area of investigation obviously requires more experiments over larger beam spot sizes and correspondingly larger laser energies. (The above experiments were done with 25 joules of CO_2 laser energy). Theoretical analysis of melt removal by a partially vaporizing surface leads to the expectation that high specific mass removal efficiencies can be obtained, even in the absence of an external wind or gravity. This results from the gradient of the vapor pressure causing a radial flow of the liquid metal surfaces. The analysis developed should be improved, however, and additional data presented.

APPENDIX A

VAPOR PRESSURES AND EVAPORATION RATES

When two different phases (solid, liquid or gas) of a substance are in equilibrium, the temperature T , pressure P and chemical potential μ must be equal ⁽²⁴⁾

$$\mu_1 \{P, T\} = \mu_2 \{P, T\} \quad (A1)$$

so that the pressure and temperature of phases in equilibrium can be expressed as functions of each other. When one of these quantities (P, T) is given the other is completely determined. Differentiating the chemical potential equation with respect to the temperature yields

$$\frac{\partial \mu_1}{\partial T} + \frac{\partial \mu_1}{\partial P} \frac{dP}{dT} = \frac{\partial \mu_2}{\partial T} + \frac{\partial \mu_2}{\partial P} \frac{dP}{dT} \quad (A2)$$

Then, using the identity

$$d\mu = -s dT + v dP \quad (A3)$$

in which s is the molecular entropy and v is the molecular volume, and the expression for the latent heat Ω of the transition

$$\Omega = T(s_2 - s_1) \quad (A4)$$

gives the Clausius - Clapeyron equation

$$\frac{dP}{dT} = \frac{\Omega}{T(v_2 - v_1)} \quad (A5)$$

This equation gives the change of pressure with change of temperature along the phase equilibrium curve.

24. Landau, L. D. and Lifshitz, E. M., Statistical Physics, Addison-Wesley Publishing Company, Inc. 1958.

The molecular volume of a gas $v_2 = \frac{kT}{P}$ is generally much larger than the molecular volume of the condensed phase so for the case of a solid or liquid in equilibrium with its vapor, v_1 can be neglected and the Clausius-Clapeyron equation becomes

$$\frac{dP}{dT} = \frac{\Omega P}{kT^2} \quad (A6)$$

If the latent heat of vaporization were constant the vapor pressure would vary exponentially with the reciprocal of the temperature.

$$P = P_0 \exp \left\{ - \frac{\Omega}{kT} \right\} \quad (A7)$$

Figure A1 shows the specific heats of aluminum, titanium and molybdenum. The specific heats of the liquids are constant. The specific heat of aluminum gas near the boiling temperature $T_b = 2766.8^\circ K$ (at which the vapor pressure is one atmosphere) is very nearly constant so that the latent heat of vaporization is a linear function of the temperature.

Thus

$$\Omega = (\epsilon_{02} - \epsilon_{01}) + (C_{p2} - C_1) T \quad (A8)$$

where

$$\epsilon_{02} - \epsilon_{01} = \Delta H_v - (C_{p2} - C_1) T_b$$

is the latent heat of vaporization extrapolated to zero temperature. With equation A8 the solution of equation A6 becomes

$$P = \left(\frac{T}{T_b} \right)^{\frac{(C_{p2} - C_1)}{k}} \exp \left[- \frac{(\epsilon_{02} - \epsilon_{01})}{k} \left(\frac{1}{T} - \frac{1}{T_b} \right) \right] \text{ Atmospheres } (A9)$$

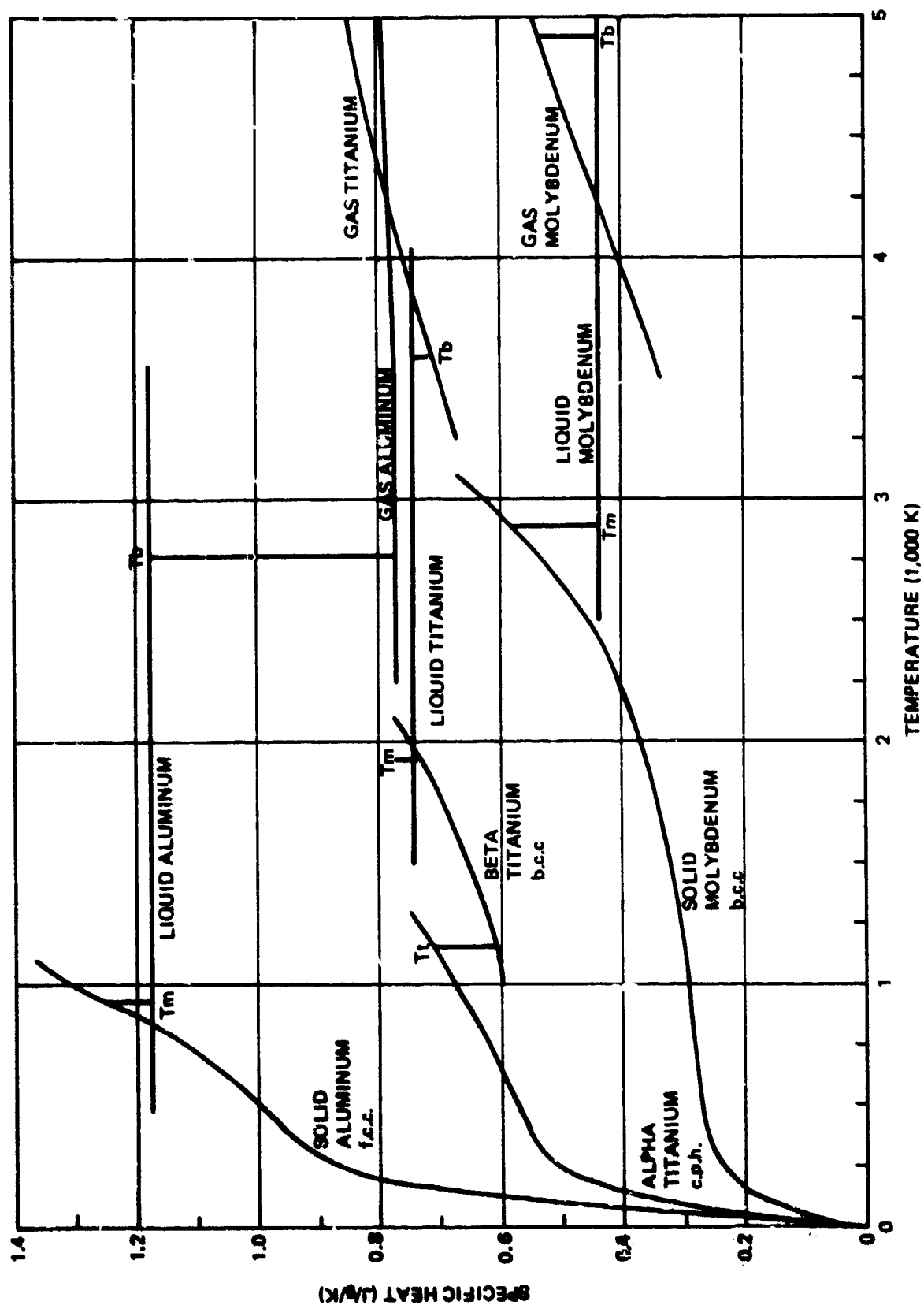


Figure A1. Specific Heats

Using the JANAF tables, reference 25, one obtains (for aluminum)

$$\frac{C_{p2} - C_1}{k} = -1.32 \quad (A10)$$

$$\frac{\epsilon_{02} - \epsilon_{01}}{k} = 38,620^\circ \text{K}$$

The vapor pressure of aluminum, found from equations A9 and A10, is plotted in Figure A2. The x symbols are from Reference 25, the + symbols are from reference 26 and the other symbols are from other references.

From equation A9, one finds at $T = T_b = 2767^\circ \text{K}$ that

$$\frac{dP}{dT} = 12.64 \frac{P}{T} \quad (A11)$$

Thus, from the assumption of Section 7.2 for the vapor pressure variation with transverse distance $[P = P_0 (1 - r^2/R_p^2)]$ and assuming that

$$T = T_s (1 - r^2/R_T^2) \quad (A12)$$

one finds that (for aluminum)

$$k_p = 0.28 R_T \quad (A12)$$

At other temperatures, one finds from equations A5 and A8,

$$\left. \frac{R_T}{R_p} \right|_{\text{Aluminum}} = \left(\frac{38620}{T} - 1.32 \right)^{1/2} \quad (A13)$$

25. JANAF Thermochemical Data, The Dow Chemical Company, Thermal Laboratory, Midland, Michigan, 1968.
26. Handbook of Chemistry and Physics, p. D-142 of 49th Edition, The Chemical Rubber Co., Cleveland, Ohio, 1969.

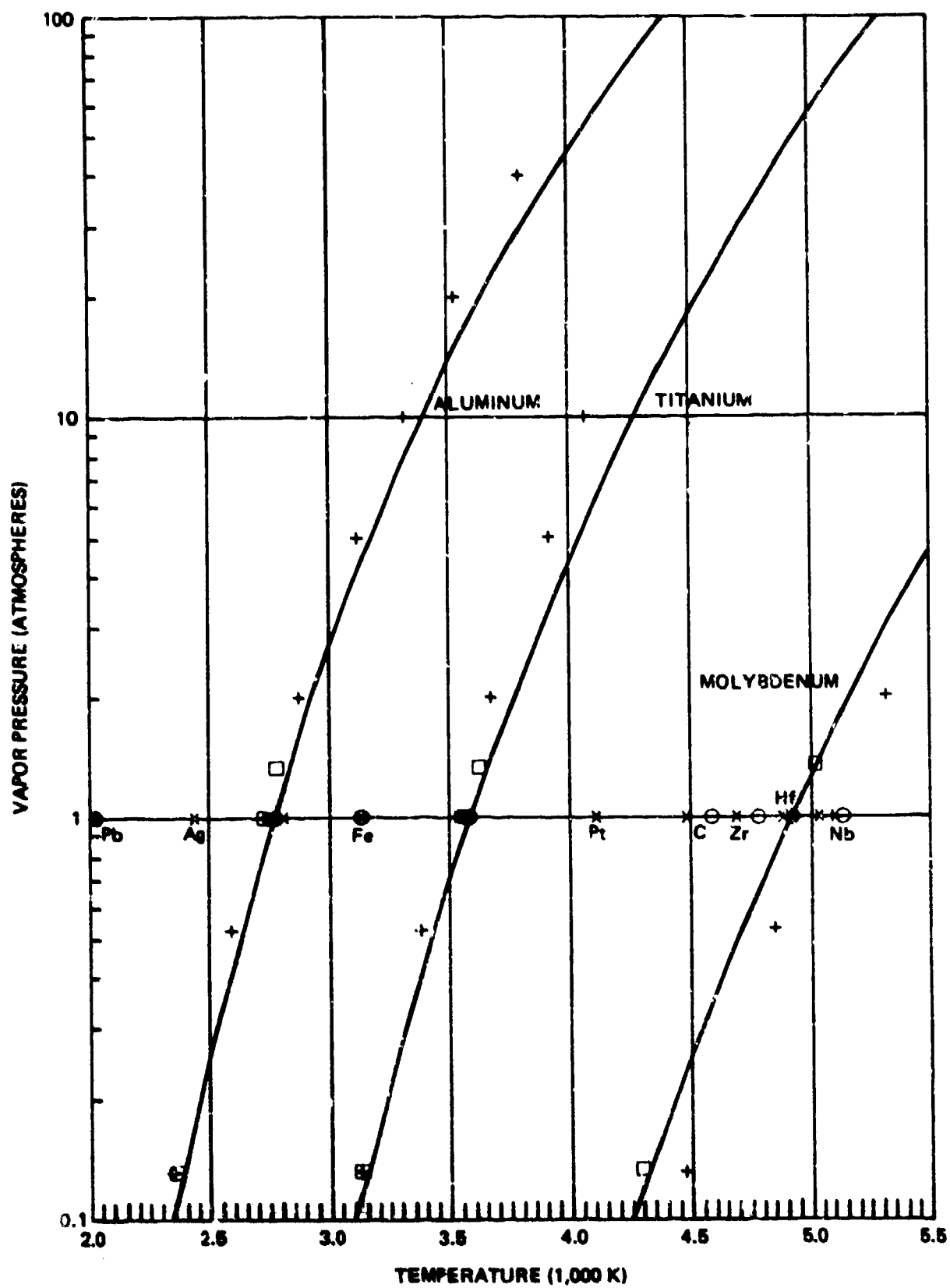


Figure A2. Vapor Pressures

As expected the scale length of the pressure profile is considerably smaller than the temperature scale length.

The solution of the Clausius-Clapeyron equation for titanium is somewhat more complicated than for aluminum due to the increase of specific heat of the gas with temperature. As seen from Figure A1 one may approximately write

$$C_{p2} = C_p + C'_p (T - T_D)$$

$$\Omega = \epsilon_{02} - \epsilon_{01} + (C_p - C_1 - C'_p T_D)T + C'_p \frac{T^2}{2} \quad (A14)$$

$$\epsilon_{02} - \epsilon_{01} = \Delta H_v - (C_p - C_1)T_b + \frac{C'_p T_D^2}{2}$$

Using equations A14 and A6, and numerical parameters found in reference 23, one determines (for titanium)

$$P = \left(\frac{T}{3591} \right)^{-2.68} \exp \left[-56280 \left(\frac{1}{T} - \frac{1}{3591} \right) + \frac{(T-3591)}{2880} \right] \text{ Atmospheres} \quad (A15)$$

Equation A15 is plotted in Figure A2.

Again one can determine (by the same technique as used for aluminum) the ratio of temperature and vapor pressure scale lengths for a titanium target material.

$$\left. \frac{R_T}{R_p} \right|_{\text{Titanium}} = \left(\frac{56280}{T} - 2.68 + \frac{T}{2880} \right)^{1/2} \quad (A16)$$

For titanium then, one finds for $T_s = 3591^\circ\text{K}$ and $P = 1\text{Atm}$ that $R_T/R_p = 3.77$.

Raising the titanium surface temperature to 5000°K ($P = 55.7\text{ Atm}$) leads to $R_T/R_p = 3.21$.

For molybdenum, the same type analysis as used for titanium applies as can be seen from Figure A1. The vapor pressure is found to be

$$P = \left(\frac{T}{4919} \right)^{-6.36} \exp \left[-83590 \left(\frac{1}{T} - \frac{1}{4919} \right) + \frac{T-4919}{1305} \right] \text{ Atmospheres} \quad (\text{A17})$$

Equation A17 is again plotted in Figure A2. The scale lengths for temperature and pressure are again found to be related by

$$\frac{R_T}{R_p} = \left(\frac{83590}{T} - 6.36 + \frac{T}{1305} \right)^{1/2} \quad (\text{A18})$$

At atmospheric pressure, $T = 4919$ K, one obtains $R_T = 3.8 R_p$.

When calculating forces on laser vaporized surfaces, it is worthwhile to recall several elementary principles. First of all, the reaction pressure due to vaporization is one half the corresponding vapor pressure as determined above. This occurs because of the momentum reversal of molecules incident on a noncondensing surface. The rate of molecular transfer \dot{n} through the vaporizing surface is given by

$$\dot{n} = n_0 \left(\frac{kt}{2\pi m} \right)^{1/2} \text{ particles/cm}^2/\text{sec} \quad (\text{A19})$$

where n_0 is the gas density and m is the mass of the vapor molecule. Since $P_v = nkT$, equation A19 can be rewritten

$$\dot{n} = \frac{P_v}{(2\pi mkt)^{1/2}} \quad (\text{A20})$$

Since the equilibrium rate of transfer of particles across a surface in one direction is the same as in vacuum, equation A20 leads to the recession rate v_v of the liquid surface. From continuity of mass

$$\begin{aligned} v_v &= \frac{\dot{n}A}{N_0 \rho_L} \\ &= 44.3 \frac{P_v}{\rho_L} \left(\frac{A}{T_s} \right)^{1/2} \text{ cm/sec} \end{aligned} \quad (\text{A21})$$

In equation A21, A is the atomic weight, N_0 is Avogadro's number, and ρ_L is the mass density of the liquid.

The kinetic energy transfer through the liquid-gas surface q_k is similarly found to be

$$q_k = 2kT \dot{n} \text{ watts/cm}^2 \quad (\text{A22})$$

The total power loss from the surface q_v includes the heat of vaporization so that

$$\begin{aligned} q_v &= n(2kT + \Omega) \\ &= 369. \frac{P_v(2T_s + \frac{\Omega}{k})}{(AT_s)^{1/2}} \text{ watts/cm}^2 \end{aligned} \quad (\text{A23})$$

where P_v is given in atmospheres.

From Reference 25 we obtain

$$\begin{aligned} \frac{\Omega}{k}_{Al} &= 38,620 - 1.32 T_s \\ \frac{\Omega}{k}_{Ti} &= 56,280 - 2.68 T_s + \frac{T_s^2}{2880} \\ \frac{\Omega}{k}_{Mo} &= 83,590 - 6.36 T_s + \frac{T_s^2}{1305} \end{aligned} \quad (\text{A24})$$

Thus we see that the heat of vaporization terms are considerably larger than the corresponding kinetic energy terms of equation A23.

APPENDIX B
FUNCTIONS RELATED TO THE TWO-DIMENSIONAL
HEAT FLOW SOLUTION

Section 7.3 describes the two-dimensional temperature distribution in terms of several functions and parameters.

$$A = \frac{v_{mo} s}{\kappa}$$

$$B[r, x] = B_0[x] + B_1[x] \frac{r^2}{R_{ill}^2}$$

$$B_0[x] = \frac{x}{s} - \frac{1}{3} \frac{x^3}{s^3} v$$

$$B_1[x] = -\frac{x}{s} + \frac{v_{mo} t}{s^3} x^2 v + \frac{1}{3} \left(\frac{x}{s}\right)^3 v'$$

$$v = 1 - \frac{v_{vo}}{v_{mo}}$$

$$v' = 1 - \frac{v_{vo}}{v_{mo}} \frac{R_m^2}{R_v^2}$$

$$D[r, x] = \frac{v_r}{\kappa_L} \frac{\partial T}{\partial r} - \frac{1}{r} \frac{\partial}{\partial r} \left(r \frac{\partial T}{\partial r} \right)$$

Including only the first two terms in the expansion of equation B4 yields

$$D[r, x] = \frac{4T_s D[x]}{R_T^2} \left(1 + \frac{AVxr^2}{2s^3} \right)$$

The functions F_0 , F_1 , F_2 , and F_3 are numerically determined and are defined by

$$F_n [A, V, W] = \int_0^W w^n D[w] \exp \left[-A(w - \frac{1}{3} Vw^3) \right] dw \quad (B6)$$

The integrations of equation B6 were carried out using the trapezoidal rule and 10^3 steps.

The function E_n , G_n and H_n (where $n = 0, 1, 2, 3$) which define the temperature profile (see equation 82) are defined by

$$E_n [A, V, W] = \int_0^W w^n \exp \left[A(w - \frac{1}{3} Vw^3) \right] dw \quad (B7)$$

$$G_n [A, V, W] = \int_0^W w^n F_0 [A, V, w] \exp \left[A(w - \frac{1}{3} Vw^3) \right] dw \quad (B8)$$

and

$$H_n [A, V, W] = \int_0^W F_n [A, V, w] \exp \left[A(w - \frac{1}{3} Vw^3) \right] dw \quad (B9)$$

In equations B8 and B9 the functions F_n are defined by equation B6.

REFERENCES

1. Hall, R. B., Maher, W. E., McClure, J. D., Nichols, D. B., and Pond, C. R. "Laser Beam Target Interaction," Vol. I, 2.8 Microns Wavelength, AFWL-TR-75-342, July 1976.
2. Maher, W. E., Hall, R. B., and Johnson, R. R., "Experimental Study of Ignition and Propagation of Laser-Supported Detonation Waves," J. Appl. Phys. 45, 2138, 1974.
3. Rudder, R. R. and Augustoni, A. L., "Thermal Deposition Experiments with Microsecond Duration CO₂ Laser Radiation," Laser Digest, AFWL-TR-75-229, 1975.
4. Hall, R. B., Wei, P. S. P., and Maher, W. E., "Laser Beam Target Interact Vol. II, Laser Effects at 10.6 Microns, AFWL-TR-75-342, July 1976.
5. Nichols, D. B., Hall, R. B., and McClure, J. D., "Photoinitiation F₂ + H₂ Chain-Reaction Laser with High Electrical Efficiency," J. Appl. Phys. 47, 4026, 1976.
6. Pond, C. R., Hall, R. B., and Nichols, D. B., "HF Laser Spectral Analysis Using Near-Field Holography," Appl. Opt. 16, 67, 1977
7. Raizer, Y. P., "Heating of a Gas by a Powerful Light Pulse," Soviet Phys JETP 21, 1009, 1965.
8. Lowder, S. E. and Pettingill, L. C., "Double-Pulse Pressure and Impulse Measurements," Lincoln Laboratory Optics Research, No. 2., 1973, p. 29, April 24, 1974.
9. Pirri, A. N., "Theory for Momentum Transfer to a Surface with a High-Power Laser," Phys. Fluids 16, 1435, 1973.
10. Walters, C. T., Barnes, R. H., and Beverly, R. W., "An Investigation of Mechanisms of Initiation of Laser-Supported Absorption (LSA) Waves," Battelle Columbus Laboratories, Final Report on Contract DAAH01-73-A-0776, 1975.
11. Thomas, P. D. and Musal, H. M., "A Theoretical Study of Laser-Target Interaction," LMSC-D352890 Lockheed Missiles and Space Group Report, August 1973.
12. Carslaw, H. S. and Jaeger, J. C., Conduction of Heat in Solids, Clarendon Oxford, 1959.
13. Marcus, S., Lowder, J. E., Manlief, S. K., and Mooney, D. L., "Laser Heating of Metallic Surfaces," Project Report LTP-31, Lincoln Laboratory May 1976.

REFERENCES

14. McKay, J., "High Intensity Coupling Phenomena," Third DOD High Power Laser Conference, Colorado Springs, November 1976.
15. Hall, R. B., Maher, W. E., and Wei, P. S. P., "An Investigation of Laser-Supported Detonation Waves," AFWL-TR-73-28, June 1973.
16. Hall, R. B., Maher, W. E., and Nelson, D. J., "Double-Pulse Laser Interaction Experiments," AFWL-TR-73-296, July 1974.
17. Pirri, A. N., "Enhanced Thermal Coupling," Second DOD High Energy Laser Conference, Colorado Springs, November 1976.
18. Fox, J. A., "A Method for Improving Continuous Wave Laser Penetration of Metal Targets," Appl. Phys. Lett. 26, 682, 1975.
19. O'Keefe, J. D. and Johnson, R. L., "Laser Melt-Through Time Reduction Due to Aerodynamic Melt Removal," AIAA J. 14, 776, 1976.
20. Robin, J. E., and Nordin, P., "Effects of Gravitationally Induced Melt Removal on CW Laser Melt-Through of Opaque Solids," Appl. Phys. Lett. 27, 593, 1975.
21. Robin, J. E. and Nordin, P., "Improved CW Laser Penetration of Solids Using a Superimposed Pulsed Laser," Appl. Phys. Lett. 29, 3, 1976.
22. Masters, J. I., "Problem of Intense Surface Heating of a Slab Accompanied by a Change of Phase," J. Appl. Phys. 27, 477, 1956.
23. Touloukian, Y. S., Powell, R. W., Ho, C. Y., Klemens, P. G., Nicolaou, M. C., Kirby, R. K., Taylor, R. E., and Desai, P. D., Thermophysical Properties of Matter, Thermal Conductivity, Volume 1, Thermal Diffusivity, Volume 10, and Thermal Expansion, Volume 12, IFI/Plenum, 1970-1975.
24. Landau, L. D. and Lifshitz, E. M., Statistical Physics, Addison-Wesley Publishing Company, Inc. 1958.
25. JANAF Thermochemical Data, The Dow Chemical Company, Thermal Laboratory, Midland, Michigan, 1968.
26. Handbook of Chemistry and Physics, p. D-142 of 49th Edition, The Chemical Rubber Co., Cleveland, Ohio, 1969.